

UNCLASSIFIED

AD NUMBER

AD902890

NEW LIMITATION CHANGE

TO

Approved for public release, distribution
unlimited

FROM

Distribution authorized to U.S. Gov't.
agencies only; Test and Evaluation; JUL
1972. Other requests shall be referred to
Air Force Rocket Propulsion Lab., Edwards
AFB, CA.

AUTHORITY

AFRPL ltr, 31 Jan 1974

THIS PAGE IS UNCLASSIFIED

AD902890

1
2

FINAL REPORT
EXPANSION DEFLECTION NOZZLE

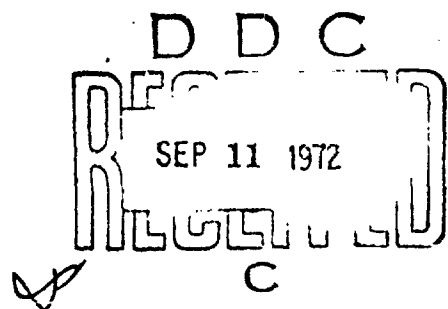
CONTRACT F04611-71-C-0056

FOR
AIR FORCE ROCKET PROPULSION LABORATORY
EDWARDS AIR FORCE BASE, CALIFORNIA

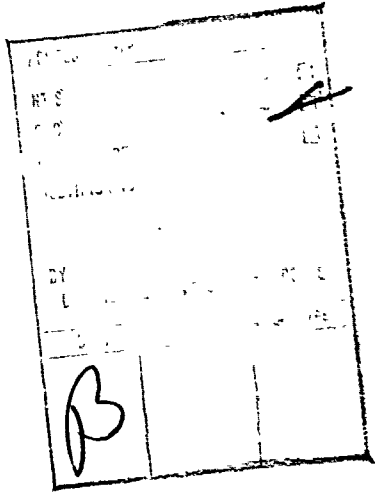
Report AFRPL-TR-72-74

12 July 1972

DD FORM 1
10-65 FILE COPY



AEROJET LIQUID ROCKET COMPANY
A DIVISION OF AEROJET-GENERAL ©
SACRAMENTO, CALIFORNIA



Report AFRPL TR-72-74

(6) EXPANSION-DEFLECTION NOZZLE.

(9) Final Report. 1 May 71-24 Jan 72,

(11) 12 Jul 72

(12) 22 p.

(10) Prepared by

R. C. Schindler ■ S. D. Mercer

(15) F04611-71-C-0056

For

Air Force Rocket Propulsion Laboratory
Edwards Air Force Base, California 93523

Distribution limited to U.S. Gov't agencies only: test
and evaluation data; July 1972. Other requests for this
document must be referred to AFRPL (STINFO/D07),
Edwards, CA 93523.



AEROJET LIQUID ROCKET COMPANY

SACRAMENTO, CALIFORNIA • A DIVISION OF AEROJET-GENERAL G

405 880 ✓

mt

FOREWORD

This report presents the work accomplished on the Expansion-Deflection Nozzle Program under Air Force Contract F04611-71-C-0056. The work reported herein was conducted by Aerojet Liquid Rocket Company, Sacramento, California, under the technical direction of Capt. R. Jamieson, Project Engineer, Air Force Rocket Propulsion Laboratory, Edwards, California.

ALRC program manager was R. C. Schindler. Mr. A. A. Oare was ALRC project engineer from 1 May to 1 December 1971; thereafter, Mr. S. D. Mercer was assigned that position.

This report, which covers the contract period 1 May 1971 through 24 January 1972, has been reviewed and approved.

Capt. Robert A. Jamieson
AFRPL Project Engineer

ABSTRACT

A nine-month exploratory development program was conducted to analyze, design, fabricate, and test hardware to gather data on the operation of an expansion-deflection nozzle. The technical effort consisted of the analysis and design of a nominal 25,000-lb thrust, 1500 psia chamber pressure, expansion-deflection thrust chamber using LO_2/LH_2 propellants at a mixture ratio of 6:1. Several chamber segments and an annular uncooled thrust chamber were designed using an anticipated flight configuration thrust chamber design as a baseline. An annular and a segment injector were analyzed and designed for use on the thrust chambers. The segment injector and both water-cooled and heat sink chambers were fabricated and tested at sea level conditions.

The injector demonstrated acceptable operation at chamber pressures of 300 and 750 psi. Failure of the water-cooled chamber precluded testing at the higher pressure levels.

TABLE OF CONTENTS

	<u>Page</u>
Foreword	ii
Abstract	iii
Nomenclature	xi
I. Introduction and Summary	1
A. Introduction	1
B. Summary	3
II. Conclusions	5
III. Discussion	7
A. Design	10
1. Baseline Thrust Chamber Design	10
a. Nozzle Design Analysis	10
b. Vaporization Analysis	10
c. Stability Analysis	35
d. Nozzle Performance	36
e. Regeneratively Cooled Chamber Design	43
2. Thrust Chambers	55
a. Annular Chambers	55
b. Sector Chambers	55
3. Injectors	86
a. Injector Selection	86
b. Annular Injector Design	88
c. Sector Injector Design	102
B. Fabrication	107
1. Sector Injector	108
a. Vane Fabrication	108
b. Injector Body Fabrication	117
c. Vane-to-Body Assembly	120
d. Injector Assembly Flow Testing	128
e. Conclusions Regarding Injector Fabrication	141

TABLE OF CONTENTS (cont.)

	<u>Page</u>
2. Water-Cooled Axial Throat Thrust Chamber Sector	141
a. Component Fabrication	141
b. Braze Evaluation Program	148
c. Thrust Chamber Assembly	172
d. Conclusions Regarding Chamber Fabrication	177
C. Testing	179
1. Ignition Analysis and Testing	179
2. Sector TCA Testing	188
References	206

TABLE LIST

<u>Table</u>		<u>Page</u>
I	E-D Nozzle Point Design Criteria	8
II	Contour Coordinates	17
III	E-D Nozzle Performance Summary	38
IV	Calorimeter Chamber Hydraulic Analysis - Low Flow Circuit	80
V	Calorimeter Chamber Hydraulic Analysis - High Flow Circuit	84
VI	Injector Design Concepts	89
VII	Injector Vane PN 1161427 - Calculated Element-to-Element Mass Distribution	105
VIII	Chamber Braze Experiments	164
IX	TCA Testing Nomenclature	192
X	Sector Thrust Chamber Test Data Summary	194

FIGURE LIST

<u>Figure</u>		<u>Page</u>
1	25,000 lb Thrust E-D Nozzle Engine Concept	2
2	Weight Biased Performance vs Overall Area Ratio	12
3	Cooling Limitations - Heat Flux	14
4	Nozzle Contour	16
5	E-D Nozzle Internal Expansion Region	18
6	Oxygen Vaporization Characteristics at 300 psia	25
7	Oxygen Vaporization Characteristics at 600 psia	26
8	Oxygen Vaporization Characteristics at 1500 psia	27
9	Effect of Oxygen Injection Velocity	29
10	Effect of Contraction Ratio	30
11	Effect of Gas/Liquid Velocity Differential	31
12	Effect of Element Type	32
13	Comparison of Results from Two Oxygen Vaporization Models	34
14	Neutral Stability Plots for E-D Thrust Chamber	37
15	Possible Cooling Schemes	49
16	E-D Nozzle Point Study - Centerbody Throat	51
17	Predicted Operating Conditions - Regeneratively Cooled Chamber	53
18	Preliminary Design Layout, PN 1161519	54
19	Uncooled Engine Assembly	56
20	Water-Cooled Axial Throat Chamber Assembly	60
21	Water-Cooled Calorimeter Chamber	62
22	Predicted Gas-Side Wall Temperature vs Gas-Side Heat Transfer Coefficient and Coolant Velocity and Temperature	65
23	Predicted Burnout Heat Flux Ratio vs Gas-Side Heat Transfer Coefficient and Coolant Velocity and Temperature	66
24	Burnout Heat Flux and Wall Temperature Limit Lines	67
25	Burnout Heat Flux and Wall Temperature Limit Lines	69
26	Burnout Heat Flux and Wall Temperature Limit Lines	70
27	Burnout Heat Flux and Wall Temperature Limit Lines	71
28	Nodal Locations on Inner and Outer Contours	72
29	Inner and Outer Body Design Data	73
30	Low Pressure Coolant Section Design Data	75
31	Nodal Locations on Side Plates	76

FIGURE LIST (cont.)

<u>Figure</u>		<u>Page</u>
32	Side Plate Design Data	77
33	Inlet Coolant Passage Circuit Designations	81
34	Outlet Coolant Passage Circuit Designations	82
35	Uncooled Chamber - Centerbody Throat Station	85
36	Uncooled Chamber Assembly	87
37	Full-Scale Annular Injector	90
38	Injector Vane Construction	92
39	Oxidizer Metering Platelet - PN 1161422	93
40	Oxidizer Metering Platelet - PN 1161427	94
41	Injector Element Spray Fan Distribution	95
42	Injector Interpropellant Heating	100
43	Effect of Hydrogen Inlet Temperature on Oxygen Heating	101
44	Sector Injector	103
45	Injector Vane Pressure Drop Characteristics	106
46	Injector Vane Water Flow (Side View)	110
47	Injector Vane Water Flow (Angle View)	111
48	Predicted Injector Vane Mass Distribution	113
49	Injector Vane Water Flow Data Summary	115
50	Selected Vanes for E-D Sector Injector SN 1	116
51	Injector Vane Thermal Instrumentation	118
52	Injector Components, Assembled	119
53	Injector Components	122
54	Injector Brazement (Face View)	123
55	Injector Brazement (O_2 Manifold View)	123
56	Injector Vane to Body Braze Specimen (Side View)	125
57	Vane Specimen Showing Vane End to Manifold Wall Clearance (Side View)	125
58	Vane Specimen Showing Vane End to Manifold Wall Clearance (Top View)	125

FIGURE LIST (cont.)

<u>Figure</u>		<u>Page</u>
59	Assembled Sector Injector (Back)	126
60	Assembled Sector Injector (Front)	127
61	Gas Distribution Plates	132
62	Gas Distribution Obtained with Modified Radial Distribution Plate	133
63	Oxidizer Circuit Mass Distribution	136
64	Vane Flow Distribution Measured Prior to and Following Installation	138
65	Injector Combustion Temperature Distribution	140
66	Axial Throat Sector (End View)	143
67	Chamber Centerbody Side Components	144
68	Chamber Outboard Side Components with Braze Foil Pattern Installed	145
69	Centerbody Which Ruptured During Proof Test	147
70	Chamber Centerbody and Side Panel Components After Proof Test	149
71	Chamber Side Panel Installed in Proof Test Fixture	149
72	Sectioned Braze Specimen	151
73	Specimen No. 1 After Fitup Check	153
74	Method of Applying Braze Foil to Curved Specimen Body	154
75	Method of Brazing Specimen Assembly	155
76	Specimen No. 2 After Fitup Check	157
77	Specimen No. 3 After Fitup Check	158
78	Specimen No. 4 After Fitup Check	158
79	Braze Setup to Evaluate Effect of Angle	159
80	Specimen No. 5 After Fitup Check	161
81	Template Used to Layout Braze Alloy Prior to Placement on Curved Section Body	162
82	Method of Cutting and Applying Braze Foil to the Curved Sector Body	163
83	Braze Sample Pull Test Results	165
84	Specimen No. 2 After Brazing	167
85	Specimen No. 1 After Pull Test	168
86	Specimen No. 2 After Pull Test	168

FIGURE LIST (cont.)

<u>Figure</u>		<u>Page</u>
87	Specimen No. 3 After Pull Test	169
88	Specimen No. 3 After Brazing	170
89	Specimen No. 4 After Pull Test	171
90	Water-Cooled Axial Throat Chamber (Forward End)	174
91	Copper Axial Throat Sector Chamber	175
92	Copper Axial Throat Chamber (Aft End)	176
93	O ₂ /H ₂ Torch Ignition Mechanism	180
94	E-D Nozzle TCA Igniter System	182
95	Effect of Igniter MR on Ignition	183
96	Effect of Igniter P _c on Ignition	184
97	Effect of Igniter Throat Size on Ignition	185
98	Injector Start Sequence	187
99	Ignition Test Apparatus	189
100	Ignition Test Results	190
101	Test Schematic for Water-Cooled Chamber/Sector Injector	191
102	Mounted Thrust Chamber and Injector	193
103	Test 3K-6-104 Oscillograph Trace	195
104	E-D Sector Thrust Chamber Test Performance	201

NOMENCLATURE

English Letters

A	- area
C_D	- discharge coefficient
C_f	- nozzle thrust coefficient
C_L	- bulk temperature correction
D_H	- hydraulic diameter
ERE	- energy release efficiency
g	- gravitational constant
h	- heat transfer coefficient
$h_{e\ eff}$	- effective coolant side heat transfer coefficient
h_g	- gas-side heat transfer coefficient
h_l	- liquid-side heat transfer coefficient
I_{sp}	- specific impulse
k	- thermal conductivity
KW	- flow admittance factor = $(w/\sqrt{\Delta P} SG)$
L'	- combustion chamber length
L*	- characteristic chamber length
L_{gen}	- generalized length
MR	- mixture ratio
MRC	- mixture ratio control
MRD	- mixture ratio distribution
MW	- molecular weight
P_c	- chamber pressure
Pr	- Prandtl number
Q/A	- heat flux
R_{BO}	- ratio of design heat flux to burnout heat flux
Re	- Reynolds number
SG	- specific gravity
St	- Stanton number
t	- wall thickness
T	- temperature

NOMENCLATURE (cont.)

English Letters (cont.)

T_{sat}	- saturation temperature
T_{WG}	- gas-side wall temperature
T_{WL}	- liquid-side wall temperature
ΔT_{sub}	- subcooling ($T_{sat} - T_b$)
U	- overall heat transfer coefficient
V	- velocity
w	- flow rate

Subscripts

b	- bulk conditions
Bo	- burnout
C	- coolant
cu	- curved conditions
e	- exit
f	- film conditions
g	- gas
o	- stagnation
r	- recovery
s	- straight conditions
SL	- sea level
t	- throat
w	- wall
$2-D$	- two-dimensional values
∞	- free stream

NOMENCLATURE (cont.)

Greek Letters

α	- Mach angle
γ	- ratio of specific heats
δ^*	- boundary layer displacement thickness
ϵ_b	- base area ratio - $A_{\text{plug}}/A_{\text{throat}}$
ϵ_o	- overall area ratio
η_{c^*}	- c^* efficiency
θ	- flow angle
θ_T	- throat angle
μ	- viscosity
ρ	- density

I. INTRODUCTION AND SUMMARY

A. INTRODUCTION

Recent interest in LO₂/LH₂ space maneuvering engines has caused review of engines that deliver high performance in a restricted engine length. The expansion-deflection (E-D) nozzle combined with high operating pressure is one of the engine design candidates for length-limited applications. Although the E-D concept is not new, neither the actual altitude performance nor feasibility of regeneratively cooling this type of nozzle have been demonstrated. Earlier work with storable propellants had indicated cooling to be a problem. Advances in thrust chamber design, namely nontubular construction, combined with the use of LH₂ as a coolant appear to offer good potential to regeneratively cool an E-D nozzle.

An exploratory development program sponsored by the Air Force Rocket Propulsion Laboratory, Contract F04611-71-C-0056, was awarded to ALRC. The objective of this program was to analyze, design, fabricate, and test hardware to gather data on the operation of an expansion-deflection nozzle. The technical effort was to consist of analysis and design of a nominal, 25,000-lb thrust, 1500 psia chamber pressure, expansion-deflection thrust chamber using LO₂/LH₂ propellants at a mixture ratio of 6:1. An artist's concept of a nominal 25,000-lb-thrust engine is shown in Figure 1. Several chamber segments and an annular uncooled thrust chamber were to be designed using an anticipated flight configuration thrust chamber design as a baseline. Injectors were to be designed and analyzed for use on the chambers. Finally, a water-cooled segment chamber, an uncooled segment chamber, and a segment injector were to be fabricated and tested.

The technical effort was divided into six complementary subtasks: (1) design of an E-D nozzle and thrust chamber assembly compatible with an envelope of 82 in. length and 87 in. diameter, (2) a vaporization analysis

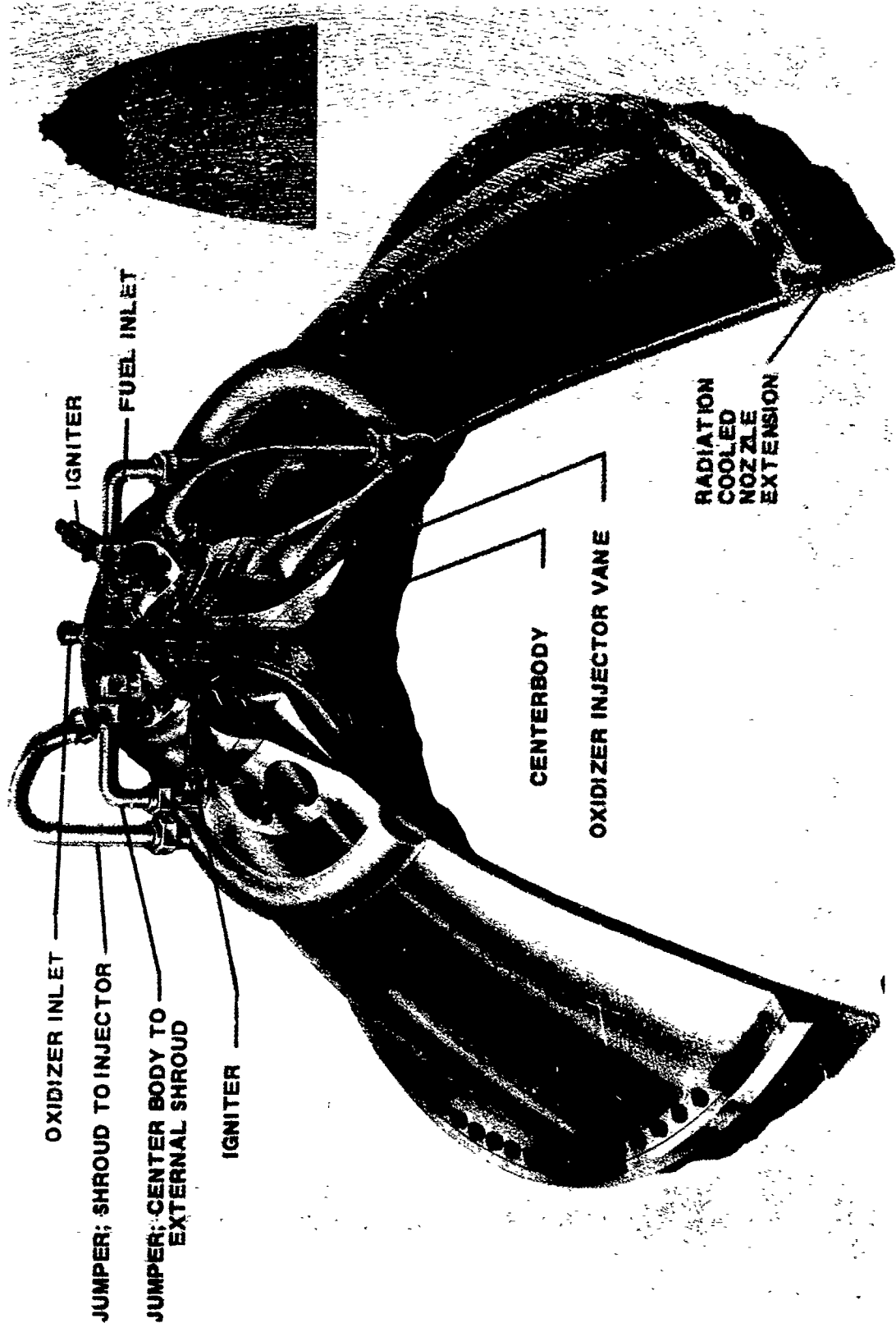


Figure 1. 25,000 lb Thrust E-D Nozzle Engine Concept

I, A, Introduction (cont.)

to determine the required combustor length to theoretically product 99.5% energy release efficiency (ERE)*, (3) the design of several thrust chambers using the 25K thrust chamber as a base, (4) the design of a full annular and a 1/7-segment (sector) of a full annular injector, (5) fabrication of a sector injector and two sector thrust chambers (one cooled and one uncooled), and (6) testing of a sector TCA at ambient conditions. The annular designs were used as a base to ensure that the sector hardware was representative in terms of all pertinent design parameters.

This report describes the technical effort conducted on the program, which included the preliminary design of an E-D nozzle thrust chamber assembly and the design, fabrication and testing of a one-seventh sector thrust chamber assembly.

B. SUMMARY

The major effort of the program encompassed an eight-month period. Program accomplishments include the analysis and design of a full-scale (25K lb, 1500 psia) annular injector, a stability analysis of the E-D nozzle thrust chamber, the design of an optimized baseline E-D nozzle contour, and the preliminary design of a full-scale regeneratively cooled thrust chamber. Several sector (one-seventh of the annulus) components were designed including a sector injector, a water-cooled and a heat sink thrust chamber with axial throats (for sea level performance evaluation), and a water-cooled calorimetric thrust chamber which was a sector of an E-D nozzle. The sector injector and two axial throat sector thrust chambers (one heat sink and one water-cooled) were fabricated and tested.

*Energy Release Efficiency - ERE is injector performance efficiency due to incomplete propellant vaporization, incomplete microscale mixing, and incomplete reaction.

I, B, Summary (cont.)

Testing was accomplished at nominal chamber pressure levels of 300 and 700 psia (the 300 psia corresponds to the minimum P_c of the required engine throttling range of 5:1). Injector performance of 97% ERE and smooth operation were demonstrated in a chamber length of 3 in. The injector consisted of radial vanes which injected oxidizer from orifices on their trailing edges. The gaseous fuel flowed between the vanes. Insulator platelets within the vanes proved to be effective in preventing two-phase oxidizer flow even at the 300 psia (minimum thrust) level.

Fabrication problems encountered during the brazing of the water-cooled axial throat sector chamber led to the development of techniques for fitting and brazing heavy walled components of compound curvature.

II. CONCLUSIONS

1. Regenerative cooling of E-D nozzle thrust chambers requires that combustor lengths be minimized. Vane-type injectors (a version of ALRC's HIPERTHIN) are suitable to this application. An energy release efficiency of 97% was demonstrated with this type injector in a 3-in. combustor length at 300 psia chamber pressure.

2. Vane-type injectors which employ oxidizer cooling are applicable to high pressure, throttleable O_2/H_2 engines. Vanes incorporating insulator platelets were tested at 300 psia (5:1 throttling) with no evidence of two-phase oxidizer flow. This exceeded the 2:1 throttling limit (or approximately 800 psia) predicted by analysis.

3. The program performance goal of 99.5% ERE was not demonstrated; however, the hot fire data and analysis indicate that this is achievable in a 3.0-in.-long combustor. The demonstrated value of 97% is based on a calculated mixture ratio distribution loss of approximately 6%, which was obtained from measured propellant distribution using water and CN_2 as propellant simulants during injector cold flow testing. Testing of a second unit with acceptable propellant distribution is required to more accurately assess the performance of the basic injector design.

4. Injector cold flow characterization proved to be a valuable development tool. Cold flow tests on the tested sector injector allowed identification of the 6% propellant maldistribution (mixture ratio) loss that precluded the achievement of the program performance goal. This loss was subsequently used to evaluate the hot firing results.

5. Brazing of rigid heavy walled components of compound curvature can be accomplished. Success is primarily dependent on the ability to attain and quantify component fitup at the braze interface. Postmachining fitup by the use of EDM machining to "burn" the components together at the braze interface

II, Conclusions (cont.)

removes burrs and assures proper fit. Component fit can be inspected by using measured quantities of Dykem blue* applied to one part and transferred to the other during fit check at the interface.

6. Inspection of chamber brazements by ultrasonic methods is not adequate for determining bond quality when the brazed surface does not lie in a plane.

7. Use of heavy walls (gas side) which are later machined to the required thickness following brazing to support members is a viable technique for nontubular thrust chamber fabrication. This process avoids the need for extensive tooling (i.e., expandable bladders) to contain thin-wall gas-side members.

8. The two technical uncertainties that preclude the use of E-D nozzles (namely, nozzle performance and cooling feasibility) remain unanswered. The program was unable to obtain sufficient data relative to nozzle shape and heat transfer coefficient to demonstrate the feasibility of regenerative cooling. Data examined during the program indicates that the concern over the heat transfer coefficient value is warranted. Future investigations concerned with the utility of the E-D nozzle concept should concentrate on the heat transfer characterization of the E-D nozzle configurations prior to further TCA development.

*Dykem Hi-Spot Blue No. 107 is developed by the Dykem Co., St. Louis, Mo., specially for showing the high spots to be scraped off in truing all kinds of round and flat bearing surfaces and other close fits.

III. DISCUSSION

As indicated in Section I, the technical effort consisted of three basic subtasks, namely, design, fabrication and test. The design task consisted of the baseline design of a regeneratively cooled E-D nozzle thrust chamber assembly that satisfied the criterion specified in Table 1. Secondly, several chamber segments, corresponding to a one-seventh sector of a full annulus, and a sector injector were designed using the geometry and design constraints determined from the baseline design. Analytical efforts which were conducted in support of the design phase included optimization of the nozzle contour, vaporization analysis, stability analyses and performance and heat transfer studies.

The vaporization analyses defined the required chamber length for complete vaporization of the oxidizer to theoretically produce 99.5% energy release efficiency. Combustion stability analyses indicated that damping devices were not required in the thrust chamber. A performance analysis using the optimized contour was used to predict a theoretical performance level of 470.8 sec at the nominal operating conditions ($MR = 6$, $P_c = 1500$ psia). The heat transfer analyses were used to (1) select the engine base area ratio (area of plug/area of throat) of 10, (2) provide the preliminary design of a regeneratively cooled thrust chamber, and (3) support the design of the injectors and thrust chambers.

Following configuration of the baseline thrust chamber assembly, the following thrust chambers were designed:

- (1) A water-cooled axial throat segment sized to accept a 1/7-segment of the injector for the baseline thrust chamber. The purpose of the unit was to obtain sea level performance data with the sector injector at 1500 psia chamber pressure as well as intermediate P_c values.

TABLE I
E-D NOZZLE
POINT DESIGN CRITERIA

Propellants	LO ₂ /LH ₂
Thrust (lbf)	25,000
Chamber Pressure (psia)	1,500
Mixture Ratio	6.0 \pm 1.0
Life Coal, cycles	100
Nozzle Expansion Ratio	To provide optimum expansion of gases, biased by weight and length (>250:1).
Throttle Ratio	.3:]
Thrust Chamber, noclant passage construction	Non-Tubular
Nozzle	Cooled and/or Uncooled

III, Discussion (cont.)

(2) The second sector thrust chamber design was identical to the first except that it was heat sink cooled. The purpose of this unit was to checkout the injector and obtain performance data at low chamber pressure.

(3) The third thrust chamber design was a water-cooled calorimetric segment containing transverse cooling passages for the purpose of obtaining heat flux versus axial station data. The contour of this unit was identical to that of the baseline thrust chamber.

(4) The fourth design was an uncooled segment with a contour identical with item (3). The purpose of this unit was to obtain thermal data on an E-D nozzle contour at low chamber pressure.

(5) The fifth design was an uncooled annular chamber with a contour identical to the baseline design.

Two injectors were also designed: (1) a full annular design capable of throttling 5:1 with a predicted theoretical energy efficiency of 99.5% and (2) a segment design which represented 1/7 of the annular design. Both units employed a HIPERTHIN injection scheme.

Of the designs delineated above, the first two chamber designs and the sector injector were fabricated. The sector injector and the matching water-cooled axial throat chamber were selected for fabrication in order to establish baseline performance data. The uncooled heat sink chamber was initiated as a fabrication experiment to verify the fitup techniques and procedures required in the later stages of the cooled chamber fabrication. The unit was subsequently completed in order to allow test facility checkout fire tests with minimal risk to the water-cooled sector thrust chamber. Fabrication problems encountered in brazing both the injector and the water-cooled segment resulted in brazing

III, Discussion (cont.)

studies and experiments during the fabrication phase of the program. The solution of problems in the areas of brazing technique and component fitup represents a major accomplishment of the program and is discussed in the later sections of this report.

Testing was accomplished in two areas, namely, igniter checkout and verification and sector TCA testing. Igniter testing proved the successful operation and durability of the igniter. Sector TCA tests were conducted at sea level using both the uncooled and water-cooled chambers. Testing was terminated at the 700 psi level with a failure of the water-cooled chamber. Preceding tests at 300 psia chamber pressure verified smooth injector operation and the capability of the injector to operate at 1/5 nominal thrust.

The design, fabrication and testing subtasks are discussed separately. In the following sections, support analyses are included where applicable in the discussion of the individual component designs.

A. DESIGN

1. Baseline Thrust Chamber Design

The design of a baseline thrust chamber which provided an anticipated final design was necessary to ensure that the segment hardware were realistic 1/7 sectors of a flight type design. Activities conducted to define the baseline design consisted of nozzle design analysis, vaporization studies, stability analysis, performance and heat transfer studies.

a. Nozzle Design Analysis

The nozzle design process consisted of three interrelated tasks: (1) performance optimization study to select the exit plane area ratio for a maximum engine stowed length of 82 in., (2) selection of a base area ratio ($\epsilon_b = A_{\text{plug}} / A_{\text{throat}}$), and (3) final contour design.

III, A, Design (cont.)

(1) Optimization Study

An optimization study was conducted to establish the baseline design. The results of this overall performance optimization are displayed on Figure 2, where weight-biased specific impulse is plotted versus exit area ratio for a range of base area ratios from 10 to 40. When the 82-in. engine length limitation is factored into the analysis, the primary conclusions are:

- (a) The highest performing configurations utilize the entire allotted length envelope.
- (b) For the assumptions used in the study, optimum performance is not significantly influenced by base area ratio selection.

However, two factors which are quite sensitive to base area ratio were not included in this optimization analysis. The first factor was the variation of heat flux as the throat gap varies with base radius ratio. Heat transfer analysis indicates that the calculated heat flux for an $\epsilon_b = 10$ configuration could be accommodated by the proposed regenerative cooling system without requiring zone mixture ratio control (see below). The throat heat flux increases as base area ratio increases. Configurations with an $\epsilon_b = 23.8$ require zone mixture ratio control beyond practical considerations. Although a quantitative factor for this heat flux variation with ϵ_b was not included in the study, it was concluded that the $\epsilon_b = 10$ configuration is favored when consideration is given to this effect.

The other factor not included in the study is the combustion stability index variation as a function of base area ratio. The stability analysis discussed in a later section indicates that stability damping devices are more easily accommodated as the base area ratio and chamber diameter

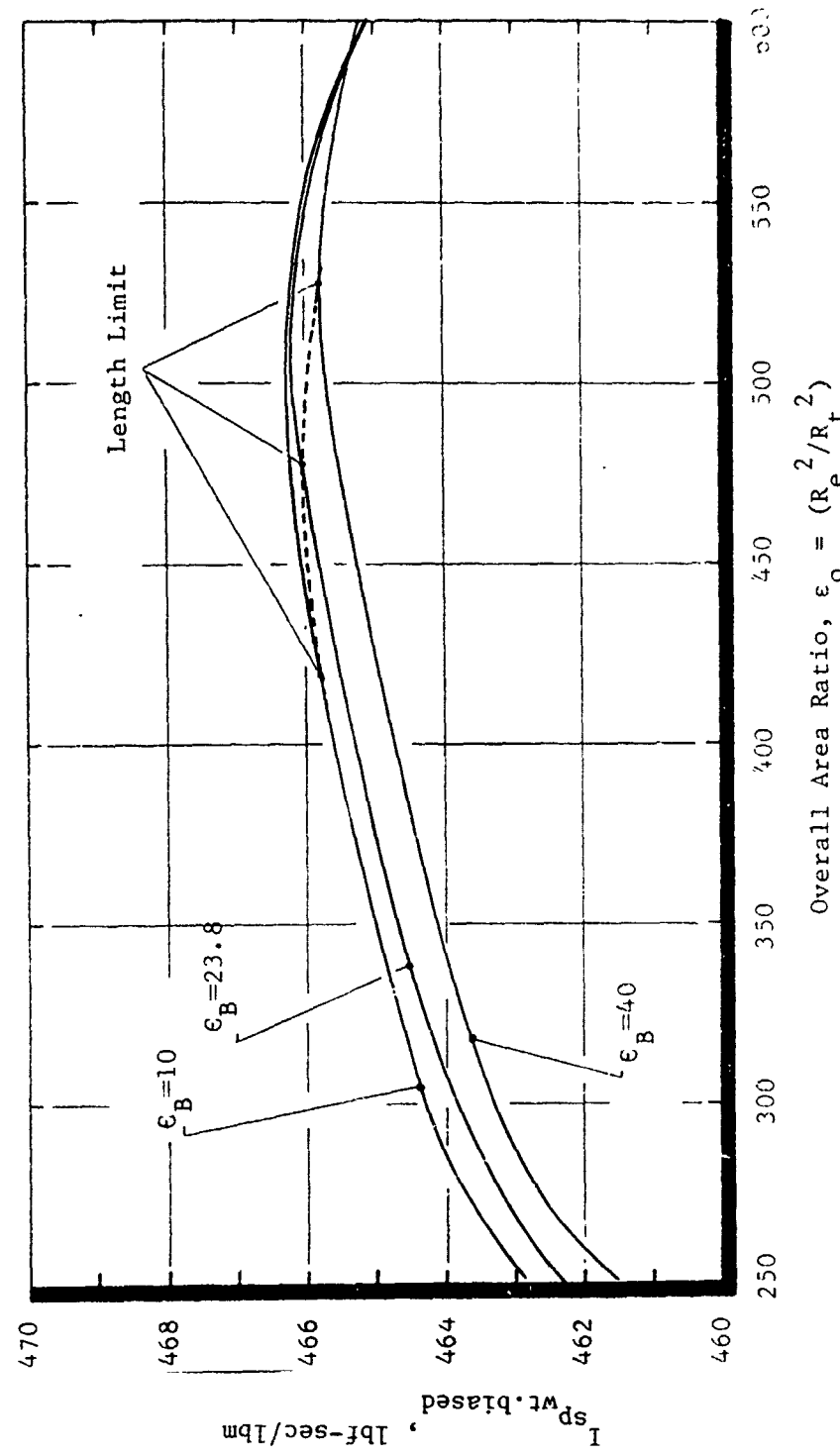


Figure 2 . Weight Biased Performance vs Overall Area Ratio

III, A, Design (cont.)

are reduced. This results in an increase in the frequency of any combustion oscillation, which decreases the length requirement for dampening devices. Therefore, stability considerations also tended to favor the $\epsilon_b = 10$ configuration.

(2) Base Area Ratio Selection

The annular combustion chamber and throat result in large cooled surface area and, consequently, higher total heat load compared to a conventional nozzle. In addition, the throat heat flux increases with decreasing throat gap. For a given thrust level, the geometrical proportionalities are shown below:

$$\text{Surface area} \propto \sqrt{\epsilon_b}$$

$$\text{Throat gap} \propto \frac{1}{\sqrt{\epsilon_b}}$$

A thermal analysis was used to define the effects of base area ratio on thrust chamber cooling at the nominal 25K thrust level. The results (Figure) indicate that the approximate bounds on heat flux and chamber area ($70 \text{ Btu/in.}^2\text{-sec}$ and 260 in.^2) are achieved at a base area ratio of 10. Further, when the possibility of zone mixture ratio control (MRC) was investigated, it was concluded that operation without MRC is not feasible unless the base area ratio is on the order of 10 or less. Calculations indicated that, if the thrust chamber has a base area ratio in excess of 24 and the throat is at nearly the same radial location, the mixture ratio at the boundary layer should be 2.3 or less in order to maintain a gas-side wall temperature less than 1000°F .

Combustion Chamber Wall Area, in.²

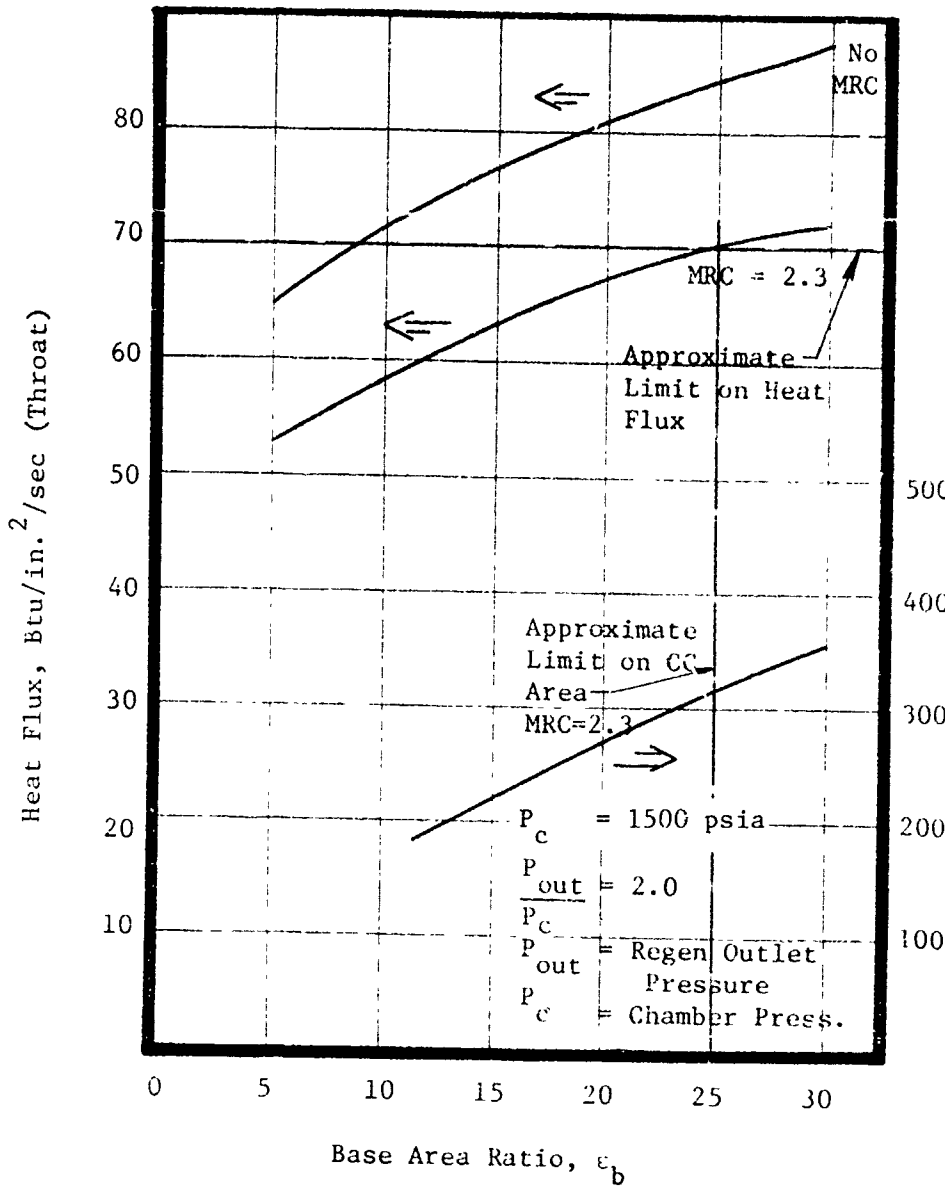


Figure 3. Cooling Limitations - Heat Flux

III, A, Design (cont.)

(3) Nozzle Contour Design

The nozzle contour was established by modifying previously developed computer programs for design of various thrust expansion-deflection nozzles. The modified programs employed a flow field patching technique for mating internal expansion sections to maximum thrust external expansion contours. The method yields an exact (finite difference solution) potential flow contour for axisymmetric flow as opposed to simple vane methods, which result in approximate solutions for the axisymmetric case.

The principal modification was a free boundary subroutine to obtain a null boundary. The null boundary is one along which the rate of change of Mach number along the incident characteristic is zero. In an axisymmetric flow, the null boundary results in a flow which is analogous to a simple vane expansion in plane flow. The null boundary subroutine is used for design of the centered expansion/internal expansion section. Other minor modifications were required to facilitate patching of the flow field solutions together to form a nozzle having internal expansion, transition and external expansion sections.

(a) General

The entire nozzle contour is shown graphically in Figure 4 and the contour coordinates are presented in Table II. Figure 5 shows details of the internal expansion region.

The contour was designed in three discrete segments: (1) external contour, (2) internal contour, and (3) transition contour. These regions are shown in Figure 5. The internal contour extends from Point B at the throat to Point A on the plug lip curvature. It also includes the radius

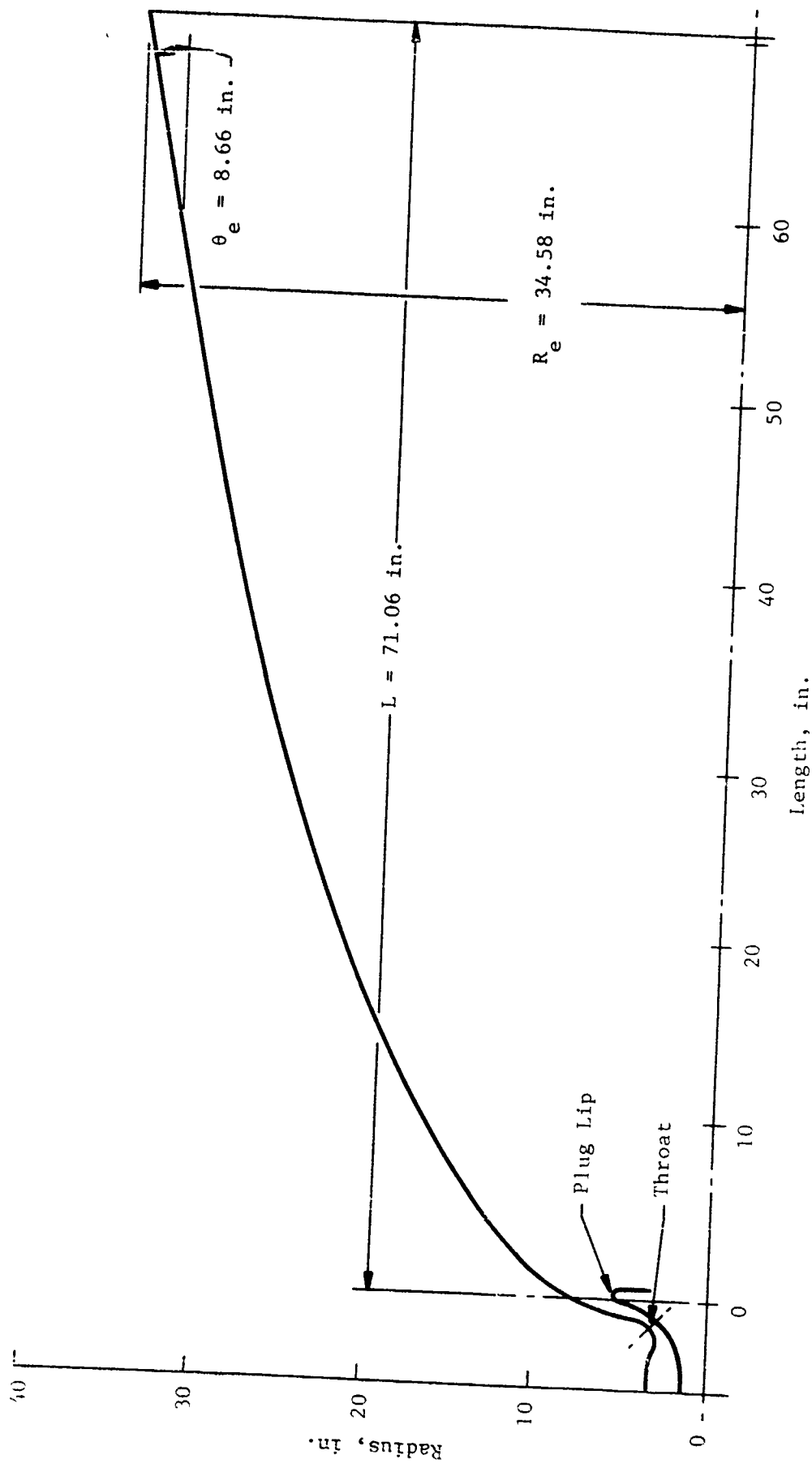


Figure 4. Nozzle Contour

TABLE II
CONTOUR COORDINATES

$$\begin{aligned}\epsilon_o &= 435 \\ \epsilon_b &= 10\end{aligned}$$

$$\begin{aligned}\text{Throat Gap} &= 0.4976 \text{ in.} \\ \text{Throat Area} &= 8.65 \text{ in.}^2\end{aligned}$$

$$\begin{aligned}\text{Throat Angle} &= 45^\circ \\ R_{\text{lip}} &= 7/16 \text{ in.}\end{aligned}$$

Shroud Contour		Plug Contour	
X, in.	R, in.	X, in.	R, in.
-1.4282	2.9433	-1.0763	2.5915
-1.3878	2.9859	-0.9699	2.6979
-1.3497	3.0305	-0.9349	2.734
-1.3027	3.0929	-0.8911	2.781
-1.2808	3.1253	-0.8351	2.846
-1.2502	3.1753	-0.7629	2.936
-1.222	3.2268	-0.6709	3.064
-1.1969	3.2798	-0.6202	3.141
-1.1745	3.3339	-0.5706	3.220
-1.1549	3.3892	-0.5214	3.3050
-1.1263	3.4511	-0.4733	3.3938
-1.02	3.900	-0.4256	3.4887
-0.90	4.380	-0.3792	3.5889
-0.7927	4.8421	-0.3333	3.6969
-0.7050	5.2272	-0.2892	3.8111
-0.6151	5.6434	-0.2460	3.9354
-0.5219	6.0995	-0.2050	4.0680
-0.4871	6.2767	-0.1659	4.2124
-0.2968	6.9461	-0.1298	4.3676
0.0084	7.6647	-0.0971	4.5337
1.0486	9.3848	-0.0688	4.7200
2.6741	11.2596	-0.0516	4.8609
4.821	13.192		
7.519	15.185	-0.0215	4.9781
10.766	17.206	0.0495	5.0951
14.576	19.237	0.1023	5.1478
18.970	21.266	0.1408	5.1766
23.946	23.266	0.1823	5.2010
29.520	25.225	0.2261	5.2208
35.700	27.127	0.2626	5.2330
42.491	28.956		
49.868	30.692		
57.889	32.335		
66.501	33.862		
71.055	34.584		

$$A_t = 8.65 \text{ in.}^2$$

Throat gap = 0.4976 in.

$$\epsilon_b = 10$$

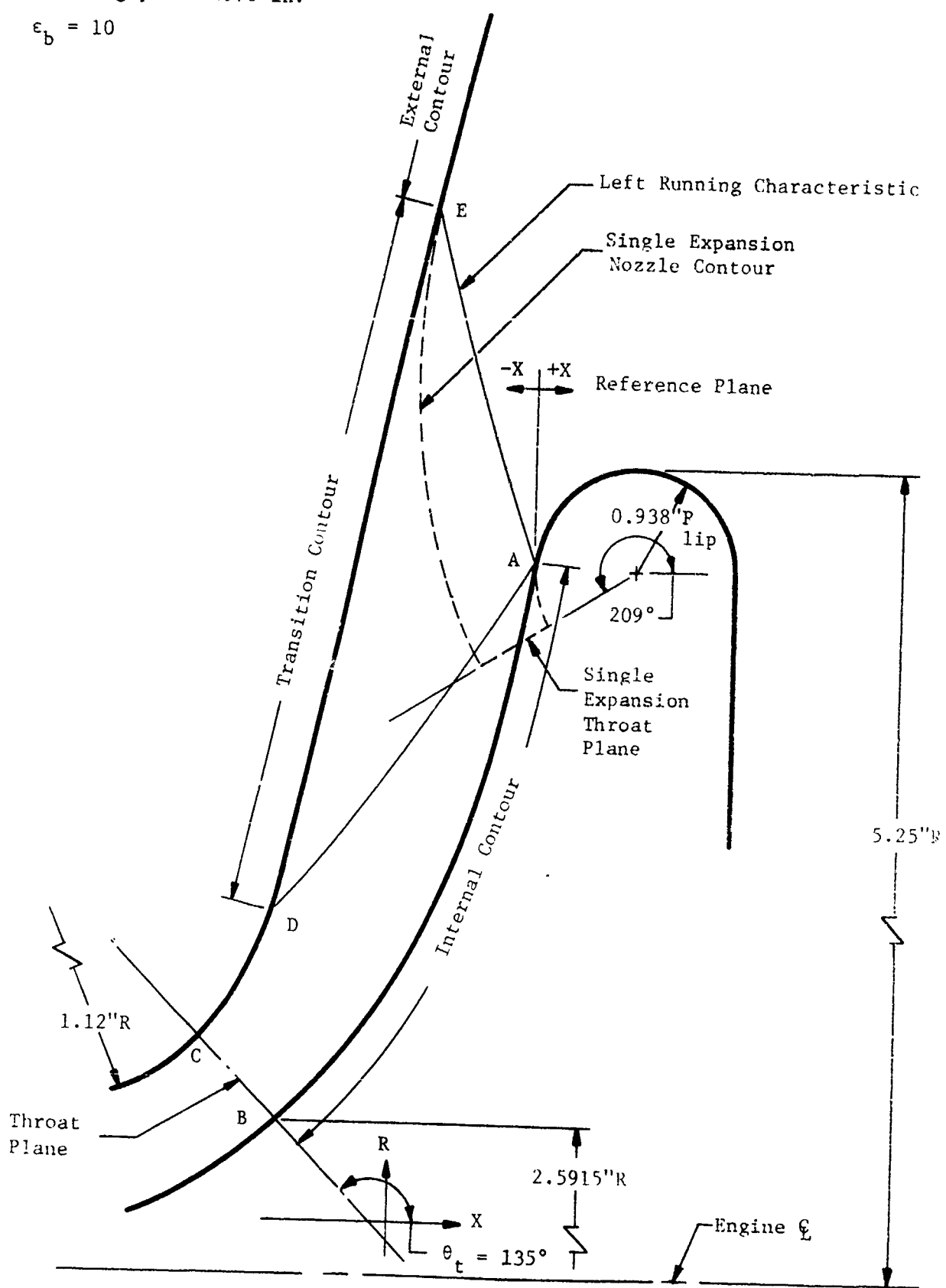


Figure 5. E-D Nozzle Internal Expansion Region

III, A, Design (cont.)

of curvature CD on the outboard contour. The transition contour extends from Point D to Point E on the outboard contour. The external contour extends from Point E to the exit (not shown in Figure 5). The right running characteristic AD marks the end of the internal expansion region in which the flow is being turned in the positive direction away from the axial direction. The left running characteristic AE marks the beginning of the external expansion region in which the flow is turned toward the axis. Essentially no expansion occurs in the transition region.

The parameters which were used as a basis in defining the nozzle contour are listed below:

Ratio of specific heats (γ) = 1.2
Overall area ratio (ϵ_o) = 435
Base area ratio (ϵ_b) = 10
Total engine length (L_o) = 82 in.
Throat angle (θ_t) = 45 degrees
Throat area (A_t) = 8.65 in.²
Plug lip radius (R_{lip}) = 0.438 in.

Upstream radius of curvature at throat on outboard side:

$$(R_{u_o}) = 1.120 \text{ in.}$$

Downstream radius of curvature at throat on outboard side:

$$(R_{d_o}) = 1.120 \text{ in.}$$

Upstream radius of curvature at throat on inboard side:

$$(R_{u_i}) = 6.00 \text{ in.}$$

III, A, Design (cont.)

The ratio of specific heats ($\gamma = 1.2$) was selected as representative of O_2/H_2 propellants at a mixture ratio of 6.0 and chamber pressure of 1500 psia. The magnitude of the overall area ratio (ϵ_0) was based on the previously described optimization study. This study considered the tradeoff between engine weight and performance as defined by the following exchange ratios:

$$\frac{\Delta \text{ Payload}}{\Delta I_{sp}} = 151 \text{ lb/sec}$$

$$\frac{\Delta \text{ Payload}}{\Delta \text{ Burnout Weight}} = -3.68$$

The base area ratio, which was also evaluated in the above mentioned optimization, was found to have only a small effect on performance over the range of interest. A base area ratio of 10 was selected as a compromise between performance, heat transfer, and combustion stability considerations.

The optimization study also showed that maximum performance was realized by utilizing the full 82 in. of envelope length. Of the 82 in., 10 in. were required for the combustion chamber (gimbal block to throat station) and approximately one inch was required for the internal expansion region. Thus, the nozzle length from the reference plane (Figure 4) to the exit plane was 71 in.

The radii of curvature adjacent to the throat and at the plug lip were based on fabrication and cooling considerations. Namely, the minimum cutter size possible for use was based on the estimated slot depth at those locations.

III, A, Design (cont.)

(b) External Expansion Contour

The calculus of variations was utilized to establish the external contour producing the maximum thrust within the maximum allowable engine length of 82 in. The method is similar to that which was developed by Rao (Ref 1) and is in wide use for the design of optimum conventional nozzles. Rao (Ref 2, 3) has documented the extension of his optimization technique to the E-D nozzle and this method has been programmed for the UNIVAC 1108 computer.

As previously stated, the external contour shown in Figure 4 was generated as a segment of a single expansion (i.e., having no internal expansion) E-D nozzle. The single expansion contour was designed to yield maximum thrust for the given length (71 in.), base area ratio (10), and ambient pressure (vacuum). The resulting area ratio was 435, which was in good agreement with the optimum area ratio previously calculated using a less rigorous technique. The resulting angle between the throat plane and the nozzle axis of the single expansion nozzle was 209°. The low area ratio portion of the single expansion nozzle (shown as a dashed line in Figure 5) was replaced subsequently by an internal expansion section which produced identical flow conditions along the patch line AE. Thus, such a modification of the initial contour does not alter the overall nozzle performance.

The initial point on the external contour (Point E) is defined by the intersection of the left running characteristic from Point A with the single expansion contour. The method for locating Point A is described in the internal expansion contour section.

III, A, Design (cont.)

In generating the contour of the single expansion nozzle, the plug geometry at the throat and downstream (R_{lip} in Figure 5) was made circular with a 0.438-in. radius of curvature. The external contour between the throat and that portion of the nozzle defined by the variational design technique was assumed to be a null expansion boundary. A null expansion boundary is defined as one wherein the rate of change of Mach number with respect to length along the characteristics is equal to zero at the boundary. This type of boundary was selected because it permits the design of isentropic nonzero kernel single expansion nozzles in a manner analogous to the case of plane flow.

(c) Internal Expansion Contour

Internal expansion is employed in the E-D nozzle to reduce the angle of the throat plane from 209° of the pure external expansion nozzle to, in this case, 135° . Thus, considerably less turning is required of the gases from the axial combustion chamber to the throat, reducing both the heat loads and plug ejection loads. However, some throat inclination was desirable in order to allow throat area variation by translating the plug. Based on the above considerations, a throat angle of 135° was selected as a compromise.

The contour of the outboard boundary of the internal expansion section (CD of Figure 5) was defined by a radius of curvature of 1.120 in. This value again was estimated to be a minimum due to fabrication limitations. The contour on the inboard or plug side (boundary AB) was calculated using the method of characteristics assuming a null expansion boundary. That is, the boundary point along each right running characteristic was located assuming the rate of change of Mach number with distance along the characteristic was zero at the wall. The use of a null expansion boundary results in an axisymmetric expansion process equivalent to a simple wave expansion in plane flow. The expansion section has a minimal effect on delivered performance since a null expansion contour has the property that a maximum rate of gas flow turning is

III, A, Design (cont.)

achieved while maintaining an isentropic flow. The result is a small internal expansion section having the least performance loss (due to viscous shear at the walls and divergence efficiency of the complete nozzle) and permits the largest chamber mean diameter for a particular base area ratio.

The particular internal expansion section which can be patched onto the external expansion section must be found by a trial-and-error process since the radial location of the throat plane is not known a priori. The conditions which must be satisfied are continuity and the Mach numbers at the point of tangency between the internal expansion section contour and the plug lip radius (Point A in Figure 5) must be the same for both internal and external expansion section solutions. The radial throat location is varied parametrically until these conditions are satisfied. The conditions of continuity and a common point (Point A) on two characteristics of opposite family are sufficient to assure that a transition contour can be found which connects the internal and external expansion sections.

(d) Transition Contour

The flow properties along the left running characteristic AE are known from the external contour calculation and the flow properties along the right running characteristic AD are known from the calculation of the internal expansion section. The transition contour (DE in Figure 5) was established by using these data to generate the characteristic net in the region ADE to define the flow, and subsequently the boundary points are established from continuity considerations. The resulting Mach numbers along the transition contour are very nearly constant at about 2.34.

b. Vaporization Analysis

The need to minimize combustion chamber length (L') while maintaining a high level of performance was of prime importance to the design of an E-D nozzle engine. The requirement for minimizing L' is as follows. First,

III, A, Design (cont.)

minimum combustion length results in a smaller thruster package because of a shorter length chamber. Second, minimum L' is important with regard to thrust chamber cooling. Reduced L' may be the difference between the need for or absence of barrier cooling and, hence, between success and failure of the thermal design. Other benefits which also accrued from reduced L' were reduced weight and cost and the simplification of the chamber structure required to maintain throat concentricity.

In order to minimize the L' without loss of combustion efficiency, it is necessary to complete propellant vaporization rapidly. This requires that the injector produce fine droplets so that a maximum amount of liquid surface is exposed. This requires an extremely fine and uniform injection pattern.

To this end, a vaporization analysis was conducted which examined orifice size in conjunction with chamber pressure, chamber length, injection velocity, contraction ratio, and the gas/liquid velocity differential.

The effect of chamber pressure and orifice jet diameter on oxygen vaporization is presented in Figures 6 through 8, where evaluations were made for pressures of 300, 600 and 1500 psia, respectively, and jet diameters of 0.02, 0.05 and 0.08 in. These data indicate that lower chamber pressure results in lower propellant vaporization. These results are obtained since the generalized length (L_{gen}) of Reference 4 (where % vaporized = $f(L_{gen})$) is proportional to chamber pressure to the 0.66 power. Since the other parameters such as injection velocity were held constant for all chamber pressures, the data in Figures 6 through 8 are not directly representative of a throttling configuration. Increasing orifice jet diameter (i.e., $C_D D$) also results in lower vaporization efficiency since larger propellant droplets are formed.

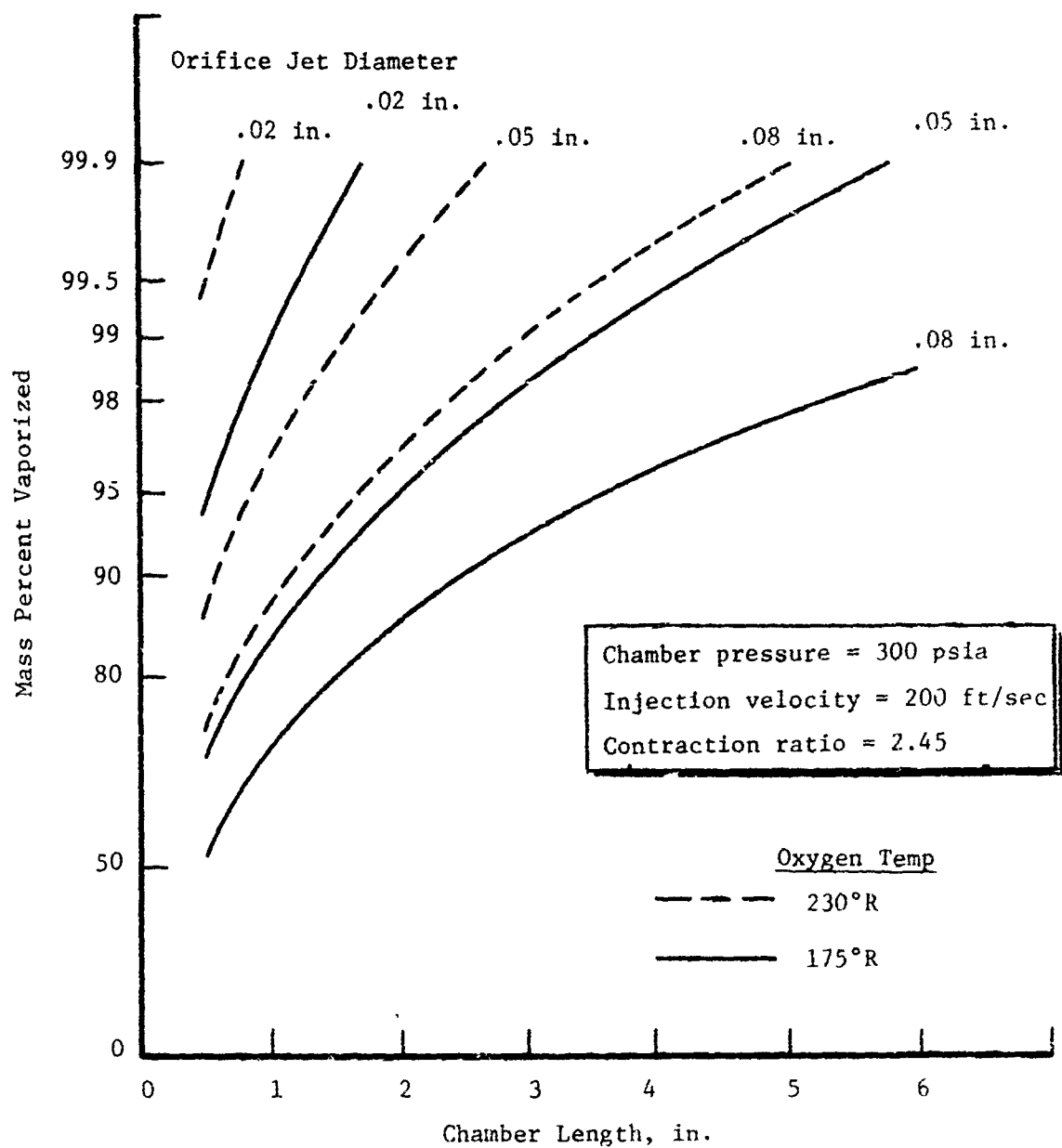


Figure 6. Oxygen Vaporization Characteristics at 300 psia

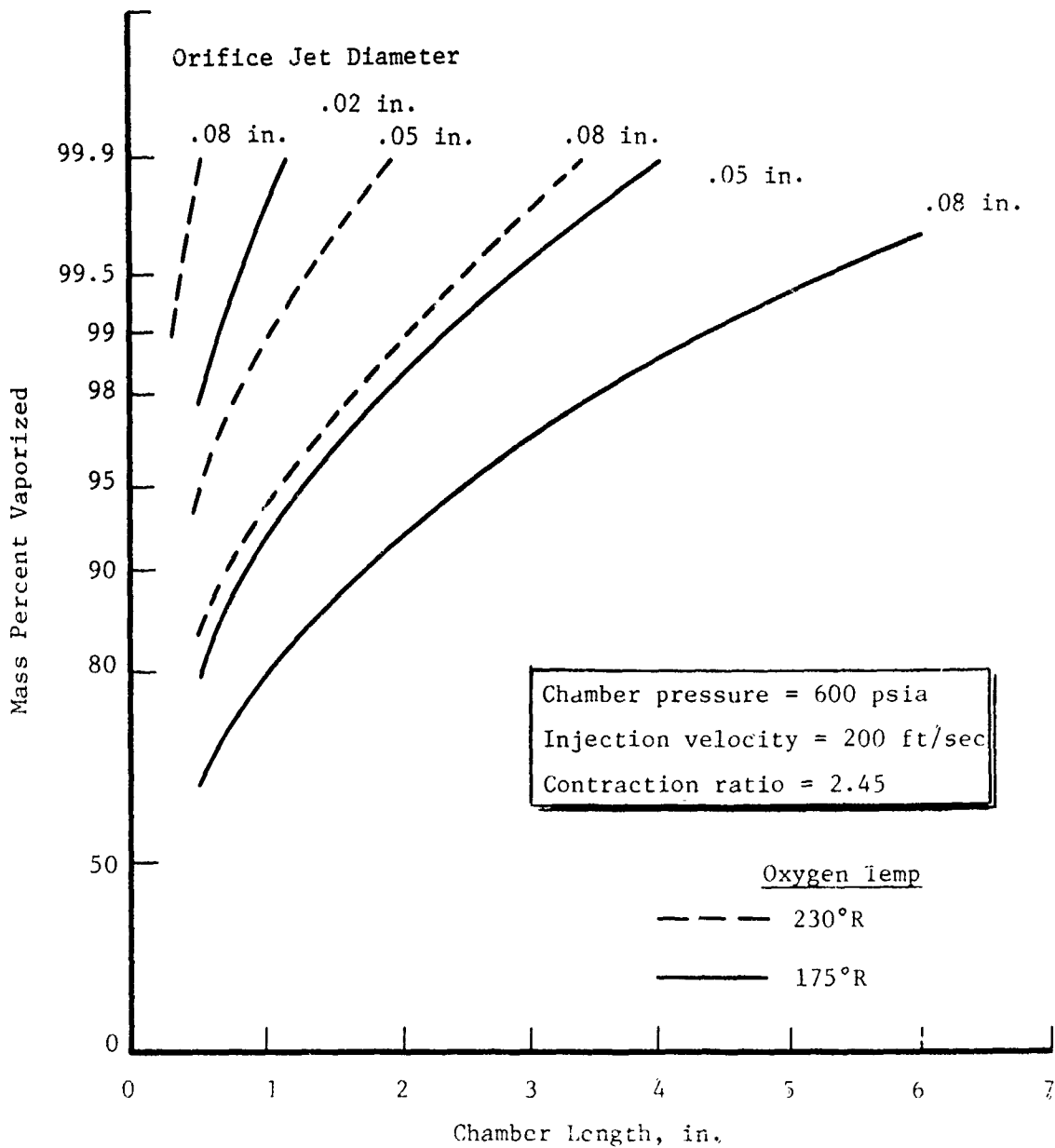


Figure 7. Oxygen Vaporization Characteristics at 600 psia

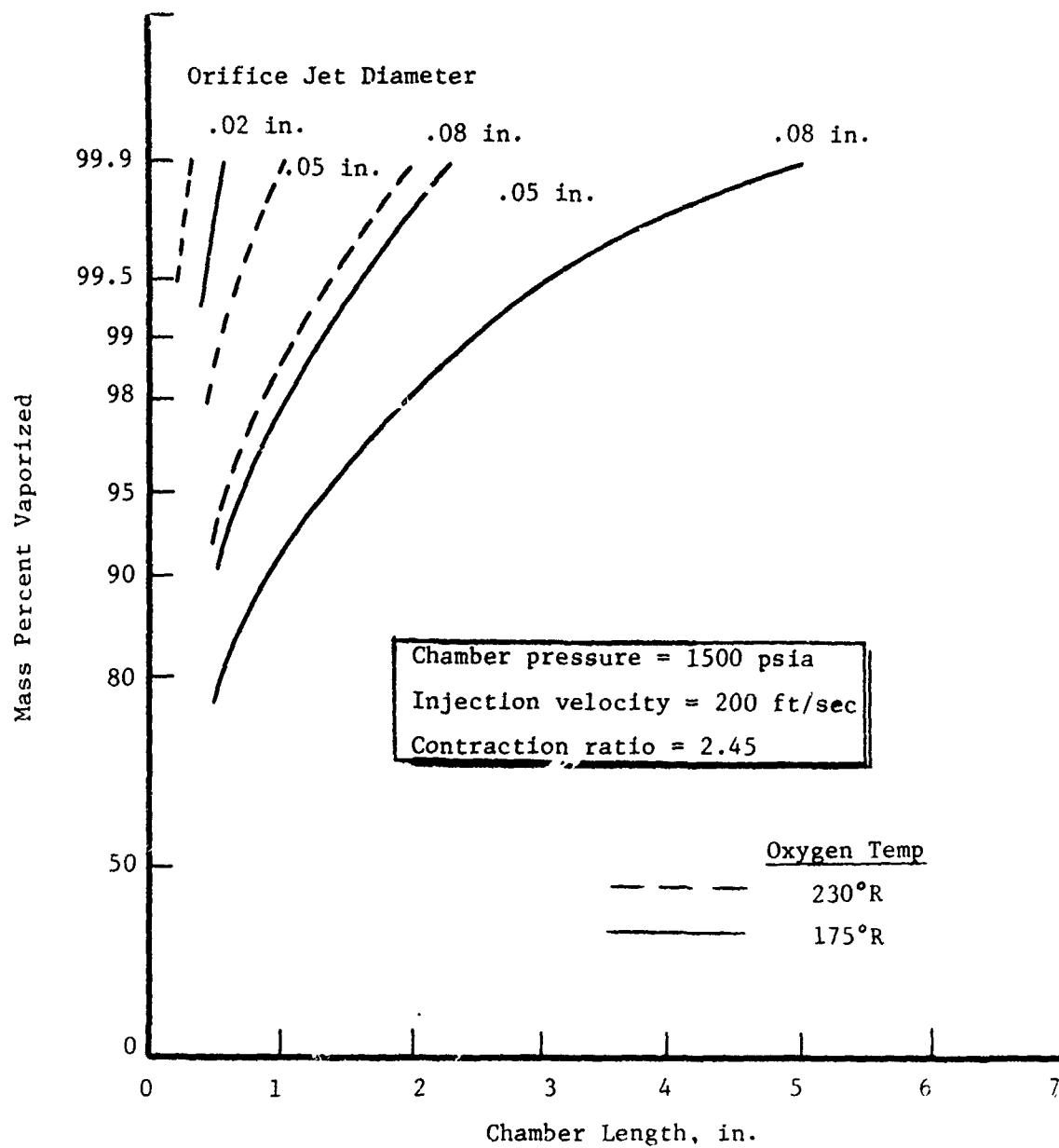


Figure 8. Oxygen Vaporization Characteristics at 1500 psia

III, A, Design (cont.)

The effect of oxygen injection velocity is shown in Figure 9. Injection velocity has two opposite effects on the propellant vaporization process. First, increased injection velocity decreases the resulting mass median droplet size, thus increasing the propellant vaporization rate. Second, however, the increased injection velocity reduces the droplet stay time within the combustion chamber, reducing the amount of vaporization achieved. Since the stay time reduction has a larger effect on the propellant vaporization than the droplet size reduction, the net effect of increased injection velocity is a reduction in the resulting propellant vaporization as shown in Figure 9.

The effect of combustion chamber contraction ratio on the propellant vaporization is shown in Figure 10. These data indicate that decreasing the contraction ratio slightly improves the vaporization efficiency, but the effect is generally of second order. However, all of the droplet heating correlations presented in Reference 4 have an implicit assumption concerning the relative velocity difference between the liquid droplet and the surrounding gas, which affects the droplet atomization efficiency. Investigations have indicated that the appropriate gas/liquid ΔV inherent within these calculations is approximately 150 ft/sec. Therefore, another effect of contraction ratio which is not included in Figure 9 is its influence on the gas velocity and, thus, the gas/liquid ΔV . A contraction ratio which results in a ΔV less than 150 ft/sec would also result in lower vaporization efficiency than predicted by this analysis. On the other hand, a ΔV greater than 150 ft/sec would result in higher vaporization efficiencies. This effect is illustrated in Figure 11.

The relative differences in the vaporization efficiency of doublet and showerhead element configurations is illustrated in Figure 12. Note that, for the conditions shown, high vaporization efficiency (99.5%) can be achieved with doublet orifices having a jet diameter of approximately 0.05 in.

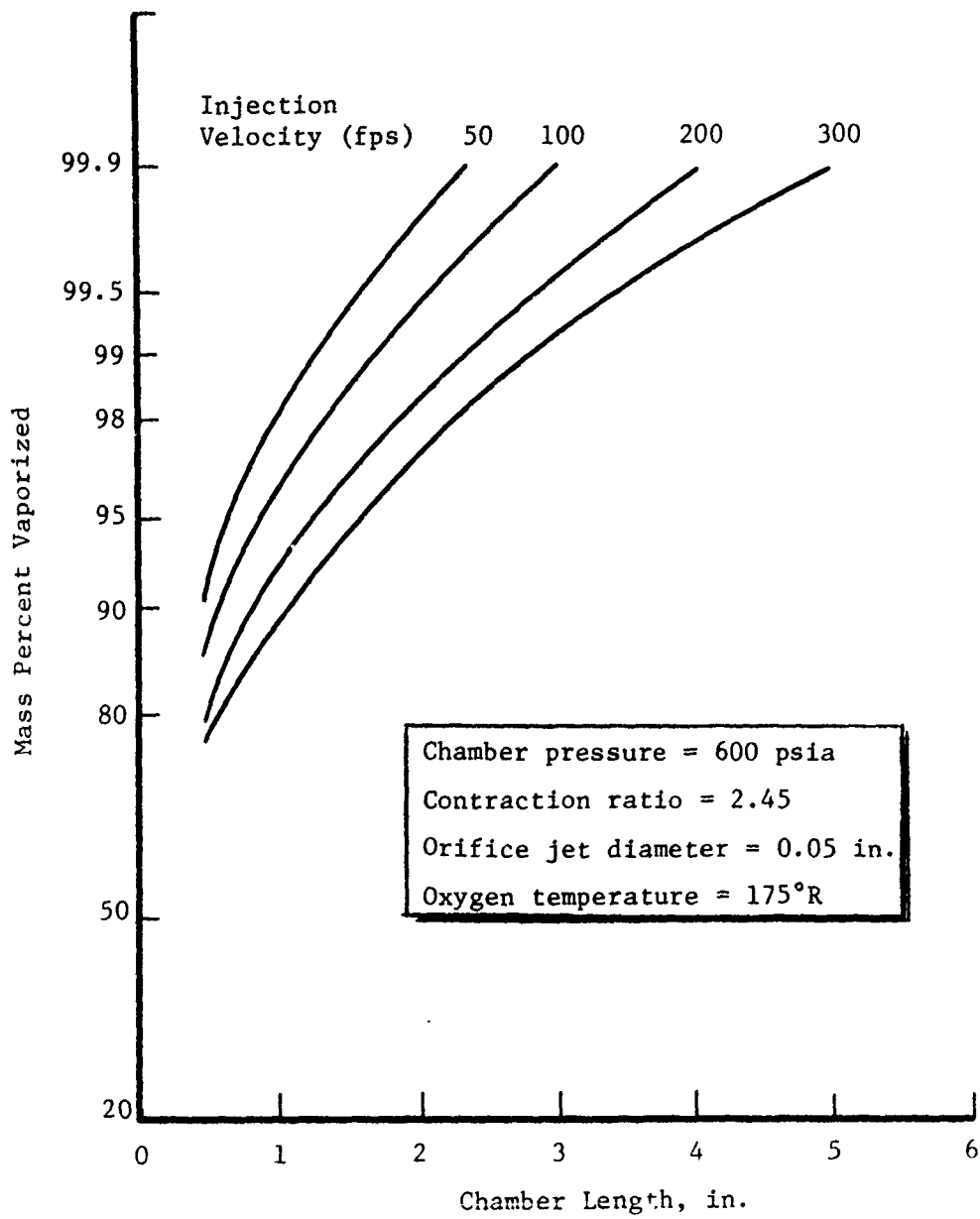


Figure 9. Effect of Oxygen Injection Velocity

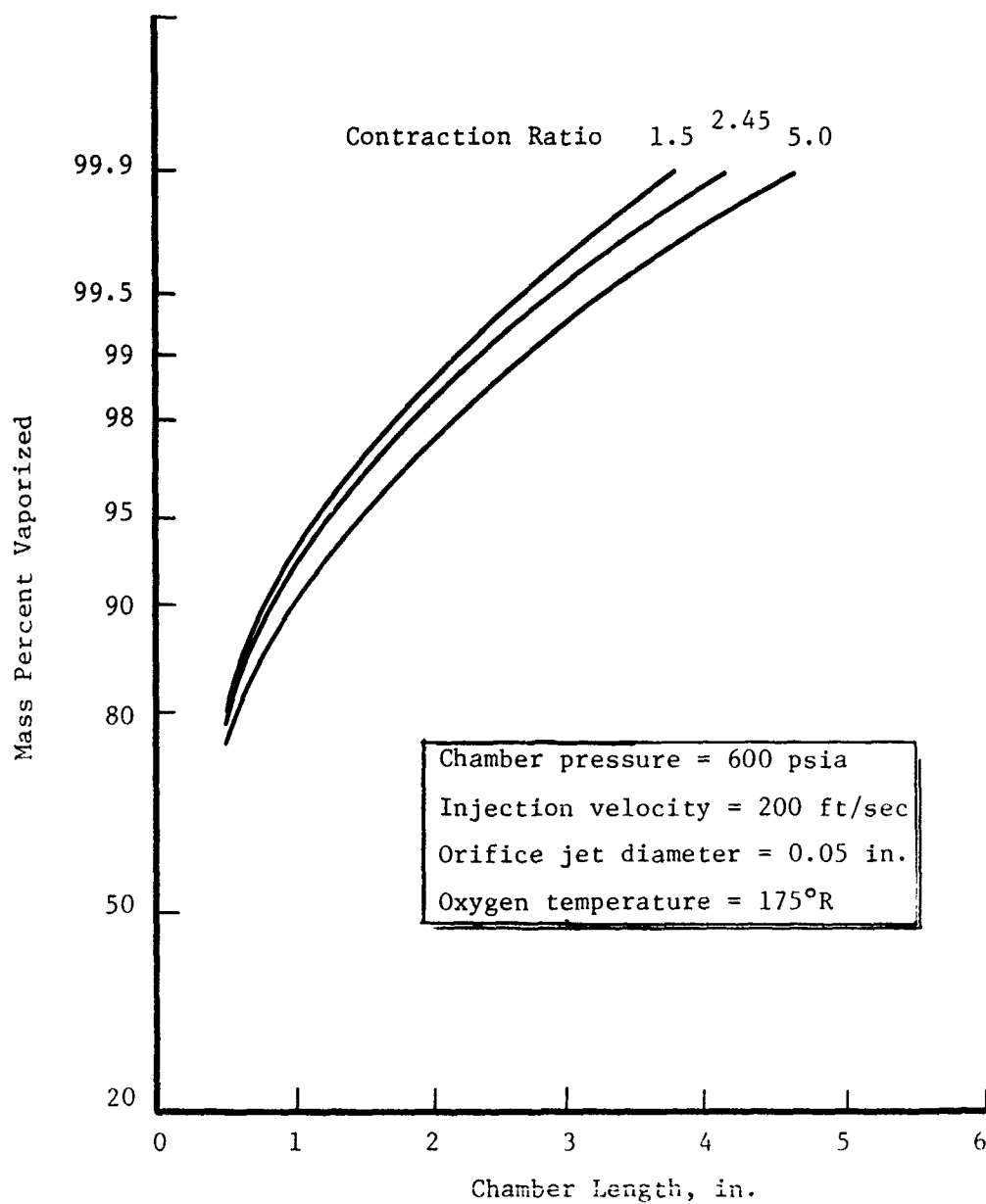


Figure 10. Effect of Contraction Ratio

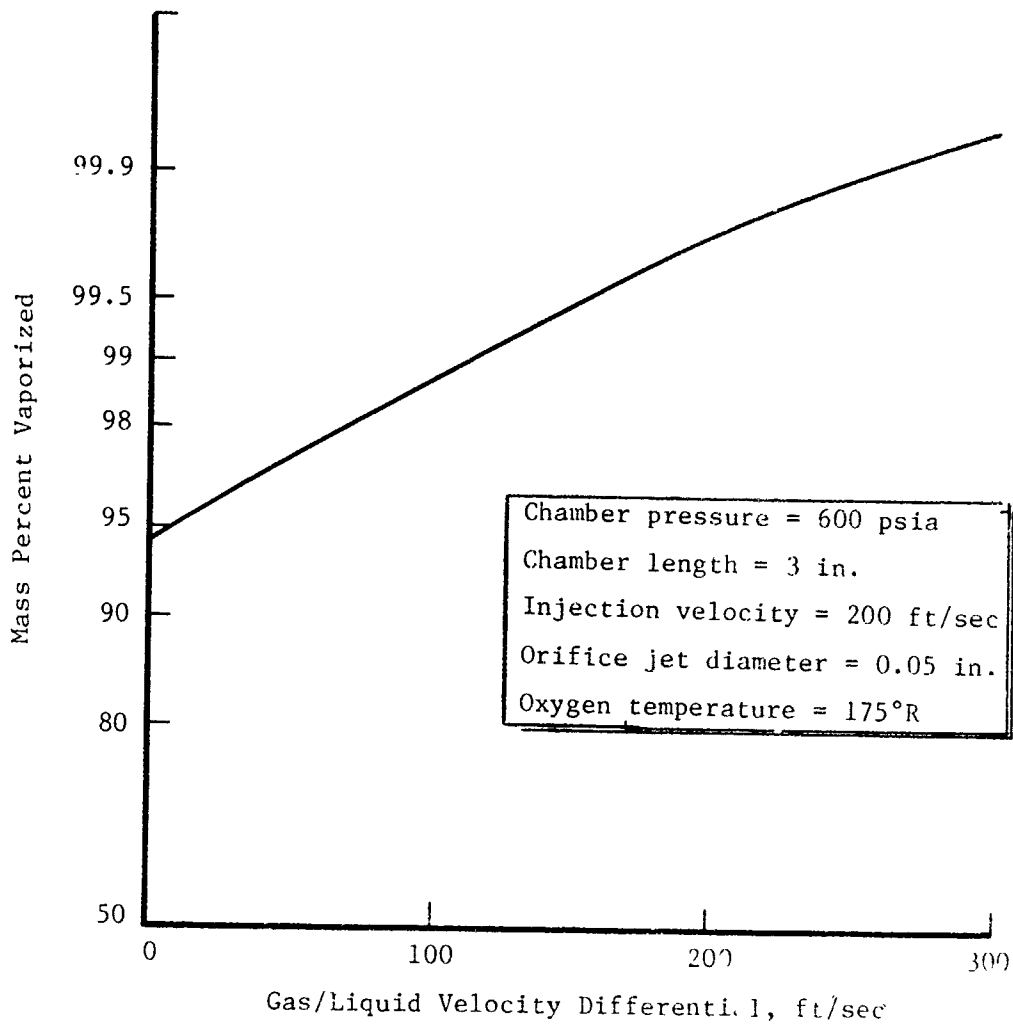


Figure 11. Effect of Gas/Liquid Velocity Differential

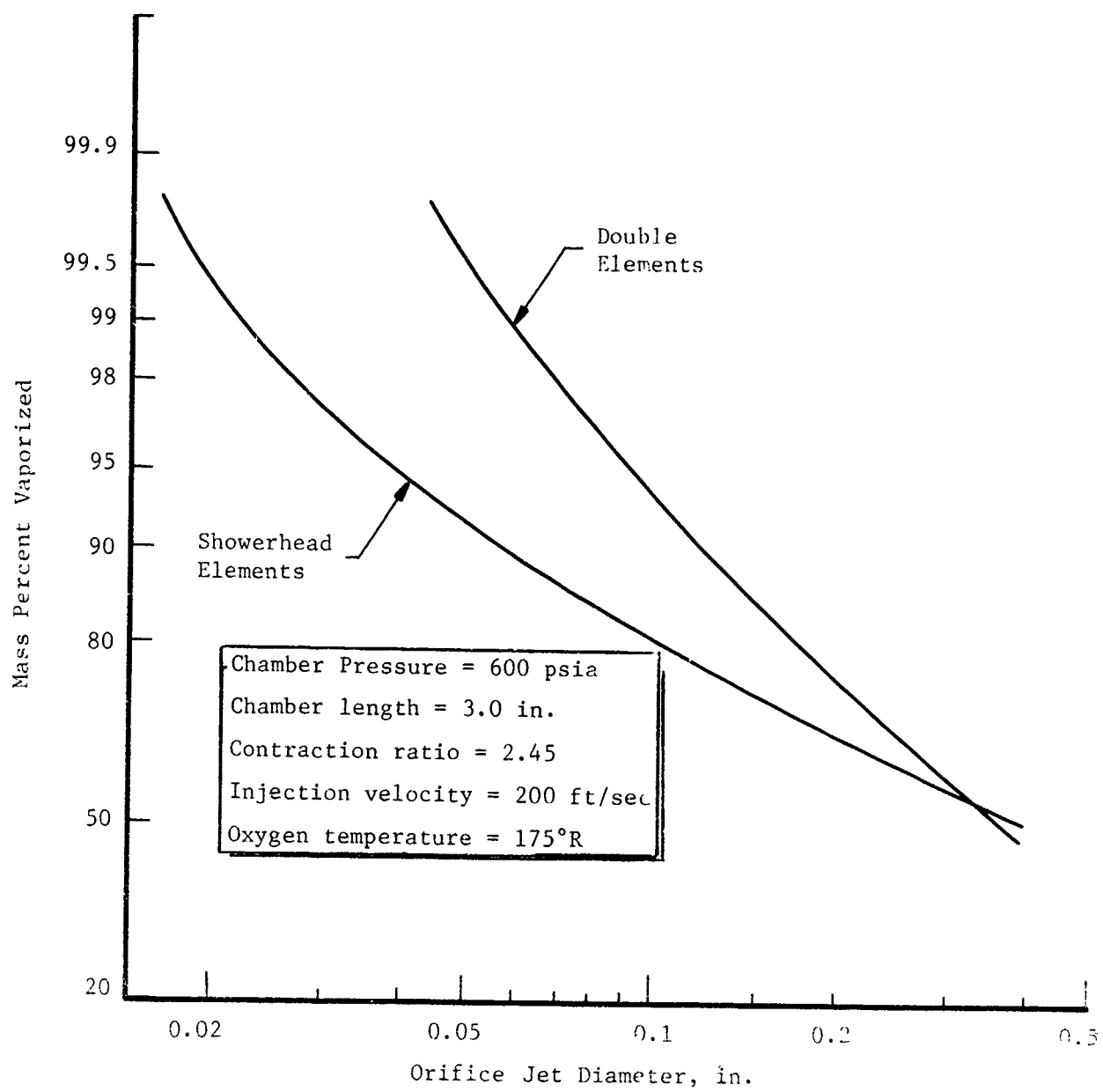


Figure 12. Effect of Element Type

III, A, Design (cont.)

while showerhead elements would require orifice jet diameters of approximately 0.02 in. to achieve the same vaporization efficiency. Thus, more than six times as many showerhead orifices than doublet orifices would be required to achieve the same performance.

Finally, a comparison of the droplet heating vaporization model of Reference 4 and the Distributed Energy Release (DER) supercritical vaporization model of Reference 5 is presented in Figure 13. The droplet heating model considers the vaporization process at supercritical pressures completed when the droplet temperature reaches the critical temperature. The DER supercritical vaporization analysis, on the other hand, considers the supercritical diffusion limitations in addition to the droplet heating. As a result, the DER supercritical analysis predicts a much lower vaporization efficiency than the droplet heating model. It should be noted, however, that the supercritical model has never been correlated with actual test results, while the droplet heating model has an extensive history of correlation with test data including some data at supercritical pressures. As a result, it was felt that the supercritical vaporization model was very conservative in its vaporization predictions and thus provided a lower limit for these calculations. The droplet heating model, on the other hand, provided an estimate of the upper limit of "vaporization" potential at supercritical pressures since it completely ignored the propellant diffusion limitations.

Based on the preceding analysis, the selected oxidizer injector orifice configuration, which consisted of 630 impinging doublets of 0.025 x 0.028 in. size, assured 99.5% oxygen vaporization within the 3-in.-long chamber at all operating pressures.

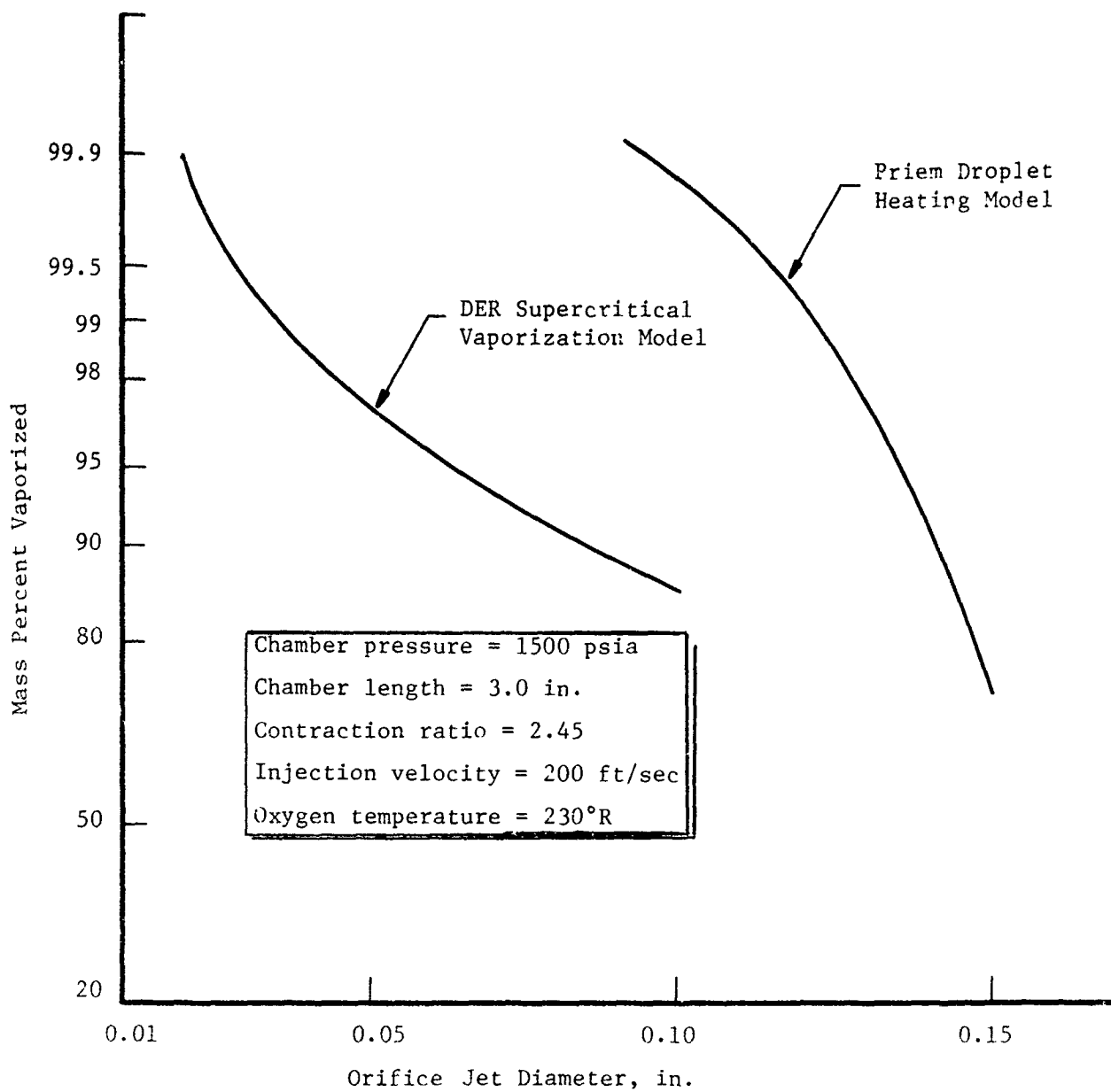


Figure 13. Comparison of Results from Two Oxygen Vaporization Models

III, A, Design (cont.)

c. Stability Analysis

It was found that, in its most general form where the inner and outer contours were arbitrary functions of axial distance, the method of separation of variables usually used to analyze chamber and nozzle acoustics was not applicable. Two alternate methods of analyzing the acoustics of the chamber were:

- (1) An axisymmetric analysis which assumes the inner contour is a constant proportion of the outer contour.
- (2) A two-dimensional analysis where the chamber contour is symmetrical about a plane. If the ratio of inner radius to outer radius of an annular chamber is sufficiently large, a two-dimensional nozzle is a good approximation (i.e., the annulus can be approximated by a rectangle).

It was decided to use the two-dimensional analysis. ALRC's two-dimensional analysis, which was developed specifically for a triangle-shaped nozzle, was modified to use an arbitrary nozzle height. Also, the third dimension of the chamber was added to account for the effect of the wave motion around the annulus. The computer code for this analysis was modified, checked out, and the chamber shape put into a form which allowed its use in the analysis described above. Since the two-dimensional analysis applies to a chamber which is symmetrical about a plane, the equivalent chamber conceived had roughly the same flow area versus length and conformed to the symmetry requirements of the analysis.

The overall stability of the engine is determined by combining the effect of the nozzle analysis, injector analysis, and combustion response. The injector admittance and nozzle admittance are combined by considering that the volume flow at the interface must be conserved. Volume flow was used instead of mass flow since the injector contains hydrogen and the chamber contains products of combustion which have different densities. Also, the pressure must

III, A, Design (cont.)

be continuous in going from the injector into the chamber. Combining the injector admittance and nozzle admittance appropriately, a curve of combustion gain required for neutral stability versus frequency can be drawn. This is shown in Figure 14 for the 1T, 2T, and 3T modes. The 1L mode was also analyzed but it was so stable it is not shown. Figure 13 uses cross hatched boxes to show the estimated range of sensitive frequency of combustion.

Figure 14 shows that the chamber with no baffle at all is equally as stable as any other case and is therefore recommended. The 1.6-in. baffle shows all three modes analyzed to be below the range of sensitive frequencies of combustion. If higher modes had been analyzed, there would have been some modes in or above the range of sensitive frequency of combustion. The high gain required in the range of sensitive frequency is caused by the Helmholtz resonance in the hydrogen feed system. The frequency of the Helmholtz resonance can be changed by changing the distance between the fuel distribution plate and the upstream edge of the oxidizer injection vanes.

d. Nozzle Performance

(1) General

The predicted delivered performance for the E-D nozzle is summarized in Table III. Included in this table are the various performance losses as well as the estimated delivered performance for chamber pressures of 1500, 700, and 300 psia.

The predicted performance values were calculated using the model recommended by the JANNAF Performance Standardization Working Group (Ref 6). The energy release process was characterized by a vaporization limited mass defect model which is similar to one currently being developed to be incorporated

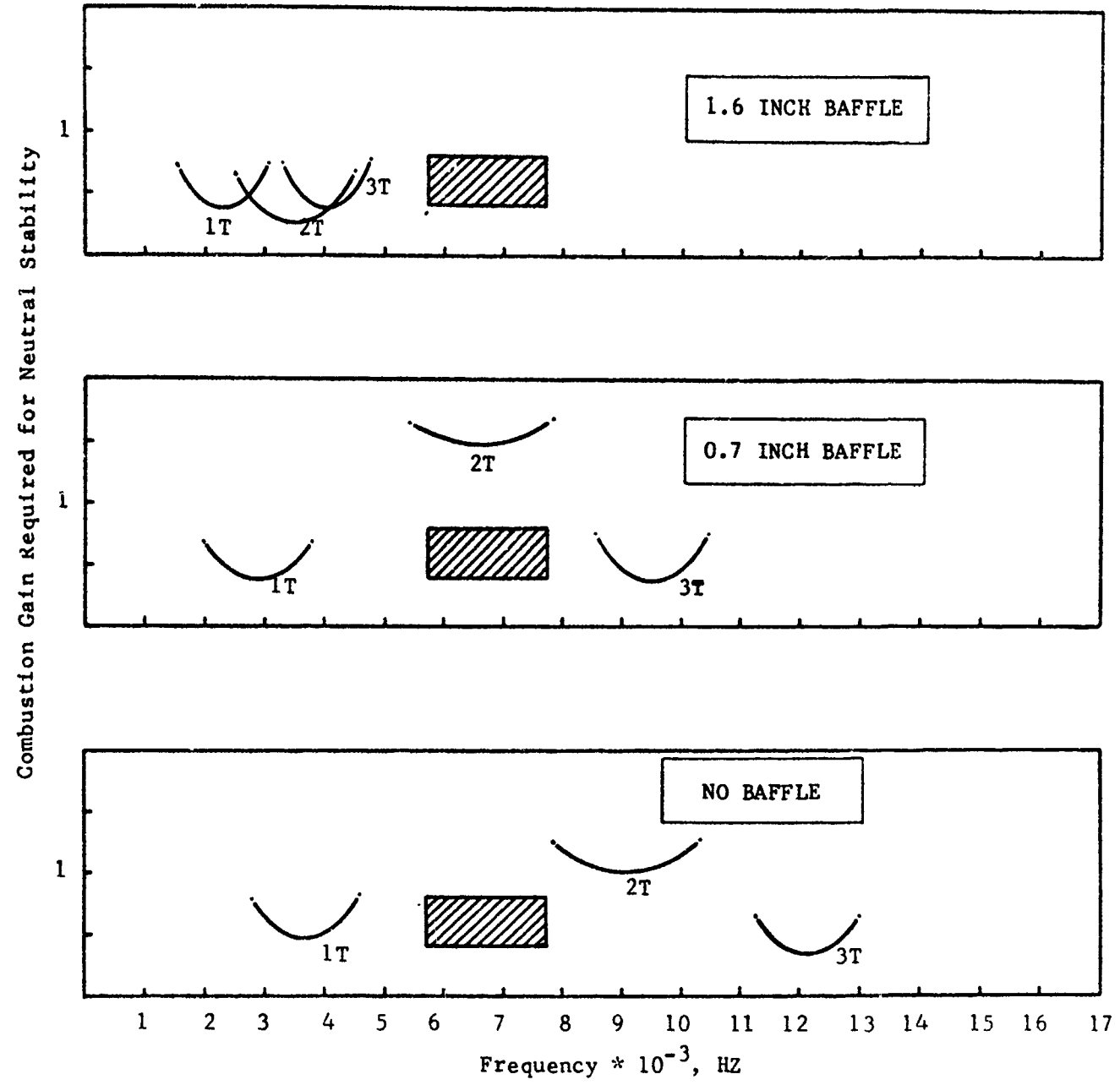


Figure 14. Neutral Stability Plots for E-D Thrust Chamber

TABLE III
E-D NOZZLE PERFORMANCE SUMMARY

$\epsilon_o = 435$
 $\epsilon_b = 10$
 $L_o = 82$ in.

O/F = 6.0

	1500	700	300
P_c , psia			
$I_{sp_{ODE}}$, sec	486.3	485.9	485.3
Propellant impurity loss, sec	1.2	1.1	1.0
Kinetic loss, sec	0.7	2.5	7.2
Boundary layer loss, sec	5.0	5.8	6.9
(1) Energy release loss, sec	2.4	2.4	2.4
(2) Divergence loss, sec	6.2	6.2	6.2
I_{sp} delivered vac, sec	470.8	467.9	461.6

(1) Based on Energy Release Efficiency (ERE) = 99.5%.
(2) Based on $\epsilon_o = 435$, base pressure negligible.

III, A, Design (cont.)

into the JANNAF methodology, in lieu of the initial nonmechanistic enthalpy reduction model. The following paragraphs provide a discussion of the general methodology as well as the specific loss calculations as applied to the E-D nozzle.

The technique used for evaluation and prediction of performance considered the one-dimensional equilibrium (ODE) flow conditions to be the base case. As shown in the following equation, all performance losses are subtracted from the base case:

$$I_{sp\text{ delivered}} = I_{sp\text{ ODE}} - \sum I_{sp\text{ losses}}$$

Theoretical thermochemical performance ($I_{sp\text{ ODE}}$) was evaluated using the NASA/LeRC One-Dimensional Equilibrium (ODE) Computer Program (Ref 7). This documented program computes one-dimensional flow in chemical equilibrium and is the basis for all % I_{sp} quotations.

Five primary specific impulse losses (shown in Table III) are considered in the performance methodology: (1) kinetic, (2) boundary layer, (3) nozzle divergence, (4) mixture ratio distribution/cooling, and (5) energy release performance losses. These losses are described in the following paragraphs.

(2) Kinetic Loss

The kinetic performance loss accounts for the performance degradation because of chemical recombination lag during the gas expansion process. This loss may be calculated for a conventional nozzle using either the ODK (one-dimensional kinetic) (Ref 8) or the more exact TDK (two-dimensional

III, A, Design (cont.)

kinetic) (Ref 9) computer programs, incorporating revised reaction rate data (Ref 10). However, for the E-D nozzle, neither of the above programs for evaluating kinetic flow were directly applicable. The ODK computer program is inappropriate as commonly used because the flow expands about the plug lip and is thus grossly non-one-dimensional. Moreover, the TDK in its present form is restricted to conventional (non-annular) nozzles.

The method which was adopted for the E-D nozzle involved: (1) calculating the flow properties along a mass-mean streamline, (2) defining a conventional nozzle which would produce these flow properties assuming one-dimensional flow, and (3) evaluating the equivalent conventional nozzle using the ODK computer program. This approximate method could be improved by dividing the flow into several, rather than just one, equal mass streamtubes and evaluating the kinetics loss along the mean streamline of each streamtube.

(3) Boundary Layer Loss

The boundary layer loss accounts for the degradation in performance due to shear drag and heat transfer at the thrust chamber walls. This loss is considered to be composed of three components:

(a) A loss due to shear drag and heat loss through the thrust chamber walls. This loss is evaluated as described in Reference 10 using boundary layer properties calculated from the Turbulent Boundary Layer Program (Ref 11).

(b) A gain in performance due to preheating the propellants in the cooling tubes. The heat transferred from the hot gases to the propellant in the cooling tubes was calculated using the Turbulent Boundary Layer Computer Program. This increase in propellant inlet enthalpy was then input to the ODE computer program to determine the performance gain associated with the regenerative cooling.

III, A, Design (cont.)

(c) A loss in performance due to a reduction in the effective overall area ratio considering boundary layer displacement thicknesses at the throat and exit.

(4) Divergence Loss

The divergence loss for a conventional nozzle is due essentially to non-axially directed gas momentum at the nozzle exit plane. For the E-D nozzle, this interpretation was expanded to also include the inefficient utilization of the plug surface area for the production of axial thrust. This loss is calculated from the following equation:

$$\Delta I_{sp_div} = (I_{sp_ODE} - \Delta I_{sp_ERE} - \Delta I_{sp_MRD}) (1 - C_f / C_{f_one-dim})$$

where: I_{sp_ERE} = loss due to incomplete energy release
 I_{sp_MRD} = loss due to mixture ratio maldistribution
 C_f = thrust coefficient for constant gamma with axisymmetric flow, including base pressure thrust
 $C_{f_one-dim}$ = thrust coefficient for constant gamma with one-dimensional flow corresponding to the overall area ratio (c_o)

As defined above, the thrust coefficient C_f includes the thrust contribution due to pressure acting on the face of the plug. The base pressure was calculated by applying a model (Ref 12) for turbulent supersonic flow parallel to the axis of a truncated cylinder. The model indicated that, for vacuum operation, the base pressure was sufficiently small that the plug base contribution to axial thrust was essentially zero.

III, A, Design (cont.)

(5) Mixture Ratio Maldistribution Loss

This performance loss accounts for the inefficiency resulting from gross mixture ratio nonuniformities. The nonuniformities can be intentional, such as the use of film or barrier cooling, or nonintentional, such as those resulting from nonuniform injector hydraulic resistances or injector/chamber design constraints. The mixture ratio maldistribution performance loss for the anticipated final engine design is zero due to the absence of film or boundary cooling. The E-D sector injector was evaluated on the basis of gas/liquid cold flow testing and the results are described in Section III,B.

(6) Energy Release Performance Loss

This performance loss accounts for the inefficiency resulting from incomplete propellant vaporization, incomplete microscale mixing, and incomplete reaction. The actual energy release performance loss of the E-D sector injector/chamber configuration was determined experimentally (Reference III,C). The value shown in Table III is the development goal of 0.5% (99.5% efficiency). The injector is designed to completely vaporize the liquid oxygen at the nozzle throat so the actual energy release loss will result primarily from incomplete microscale mixing and/or reaction.

III, A, Design (cont.)

e. Regeneratively Cooled Chamber Design

The goal of this subtask was to conduct a thermal analysis to establish the preliminary design of a regeneratively cooled thrust chamber. The purpose of this effort was to (1) aid in the selection of the base area ratio, (2) provide an engine design pressure schedule, (3) establish design inlet conditions for the injector design, and (4) establish the feasibility of regeneratively cooling an E-D nozzle thrust chamber.

Activities associated with the base area ratio selection are discussed in an earlier section on nozzle design.

A key factor discussed herein is the effect of increased gas-side heat transfer as the hot gas is turned through the throat. This phenomenon has been observed in similar thrust chamber geometries and can impact the chamber design requirements to the degree that nonstandard fabrication techniques and/or advanced materials are required for regeneratively cooled E-D thrust chambers.

(1) General

Recent advances in regenerative cooling techniques for LH₂/LO₂ rocket engine combustion chambers have made it possible to extend the maximum heat flux limit for cooled chambers. The use of high conductivity copper for the wall and the development of fabrication techniques for producing walls with precisely controlled coolant passage area and geometry have resulted in this increase in flux limit. Liquid hydrogen has excellent thermal transport and capacitive properties and, when it is combined as a coolant with the copper chamber of nontubular construction, it becomes feasible to consider the use of

III, A, Design (cont.)

advanced thrust chamber concepts. The E-D nozzle is such a concept which produces high performance within significantly shorter engine lengths, but which requires an annular combustion chamber with an attendant increase in cooled surface area and heat flux.

Most future rocket engines will be required to be reusable and, thus, cycle life becomes an important consideration in the design of the thrust chamber and becomes a primary factor in establishing the design criteria. The cycle life of a regeneratively cooled thrust chamber is primarily a function of the severity of thermal stress, which in turn is related directly to the maximum gas-side wall temperature and the temperature difference across the wall. For a 100 life cycle design, it has been established that the gas-side wall temperature must be $\leq 1000^{\circ}\text{F}$ and that the maximum temperature difference between the gas-side and the backside temperatures must be $\leq 900^{\circ}\text{F}$. Additional constraints on the cooling system design are a result of the interaction with the propellant feed system. The coolant system pressure drop requirement must be maintained within the capability of the feed system or the effect of pressure drop on engine feed system weight/performance must be considered. Two feed system constraints which were used for purposes of preliminary cooling system design are: (1) the coolant Mach number be $\ll 1$ to prevent choking in the coolant passages at reduced thrust and (2) the coolant passage pressure drop not exceed 1000 psi.

The cooling requirements of an E-D nozzle system are a strong function of the base area ratio. The E-D nozzle requires an annular combustion chamber and the total surface area of the chamber increases approximately with $\sqrt{\epsilon_b}$ and the throat gap varies inversely with $\sqrt{\epsilon_b}$. The total cooling load is increased both due to the increase in cooled surface and to the increase in heat flux caused by a reduction in the gas passage characteristic dimension.

III, A, Design (cont.)

The capacity of the coolant to absorb heat is limited by the maximum bulk temperature, which can be achieved while still meeting the requirements on pressure drop and thermal stress. The finite capacity of the coolant defines a maximum base area ratio which can be used without resorting to zone mixture ratio control to impose a barrier of cooler combustion gas between the chamber wall and the main combustion zone. Further increase in base area ratio results in increased barrier flow with attendant reduction in combustion efficiency due to mixture ratio maldistribution. The interaction between nozzle geometry, cooling requirements, and engine performance must be considered in establishing an optimum configuration.

(2) Methods

(a) Gas-Side Heat Transfer

A modified form of the simplified Bartz correlation, based on hydraulic diameter, was used to calculate the film coefficient:

$$h_g = 0.026 \frac{k_f}{D_H} \left[\frac{WD_H}{A\mu_f} \right]^{0.8} Pr_f^{0.4} \left[\frac{T_\infty}{T_f} \right]^{0.8} \left[\frac{T_{2-D}}{T_\infty} \right]^{0.8} \left[\frac{\rho V_{2-D}}{W/A} \right]^{0.8}$$

The accuracy of this relationship has been well established for conventional rocket engines. In extending the method to the annular chamber, the assumption is made that the boundary layer development is related to the hydraulic diameter in the annular chamber in the same way it is in the circular chamber.

For the case of an E-D nozzle where the hot gas is forced to turn through the throat, the film coefficient may be increased in the outer region of the turn. The effect of this increase cannot be ignored due to its impact on the chamber design. The method used to predict the magnitude of this increase was to employ Reynolds' analogy with Ito's (Ref 13) friction factor correlation for curvature.

III, A, Design (cont.)

$$\frac{h_g_{\text{curved}}}{h_g_{\text{straight}}} = \left[\frac{\text{Re}_{D_H}}{\text{Re}_{R_{cu}}} \left(\frac{D_H}{R_{cu}} \right)^2 \right]^{0.05}$$

Using this technique, the increase of 70% in h_g is predicted in the throat of the contour described in Section III,A,1,a.

(b) Liquid-Side Heat Transfer

Determination of coolant-side heat transfer includes analysis of coolant flow, land effects, and coolant film coefficient enhancement due to channel curvature. It has been shown (Ref 14) that the Hess and Kunz correlation, modified by a bulk temperature correction (Ref 15), is well suited for supercritical flow. The following relationship was used in the preliminary design of the centerbody and nozzle.

$$h_l = 0.0208 C_L \frac{k_f}{D_H} \text{Re}_f^{0.8} \text{Pr}_f^{0.8} \left(1 + 0.0146 \frac{\mu_w}{\mu_b} \right)$$

It was anticipated that the final design would include an evaluation of a more recent correlation developed by Taylor (Ref 16) from nuclear rocket data, namely:

$$h_l = 0.025 \frac{k_b}{D_H} \text{Re}_b^{0.8} \text{Pr}_b^{0.4} \left(\frac{T_w}{T_b} \right)^{-C_1} \left[\text{Re}_b \left(\frac{D_H}{R_{cu}} \right)^2 \right]^{+0.05}$$

$$C_1 = (0.57 - \frac{1.59}{X/D})$$

The Ito correction for curvature is the same form as used on the hot gas side.

III, A, Design (cont.)

(c) Local Heat Transfer

The reason for adopting nontubular coolant passages and high conductivity materials to thrust chambers is that two-dimensional conduction effects allow operation at very high heat flux levels. The two-dimensional conduction results in an increased effective area for heat transfer on the coolant side and, hence, a lower overall thermal resistance.

In the thermal analyses conducted on the E-D regeneratively cooled chamber, the ALRC computer program, HEAT, which was developed specifically for regenerative cooling analysis, was used. This program treats the thrust chamber wall as an electrical analog of equivalent resistances. This treatment of the wall under E-D nozzle operating conditions was verified using SINDA, a widely used thermal analyzer computer program.

The local nozzle thermal conditions were then calculated as follows. The heat flux, Q/A , at any point may be expressed as

$$Q/A = U (T_r - T_c)$$

where T_r , the recovery temperature, is defined as

$$T_r = T_\infty + \sqrt[3]{Pr} (T_o - T_\infty)$$

and U , the overall heat transfer coefficient, is defined as

$$U = \frac{1}{\frac{1}{h_{eff}} + \frac{t}{k_w} + \frac{1}{h_g}}$$

III, A, Design (cont.)

h_{eff} is the effective coolant side heat transfer coefficient and includes the two-dimensional "fin effect" by which heat is conducted through the copper to the backside of the coolant channel.

(3) Thrust Chamber Coolant Circuit

A variety of flow path combinations exist that may be employed for regenerative cooling of an E-D nozzle. Three selected configurations are illustrated schematically on Figure 15. Configurations "a" and "b" were found to be unacceptable because of marginal cooling capability at the inner throat wall in "a" and because of difficulties associated with ensuring stability of the parallel circuits, extremely small passage depths, and the requirement for a mixer at the injector in "b". Configuration "c" was found to provide the best cooling margin at both the inner and outer throat stations and the required slot depths are compatible with manufacturing tolerance.

The selected coolant circuit employs a single-pass counterflow to first cool the centerbody followed in series by a single-pass parallel-flow for cooling of the outer chamber wall and divergent portion of the nozzle. The coolant bulk temperature at the centerbody throat station is approximately 50°R and at the outer wall throat station is approximately 450°R. This combination results in acceptable slot depths in both the inner and outer walls. This occurs in spite of the low temperature and attendant high density of the coolant at the throat on the centerbody side. A further advantage is that the lowest heat flux region is cooled last and decreasing flow velocities are required. This permits gradual diffusion of the coolant flow with attendant recovery of velocity head. The low discharge velocity results in small discharge pressure loss which simplifies the coolant collection manifold design and tends to ensure uniform coolant distribution.

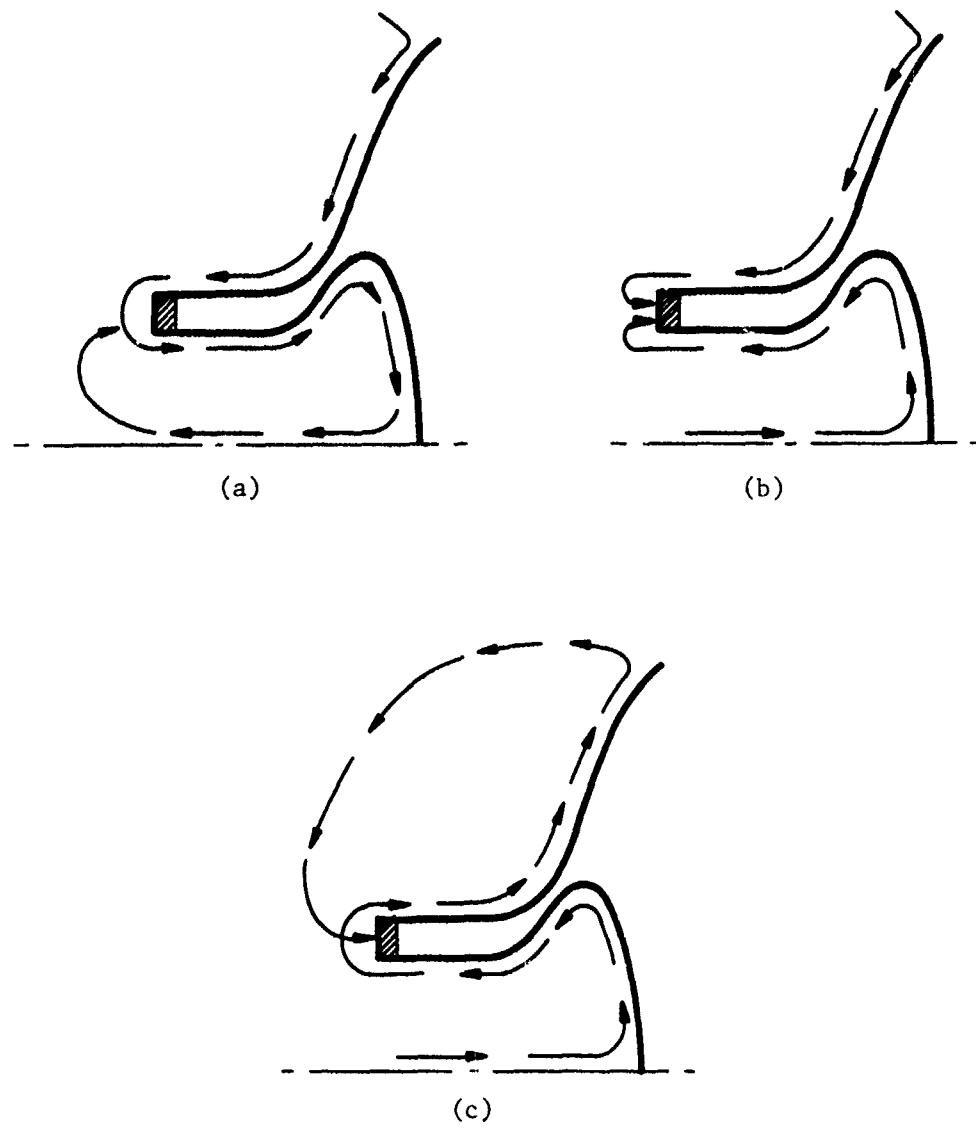


Figure 15. Possible Cooling Schemes

III, A, Design (cont.)

(4) Point Studies

A series of point studies were conducted investigating the effects of various design parameters in the centerbody throat region. One important variable in the study was the effect of gas-side enhancement on predicted values of wall temperature, the fabrication complexity, and/or materials required in order to safely accept the predicted magnitude of enhancement. Figure 16 is a summary of these studies. Two basic channel configurations were analyzed: one considered to be state-of-the-art for conventional milling techniques; the other beyond the state-of-the-art. The two configurations are identified below.

	<u>Conventional</u>	<u>Advanced</u>
Wall thickness, in.	0.040	0.030
Land width, in.	0.050	0.030
Channel width, in.	0.050	0.030

The differences in predicted wall temperatures (Figure 16) of only 300 to 400°F would at first appear to be slight; however, the real differences are quite great. A conventional thrust chamber built from OFHC is incapable of accepting any increase in heat transfer, while the smaller channels (OFHC) are capable of operating with a 30% increase. A combination of small channels and the use of ZrCu would be capable of operating with the predicted enhancement of 70%. Also shown on Figure 16 is the range of published data for a turning angle of 45°, which varies from a value of 1.08 to 2.04. Thus, it can be concluded that the unknown magnitude of the gas-side enhance creates a large obstacle to regeneratively cooled thrust chamber design. To view the problem from a different perspective, a design capable of operating at 1500 psi with no enhancement could only be safely fired at 1000 psia if the predicted 70% value actually occurred. This is also indicated in Figure 16.

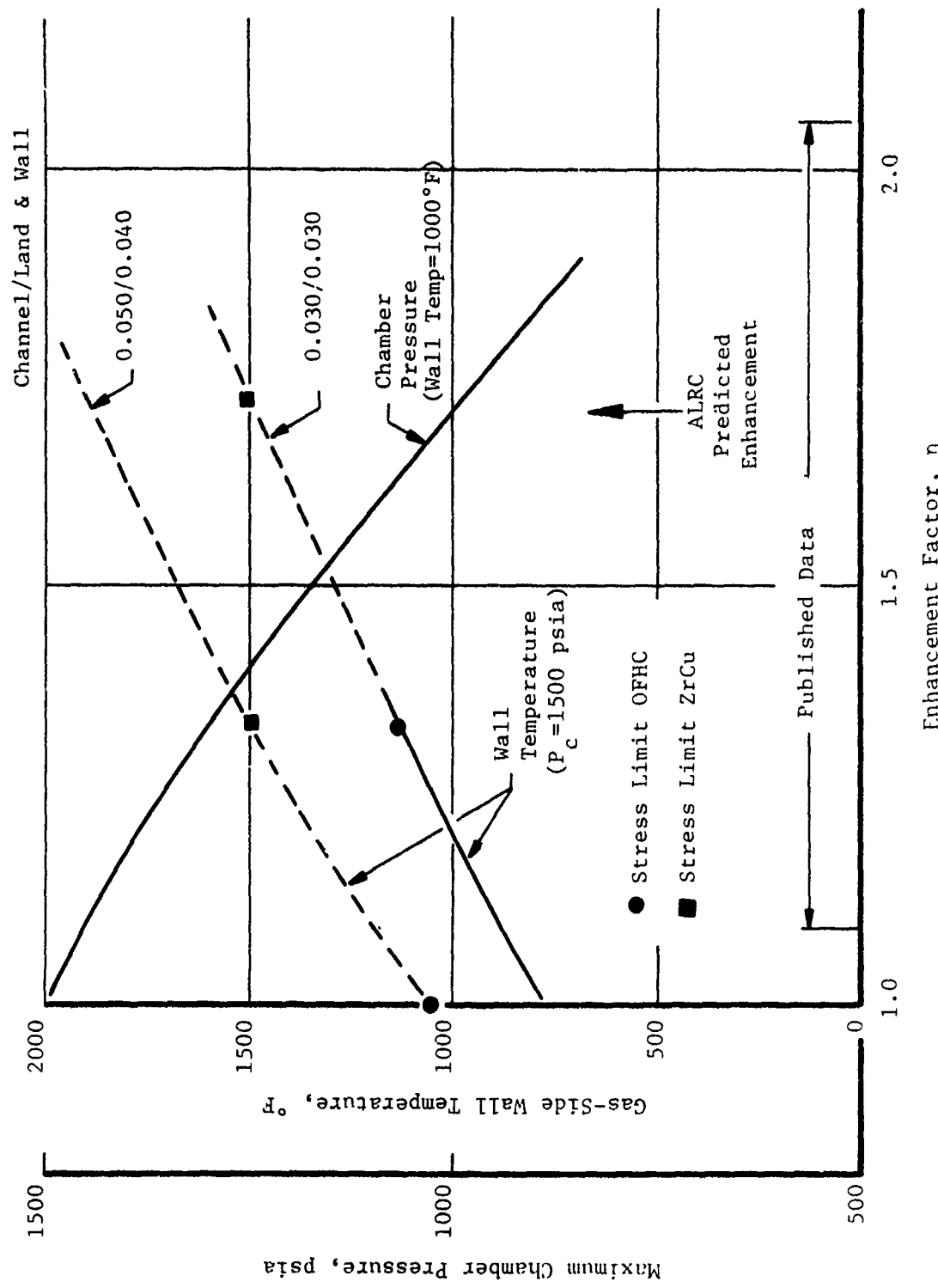


Figure 16 . E-D Nozzle Point Study - Centerbody Throat

III, A, Design (cont.)

(5) Design Analysis

The purpose of the preliminary analysis was to define what a regeneratively cooled chamber looked like, what its capabilities were, and identify possible problem areas. It is important to note that the design was not finalized nor was the effect of increased gas-side heat transfer in the throat region fully investigated during this study.

The preliminary design consisted of 200 constant width channels 0.040 in. wide. The chamber gas-side wall thickness was held constant at 0.030 in. The table below summarizes the predicted operating conditions for the design at a chamber pressure of 1500 psi and 6.9 mixture ratio; no gas-side enhancement is included.

Preliminary Design Summary

No. of channels	200
Pressure drop	785 psi
Bulk temperature rise	348°F
Maximum wall temperature	1040°F

Figure 17 is a plot of predicted local wall and bulk temperature for the design.

A preliminary layout, based upon the analyses described in the preceding sections, was completed and is shown in Figure 13. The design consists of a slotted liner (both shroud and centerbody) contained by a support structure. The shroud channels are closed out with 0.060-in. electroformed copper followed by electroformed nickel for strength.

NOTE: Gas-side enhancement not included.

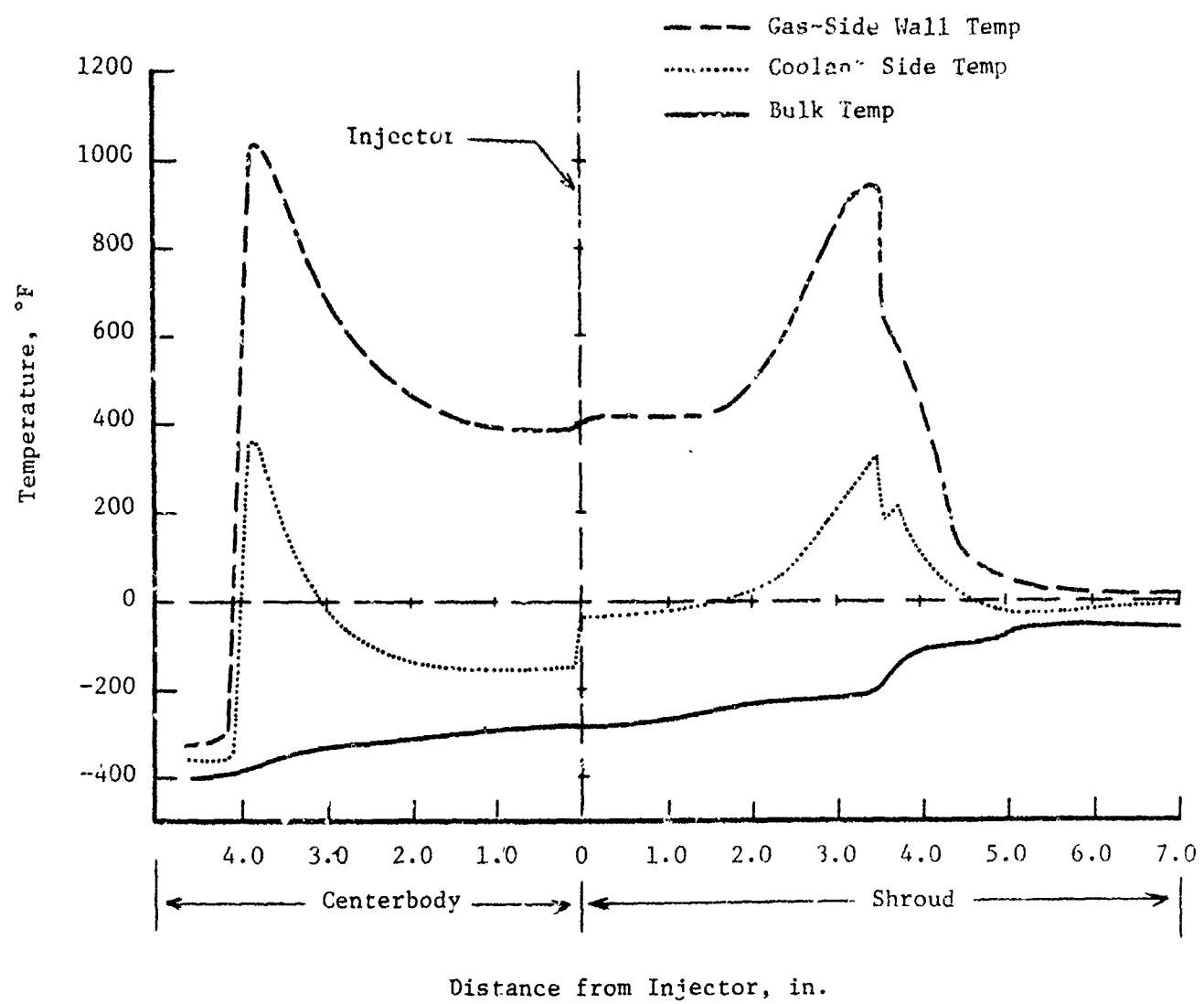


Figure 17. Predicted Operating Conditions -
Regeneratively Cooled Chamber

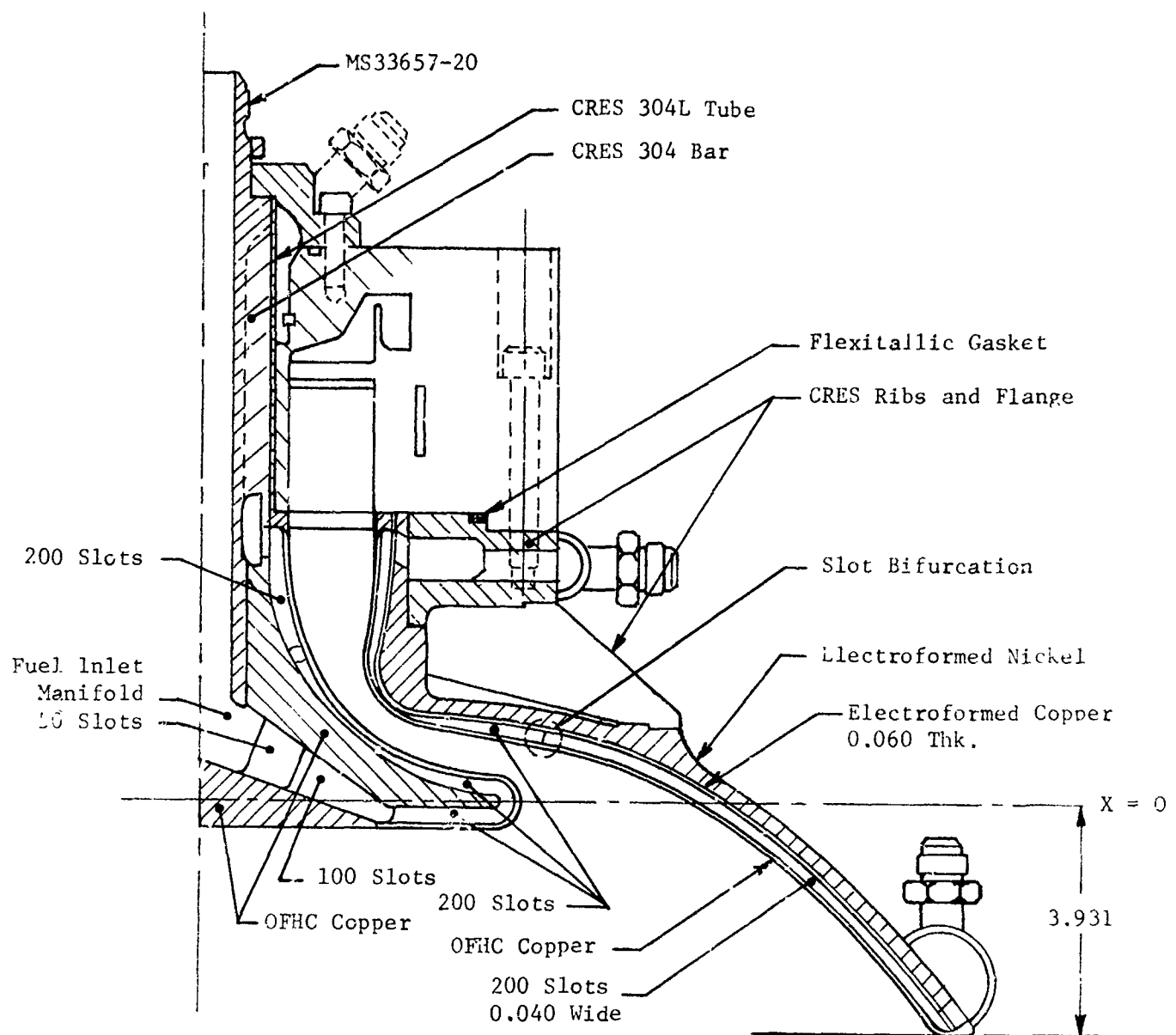


Figure 18 Preliminary Design Layout, PN 1161519

III, A, Design (cont.)

2. Thrust Chambers

As indicated earlier, several thrust chambers were designed, including cooled and uncooled sectors and an uncooled annular unit. In the following paragraphs, the design of each of the five thrust chambers will be discussed separately.

a. Annular Chambers

The uncooled annular thrust chamber design used the same contour as the baseline nozzle. The purpose of this design was to obtain full-scale sea level performance and stability data. The design approach followed was to develop a low cost, workhorse unit with a capability for varying the throat gap.

The uncooled chamber consists of five pieces which are joined to the injector as shown in Figure 19. The design shown uses ablative inserts; however, copper could be used if required. Ablatives were selected on the basis of the unknown magnitude of the throat heat transfer rate. Copper would be limited to about 500 psia and/or to very short durations. The ablative inserts offered the advantages of easy replacement and low cost.

Key features of the uncooled chamber assembly are that it is simple, can be easily assembled or disassembled, and the throat gap can be varied by shimming the centerbody. Provisions are included in the design for high frequency transducers to monitor combustion stability.

b. Sector Chambers

The purpose of the sector (one-seventh of a full annulus) was to obtain injector performance and heat transfer data at reduced cost (compared to full-scale annular hardware). As indicated at the onset of this section, both cooled and uncooled sector chambers were designed. Basically, the cooled chambers

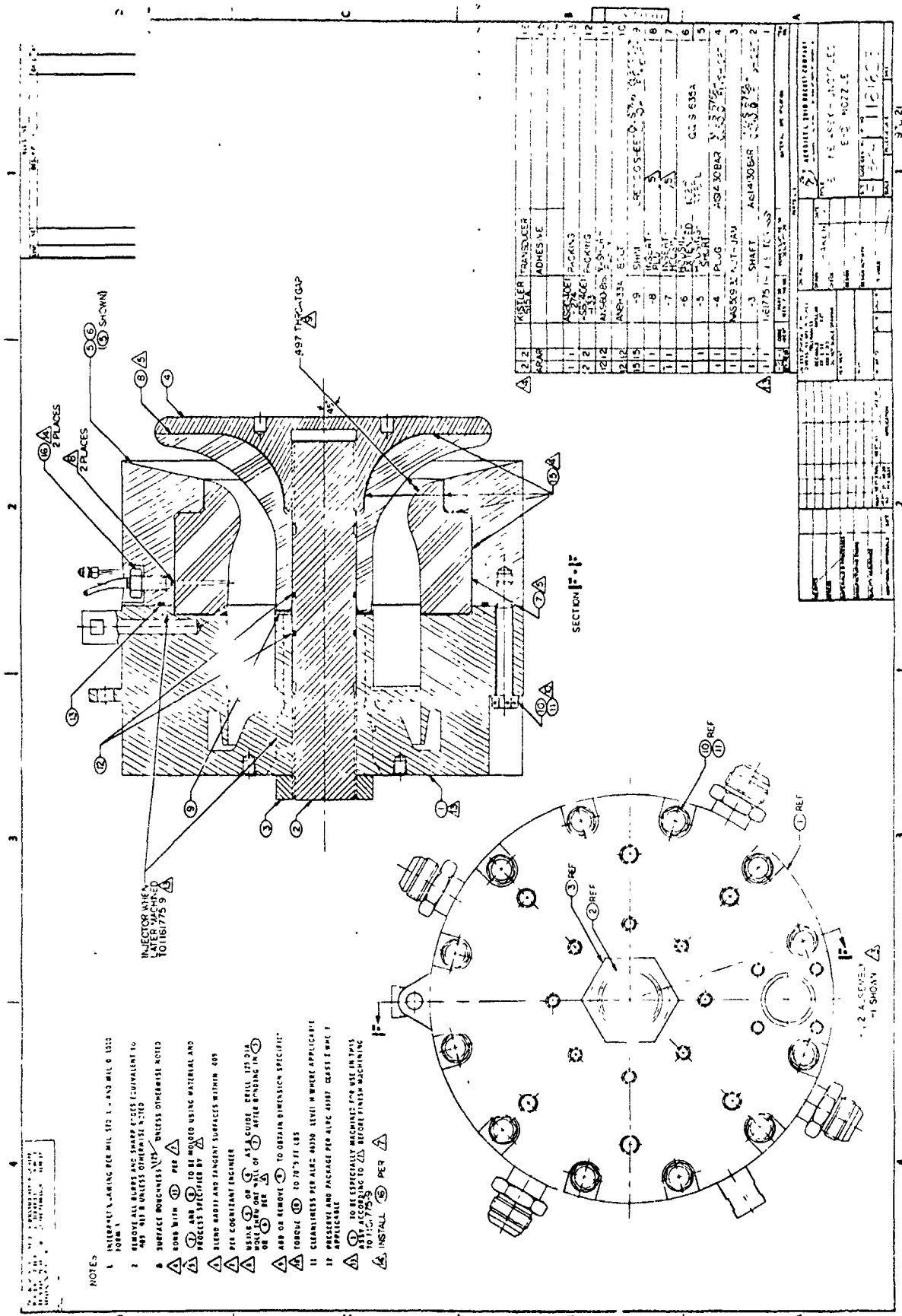


Figure 19. Uncooled Engine Assembly

III, A, Design (cont.)

were intended for use up to full chamber pressure and the uncooled hardware for reduced chamber pressure (~500 psia). In the following discussion, the design of the cooled hardware is presented first, followed by a discussion of the uncooled designs.

(1) Water-Cooled Axial Throat

The purpose of this chamber was to obtain baseline injector sea level performance data. The throat was selected to be axial (normal to the chamber axis) to permit direct measurement of thrust. If a section of the E-D contour were used, the resultant thrust vector would be skewed, making a determination of the true thrust virtually impossible. The selected contour was a true sector of an annulus (as opposed to a rectangle) such that it would interface with a true sector injector. Copper (OFHC) was selected for the gas-side material on the basis of its demonstrated fabricability and the results of stress and thermal analyses indicated it was acceptable.

Thermal Analysis

A thermal analysis of the water-cooled hardware was undertaken to ensure that reasonable wall temperatures and safety margin on burnout heat flux were maintained.

A range of mixture ratios from 5.0 to 8.0 was considered. Over this range, the gas-side heat transfer coefficient at the throat drops from 0.0162 to 0.0111 Btu/in.²-sec-°F at 1500 psia chamber pressure, based on the simplified Bartz correlation using the equivalent diameter of the 1/7 sector of the annular chamber. The gas-side heat flux to an 1100°F wall correspondingly drops from 75.6 to 56.4 Btu/in.²-sec.

III, A, Design (cont.)

The burnout heat flux for water, $(q/A)_{BO}$, is given by the equation

$$(q/A)_{BO} = 2.0 + \left(\frac{V\Delta T_{sub}}{1000} \right)^{0.95}$$

where the velocity, V, is in ft/sec and the amount of subcooling, ΔT_{sub} , equals the saturation temperature minus the bulk temperature in degrees Fahrenheit. The coolant pressure was assumed equal to the gas static pressure at the throat for design purposes. Higher pressures would yield higher burnout heat fluxes and, hence, are satisfactory, while lower pressures are not. A maximum design allowable value of 0.75 was used for the burnout heat flux ratio; i.e., the ratio of the calculated gas-side heat flux to the calculated burnout heat flux of the coolant.

To simplify the design and fabrication of the chamber, the basic coolant passage geometry parameters were predetermined and the analysis was used to determine the required water flow. The selected coolant passage geometry consisted of a constant channel cross section and wall thicknesses. The chamber geometry is summarized below:

Channel size 0.050 in. deep x 0.050 in. wide (constant)

Land width 0.050 in.

Wall thickness 0.040 in.

No. of channels

Outer body 23

Inner body 13

Side walls 15

The flow rates required for a gas-side wall temperature of 1100°F at the throat are tabulated below as a function of mixture ratio at an operating pressure of 1500 psia.

III, A, Design (cont.)

Mixture Ratio	hg_t (Btu/in. ² -sec-°F)	$(q/A)_t$ (Btu/in. ² -sec)	W_{H_2O} (lbm/sec) per channel
5.0	0.0162	75.6	0.344
6.0	0.0145	73.6	0.332
7.0	0.0125	63.2	0.283
8.0	0.0111	56.4	0.254

At the nominal mixture ratio (6.0), the predicted bulk temperature rise was 40°F.

(b) Design

The design philosophy pursued in the water-cooled chamber design was to maintain simplicity and to ensure the unit was indeed a workhorse design with maximum structural capability. Figure 20 shows the chamber top assembly. Basically, the chamber consists of four separate coolant circuits (for each of the side plates and inner and outer bodies) which flow from the injector to the nozzle exit. The copper gas-side liners are brazed to each other, then turned and brazed into a stainless steel structural can. As can be seen from the figure, the inner and outer bodies are reasonably complex structures as they represent segments of compound curvature. The mating of these parts (gas-side liner to copper back-up structure) is critical to ensure a structurally adequate braze joint. It is this joint that was responsible for the fabrication difficulties encountered with this component which are discussed in the chamber fabrication section of this report.

(2) Uncooled Axial Throat Segment

The purpose of the uncooled axial throat chamber was to test the sector injector at low chamber pressure. The design of the chamber was basically the same as the water-cooled segment shown in Figure 20; the internal contour is identical, the walls are solid copper, and the copper walls are brazed into a stainless steel can. The four copper components are externally

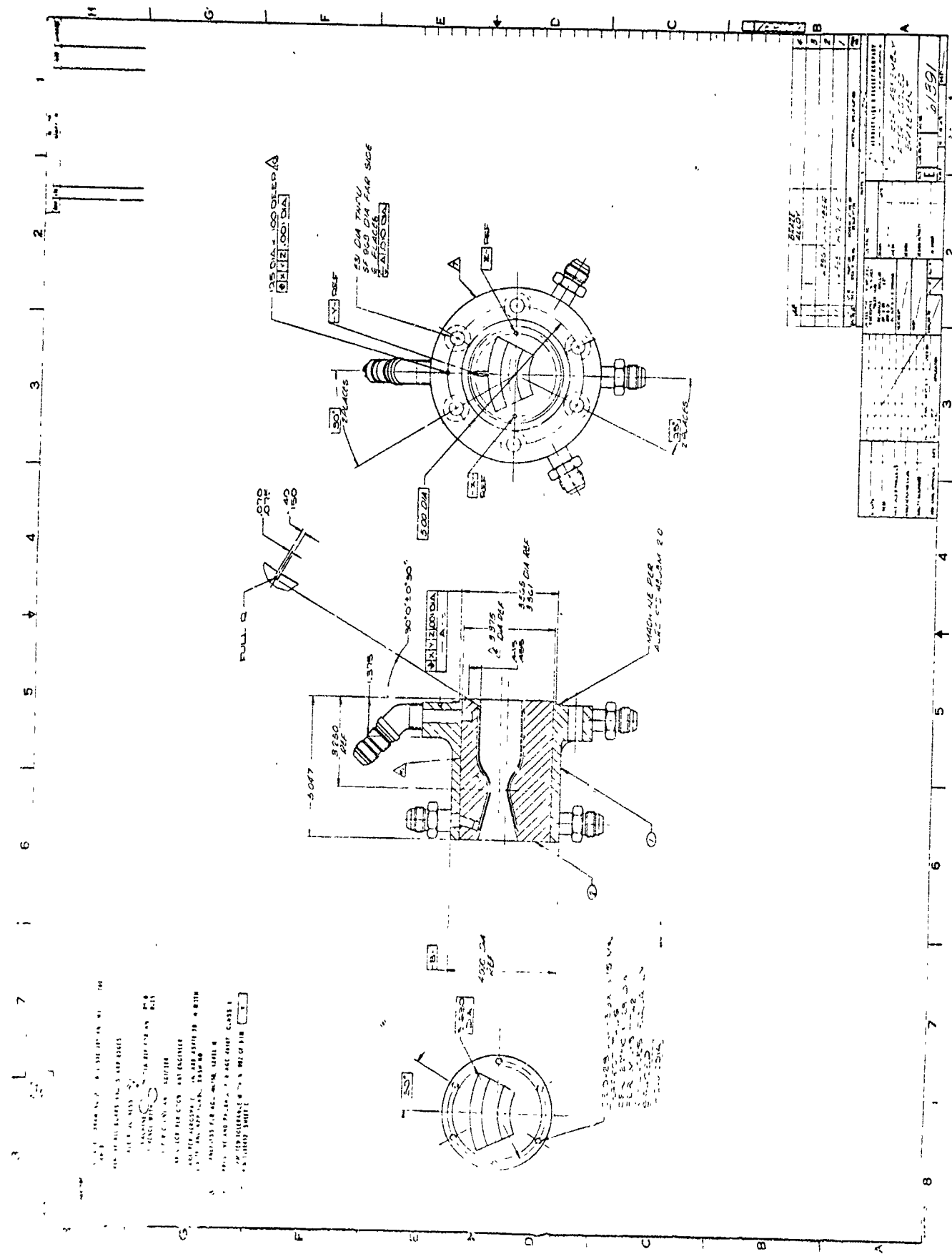


Figure 20. Water-Cooled Axial Throat Chamber Assembly

III, A, Design (cont.)

identical to the water-cooled segments, giving identical braze interfaces. This latter similarity was used to confirm the brazing techniques on the uncooled segment prior to brazing the water-cooled unit. These procedures are also discussed in the fabrication section.

(3) Water-Cooled Calorimeter Chamber

The water-cooled, circumferential-flow segment was intended for acquisition of gas-side heat transfer data along the contours of the E-D nozzle chamber. The curvature effects result in a forecast of enhancement of gas-side heat transfer on the centerbody and reduction on the outer body. Enhancement was predicted to be as much as 70%, based on the Ito correlation (Ref 13). The use of a circumferential flow (transverse to the chamber axis), water-cooled sector chamber would allow a direct determination of the gas-side heat flux from coolant bulk temperature rise measurements at various points along the nozzle contour.

A total of nine coolant channels were designed to be active measuring channels where the flow through a single channel could be measured. Combined with bulk temperature rise measurements, the heat flux could be calculated at each station. These data, in conjunction with theoretical gas temperatures, would then allow gas-side heat transfer coefficients to be calculated.

Analysis, design and detailed drawings were completed for this unit. The design shown in Figure 21 consists of the inner and outer body segments, which are circumferentially cooled, and the two side plates, in which the coolant is co-flowing with the combustion products.

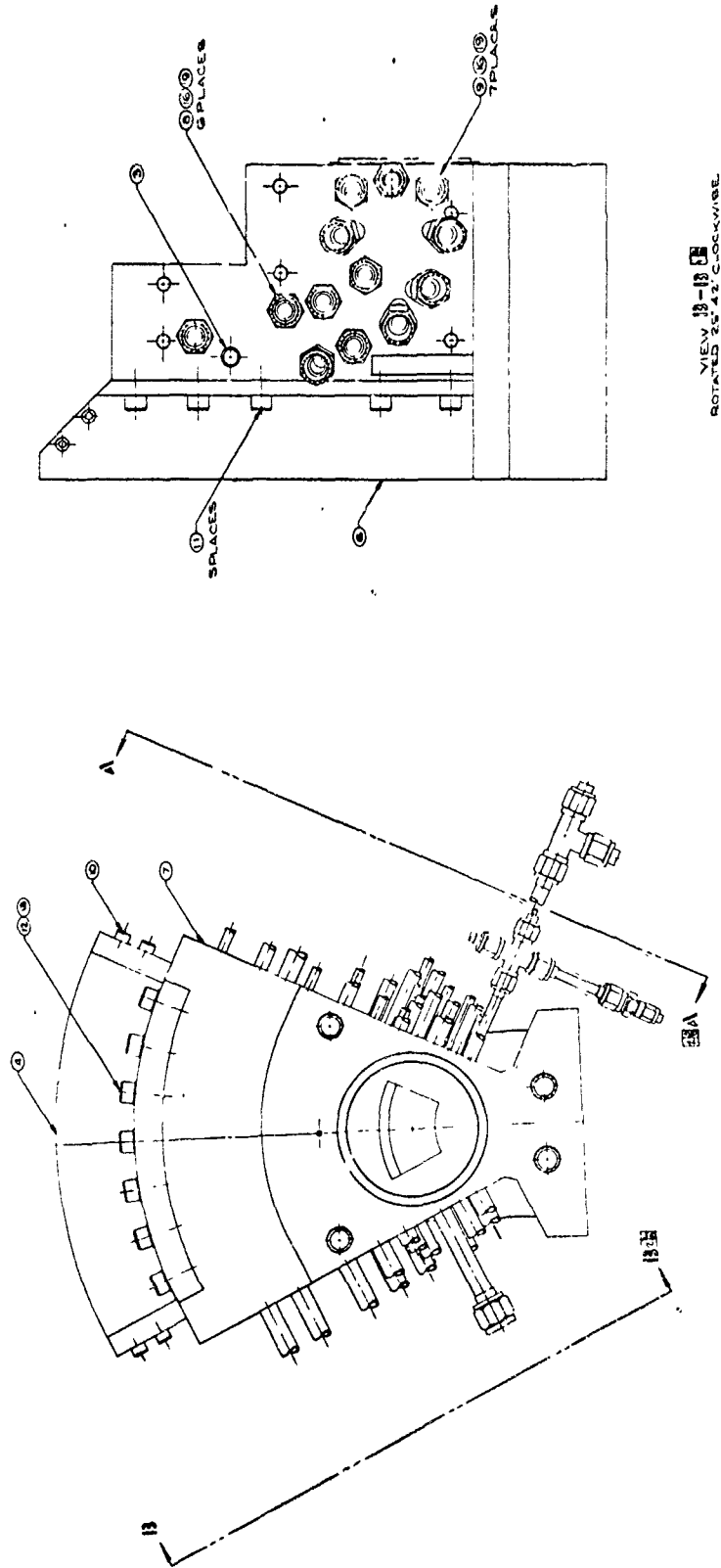


Figure 21. Water-Cooled Calorimeter Chamber

III, A, Design (cont.)

During the course of the design, it was found necessary to have three different coolant inlet pressures due to stress limitations and limited high pressure coolant flow capability. The highest pressure fluid was used only in the throat section because of its higher burnout heat flux capability, the lowest pressure was used at higher area ratios in the outer body, and the third source is the remaining areas.

(a) Thermal Analysis

The coolant heat transfer coefficient, h_L , was calculated using the Hines correlation:

$$h_L = 0.005 \frac{k_b}{d_e} (Re)_b^{0.95} (Pr)_b^{0.4}$$

For coolant-side wall temperatures above the local saturation temperature, the coefficient was modified to account for nucleate boiling:

$$\frac{h_L \text{ boiling}}{h_L \text{ convective}} = \left(\frac{T_{WL}}{T_{sat}} \right)^{13}$$

TWL being the coolant-side wall temperature and T_{sat} the coolant saturation temperature at the local coolant static pressure.

The burnout heat flux was calculated with the equation defined previously and repeated below:

$$(Q/A)_{BO} = 2.0 + \left(\frac{V\Delta T_{sub}}{1000} \right)^{0.95}$$

III, A, Design (cont.)

The simplified Bartz correlation was used to evaluate the heat transfer coefficient in the chamber section and the Elliott-Bartz-Silver correlation (TBL program) in the nozzle.

The selected design philosophy was to use uniform channel geometries and spacing throughout. During the course of the analysis, it became evident that, within stress and coolant pressure source limitations, it was not possible to safely cool the chamber if the predicted 70% increase in throat heat transfer actually occurred. The selected approach was to design the calorimeter chamber to accept a 30% increase in throat heat transfer. This value corresponds to the maximum acceptable increase for the regeneratively cooled baseline thrust chamber. In actual testing, it was envisioned that the chamber would initially be tested at reduced thrust, thus defining the order of magnitude of the enhancement under safe operating (burnout) conditions. Thus, testing could be terminated at reduced chamber pressure if the data indicated a potential problem. If it is assumed that the predicted 70% enhancement is accurate, then the maximum allowable operating chamber pressure would be approximately 80%. The heat transfer data obtained at the lower operating point would still be sufficient to define the impact of enhancement on the baseline chamber design.

Analysis of the two circumferential flow sections was done parametrically using the regenerative cooling program HEAT for general results and the thermal analyzer program SINDA for detailed verification at a few points. Predicted wall temperatures and burnout heat flux ratios are shown on Figures 22 through 24 in terms of gas-side heat transfer coefficient and coolant velocity, for a channel size 0.050 in. wide by 0.060 in. deep with 0.050-in. lands and a 0.030-in. gas-side wall thickness. Temperature values here are taken directly from the HEAT program in which the fin approximation for

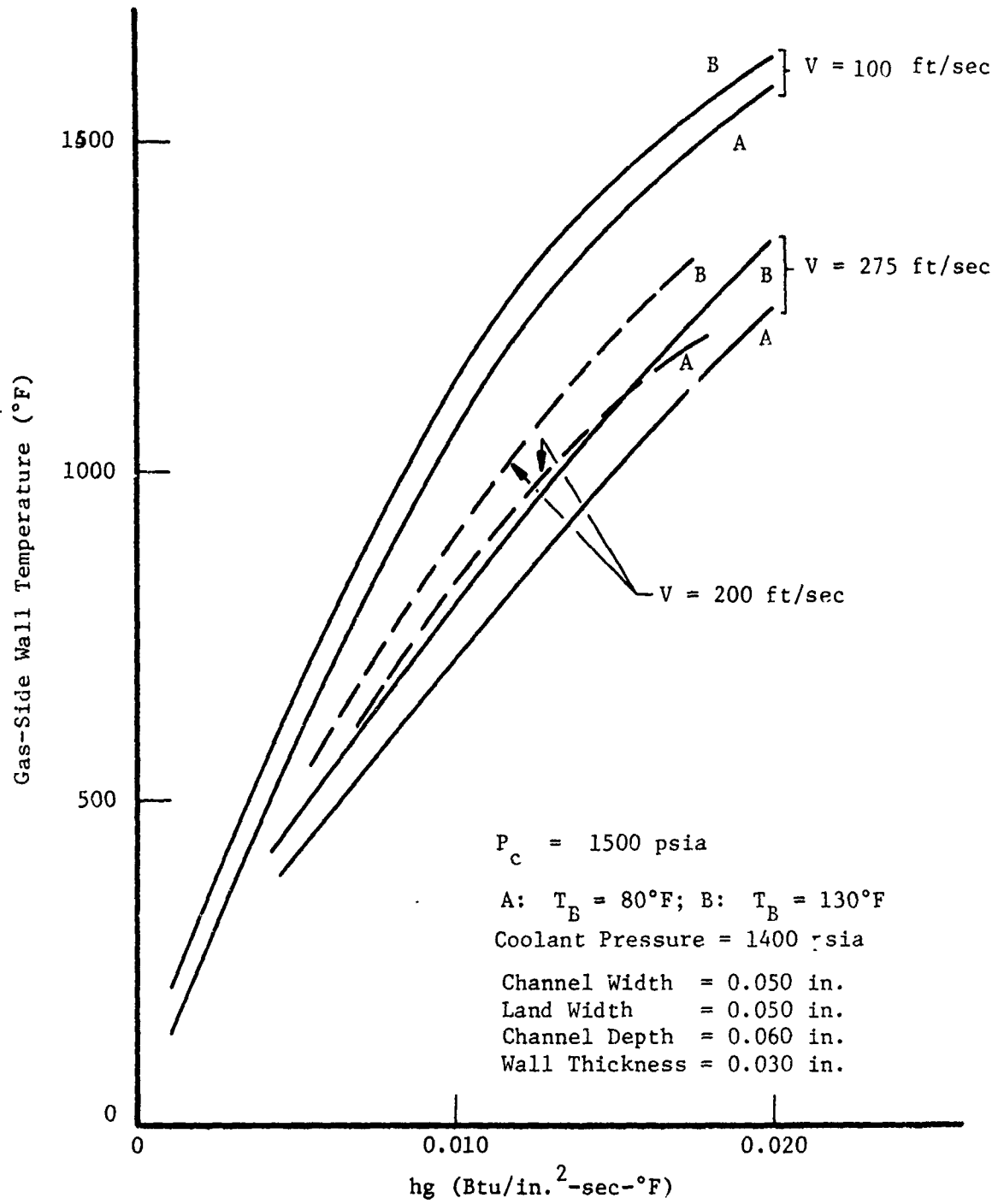


Figure 22. Predicted Gas-Side Wall Temperature vs Gas-Side Heat Transfer Coefficient and Coolant Velocity and Temperature

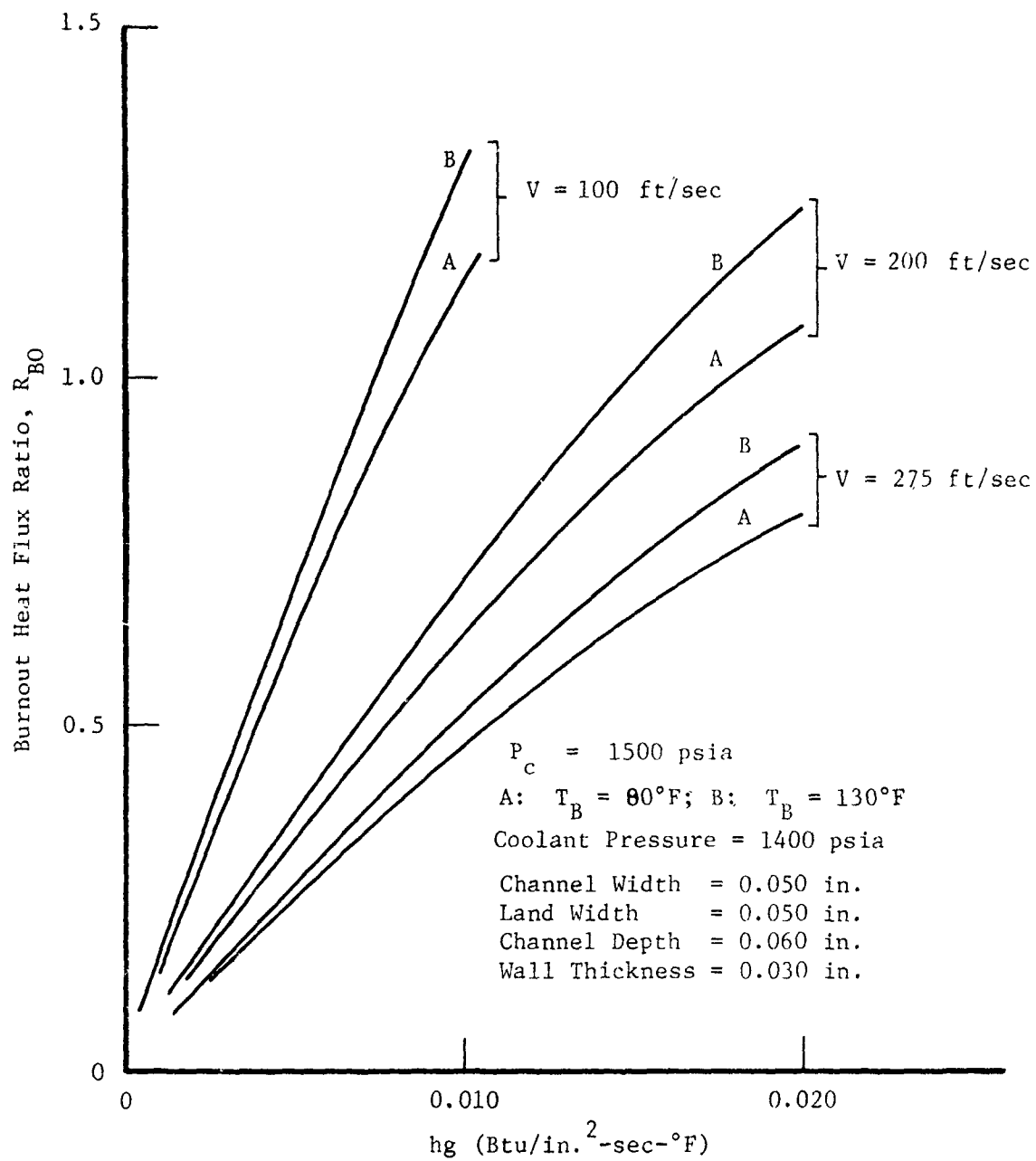


Figure 23. Predicted Burnout Heat Flux Ratio vs Gas-Side Heat Transfer Coefficient and Coolant Velocity and Temperature

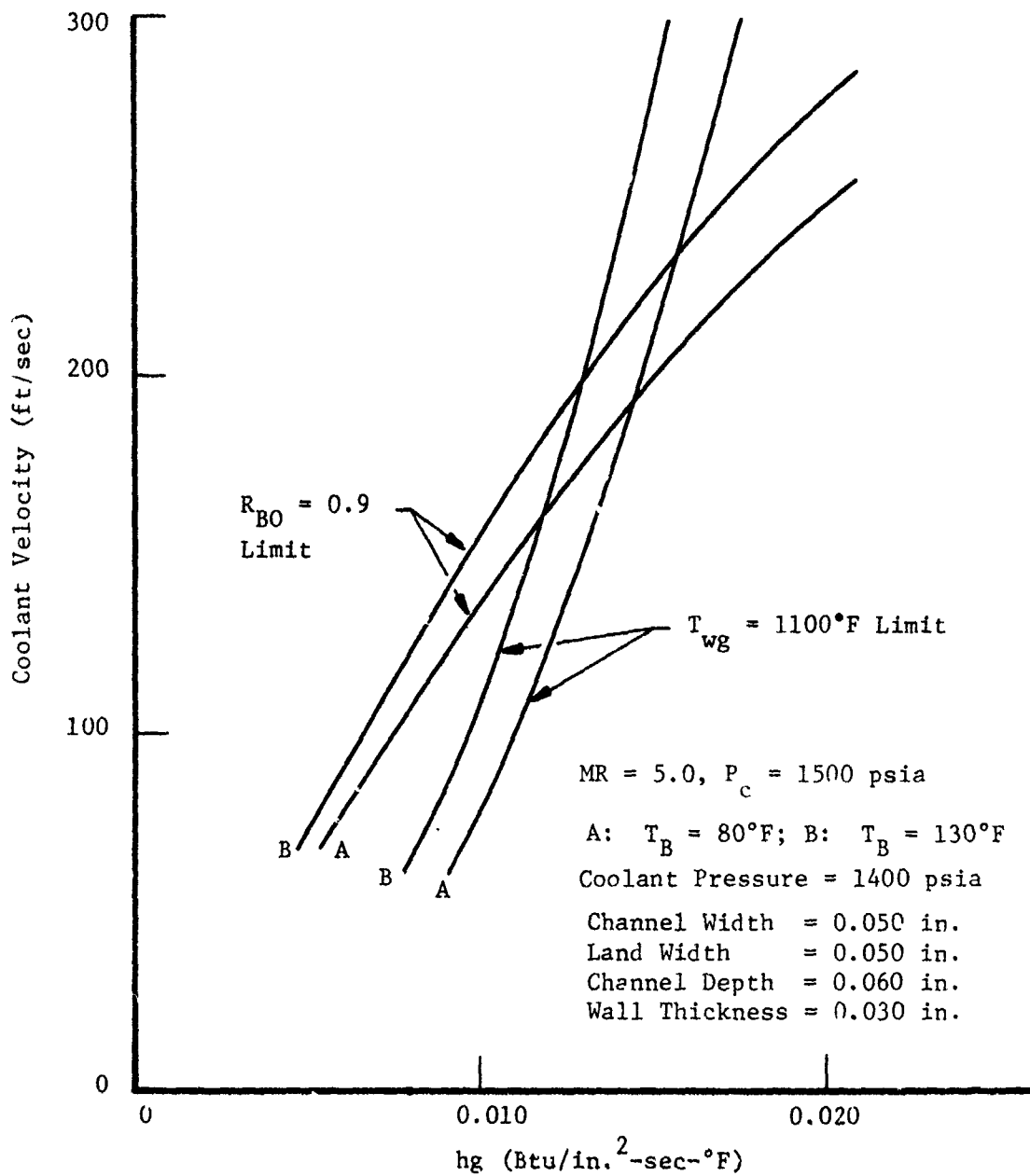


Figure 24. Burnout Heat Flux and Wall Temperature Limit Lines

III, A, Design (cont.)

heat conduction in the land was utilized. This approximation yields satisfactory agreement with more rigorous SINDA conduction analysis but is inadequate for evaluating the burnout heat flux ratio since an average wall temperature is calculated on the coolant side, while the burnout heat flux ratio should be evaluated at the point of highest temperature. Thus, the ratio was evaluated on the basis of the gas-side heat flux rather than the maximum coolant-side value. The latter is always less because of conduction in the land; at high heat fluxes, the difference is on the order of 10%. Hence, the ratio has a built-in conservative bias. Figures 22 and 23 are drawn for coolant velocities of 100, 200 and 275 ft/sec and coolant temperatures of 80 and 130°F at a pressure of 1400 psia. These data are cross-plotted in Figure 24 to show the required coolant velocity versus heat transfer coefficient for a wall temperature of 1100°F and a burnout heat flux ratio of 0.9. At low heat transfer coefficients, the coolant velocity is dictated by the burnout heat flux and, at high coefficients, by the wall temperature. Figure 25 reproduces the limiting segments of the same curves for an 1100°F wall temperature. Figure 26 shows the same types of curves for a 1200°F wall; both figures are for coolant pressures of 1400 psia. Figure 27 gives similar burnout heat flux and wall temperature limit lines for 1000 psia coolant. Pressure drops, while calculated by the HEAT program, are not presented because of the importance of entrance and exit losses, which are dependent on manifold and inlet geometries. This is discussed separately under hydraulic analysis. Pressure drops were calculated independently with an eye towards sizing orifices for flow control and manifolding channels into groups. This effort is described in the following section.

The required coolant velocities, at various stations along the inner and outer contours shown in Figure 28, are given in Figure 29, along with the design gas-side heat fluxes and predicted bulk temperature rises. The ultimate chamber pressure capability of the system would be determined by initially testing at reduced chamber pressures and comparing measured temperature rise data with predictions.

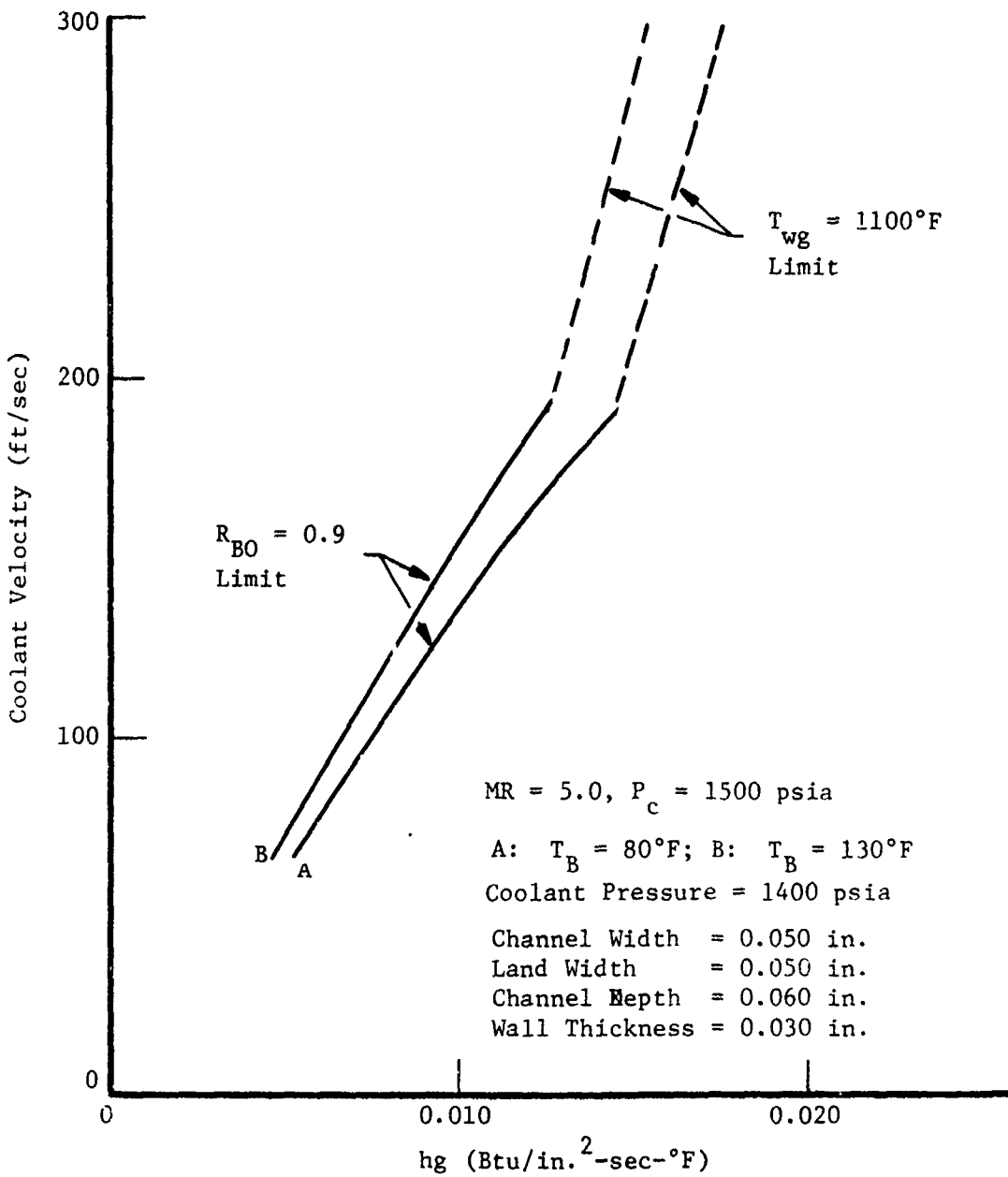


Figure 25. Burnout Heat Flux and Wall Temperature Limit Lines

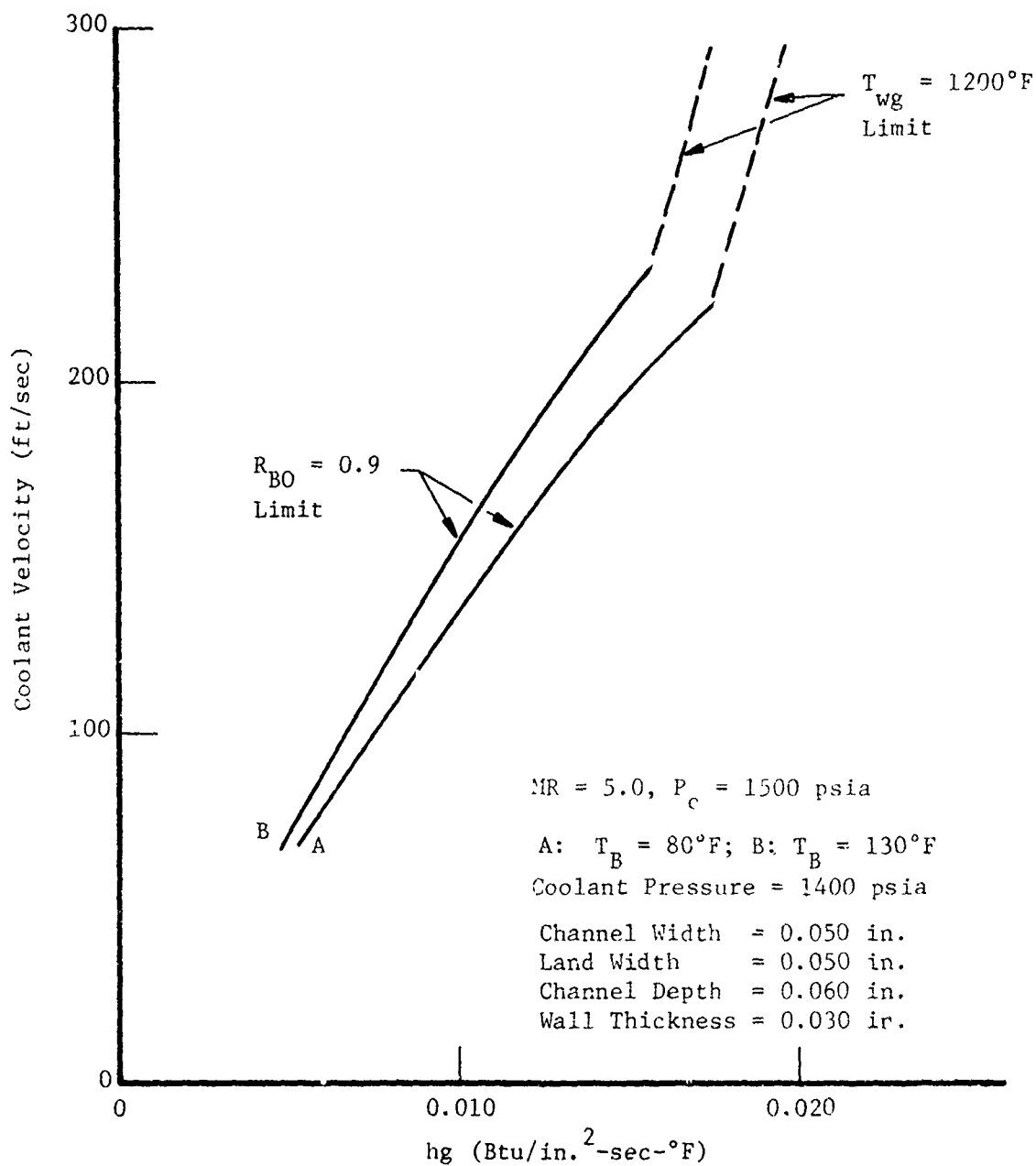


Figure 26. Burnout Heat Flux and Wall Temperature Limit Lines

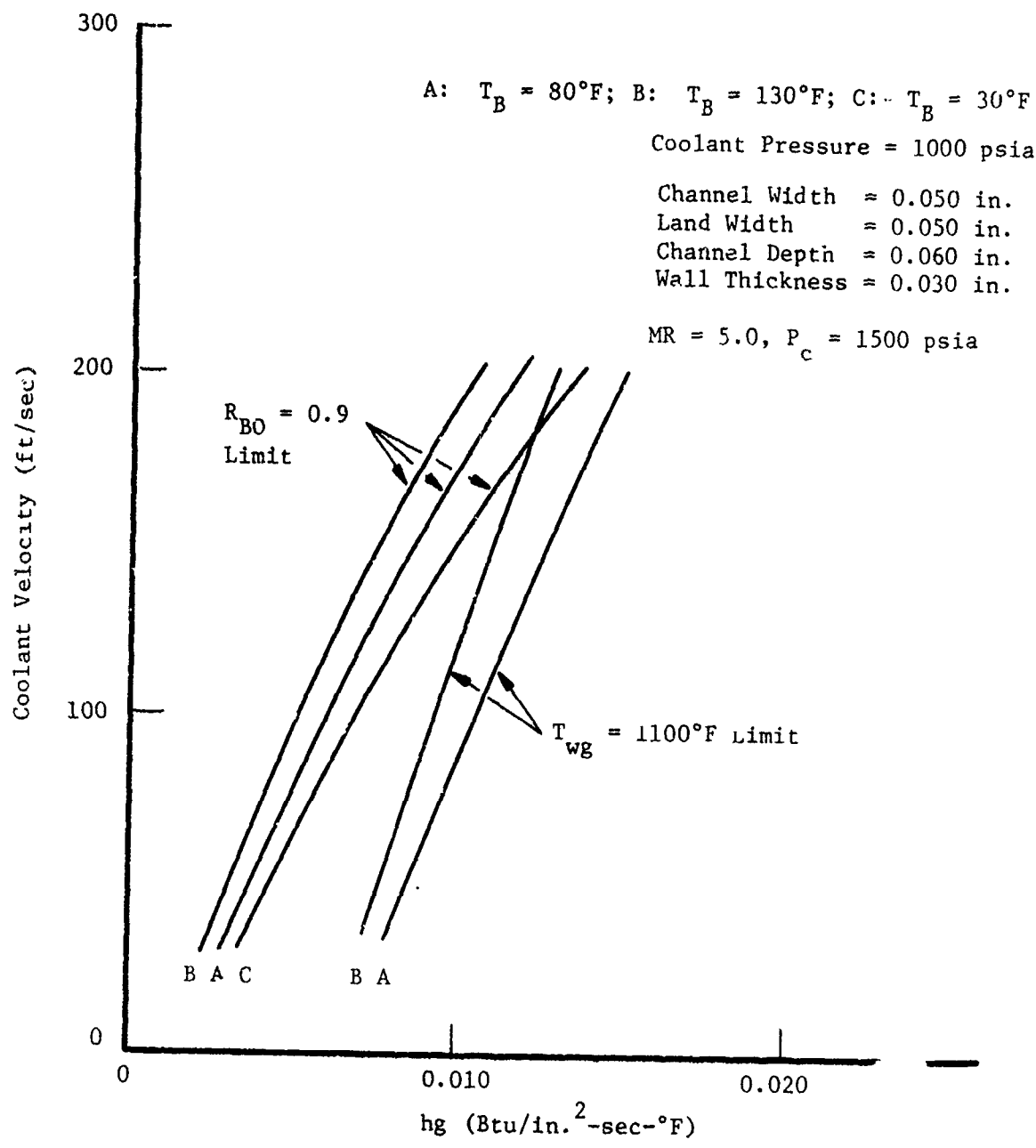


Figure 27. Burnout Heat Flux and Wall Temperature Limit Lines

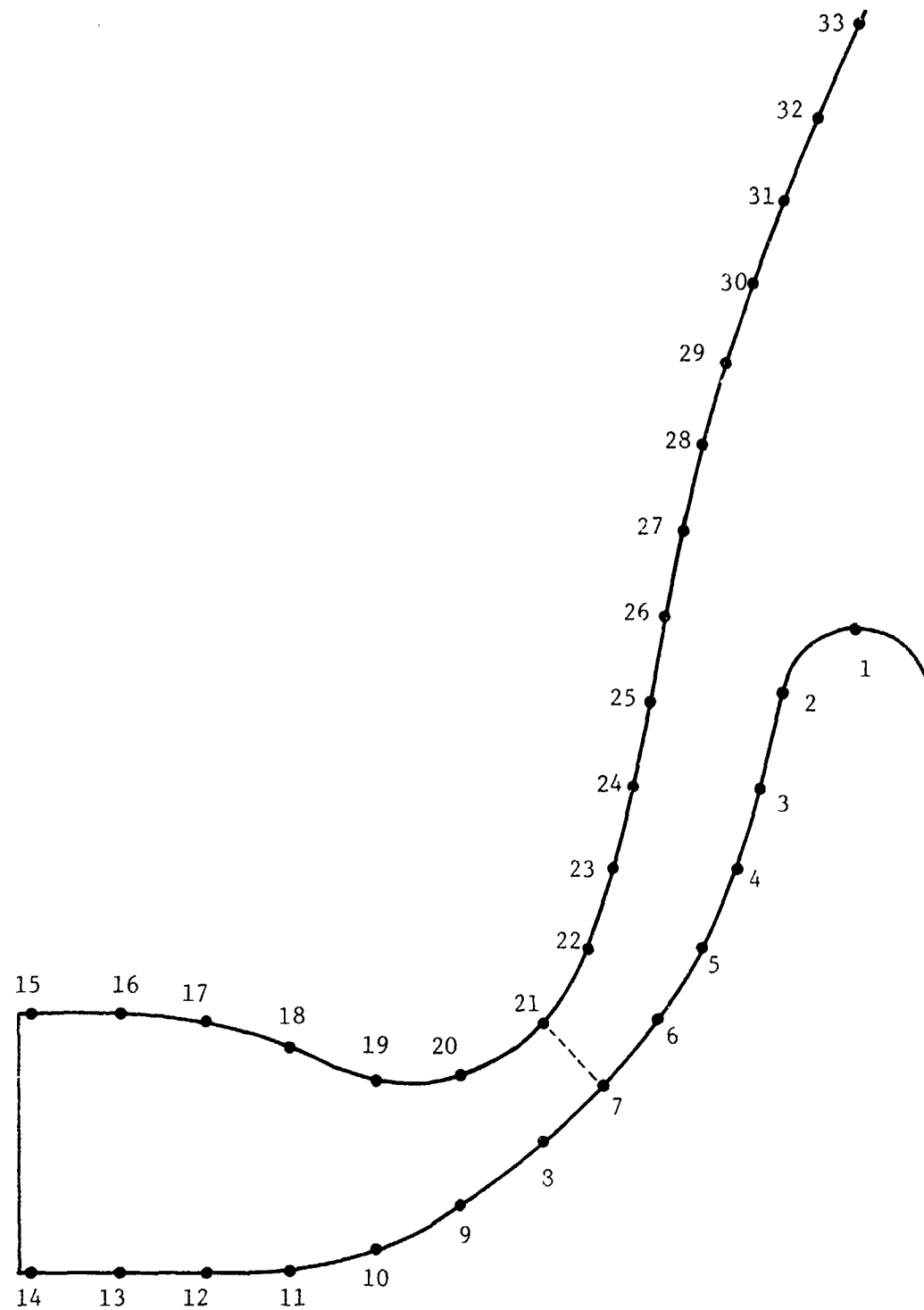


Figure 28. Station Locations on Inner and Outer Contours

Station (ref Fig 27)	(q/A) Design (Btu/in. ² -sec)	Coolant Pressure = 1400 psia		Coolant Pressure = 1000 psia	
		V (ft/sec)	ΔT _B (F)	V (ft/sec.)	ΔT _K (F)
1	7	40	64	40	64
2	7	40	58	40	58
3	7	40	57	40	57
4	20	60	35	75	28
5	50	155	78	195	62
6	70	240	61	Note 3	
7	90	280	57	Note 3	
8	90	280	47	Note 3	
9	80	240	44	Note 3	
10	65	200	38	Note 3	
11	50	155	32	195	25
12	40	120	36	160	27
13	35	105	36	140	27
14	35	105	36	140	27
15	35	105	72	140	54
16	35	105	69	140	52
17	45	140	68	180	52
18	50	155	65	195	51
19	60	185	59	220	50
20	75	225	61	Note 3	
21	75	225	69	Note 3	
22	60	185	75	220	63
23	42	135	85	175	66
24	37	115	97	150	75
25	32	95	113	135	79
26	27	80	120	110	87

NOTES:

- (1) T_B = 130°F
- (2) High pressure coolant intended for high heat flux regions only, at designer's discretion.
- (3) Lower pressure coolant inadequate in high heat flux regions.
- (4) Uniform channel geometry: 0.050 in. width, 0.060 in. depth, 0.050 in. land, 0.030 in. wall thickness.

Figure 29. Inner and Outer Body Design Data

III, A, Design (cont.)

The section of the outer body marked by stations 27 through 33 inclusive on Figure 28 (viz., at radii greater than the inner body exit radius and axially downstream of the inner body face) is designed for low pressure coolant. Minimum coolant pressure is 250 psia and the inlet manifold pressure is nominally 450 psia. The channel width and spacing are considerably larger than in the higher pressure sections: 0.200 in. width, 0.200 in. land, 0.060 in. gas-side wall thickness. Maximum gas-side wall temperature and burnout heat flux ratio are 750°F and 0.65, respectively. Design data are presented in Figure 30.

The two side plates presented a great deal of analytical design difficulty because of the large channel lengths, high velocity requirements in the throat, small increase in side plate width in the expansion section, and the usual weight-flow pressure drop tradeoff. After some preliminary hand calculations based on the above figures, HEAT runs yielded, for the locations shown in Figure 31, the channel design summarized in Figure 32. The higher heat transfer coefficient of the values on either side of the station was utilized across the entire side plate. Maximum predicted gas-side wall temperature is approximately 1050°F at the throat, with a burnout heat flux ratio of approximately 1.0 on the basis of the gas-side heat flux. The friction pressures drop in the channels combined with the inlet and exit losses was close to the available supply pressure, depending on channel location and channel geometry design details in the expansion section for the recommended water flow rate of 2.6 to 2.7 lb/sec per side at an inlet pressure of 1500 psia.

The water-cooled section as designed could not sustain full thrust heat loads arising from a 70% enhancement in heat transfer due to curvature effects. A 30% increase was tolerable, however, with a small margin

<u>Station</u> <u>(ref Fig 27)</u>	<u>(q/A) Design</u> <u>(Btu/in.²-sec)</u>	<u>V</u> <u>(ft/sec)</u>	<u>ΔT_B</u> <u>(F)</u>
27	19	120	63
28	14	104	58
29	10	91	52
30	7	75	48
31	6	60	57
32	6	40	78
33	5	40	80

NOTES:

- (1) $T_B = 130^{\circ}\text{F}$
- (2) Minimum coolant pressure is 250 psia.
- (3) Channel geometry: 0.200 in. width, 0.200 in. land, 0.060 in. depth, 0.060 in. wall thickness.

Figure 30. Low Pressure Coolant Section Design Data

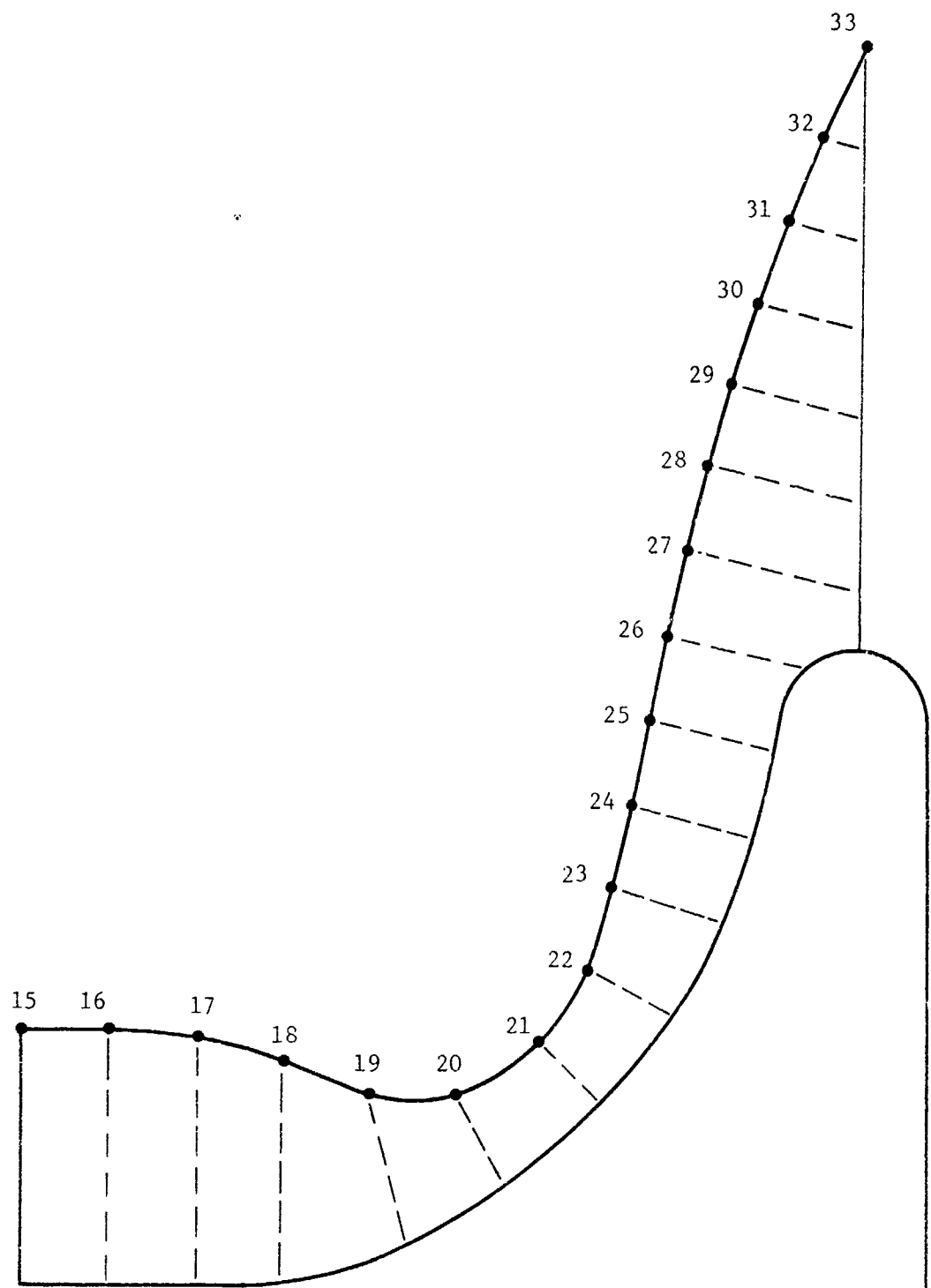


Figure 31. Nodal Locations on Side Plates

<u>Station (ref Fig 29)</u>	<u>No. of Channels</u>	<u>Width (in.)</u>	<u>Depth (in.)</u>
15	16	0.050	0.075
16	16	0.050	0.075
17	16	0.050	0.075
18	16	0.050	0.075
19	8	0.050	0.075
20	8	0.040	0.075
21	8	0.030	0.075
22	8	0.040	0.075
23	8	0.050	0.075
24	8	0.050	0.075
25	8	0.050	0.075
26	8	0.050	0.075
27	8	0.050	0.075
28	8	0.050	0.075
29	8	0.050	0.075
30	8	0.050	0.075
31	8	0.050	0.075
32	8	0.050	0.075
33	8	0.050	0.075

NOTES:

- (1) Pressure at inlet manifold is 1500 psia.
- (2) Coolant flow rate is 2.6 to 2.7 lbm/sec per side.
- (3) Coolant flow is parallel to hot gas flow.
- (4) Wall thickness = 0.030 in.
- (5) MR = 5.0, $P_c = 1500$ psia

Figure 32. Side Plate Design Data

III, A, Design (cont.)

of safety ($R_{B0} = .8$ to $.9$) on the burnout heat flux. The side plates could also withstand a 30% increase in throat heat flux but with almost no margin of safety. It was felt that low pressure testing would indicate the degree of enhancement of gas-side heating which is relatively insensitive to chamber pressure assuming the Ito correction factor applies, as well as the ultimate capability of the test section. Increased margin of safety on the burnout heat flux may be achieved by cooling the water to 40 to 50°F prior to inletting it to the test section or by operating at higher coolant pressures. The analysis assumed a range of water inlet temperatures of 80 to 130°F. Finally, it was also recognized that reduced heat loads in the corners of the test section would lead to coolant temperature rises which underestimate the average heat flux levels used in the analysis.

Discussions were presented earlier with respect to using the Ito correction in calculating the heat transfer coefficient as the hot gas is turned through the throat. The dilemma in the analysis of the side plates is to account for the increased heat transfer that will occur on the inner body side and the potential decrease on the outer body side. The selected approach was to use the highest possible heat transfer coefficient (inner body side) at each of the station locations shown in Figure 32, thus ensuring a conservative design.

The problems identified above stem from geometry considerations and the manifolding required to feed the transverse coolant passages. The result is that the side plate passages must conform to the internal chamber, resulting in long passages requiring a bifurcation at Station 18. A required flow rate is 2.6 to 2.7 lb/sec at 1500 psia inlet pressure. Maximum predicted gas-side wall temperature is 1050°F at the

III, A, Design (cont.)

throat with a burnout heat flux ratio of 1.0 on the basis of gas-side heat flux at nominal operating conditions and 30% gas-side enhancement.

(b) Hydraulic Analysis

The hydraulic analysis of the calorimeter sector chamber was conducted using the Incompressible Flow Hydraulic Network Computer Program (Ref 17). Two circuits were analyzed: a low flow rate, high pressure drop circuit located in the chamber throat region and a high flow rate, lower pressure drop circuit for the remaining region including the two chamber side plates. Individual circuit flow rates were established from the results of the heat transfer design analysis; the hydraulic analysis then established flow control orifice sizes for each individual circuit. Three pressure level coolant circuits were used for this hardware to minimize the requirement for high pressure, high flow rate water which would have had a serious impact on the test facility. Analysis of the low pressure (250 psi) divergent nozzle cooling circuit was not required.

Six individual low flow circuits were analyzed: two on the outerbody and four on the centerbody. The low flow circuit requires a minimum channel static pressure of approximately 1400 psia in order to meet the heat transfer requirements and a maximum channel static pressure of approximately 1900 psia to satisfy stress limits. These pressure requirements, together with the individual circuit flow rate requirements, define the circuit hydraulic constraints. The solution shown in Table IV meets the flow requirements described above (flow circuit identification and designations are shown in Figures 33 and 34). In order to maintain the maximum channel static pressure at approximately 1900 psi, the flow rate in circuit OG3 (inner body, reference Figure 34) was increased approximately 10% above the minimum required value for cooling. This results in a total water flow rate requirement of 10.47 lbm/sec with a corresponding inlet pressure of approximately 2940 psig.

TABLE IV
CALORIMETER CHAMBER HYDRAULIC ANALYSIS

<u>LOW FLOW CIRCUIT</u>								
<u>Side</u>	<u>Circuit</u>	<u>\dot{w} Req'd</u>	<u>\dot{w} Calc</u>	<u>p_{static} Channel Inlet</u>	<u>p_{static} Channel Outlet</u>	<u>Outlet Tube ID</u>	<u>Orifice Dia (in.)</u>	<u>ΔP Orifice (psi)</u>
Outer Body	OC3	0.36	0.367	1931	1348	0.148	0.061	1248
	OG3	3.00	3.332	1914	1360	0.242	0.186	606
Center-body	OC3	0.36	0.374	1922	1484	0.148	0.060	1381
	OG3	3.00	3.017	1907	1509	0.242	0.167	933
	OC4	0.36	0.371	1934	1379	0.148	0.061	1276
	OG4	3.00	3.010	1910	1405	0.242	0.170	825

ΔP = 2940 psi (chamber inlet to dump tube)

\dot{w}_{H_2O} = 10.47 lbm/sec

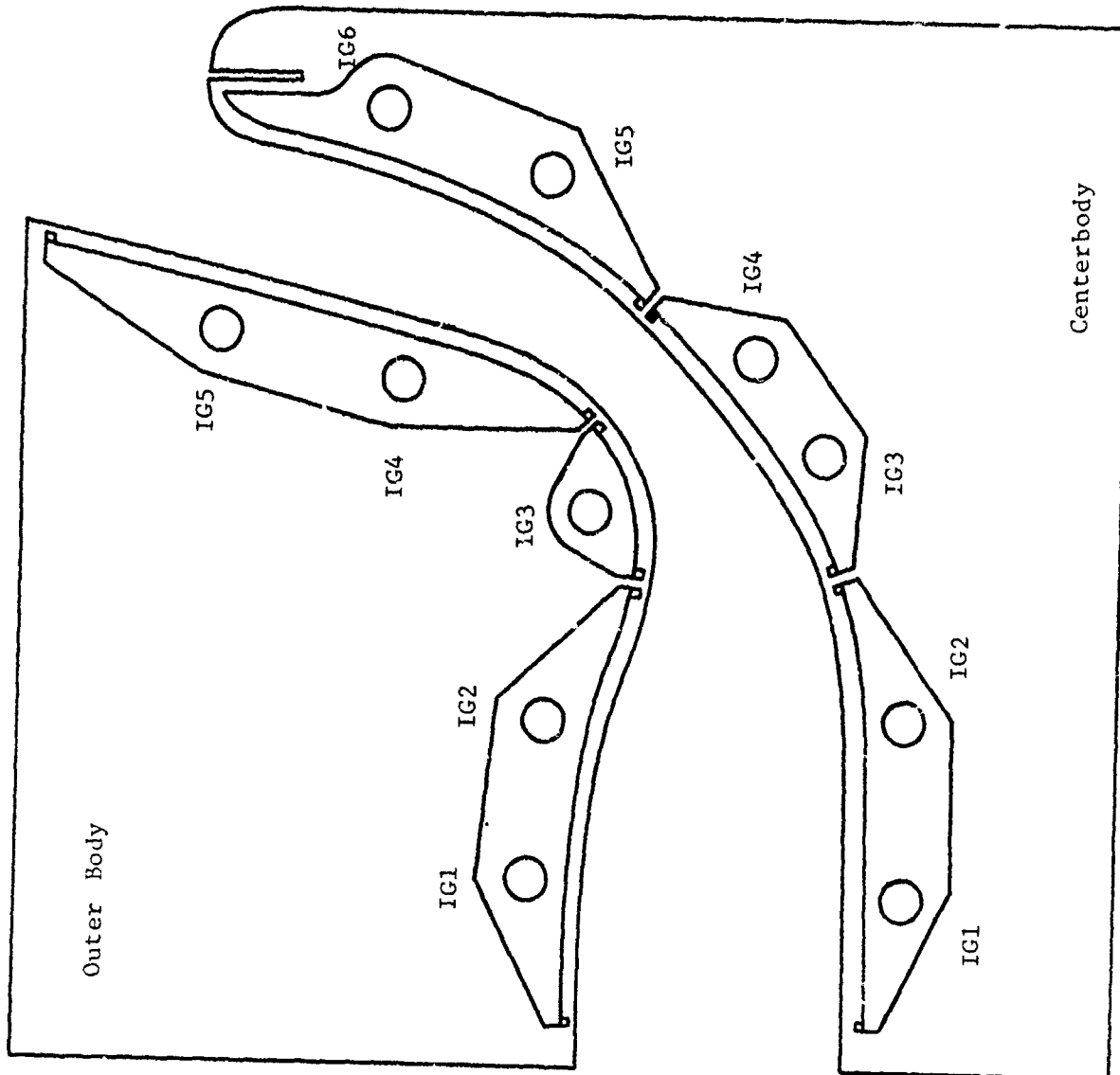


Figure 33. Inlet Coolant Passage Circuit Designations

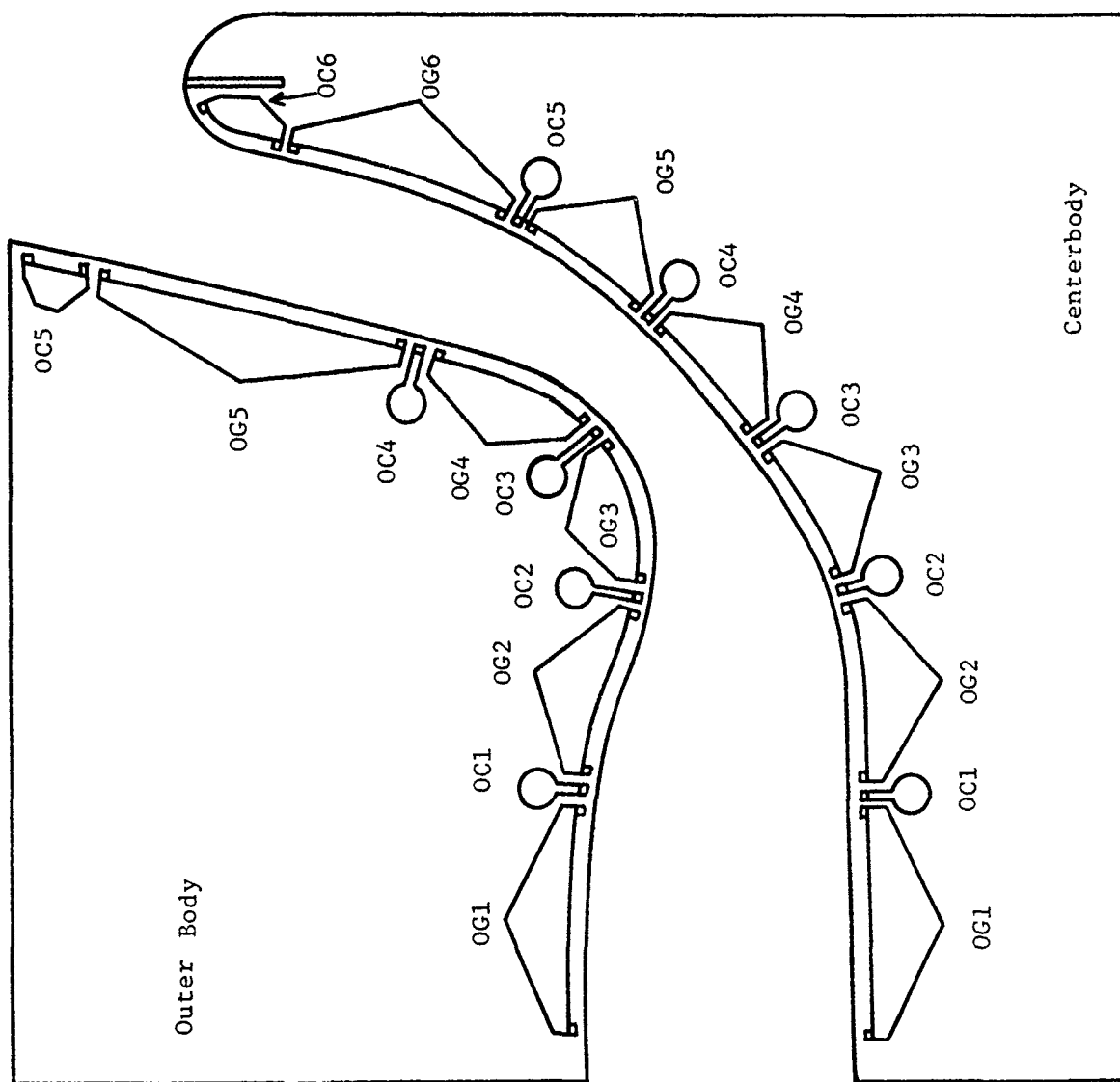


Figure 34. Outlet Coolant Passage Circuit Designations

III, A, Design (cont.)

Table V presents the results of the high flow circuit hydraulic analysis. Eighteen individual circuits are included: eight on the outerbody, eight on the centerbody, and one for each of two side plates. The high flow circuit requires a minimum channel static pressure of approximately 1000 psia in all but the side plate circuits. Adequate back pressure is maintained in the critical heat flux areas of the side plates as a result of the channel pressure loss from the critical zones to the exit header because of the axial orientation of these passages. The centerbody and nozzle channels have a maximum static pressure constraint of approximately 1900 psia while the side plate channels have a maximum static pressure constraint of approximately 2100 psia. The solution shown in Table V meets these requirements. In order to control the maximum channel static pressure, it was found necessary to increase the individual circuit flow rates in the nozzle circuits OG5 and OC5 and the centerbody circuits OG6 and OC6 to above the level required for cooling. This resulted in a total flow rate requirement of 34.78 lbm/sec of water with a corresponding inlet pressure of approximately 2307 psig.

(4) Uncooled Heat Sink Chamber

The use of an uncooled heat sink chamber to gather the required heat transfer data on an E-D nozzle was also investigated. Figure 35 summarizes the results of the analysis which considered the utility of an uncooled chamber. The time to 1800°F assumes gas-side enhancement and a step change to chamber pressure. Indicated on both curves are experimental values obtained on an ALRC storables propellant program operating at approximately 1700 psia chamber pressure.

TABLE V
CALORIMETER CHAMBER HYDRAULIC ANALYSIS

HIGH FLOW CIRCUIT

<u>Side</u>	<u>Circuit</u>	<u>\dot{w} Req'd</u>	<u>\dot{w} Calc</u>	<u>P_{static} Channel Inlet</u>	<u>P_{static} Channel Outlet</u>	<u>Dump Tube ID</u>	<u>Orifice Dia (in.)</u>	<u>ΔP Orifice (psi)</u>
Outer Body	OG1	3.00	3.011	1891	1644	0.242	0.1663	961
	OC1	0.25	0.273	1766	1420	0.085	0.0586	511
	OG2	3.00	3.017	1662	1274	0.242	0.1780	641
	OC2	0.30	0.307	1636	1267	0.085	0.0762	113
	OG4	3.00	3.031	1662	1186	0.242	0.1830	551
	OC4	0.25	0.267	1790	1358	0.085	0.0585	488
	OG5	3.00	3.976	1924	1555	0.242	0.2169	287
	OC5	0.30	0.798	1791	1114	0.148	0.1100	405
Center- body	OG1	3.00	3.018	1889	1766	0.242	0.1625	1081
	OC1	0.25	0.275	1757	1587	0.085	0.0560	663
	OG2	3.00	3.035	1656	1449	0.242	0.1715	811
	OC2	0.30	0.313	1623	1383	0.085	0.0713	191
	OG5	2.64	2.640	1534	1040	0.242	0.1715	614
	OC5	0.25	0.267	1745	1360	0.085	0.0585	489
	OG6	3.00	4.058	1871	1536	0.242	0.2301	184
	OC6	0.27	1.085	1894	1475	0.148	None	0
Side Plate		2.70	2.685	2166	40	0.402	None	0
Side Plate		2.70	2.685	2166	40	0.402	None	0

$\Delta P = 2307 \text{ psi}$ (chamber inlet to dump tube)

$\dot{w}_T = 34.78 \text{ lbm/sec}$

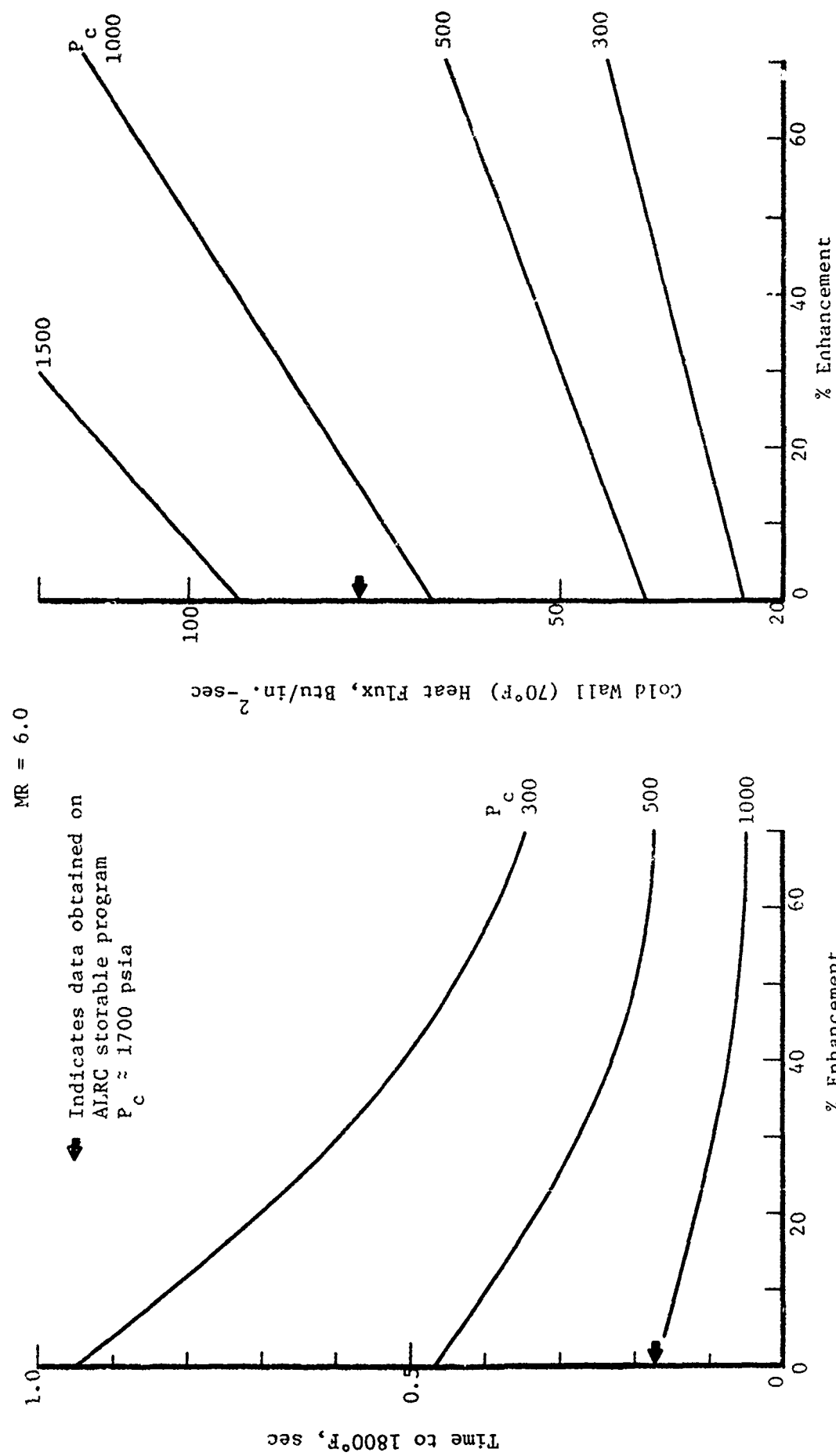


Figure 35. Uncooled Chamber - Centerbody Throat Station

III, A, Design (cont.)

The conclusion drawn from the analysis is that, with a test duration capability (from P_c rise) of approximately 0.2 sec, an uncooled chamber could be used to obtain heat flux data up to chamber pressures between 500 and 1000 psia, depending on the degree of enhancement. Extrapolation of these data to higher pressures for design purposes may be accomplished using the following simple relationship:

$$q/A \propto P_c^{0.8}$$

The enhancement factor could be taken as the ratio of measured heat flux to theoretical heat flux for a low pressure case and extrapolated to higher pressure according to:

$$\frac{Q/A_{\text{experimental}}}{Q/A_{\text{theoretical}}} = \eta_f(\text{enhancement}) \propto P_c^{0.05}$$

The final design (PN 1161977) shown in Figure 36 consists of copper inner and outer bodies and two copper side plates. Structural support is provided by a stainless steel "filler block" on the inner body side and a stainless mounting flange brazed to all five components.

3. Injectors

a. Injector Selection

Five different injector designs were evaluated. These designs were judged against a set of criteria that is both generally and specifically applicable to E-D nozzle type engines. The criteria were:

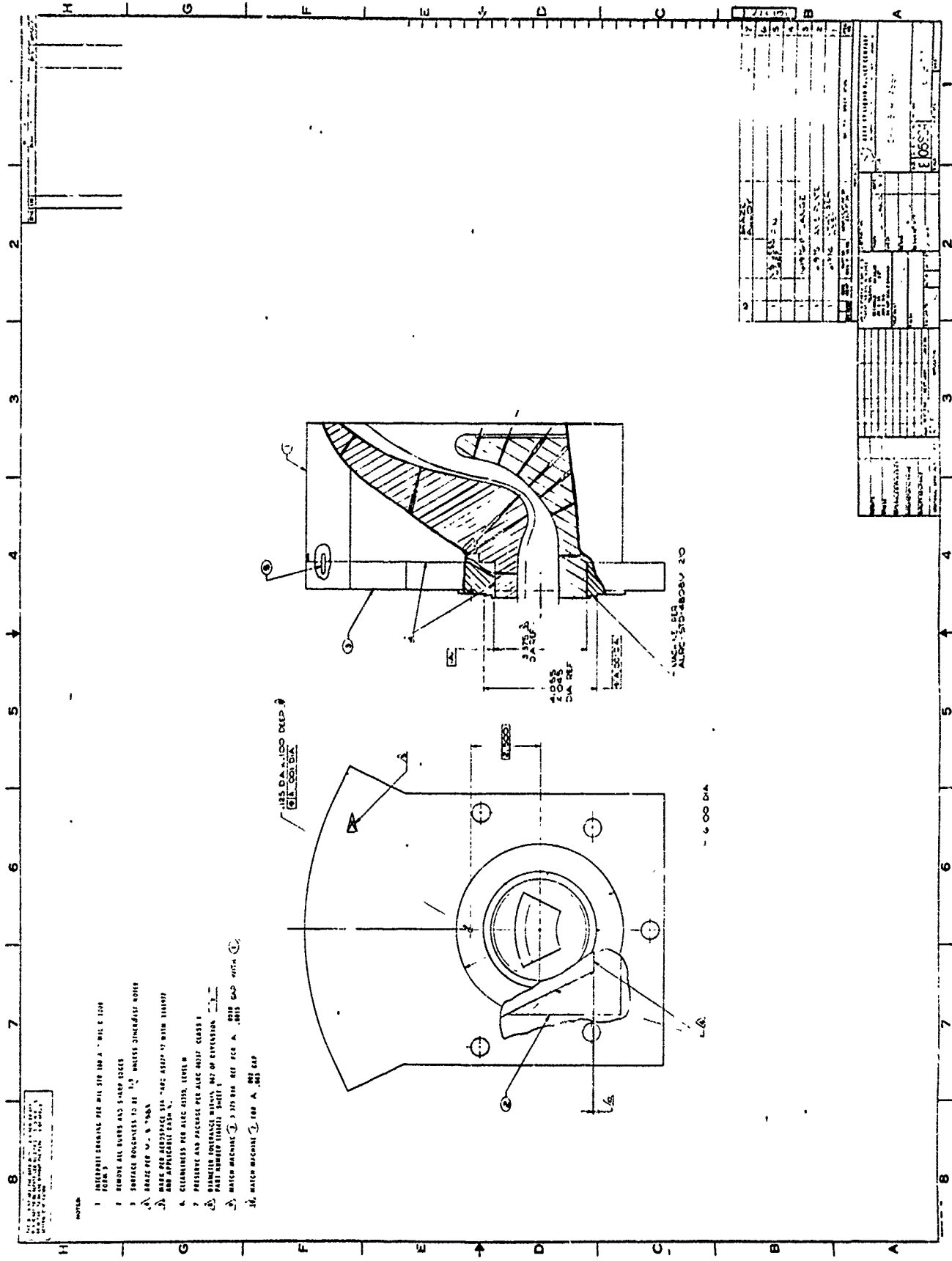


Figure 36. Uncooled Chamber Assembly

III, A, Design (cont.)

Combustion Efficiency
Throttling Capability
Stability
Compatibility
Prior Test History

The five candidate injector designs considered were:
(1) coaxial, (2) micro-coaxial, (3) transverse platelet, (4) HIPERTHIN radial outflow, and (5) HIPERTHIN axial flow. Table VI summarizes the concept evaluation.

The axial flow platelet injector was selected by ALRC as this configuration allowed more overall program flexibility for design of the plug, flange attachments, coolant lines, seals, instrumentation, and related hardware during development of the demonstration thrust chambers.

In the following sections, the design of both the annular and sector injectors is discussed. The sector design is a true one-seventh segment of the full annular design; i.e., it employs the same vane design and manifolding. Therefore, much of the analysis effort was common to both designs. In such cases, the analyses are discussed under the annular injector design section.

b. Annular Injector Design

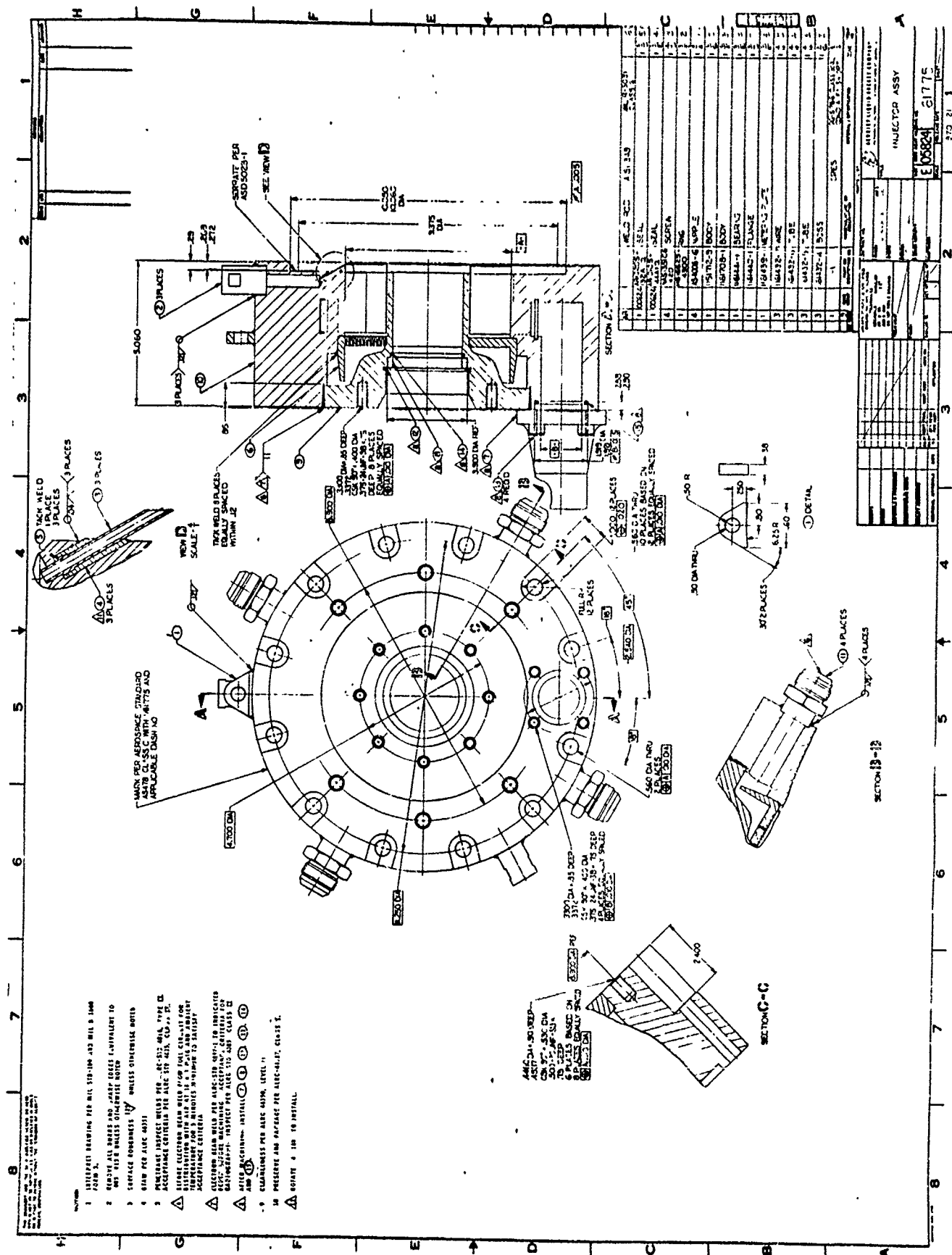
The annular injector design is shown in Figure 37 (ref PN 1161775). The vaned injector concept was chosen to take best advantage of the propellant density differences which require a relatively large fuel-to-oxidizer orifice area ratio. In addition, the etched vanes permitted the oxidizer orifices to be small and numerous, promoting complete oxygen vaporization.

TABLE VI
INJECTOR DESIGN CONCEPTS

Injector Type	Combustion Efficiency in Available L'	Throttling Potential:			Compatibility:			Proven Test History	Remarks
		- Performance		- Zone Cooling	- Pattern Uniformity		- Fit Different Engine Configs		
		- Oxidizer	Boiling	-	-	-	-		
(1) Coaxial	X	--	0		X		0		
(2) Micro-coaxial	0	--	0	--	0		--		Difficult to fabricate
(3) Transverse	0	0	--	--	--		--		
(4) Platelet radial outflow	0	0	0	0	0		X		
(5) Platelet axial flow	0	0	0	0	0		0		

LEGEND:

- X Unsatisfactory
- Marginal
- O Satisfactory



III, A, Design (cont.)

within the 3-in. chamber length. The vanes are positioned radially and feed from the outer periphery. The injector/chamber configuration is therefore not vaporization limited and performance is governed primarily by propellant distribution and mixing.

The basic vane design consists of nine photoetched platelets of three configurations. These three configurations are shown in Figure 38. The vane construction, beginning with the innermost platelets, consists of the following: (1) three through-etched platelets, one (center) of copper and two stainless; (2) two copper depth-etched platelets which, combined with (1), form the oxidizer flow circuit; (3) two stainless insulator platelets; and (4) two stainless end platelets. The selected composite construction of copper and stainless steel permitted the best properties of both materials to be functional; i.e., copper at the injection edge after tapering and stainless steel forming the outside surfaces. The copper promotes cooling of the trailing edge, preventing face erosion, and stainless steel adds strength to the vanes.

Two basic vane designs (-1 and -2) are included in the injector. The difference in the vane design lies in the size and radial location of the impinging doublet elements. These differences can be seen in the oxidizer metering plate design for the two vanes as shown in Figures 39 and 40 (PN 1161422 for the -1 vane and PN 1161427 for the -2 vane). Both vane types have seven impinging elements (numbered 1 to 7 from the injector inboard to the injector outboard radius as shown in Figures 39 and 40) which increase in size from the inboard to outboard injector radius. Such a design provides increased oxidizer flow with increasing injector radius, thus maintaining a uniform oxidizer to fuel ratio at the vane trailing edge. The injector contains alternating -1 and -2 vanes to provide a uniform doublet element spray fan distribution as shown in Figure 41.

Complete Vane Assy

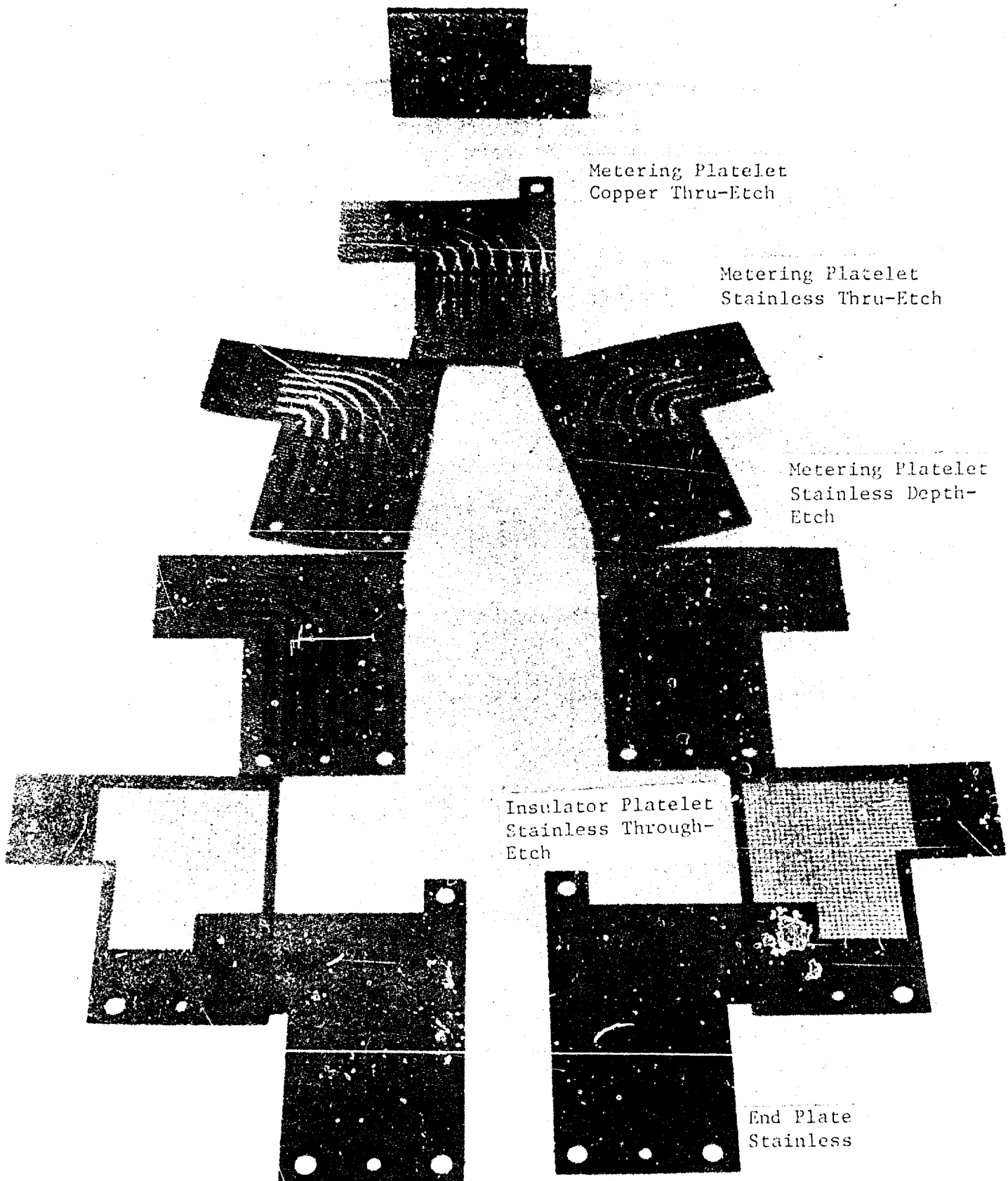


Figure 38. Injector Vane Construction

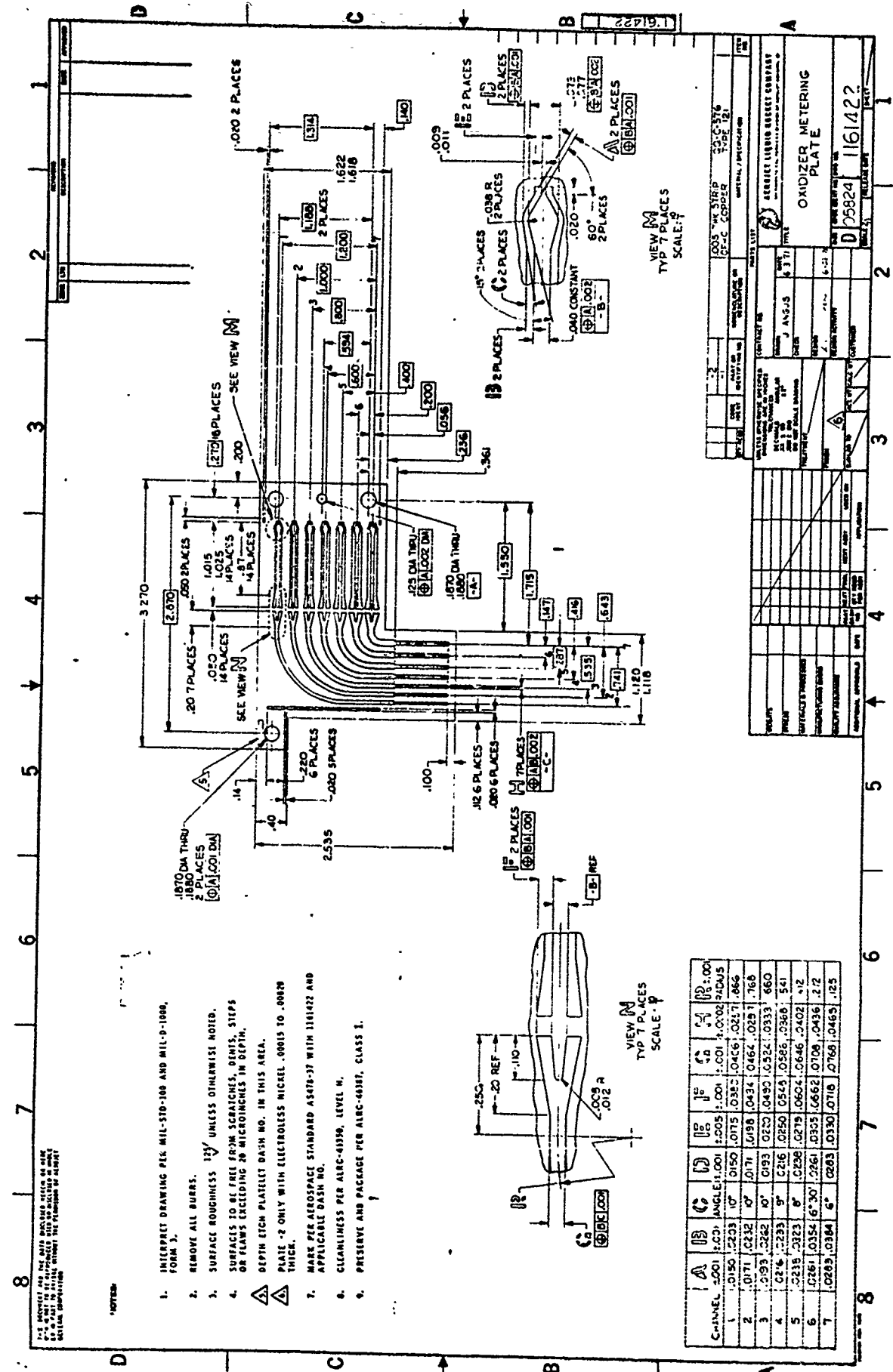


Figure 39. Oxidizer Metering Platelet - PN 1161422

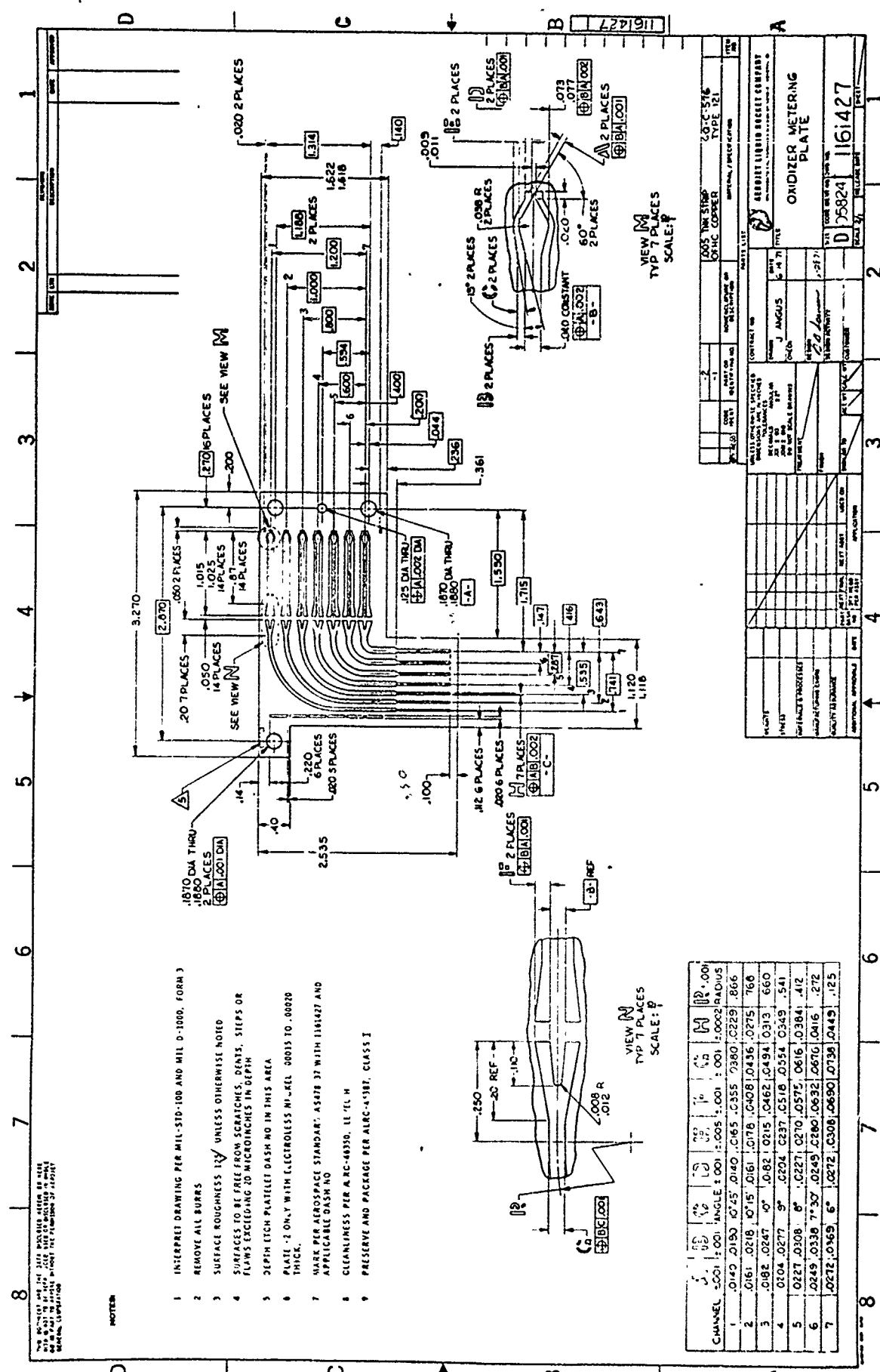


Figure 6. Oxdizer Metabolic Profile - PN 1116427

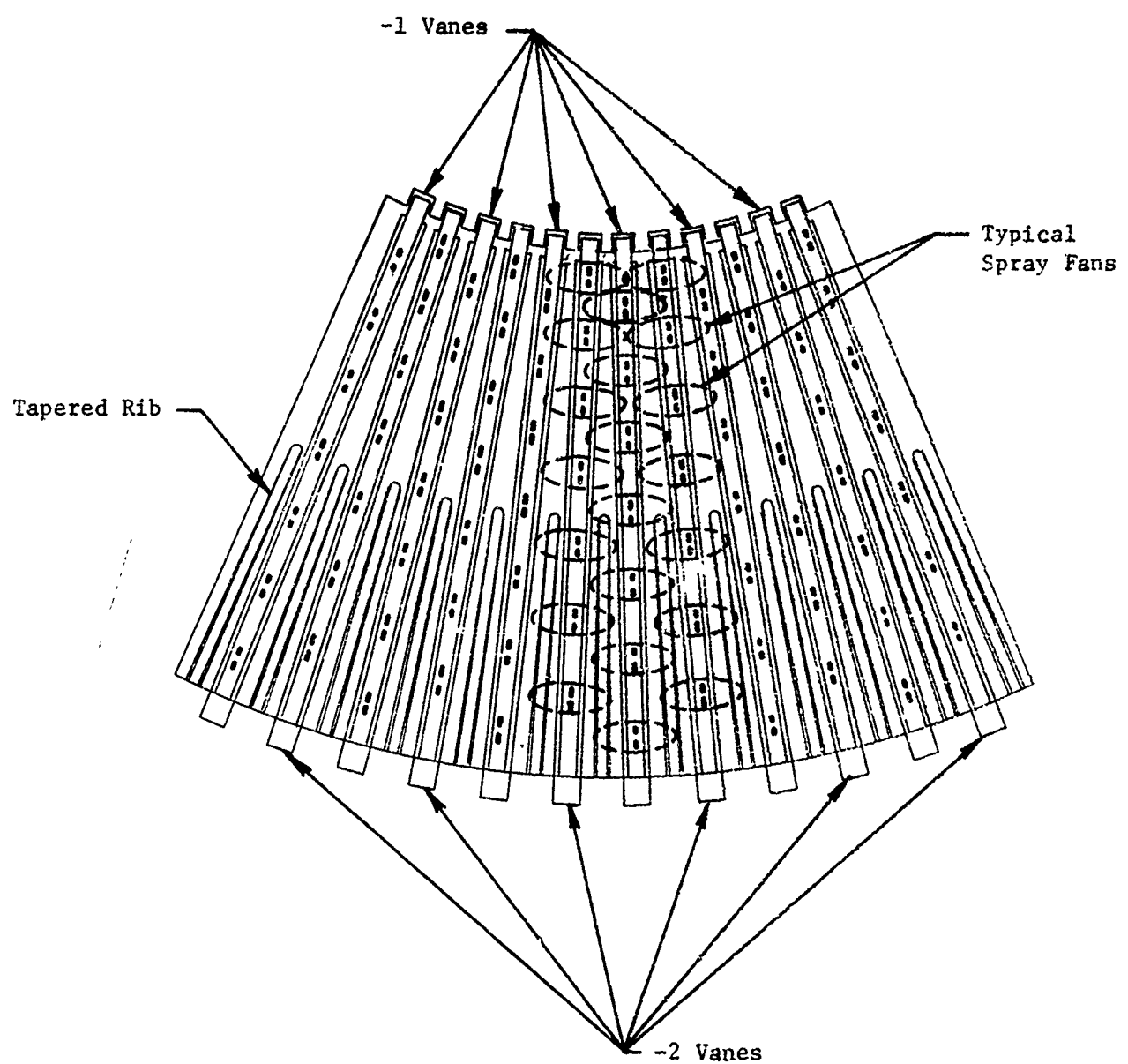


Figure 41. Injector Element Spray Fan Distribution

III, A, Design (cont.)

The vane hydraulic and heat transfer analyses are presented in detail in a later section on the sector injector design.

The oxidizer circuit was insulated from the fuel circuit with insulator plates (grids containing approximately 80% void area) in order to retard gasifying the oxygen. The insulation was predicted to be effective above 800 psia chamber pressure, and the two-phase gaseous oxygen present at lower pressures to be in sufficiently small percentages to not seriously affect the mixture ratio distribution. Ninety vanes are used in the complete injector assembly.

The oxidizer injection circuit is comprised of the etched passages within the vane. Seven like-on-like doublets are formed on each vane. Orifice size decreases radially inward in proportion to the decreasing space between vanes, thus maintaining a constant element mixture ratio. Approximately 60% of the vane pressure drop is taken near the entrance of the vane in a region of uniform oxygen temperature. This high resistance reduces the overall resistance variation of each element caused by fluctuation of density in the element orifices and provides uniform element mixture ratio during throttling.

The fuel injection circuit is the space between vanes. An orifice plate just upstream of the vanes controls flow distribution to these spaces.

The gas flow-through area between the injector vanes is a function of both the injector radius (r) and the vane thickness (t) within the inboard and outboard radii. The oxidizer distribution has been tailored to provide a uniform mixture ratio based on a fuel flow proportional to the flow-through area at the vane tip (trailing edge) as described previously. Since the

III, A, Design (cont.)

vane is tapered from the leading edge to the trailing edge (axial direction), the gas flow-through area varies with respect to the injector radius over the vane height. In order to maintain the same flow-through area radial variation between the vanes, a tapered rib which plugs up the excess area at the outer periphery of the injector was installed between each vane as shown in Figure 41.

The oxidizer manifold is an offset circle torus of rectangular cross section designed for near constant velocity. A single inlet is provided. The fuel manifold is a constant area torus fed by four radial inlets equally spaced. The torus contains a circumferential baffle that reduces adverse inlet conditions.

The igniter effluent gas ($MR = 2.0$) is fed through three tungsten tubes placed between vanes equally spaced around the annulus. The gas is injected at a 30-degree angle off the injector face and at the face plane. The igniter system has a predicted 500 millisec duration capability, limited by the transient heating of the igniter tube.

(1) Annular Injector Hydraulic Analysis

Gaseous hydrogen/liquid oxygen propellant weight flows equivalent to 25,000 lbf thrust, chamber pressure of 1500 psia, expansion area ratio of 435:1, and a nominal O/F ratio of 6.0 were computed on the basis of a delivered specific impulse of 470.8 lbf-sec/lbm. This performance results in a gaseous H_2 flow rate requirement of 7.6 lbm/sec. The following inlet conditions were used for the analysis:

III, A, Design (cont.)

$$\begin{aligned} \text{LO}_2 \ p &= 3000 \text{ psia} & T &= 230^\circ\text{R} \\ \text{GH}_2 \ p &= 1800 \text{ psia} & T &= 700^\circ\text{R} \end{aligned}$$

The liquid oxygen enters the injector through a single feed port 1.5 in. in diameter and approximately 3.5 in. in length. From this inlet port, the liquid oxygen makes a 90-degree turn and separates into a nearly constant velocity annular manifold. From the annular manifold, the flow enters the individual vane passages and is then injected into the combustion chamber. At full thrust conditions, a total liquid oxygen pressure drop of approximately 1280 psi is predicted. The total pressure drop consists of approximately 70 psi loss in the manifold (entrance, turn, and flow losses) and 1210 psi in the vanes. The liquid oxygen manifold has nearly uniform static pressure distribution which results in predicted mass flow nonuniformities of less than $\pm 1.5\%$.

The calculated fuel total pressure drop (manifold inlet to P_c) is 277 psi at full thrust conditions. Of this total, 20 psi is attributed to inlet manifold losses, 93 psi to losses associated with flow across the manifold baffle, and the remaining 164 psi is attributed to the pressure loss across the distribution plate and injector vanes. The following Mach number profile has been determined for the H_2 gas-side manifold system:

<u>Location</u>	<u>Mach No.</u>
Inlet port	0.18
Annular manifold	0.12-0.0
Baffle	0.28
Upstream of distribution plate	0.023
Orifice, distribution plate (vena contracta)	0.85
Orifice, distribution plate (exit)	0.064
Vane inlet	0.062
Vane outlet	0.033
Combustion chamber	0.023

III, A, Design (cont.)

The hydrogen gas manifold system was designed to provide nearly uniform (within $\pm 5\%$) mass flux distribution at the injector outlet. The gas distribution late, however, was the key to producing this uniformity. Without a distribution plate, the gas flow would core through the center third of the annular chamber.

The gas distribution plate is 0.312 in. thick and contains 1352 orifices equally spaced over the entire annular injector inlet. The design consists of a rounded inlet to a 0.030-in.-dia hole, 0.040 in. in length, followed by a 12-degree included angle expansion cone to an exit diameter of 0.0872 in. The purpose of this design is to provide satisfactory pressure drop across the distribution plate (necessary for uniform flow) while diffusing the flow such that the gas Mach number at the exit of the orifice is nearly equal to the local Mach number at the vane inlet.

(2) Injector Vane Thermal Analysis

The thermal analysis of oxidizer heating in the injector vane was based on one-dimensional conduction in the plane of the vane between the fuel, which is heated in the regenerative cooling circuit of the chamber, and the oxidizer. Convective coefficients for the two fluids were based on the Dittus-Boelter correlation. The oxidizer coefficient is 0.040 ± 0.002 Btu/in.²-sec-°F, depending on channel width, while the fuel coefficient ranges from 0.0084 to 0.0089 Btu/in.²-sec-°F, depending on the equivalent diameter of the radial slot. The dependency of the heat transfer coefficients, h , on the slot equivalent diameter, D_H , is shown below:

$$h \propto D_H^{-0.2}$$

III, A, Design (cont.)

In the case of a slot of width, w, and depth, d, the relationship is

$$h \propto \left[\frac{2d}{1 + d/w} \right]^{-0.2}$$

Thus, a twofold increase in slot width results in less than a 4% change in the heat transfer coefficient. Average values were used for calculational purposes. The conductance of the "waffle" pattern of the insulation platelet was based on the metal contact area; the voids were treated as nonconductive.

The calculated bulk temperature rise of the oxidizer at full thrust conditions, using the channel designation 1 to 7 and 1' to 7' radially outward in the two vane types, is shown below:

Channel	-1 Vane						
	1'	2'	3'	4'	5'	6'	7'
T _B , °F	53.3	42.4	34.2	27.7	22.1	17.6	13.5
Channel	-2 Vane						
	1	2	3	4	5	6	7
T _B , °F	62.0	48.5	38.3	31.2	25.1	20.0	15.4

The oxidizer inlet conditions were taken to be 185°R, 3000 psia; the fuel was presumed inlet at 600°R, 1800 psia, accounting for heat input to the fuel from the regeneratively cooled chamber.

In the throttle mode, the convective coefficients and, hence, the heat flux from the fuel to the oxidizer are reduced (0.8 power on P_C). However, the flow rate of the oxidizer is reduced relatively more (linear with P_C) and, consequently, the bulk temperature rise of the oxidizer increases with the amount of throttling. The predicted oxygen injection temperatures over the 5:1 throttling range are shown in Figure 42. The effect of hydrogen temperature on the oxygen injection temperature is shown in Figure 43.

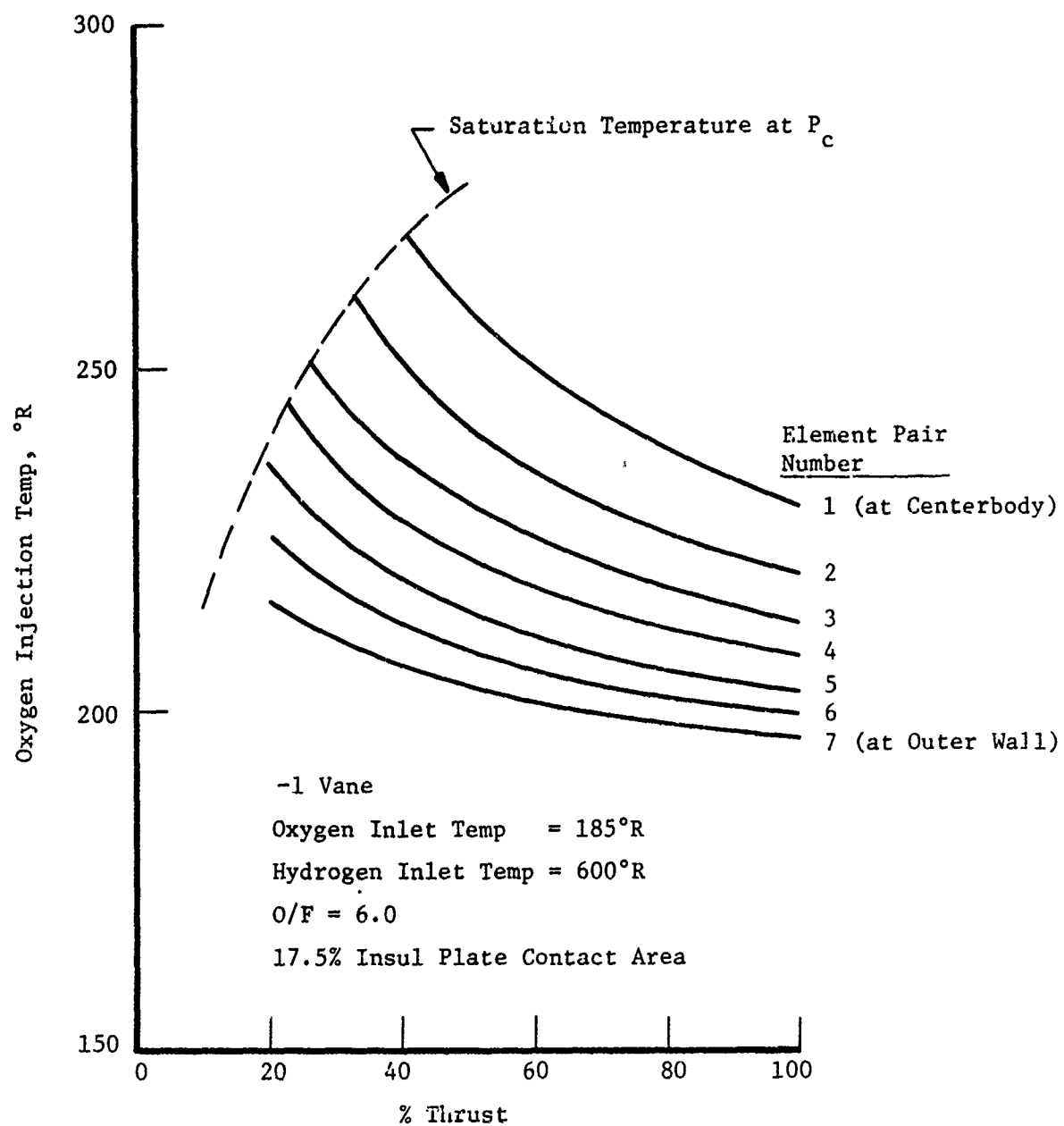


Figure 42. Injector Interpropellant Heating

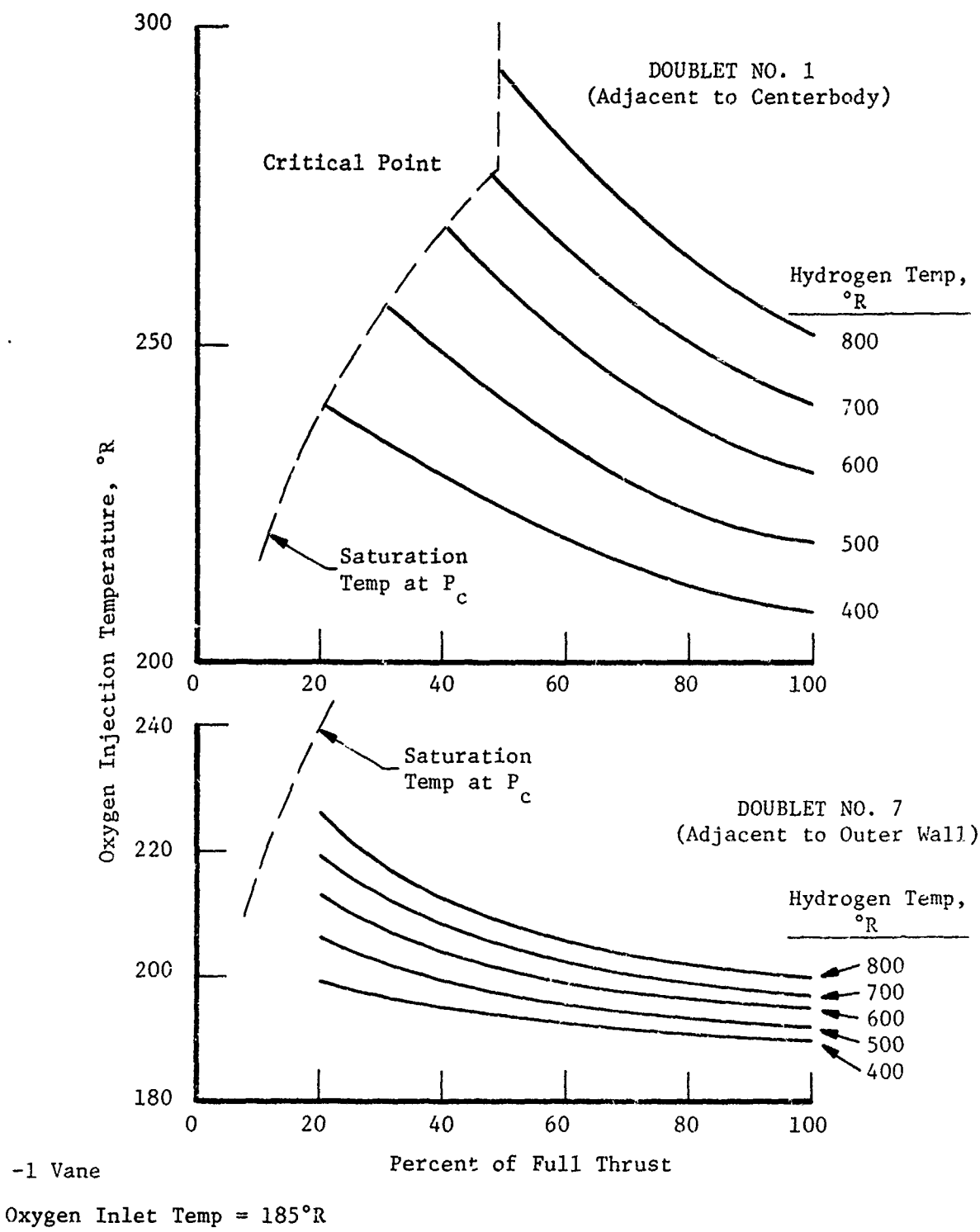


Figure 43. Effect of Hydrogen Inlet (to Injector) Temperature on Oxygen Heating

III, A, Design (cont.)

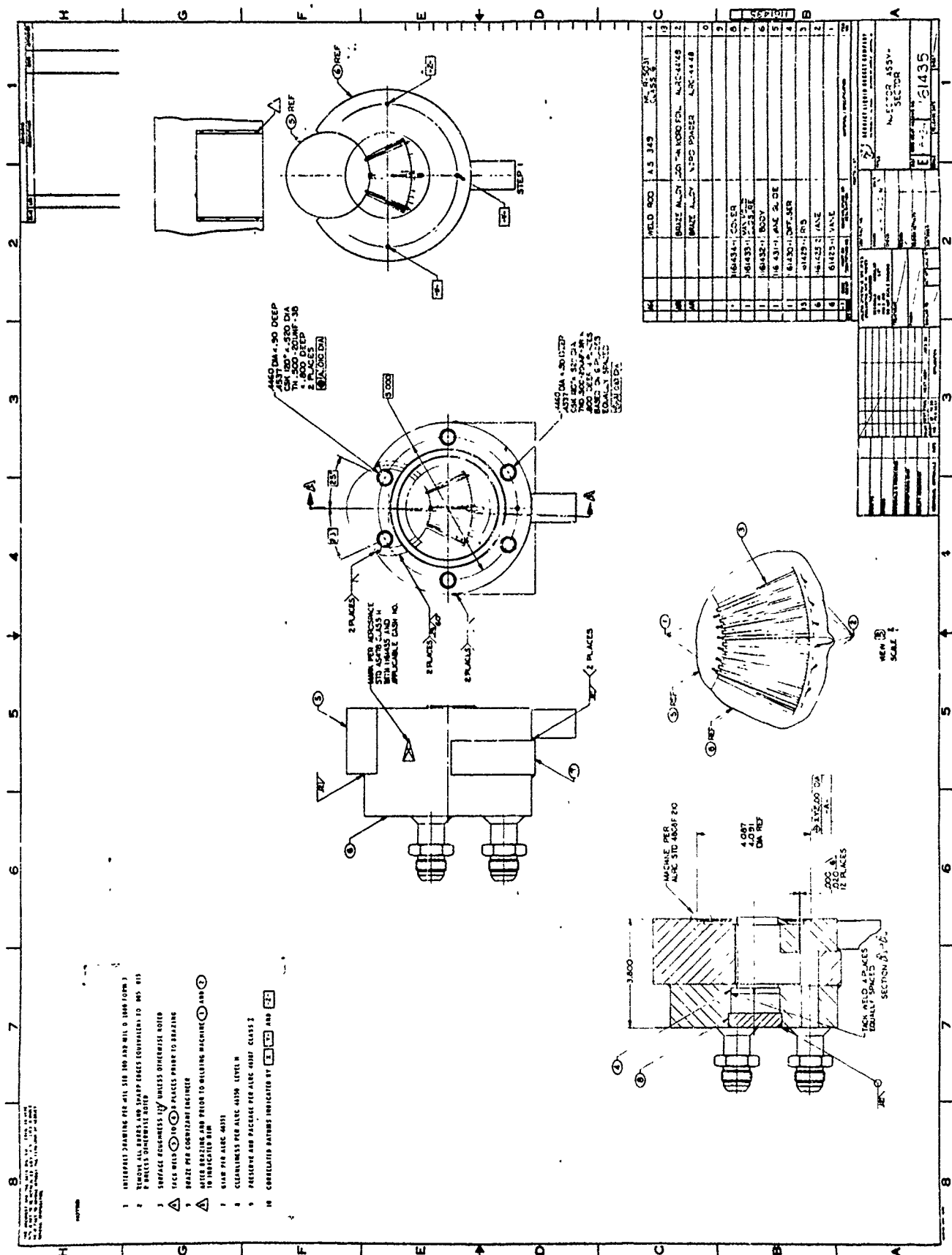
As a result of these analyses, it was concluded that throttling to about 50% thrust was possible without vaporization of the oxidizer. It should be noted that, without the waffled insulative spacer, the predicted oxidizer temperature rise would be increased by a factor of 2.3 and the critical temperature is exceeded even at full thrust.

c. Sector Injector Design

The sector injector design (PN 1161435) shown on Figure 44 is a one-seventh sector of the annular injector and contains twelve vanes which are identical to those of the annular injector. Manifolds for both fuel and oxidizer circuits are designed to simulate annular injector conditions; i.e., the fuel circuit manifold represents a null point and the oxidizer circuit manifold represents the region at the inlet. The igniter is one of the three incorporated in the annular design.

As indicated earlier, the injector vane thermal and hydraulic analyses are common to both the sector and annular injectors. These analyses were presented in the preceding section. An additional vane hydraulic analysis was conducted on the sector injector to ensure that cold flow testing during fabrication would provide meaningful data on vane flow distribution.

This hydraulic analysis was made to determine the effect of Reynolds number ($\rho Vd/\mu$) and density variations on the vane element-to-element flow distribution. The results of this analysis were used to correct the measured vane element-to-element cold flow distribution (water at $\dot{m}/\text{vane} = 0.1 \text{ lbm/sec}$) to equivalent hot fire conditions (liquid oxygen with heat input at $\dot{m} = 0.5 \text{ lbm/sec}$).



III, A, Design (cont.)

The calculated element-to-element mass flow distributions and total vane ΔP characteristics over a range of flow conditions are shown in Table VII and Figure 45, respectively. The data presented in Table VII are the element-to-element flow fractions (element flow/total vane flow) for the seven vane elements extending from the inboard to outboard injector radius (see Figures 39 and 40). This comparison shows that the vane flow distribution changes by only 1 to 2% over the entire range of flow conditions investigated and thus the cold flow distributions measured with water at low flow rate ($\dot{m} \sim 0.1 \text{ lbm/sec}$) were representative of the flow distribution obtained under hot fire conditions.

TABLE VII

INJECTOR VANE PN 1161427 CALCULATED
ELEMENT-TO-ELEMENT MASS DISTRIBUTION

ELEMENT FLOW RATE / VANE FLOW RATE					
FLUID:	Oxygen	Oxygen	Water	Water	Water
CONDITION:	Hot Fire	Cold Flow	Cold Flow	Cold Flow	Cold Flow
FLOW RATE:	0.5 lbm/sec	0.5 lbm/sec	0.5 lbm/sec	0.3 lbm/sec	0.1 lbm/sec
ELEMENT NO.:					
1	0.0876	0.0902	0.0898	0.0898	0.0890
2	0.1061	0.1091	0.1086	0.1087	0.1080
3	0.1245	0.1261	0.1258	0.1257	0.1250
4	0.1428	0.1431	0.1428	0.1430	0.1430
5	0.1615	0.1605	0.1608	0.1607	0.1610
6	0.1795	0.1771	0.1776	0.1773	0.1780
7	0.1980	0.1939	0.1946	0.1950	0.1960

E-D INJECTOR VANE PN 1161427 - CALCULATED PRESSURE DROP
CHARACTERISTICS

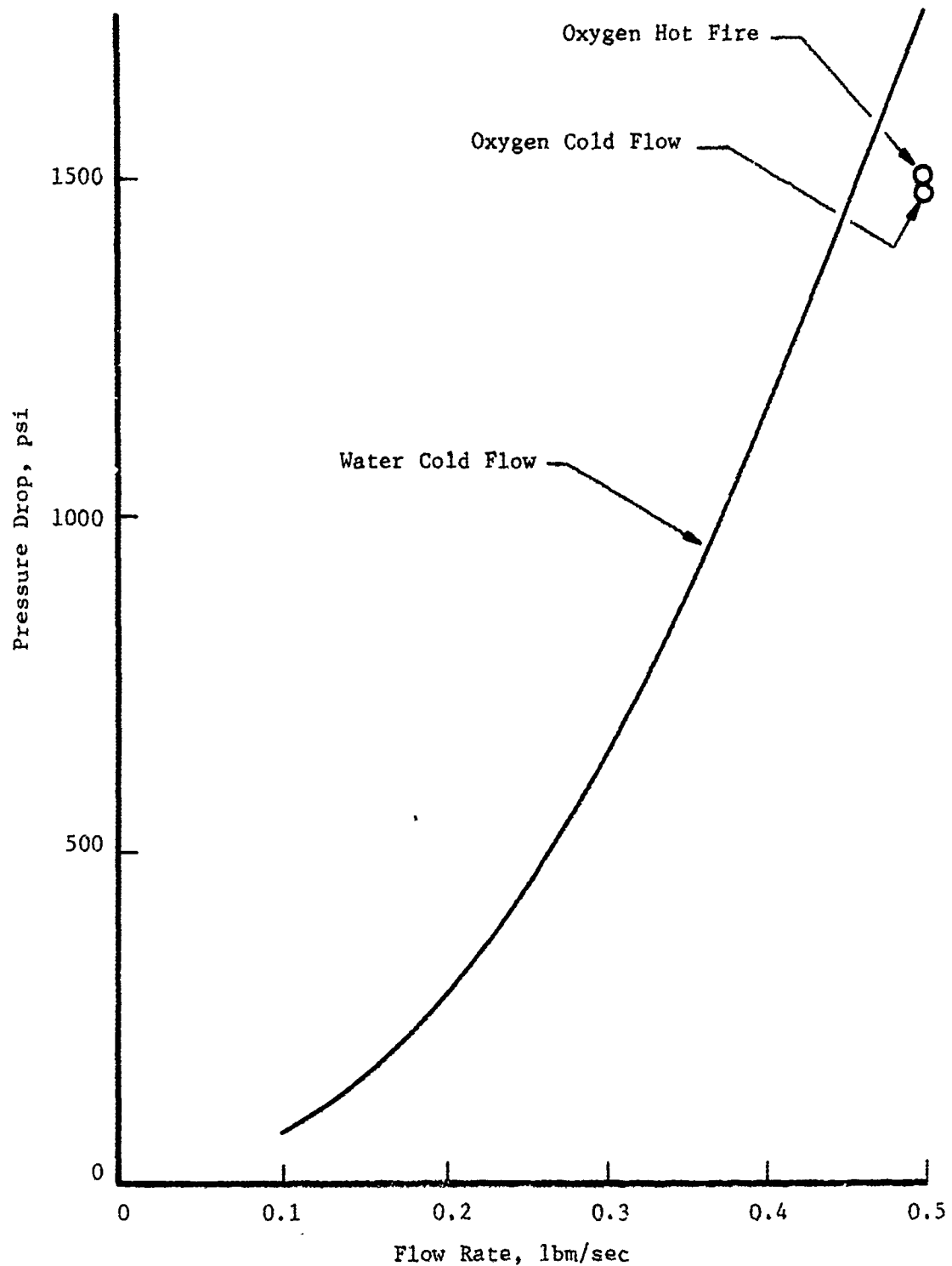


Figure 45. Injector Vane Pressure Drop Characteristics

III, Discussion (cont.)

B. FABRICATION

There were three components fabricated on the subject program. These were as follows:

Sector Injector - This vane injector represented one-seventh of the anticipated annular injector which would match the final engine design.

Water-Cooled Axial Throat Thrust Chamber Sector - This thrust chamber sector matched the sector injector and encompassed a one-seventh sector of the annular combustion chamber. Its throat was axial in order to allow direct measurement of thrust. (The anticipated E-D nozzle had a throat which was directed radially outward at 45° to the engine axis.)

Uncooled Axial Throat Thrust Chamber - This part was identical to the water-cooled sector except that it was heat sink cooled and, hence, duration limited.

Both the water-cooled sector thrust chamber and the sector injector were subjected to braze development testing during their fabrication. The following sections describe the fabrication development activities which resulted in the completion of the subject parts.

III, B, Fabrication (cont.)

1. Sector Injector

The sector injector fabrication processes included three distinct steps. These were:

- I Vane fabrication which encompassed photoetching, brazing, pressure test, and flow testing.
- II Body fabrication which was a combination of turning and milling with the vane slots ELOXed.
- III Vane to body assembly; this required inserting individual vanes into ELOXed slots and a subsequent braze operation.

a. Vane Fabrication

Individual vanes were used to supply oxidizer to the combustion process. The fuel flowed between the oxidizer vanes; hence, there were no discrete fuel orifices. The platelet array used to make an oxidizer vane is shown in Figure 38. Each vane consisted of nine individual platelets whose material and function are described in the following table:

End plate	Stainless steel
Insulator	Stainless steel
Depth-etched metering plate	Copper
Thru-etched metering plate	Stainless steel
Thru-etched metering plate	Copper
Thru-etched metering plate	Stainless steel
Depth-etched metering plate	Copper
Insulator	Stainless steel
End plate	Stainless steel

III, B, Fabrication (cont.)

The vane which resulted from the stacking and bonding of these platelets had a copper core with a stainless steel exterior surface. Grinding of a taper on the vane's trailing edge removed the stainless steel insulator plates locally, allowing the trailing edge to be regeneratively cooled with oxidizer. The remainder of the vane was sheathed with lower conductivity material which contained evacuated voids. This composite of material and insulator plates prevented transfer of heat from the warm hydrogen flowing past the vane to the liquid oxygen contained within the vane.

The fabrication of the bimetallic copper-stainless steel vane assembly was unique to this program.

Recognizing that the vanes would be subsequently brazed into the body, the vane brazement was accomplished with a higher temperature braze material as follows:

<u>Braze Operation</u>	<u>Braze Material</u>	<u>Brazing Temperature</u>
Vane fabrication	Electroless nickel	1800°F
Vane to body	Palcusil 10	1600°F

Following brazing but prior to machining the vane trailing edge, each vane assembly was proof tested to 2500 psi and then leak tested. As indicated in Figure 38, the non-machined vane contained a pressure test circuit in the region which was subsequently removed. The initial vanes were designed with these passages undersized with the result that local plugging was encountered. Modification to the etching pattern artwork corrected this difficulty.

Each machined vane assembly was then flow tested for pressure drop and distribution. Figures 46 and 47 show a typical vane (SN 23-2) being flow tested. Mass flux measurements were made with each injector vane positioned 0.0, 0.45, and 0.82 in. from a collector head. Measurements made with the vane directly on the collector head indicated the measured flow distribution was very close to



Figure 46. Injector Vane Water Flow Test (Side View)

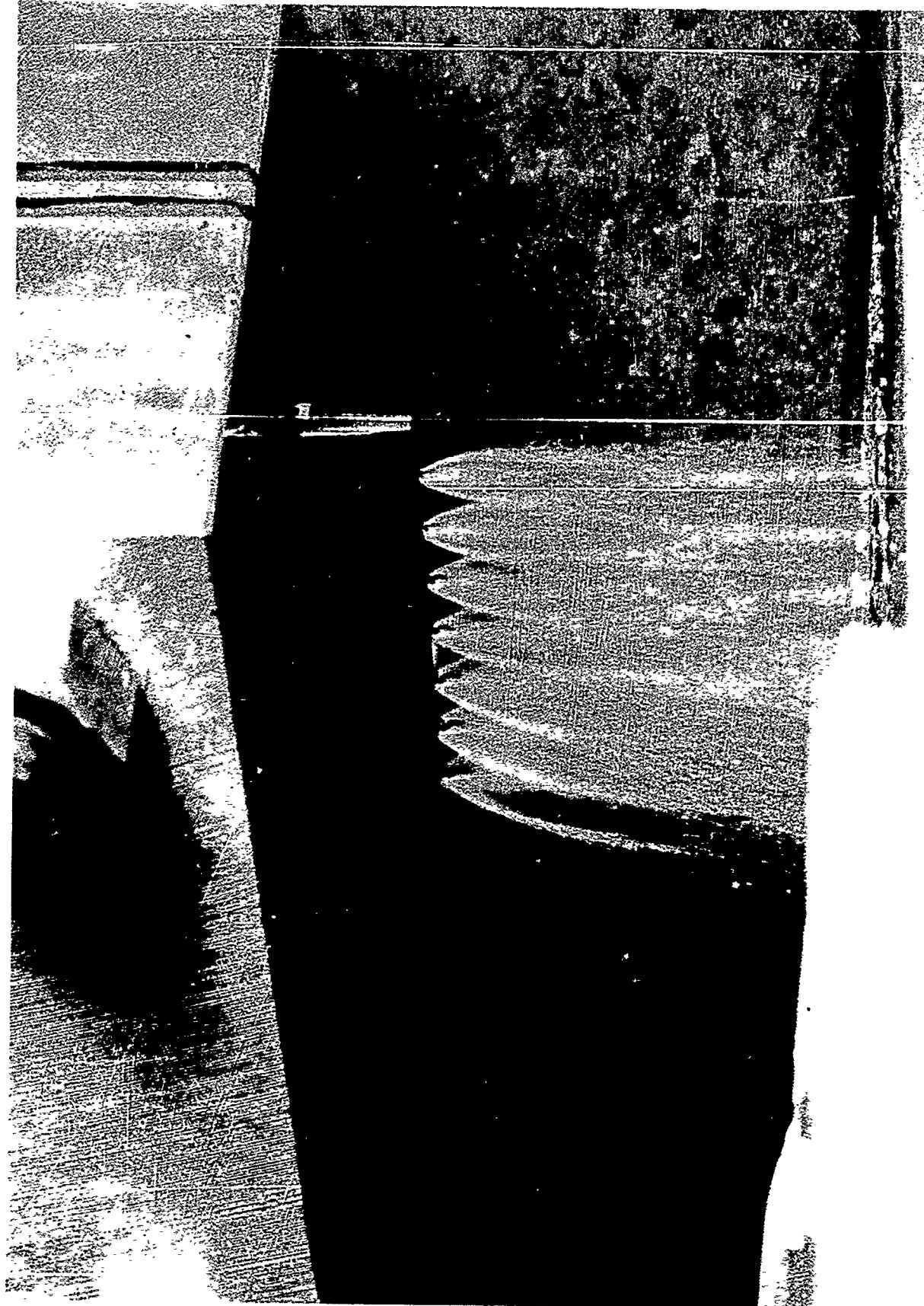


Figure 47. Injector Vane Water Flow Test (Angle View)

III, B, Fabrication (cont.)

the predicted distribution (average deviation 1%), and the measured ΔP corresponded directly to the predicted value. Mass distributions measured with the vane 0.45 and 0.82 in. from the collector head showed similar trends but the dispersion normal to the vane was on the order of +5 to 10% with one measurement $\pm 50\%$. This larger dispersion was the result of two factors: (1) the relatively large sampling grid (a 7 x 10 matrix of 0.187 square collecting tubes), and (2) nonuniformities in the orifice exit contour which could affect the element fan characteristics.

Conclusions drawn from the cold flow data were: (1) the vane hydraulic design produced the desired O_2 radial distribution and total pressure drop, (2) water flow testing with the vane stationed directly against the collector head was best suited to measuring the vane element-to-element mass distribution.

Since only gross measurement of the fan spreading rate was made during the single vane flow tests, analytical calculations of the spray fan mass flux distribution were made using the Liquid Injector Spray Program (LISP) correlations (Ref 20). The analysis included calculation of the mass flux normal to the vane for doublet elements No. 1, 4, and 7 at a distance of 0.45 in. below the element impingement plane. These data, which are presented in Figure 48, indicate an increased spray-spreading with increasing element size.

Since the LISP analysis did not include the effect of the hydrogen gas flow on the fan spreading rate, an estimate of this effect was made using the correlations developed by Ingebo (Ref 21). Considering only the velocity component normal to the vane, a maximum penetration distance was computed at a plane one inch downstream of the injection point. This penetration distance was then compared to the spreading distance predicted by the LISP calculations. The results indicate that the fan spreading rate for elements No. 1, 4, and 7 is reduced by 69, 41 and 34%, respectively. Imposing this spreading rate reduction and computing the resulting vane-to-vane O_2 mass distribution, it was

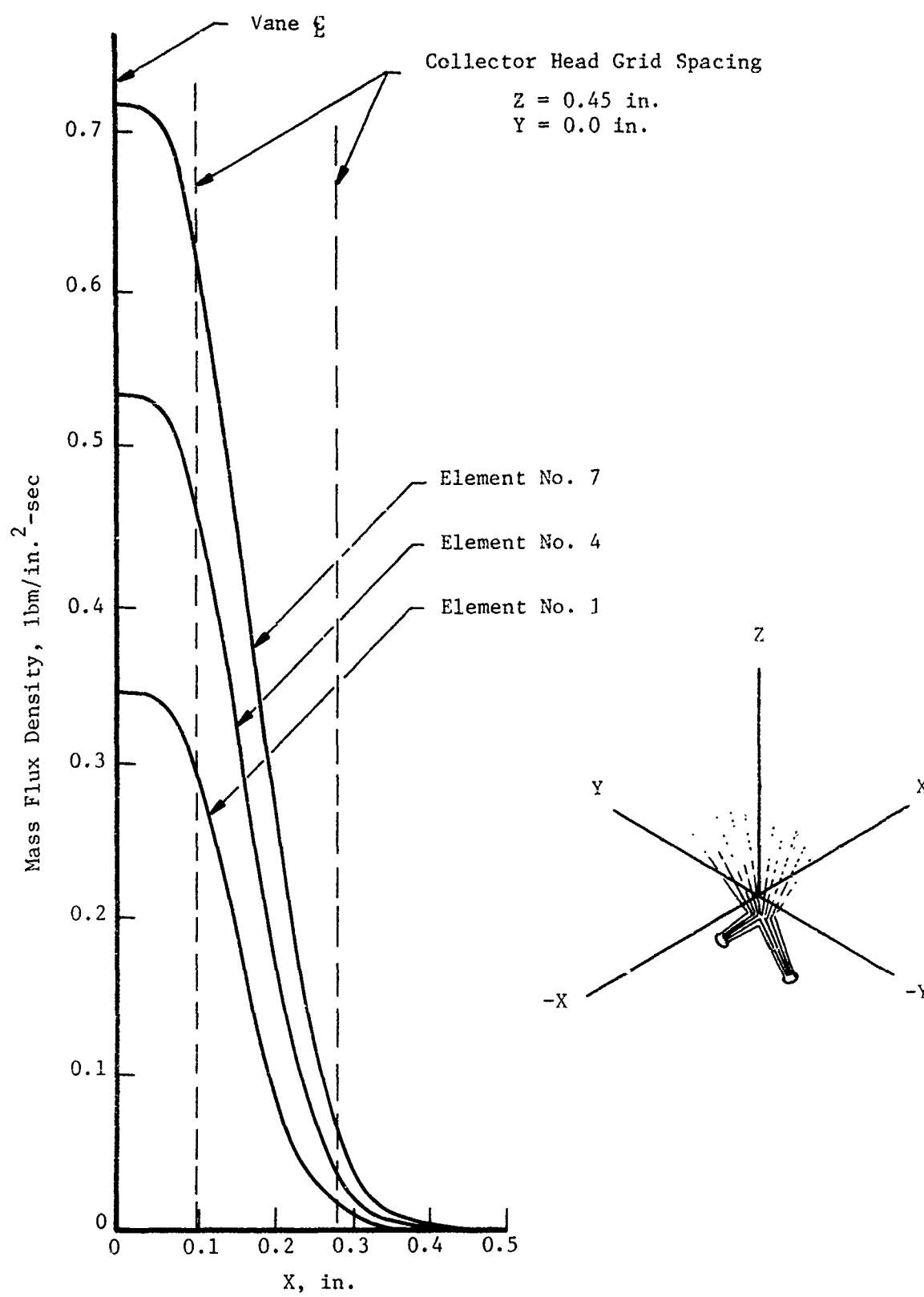


Figure 48. Predicted Injector Vane Mass Distribution

III, B, Fabrication (cont.)

found that the predicted O_2 mass distribution changed from nearly uniform to approximately $\pm 6\%$ to $\pm 10\%$ sinuous type variations. This mixture ratio variation results in predicted loss of approximately 0.5 lbf-sec/lbm in specific impulse.

The vanes for the sector injector (six each of -1 and -2 vanes required) were selected from the results of water cold flow testing. Figure 49 is a summary of the vane flow data. The vanes were selected on the basis of their measured element-to-element flow distribution, their flow admittance, $[K_w = \dot{w} / \sqrt{\Delta P S_p g}]$, and their individual element fan characteristics. A listing of the selected vanes and their selected placement within the sector injector is presented in Figure 50. The measured cold flow K_w 's were converted to equivalent hot fire K_w 's by multiplying the ratio of the analytical K_w water flow to K_2 hot fire. The element-to-element distribution shown in Figure 50 lists the largest positive and negative deviation from the design water flow rate of a single element for a particular vane.

The ratio of the average -2 to the average -1 K_w 's was exactly equal to the design value and thus assured a nominal flow split between the -1 and -2 vanes. However, because of vane-to-vane K_w differences, the following flow rate and mixture ratio variations among the selected vanes were predicted:

(a) VANE FLOW RATE VARIATIONS

	<u>\dot{w}_{min}</u>	<u>Vane SN</u>	<u>\dot{w}_{max}</u>	<u>Vane SN</u>	<u>Average \dot{w}</u>
-1 vanes	0.515	18-1	0.544	19-1	0.531
-2 vanes	0.469	10-2	0.526	23-2	0.499

(b) VANE MIXTURE RATIO VARIATIONS

	<u>O/F_{min}</u>	<u>O/F_{max}</u>	<u>Average O/F</u>
-1 vanes	5.82	6.15	6.0
-2 vanes	5.64	6.32	6.0

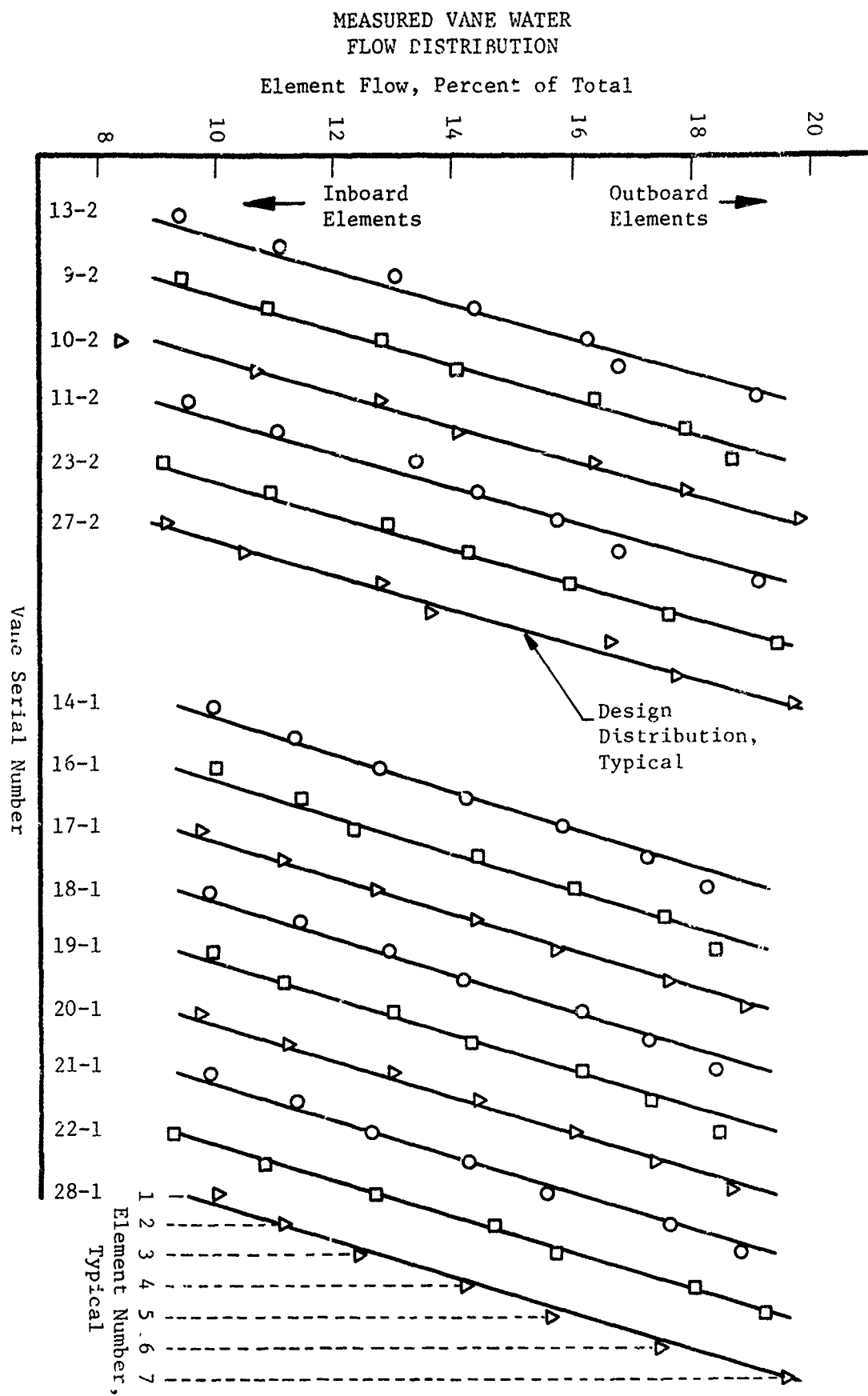


Figure 49. Injector Vane Water Flow Data Summary

1. FLOW CHARACTERISTICS

Vane SN	Meas K_w	Hot Fire K_w	Element-to-Element Distribution	
			Low	High
9-2	0.01272	0.01340	-5.26%	+4.33%
10-2	0.01172	0.01255	-6.80%	+2.28%
11-2	0.01281	0.01365	-5.91%	+7.19%
23-2	0.01327	0.01410	-1.22%	+3.27%
27-2	0.01221	0.01305	-4.88%	+2.52%
40-2	0.01277	0.01357	-3.75%	+5.76%
14-1	0.01323	0.01405	-2.50%	+7.35%
16-1	0.01365	0.01450	-4.28%	+7.60%
18-1	0.01293	0.01380	-4.75%	+5.72%
19-1	0.01372	0.01455	-4.47%	+6.19%
21-1	0.01349	0.01430	-2.55%	+5.72%
22-1	0.01319	0.01400	-2.28%	+2.42%
-2 average K_w (hot fire) = 0.01339			$-2 K_w$ (design) = 0.01225	
-1 average K_w (hot fire) = 0.01420			$-1 K_w$ (design) = 0.01300	
$K_w = \frac{\dot{w}}{\sqrt{\Delta P} S_p g}$				

2. SELECTED VANE PLACEMENT (AS VIEWED FROM CHAMBER END)

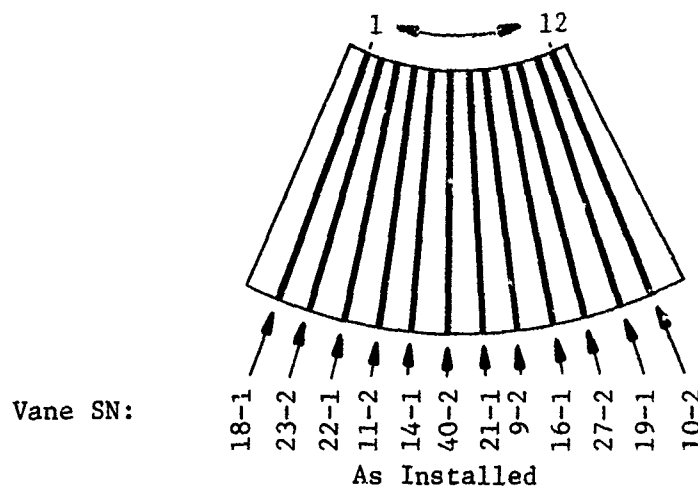


Figure 50. Selected Vanes for E-D Sector Injector SN 1

III, B, Fabrication (cont.)

In addition, the average measured vane K_w was somewhat larger than the design value so that the predicted hot fire injector ΔP was 1260 psi at full flow instead of the design value of 1500 psi.

The final vane placement, which is also shown in Figure 50, was selected to minimize the vane-to-vane flow distribution. Starting from the left, when viewing the injector from the chamber end, the -1 vane having the lowest flow (SN 18-1) is placed next to the chamber wall. This vane is followed by the -2 vane having the largest flow (SN 23-2), followed by the -1 vane having the second lowest flow (SN 23-1), and so on across the injector. This vane arrangement also supplied an average oxygen flow rate to the chamber across the entire injector face.

The sector injector was designed to incorporate thermocouples in the vanes. This instrumentation allowed the vane temperature near the inboard and outboard sides of the injector to be monitored during fire testing. The purpose of these thermocouples was to: (1) monitor values of vane temperature and (2) infer the temperature rise of the oxidizer (i.e., injection temperature). The thermocouples were 0.020 in. in diameter, brazed into small holes in the ends of the two vanes. Brazing was accomplished during the vane-to-injector body braze run. Figure 51 shows the location of and technique for installing the four thermocouples. The thermocouple lead can also be seen in the brazement photograph of Figure 52.

b. Injector Body Fabrication

The injector body, which is shown in Figure 52, was made from stainless steel. It contained an oxidizer manifold on its side which fed each of the individual oxidizer vanes. The fuel plenum was located on its top,

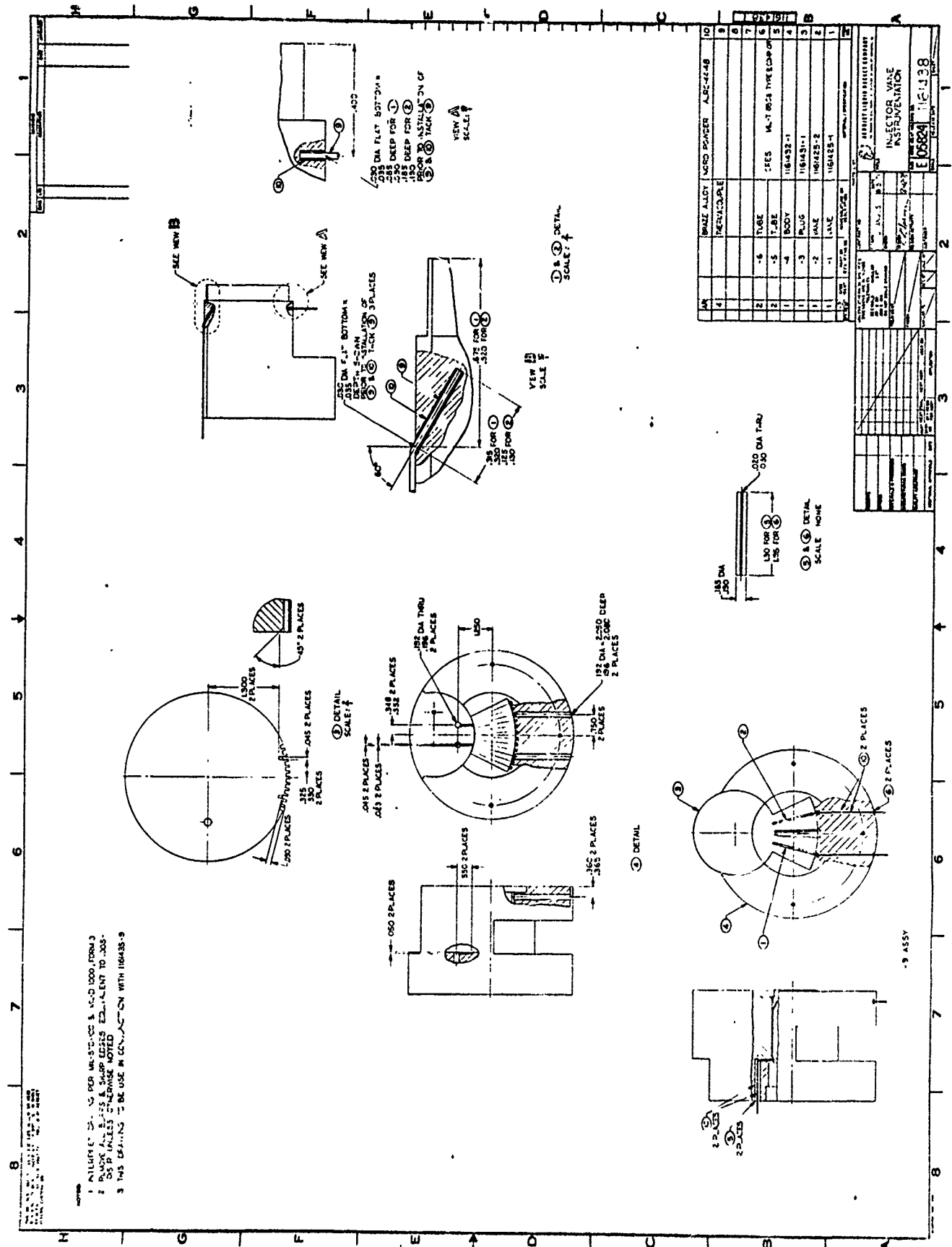


Figure 51. Injector Vane Thermal Instrumentation

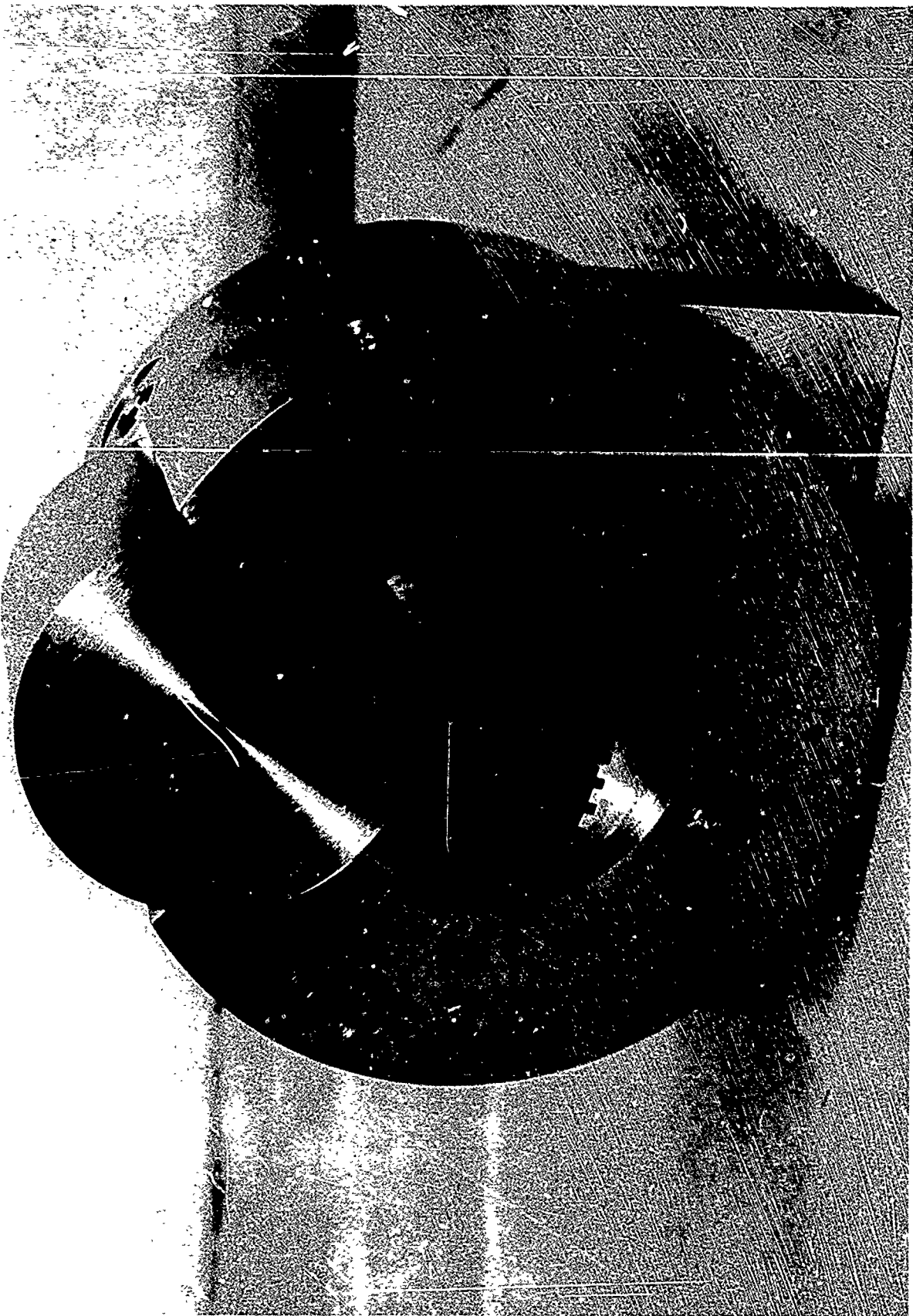


Figure 52. Injector Components, Assembled

III, B, Fabrication (cont.)

flowing the hydrogen through a distribution plate, between the vanes to the combustion zone. The centerline of the circular part shown in the top of Figure 52 would have been the axis of a full annular injector. The part shown simply supported the inboard end of the oxidizer vanes. The oxidizer manifold cover is on the opposite side.

The most significant aspect of the body fabrication was that twelve slots were needed for the engagement of the oxidizer vanes. The brazed vane-to-slot interface was subjected to the full oxidizer feed pressure and served to separate fuel and oxidizer. This required that these 0.75-in.-deep, 1.121 x 0.0835 in. slots be machined to a very close tolerance. This was accomplished after initial difficulties regarding the support of the ELOX tool were resolved.

c. Vane-to-Body Assembly

This operation was the most sensitive portion of the injector fabrication due to (1) the relatively long lead time required for the individual body and vanes, (2) the need to ensure that the vane hydraulic characteristics were unchanged, and (3) the necessity of a leak-free joint in the body-to-vane interface which was an interpropellant joint.

The braze technique used to achieve the vane-to-body joint was to wrap 0.001-in.-thick braze foil (Palcusil 10) around the root of each vane prior to its insertion in the matching slot in the body. The lower melting temperature alloy was selected to ensure that the furnace braze operation would not disturb the prior vane brazement. Stop-Off was used on the vane inlets and outlets to prevent braze flow into the vane passages. Initial braze runs were made using spare vanes and simulated body-to-vane joints to qualify the braze time and temperature. All brazing was done in a hydrogen environment.

III, B, Fabrication (cont.)

Figure 53 illustrates the injector components prior to assembly. Figures 54 and 55 show the injector face and oxidizer manifold area following the braze process.

Following a backflush operation to remove the braze "Stop-Off" from the inlet orifices, flow testing revealed that three doublet pair passages were obstructed in the metering area of the vane (near the oxygen inlet). The obstruction in the three elements of vane number 5 was found to be braze alloy containing the constituents of the Palcusil alloy used to join the vanes to the injector body. The flow and leak check also resulted in the identification of pin-hole leakage at the vane-to-body joints of four vanes.

The feasibility of operating the locally plugged injector in an "as is" condition and accomplishing its repair were both examined. Performance analysis and heat transfer analysis disclosed that the element obstructions could be accounted for in the evaluation of measured fire test performance data and local overheating of the vane would not occur.

The manufacturing review indicated that there was no safe method that could be used to remove the blockages. Although it was evident that the obstructed vane (No. 5) could be machined out and a new one brazed in place, there was concern that the rebraze cycle necessary to installation of the new vane would incur substantial risk of braze flow to other orifices and possible disturbance of the prior brazed interfaces. It was decided to use the injector with the three plugged elements. The injector has a total of 84 oxidizer elements.

Concurrently, the problem of the pin-hole leaks at the body-to-vane interface was examined. This condition was considered unacceptable due to the inability of the vane to cool if combustion were to occur in the volume

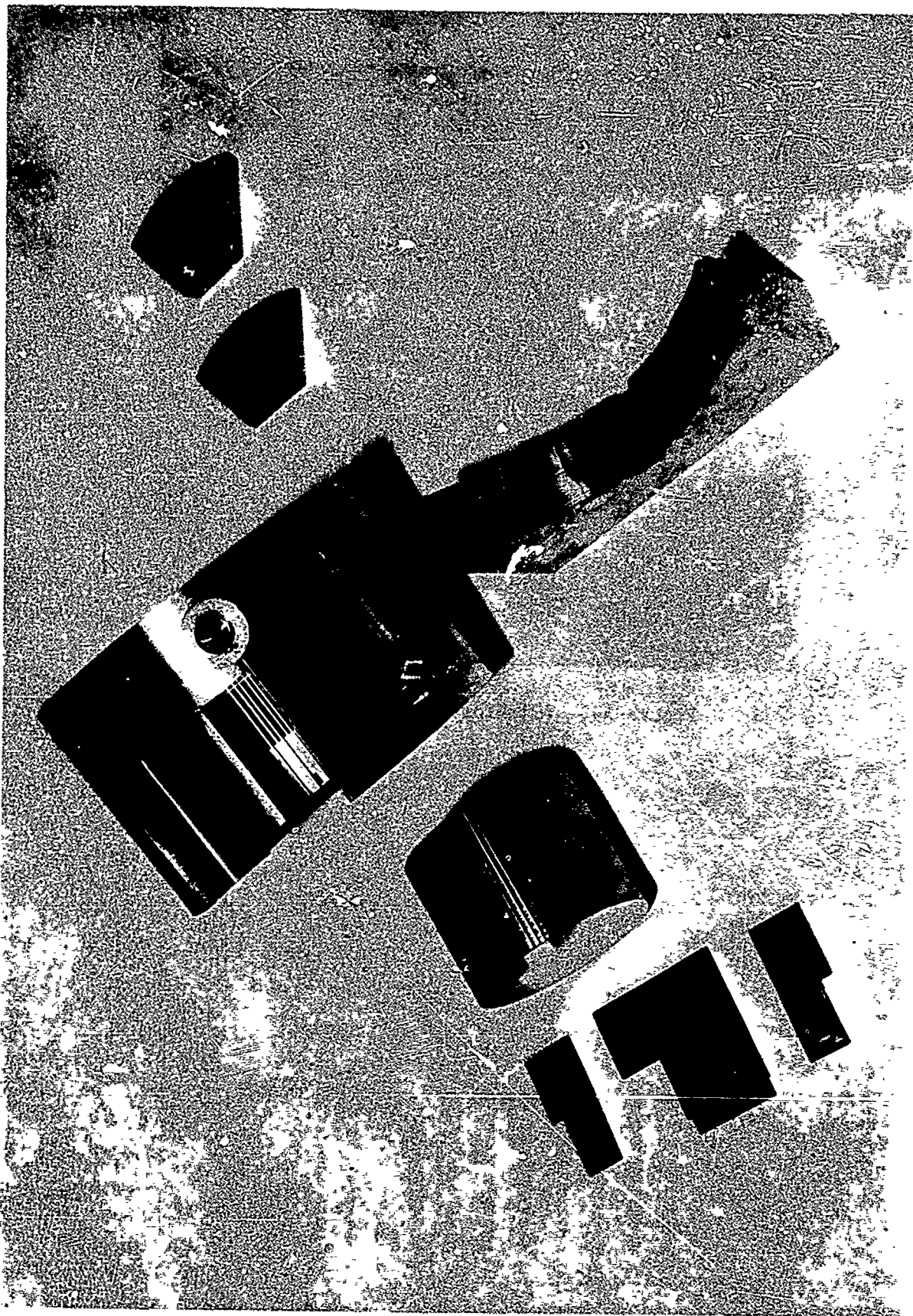


Figure 53. Injector Components

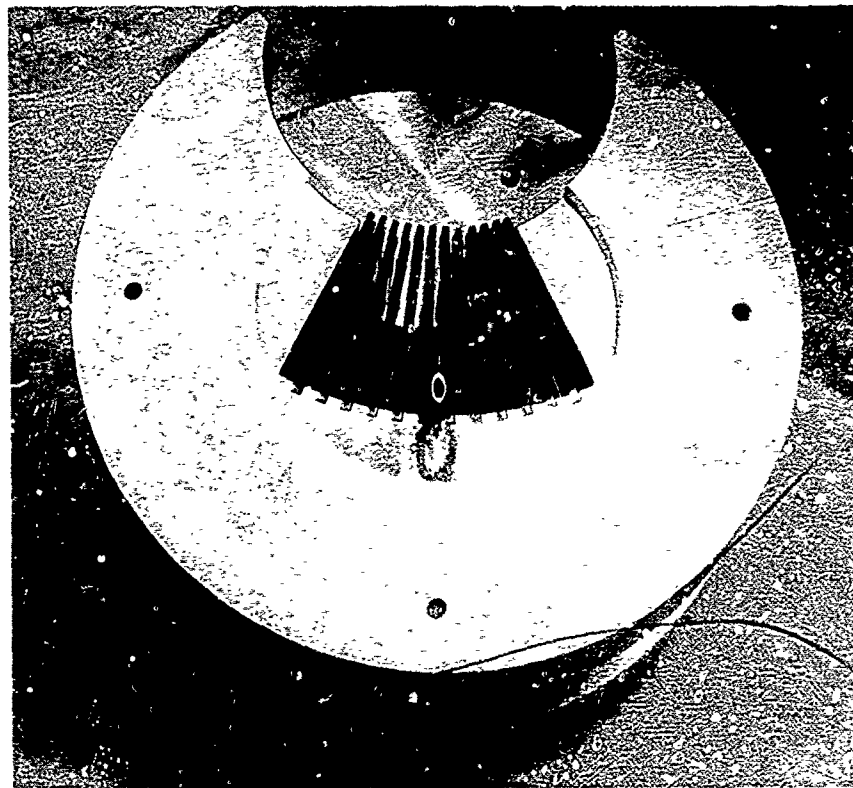


Figure 54. Injector Brazement, Face View

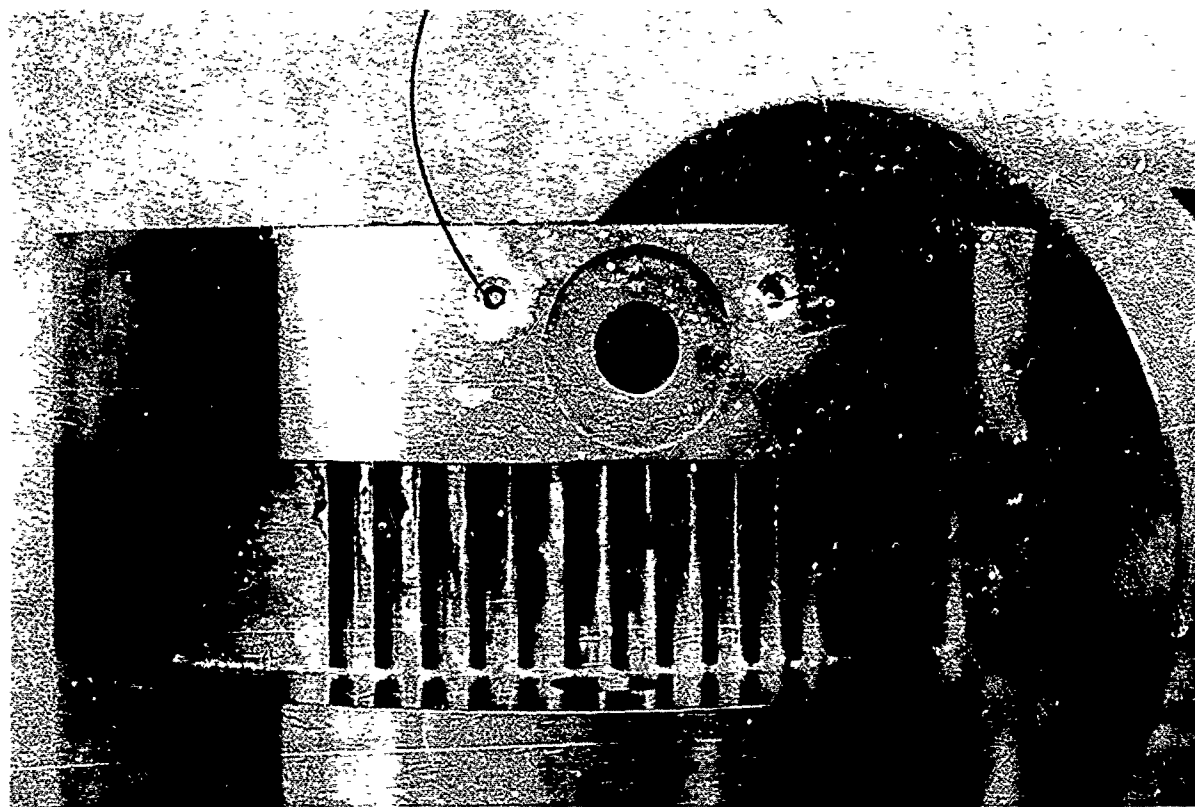


Figure 55. Injector Brazement, O_2 Manifold View

III, B, Fabrication (cont.)

between the vanes. The techniques of repair considered were: a braze recycle, electron beam melting, plating, impregnation with Teflon, and resistance heating.

The actual repair was accomplished in two steps. Palcusil 5 (Ag 68%, Cu 27%, Pd 5%) braze alloy was added to each of the leak areas and the assembly held at 1510°F for five minutes in a hydrogen furnace. This braze cycle successfully sealed three of the six leaks. The remaining leaks were sealed by using a resistance welder with a very small probe to locally melt and flow the braze alloy into the leak areas.

Argon gas was used for leak testing during the repair process to both identify the areas of leakage and to confirm their repair. Prior to the actual repair, the electron beam melting, brazing, and melting processes were all evaluated by making repairs of simulated vane-to-body braze joints. Figure 56 shows one of the simulated vanes which was used to evaluate the capability of Palcusil 5 braze alloy to fill voids. Figures 57 and 58 show side and top views of a specimen which simulated the vane end and its proximity to the wall of the injector body. The leak areas repaired were at the vane's edge which is very close to the manifold wall. The completed injector is shown in Figures 59 and 60.

The problem of metering passage blockage was attributed to the use of the Palcusil 10 braze alloys for the injector-to-body braze. This was further compounded with the subsequent repair of the pinhole leakage with Palcusil 5 alloy. Both of these alloys are designed for use at relatively low brazing temperatures (1600°F and 1510°F) and are compounded to achieve good wettability at these temperatures. Actual experience showed the braze alloy flow propensity to be excessive with the result that the control of braze flow using "Stop-Off" was very difficult. There was evidence that the Palcusil alloys migrated at the electroless nickel alloy interfaces.

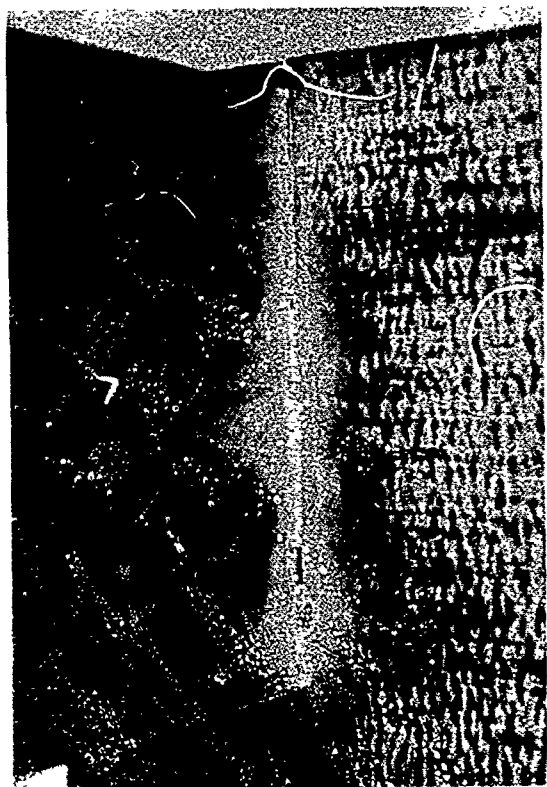


Figure 56. Injector Vane to Body Braze Specimen, Side View

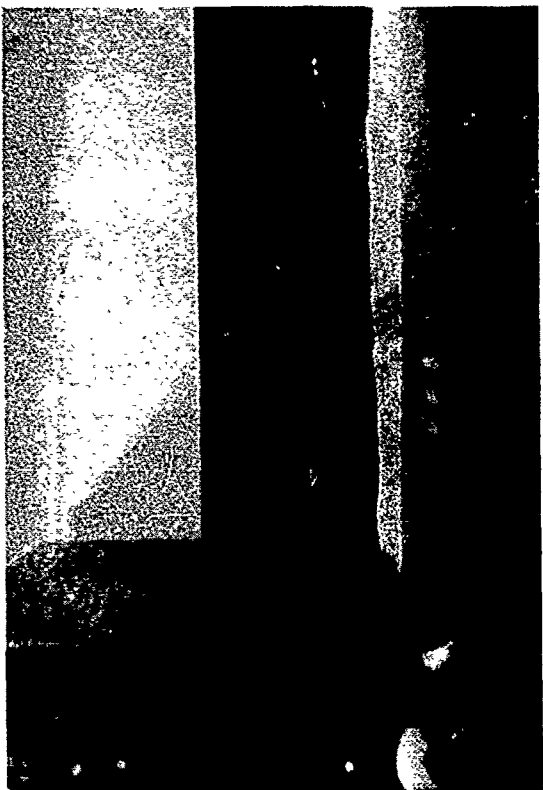


Figure 57. Vane Specimen Showing Vane End to Manifold Wall Clearance, Side View

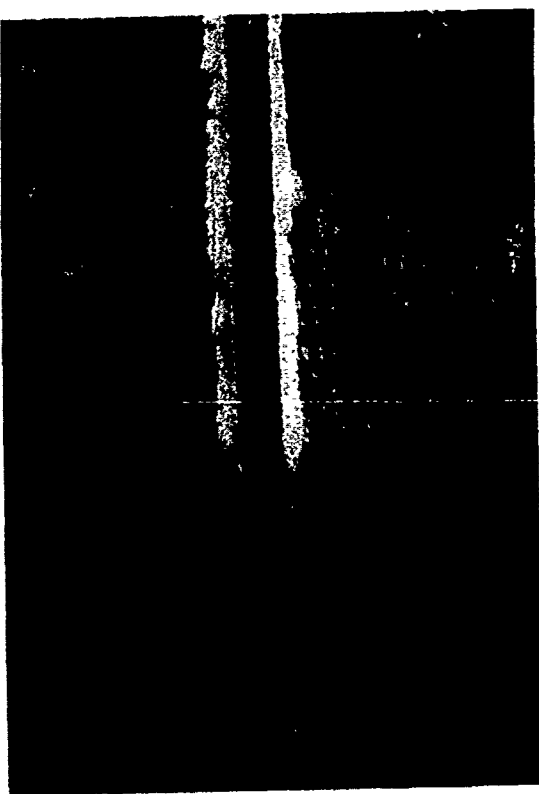


Figure 58. Vane Specimen Showing Vane End to Manifold Wall Clearance, Top View

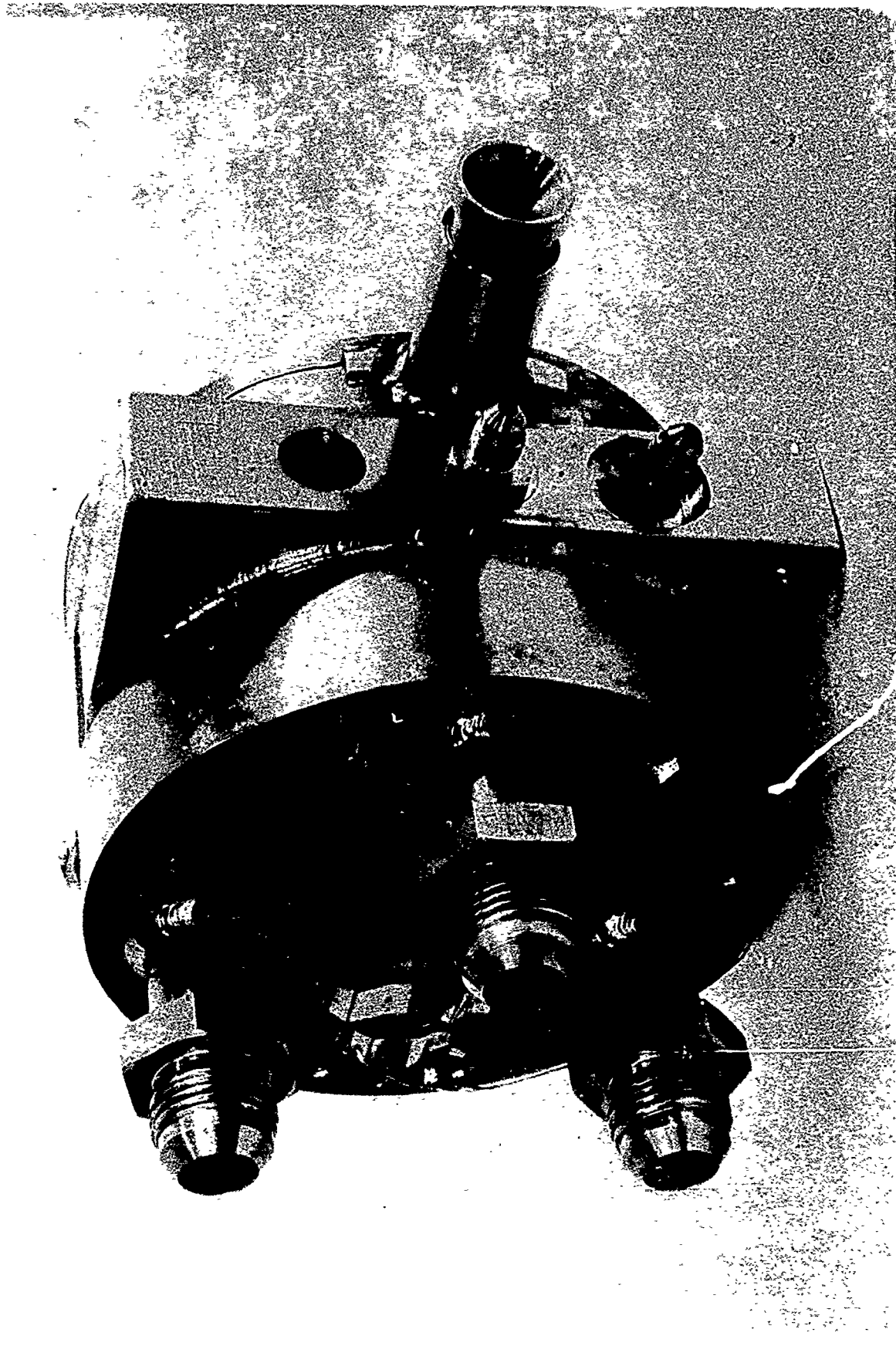


Figure 59. Assembled Section Injector (Back)

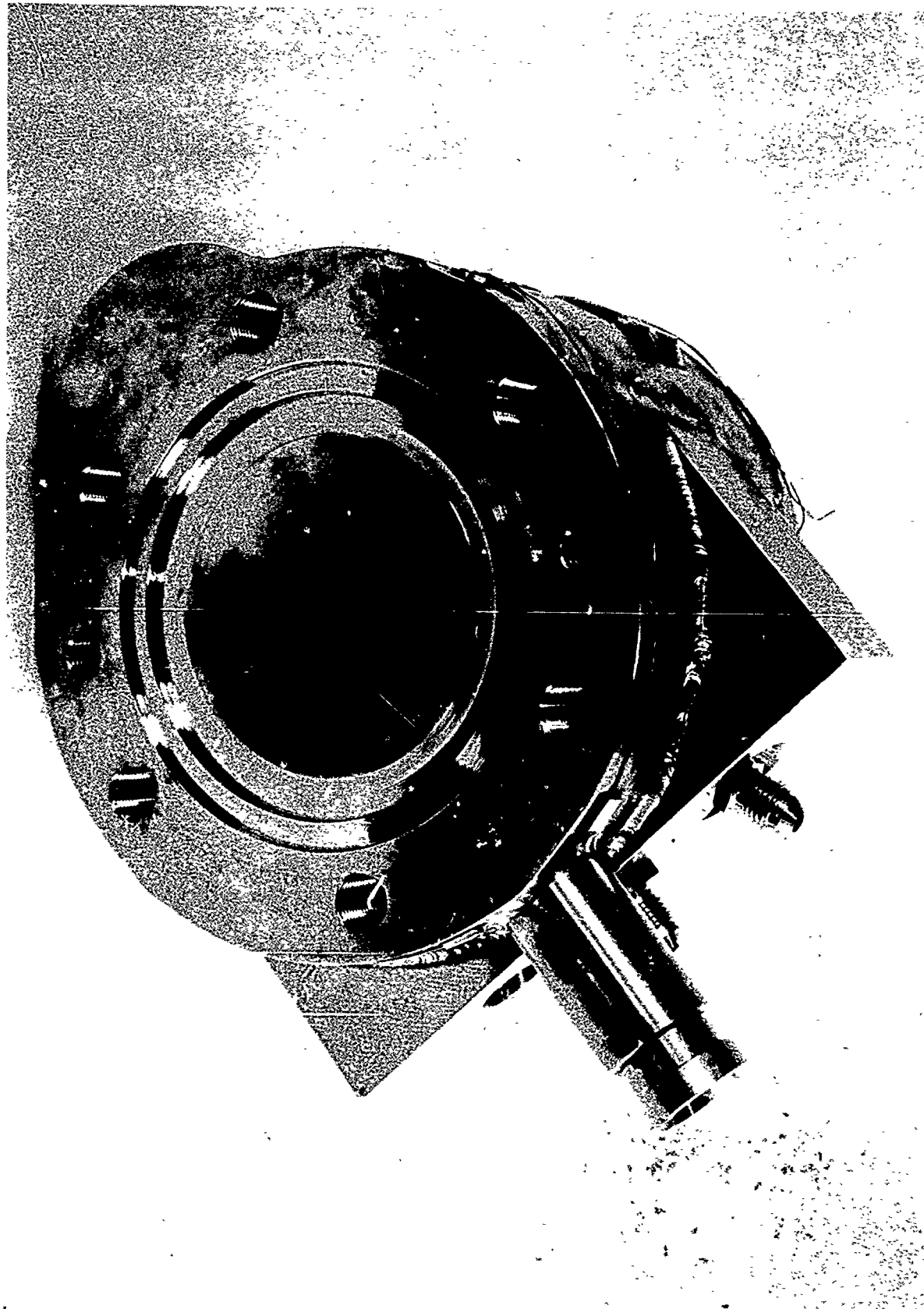


Figure 60. Assembled Sector Injector (Front)

III, B, Fabrication (cont.)

Post-fabrication review, coupled with data from other programs, reveals that the concern with the brazing of the electroless nickel bonded vanes at temperatures over 1800°F was unwarranted. The brazing procedure recommended for subsequent parts is as follows:

Vane fabrication	Electroless nickel at 1850°F
Vane to body	Nioro at 1825°F
Any subsequent braze	Nicoro 80 at 1730°F

The Nioro (82% Au, 18% Ni) and Nicoro 80 (81.5% Au, 16.5% Cu, 2.0% Ni) alloys have remelt temperatures of ~1850 and ~1800°F. The procedure described above was used successfully on the NASA/JPL-sponsored Dual Mode thrust chamber program.

Vane-to-body fitup should be held very close to minimize the quantity of braze required. The vanes should protrude further through the body slots to ensure that their open orifices are distant from the braze alloy.

d. Injector Assembly Flow Testing

Following the acceptance of the brazed injector body - vane subassembly, the fuel and oxidizer circuits were flow tested using "bolt-on" manifolds. These were later welded in place to complete the unit.

The sector injector body - vane subassembly was cold flow tested with gaseous nitrogen (fuel) and water (oxidizer) to evaluate the fuel and oxidizer circuit flow characteristics. The fuel circuit flow test data resulted in the evaluation of several fuel diffuser plates prior to the attainment of a design which provided nearly uniform distribution over the entire injector face.

III, B, Fabrication (cont.)

The results from the tests (see Section III,B,3,(3)) were then used to obtain final compatibility and performance estimated for the injector.

(1) Fuel Circuit

Cold flow testing of the gas-side of the E-D sector injector was accomplished using the Aerojet Aerophysics Laboratory facility. The hydrogen gas flow was simulated with nitrogen gas at a temperature of approximately 510°F and a total flow rate of 0.04 lbm/sec. Under these conditions, the Mach number of the nitrogen gas is equal to the Mach number of the hydrogen gas at full thrust conditions (i.e., $T_{H_2} = 500^{\circ}\text{R}$, $P_c = 1500 \text{ psia}$, $\dot{w}_{H_2} = 1.1 \text{ lbm/sec}$).

Three methods of measuring the local gas mass flux were investigated. These included: (1) measurement of the total pressure only between vanes, (2) measurement of both the total and static pressure between vanes using a pitot tube, and (3) measurement of the relative local gas flow rate between vanes using a rotameter. All three measurement techniques gave approximately the same results. The pitot tube static pressure measurement read very nearly ambient pressure. The rotameter measurement proved to be operationally the most efficient in terms of time required per measurement; however, it was impossible to select a rotameter which could adequately measure the entire range of observed local mass flux. Therefore, flow rate calculations could be made using only total pressure measurements. For ease in calculating the local mass flux, the square root of the local total pressure head (i.e., $P_o(\text{meas})$, psig) was assumed to be proportional to the local mass flux. At the low Mach numbers (<0.10) observed during these tests, the assumption is valid.

III, B, Fabrication (cont.)

The initial flow test of the "as-designed" sector injector showed the gas distribution to be nonuniform with nearly zero flow observed near the inside (centerbody side) wall from a radius of 1.5 in. to approximately 1.9 in. With the exception of the two side channels, flow increased rapidly with increasing radius, reaching a maximum near the center of the vane channel (at a radius of approximately 2.2 to 2.4 in.). Over this area, flow was approximately 25 to 50% above nominal. Flow then decreased and was generally more uniform near the outer wall (nozzle side) from a radius of approximately 2.5 to 3.0 in. The two side channels (1 and 13) had a mass flux which was more nearly uniform across the injector radius but approximately 1/3 of the nominal value.

The following were investigated to identify the cause of the observed distribution: (1) nonuniform inlet manifold distribution, (2) nonuniform distribution plate characteristics resulting from rectangular rather than radial hole distribution, and (3) the radial nonuniform gap between the vanes.

The manifold distribution was evaluated by testing with a modified inlet manifold system to determine its effect on the gas distribution. A straight-in manifold was devised by attaching a 2-in.-dia inlet pipe directly over the back of the manifold upstream of the distribution plate. Test results indicated no significant change in the gas distribution between the vanes.

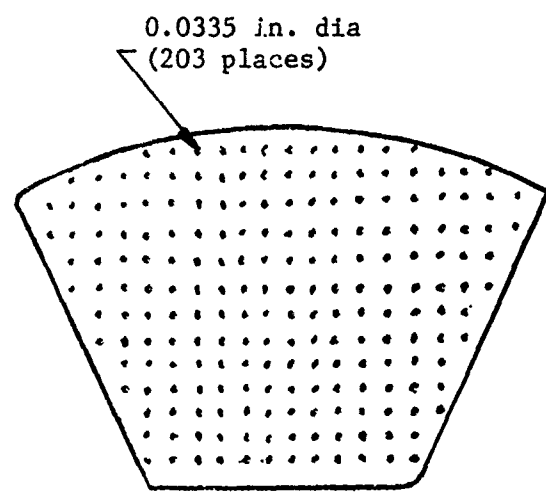
III, B, Fabrication (cont.)

In another test, the distribution plate was removed and the gas flow characteristics were measured. The results indicated little change in the resulting gas distribution. It was concluded that the fuel distribution plate upstream of the vanes would need to be modified to "force" a more uniform flow distribution.

The distribution plate was modified by blocking 46 of the orifices located between a radius of approximately 2.1 to 2.6 in. The objective of this change was to determine if the distribution plate could be used to force flow into the low flow regions from the high flow regions (i.e., from the center to the inboard side). The test results clearly showed reduced flow in the center region and increased flow at the periphery.

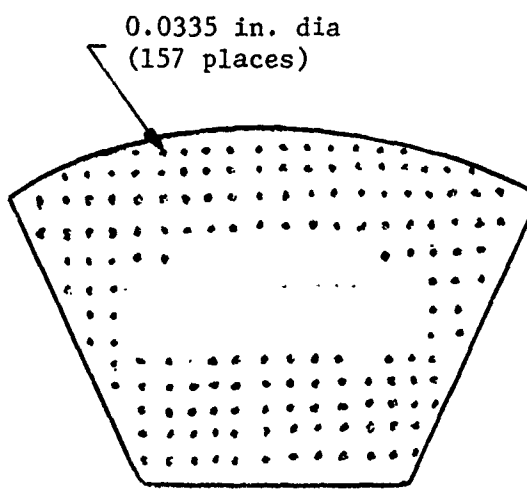
As a result of these tests, a new distribution plate was designed which placed flow control orifices on a radial distribution between active vanes. The hole distribution was biased to obtain increased flow along the inboard side and along the two radial sides, decreased flow over the middle region of the vane channel. The new, old, and old modified distribution plates are shown in Figure 61.

Test results obtained with the new radial distribution plate indicated that most of the gas flow was passing through the vane between a radius of 1.75 to 2.25 in. As a result, the outboard orifices were enlarged and three rows of orifices between a radius of 1.7 and 1.9 in. were plugged (ref Figure 61). This resulted in the flow characteristics shown in Figure 62. Below average flow was measured in the regions between a radius of 1.5 to 1.7 in. and 2.4 to 2.7 in. and above average flow was measured between a radius of 1.8 and 2.2 in. The gas flow distribution plate from the final design shown in Figure 60(d) was used subsequently for the hot fire testing data reduction.



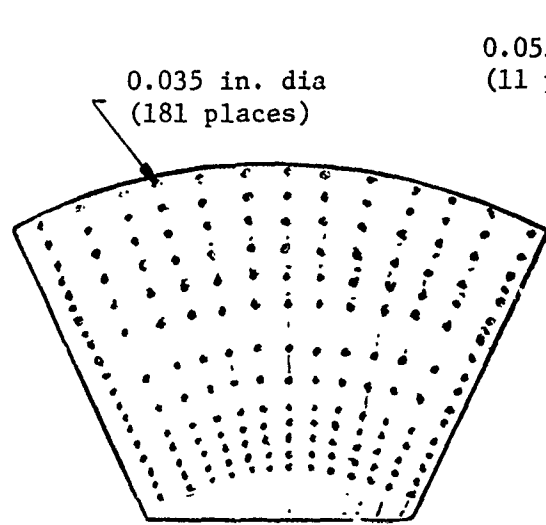
As-Designed Distribution Plate

(a)



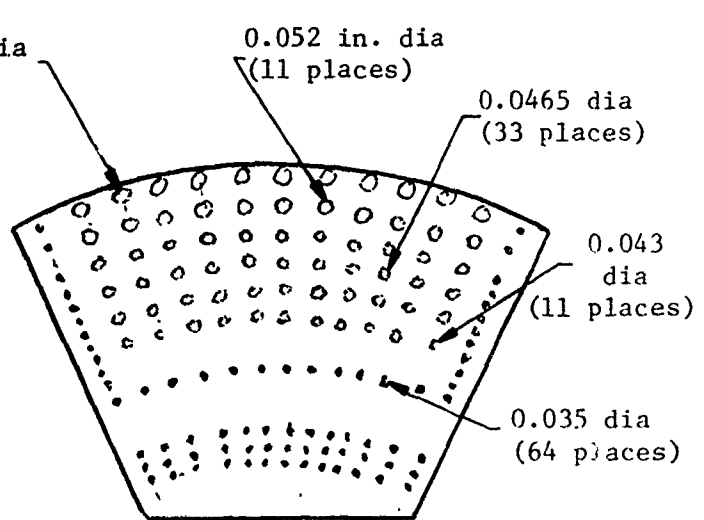
Modified As-Designed
Distribution Plate

(b)



Radial Distribution Plate

(c)



Modified Radial
Distribution Plate
(Final Design)

(d)

Figure 61. Gas Distribution Plates

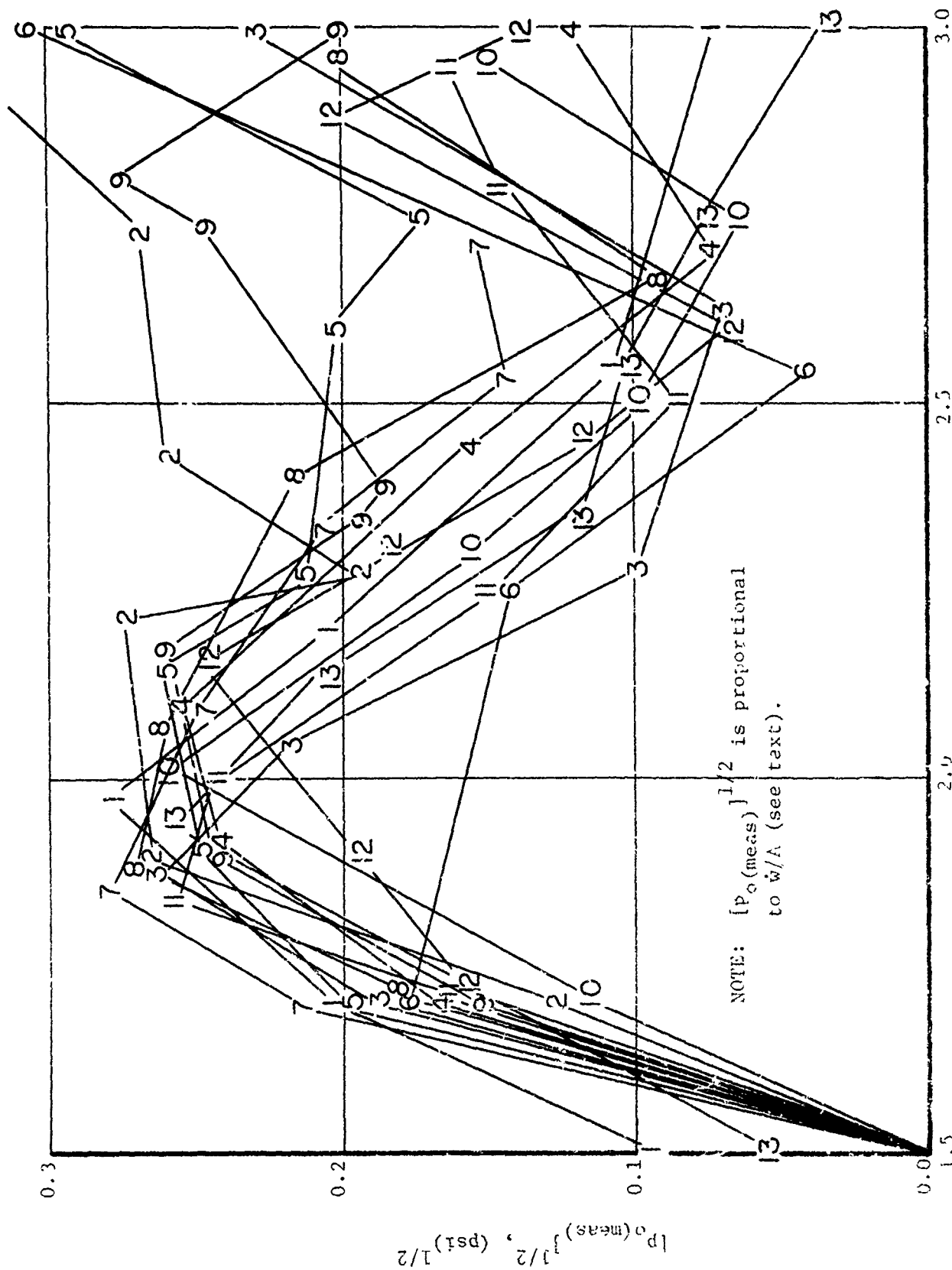


Figure 62. Gas Distribution Obtained with Modified (Figure 60d) Radial Distribution Plate

III, B, Fabrication (cont.)

Based on the results of the gas flow testing, it appeared that the boundary layer growth for flow between vanes had an appreciable effect on the chamber gas distribution. As a result, there was a review to determine if the cold flow testing could be conducted under conditions which better simulate Reynold's number. For a constant Mach number gas, Reynold's number is proportional to the ratio of the product of pressure and the square root of molecular weight divided by the viscosity ($Re \propto p \sqrt{MW/\mu}$). The boundary layer displacement thickness, δ^* , is then proportional to the Reynold's number to the -0.2 power, i.e., $\delta^* \propto 1/Re^{0.2}$. The following comparison between hydrogen, nitrogen, and helium properties illustrates the problem of simulating hot fire gas conditions:

Gas	Temp, °R	Pressure, psia	Molecular Weight	Viscosity, lbm/ft-sec	Re Hot Fire Re Cold Flow	δ^* Hot Fire δ^* Cold Flow
Hydrogen	500	1500	2.016	0.6×10^{-5}	1.0	1.0
Hydrogen	500	15	2.016	0.6×10^{-5}	100	0.40
Helium	500	15	4.00	1.2×10^{-5}	140	0.37
Nitrogen	500	15	28.02	1.8×10^{-5}	50	0.46

The above comparison showed that nitrogen best simulated hot fire conditions, although the boundary layer displacement thickness for nitrogen at ambient pressure conditions is still twice as large as the thickness for hot fire maximum thrust conditions. This means that the measured cold flow distribution shown in Figure 62 may not correspond directly to the hot fire distribution. At hot fire, the tendency would be towards reducing the maximum and increasing the minimum flows, since the vane gap differences will have a smaller effect on the resulting gas distribution.

(2) Oxidizer Circuit

Cold flow testing of the liquid side (oxygen) of the sector injector was accomplished using the Advanced Injector Distribution (AID) facility located in the Research Physics Laboratory. The liquid oxygen flow was

III, B, Fabrication (cont.)

simulated with water at ambient conditions. A total water flow rate of 1.8 lbm/sec was used which resulted in a pressure drop of 174 psi. At this flow rate, turbulent flow is maintained within the pressure vane and a hydraulic analysis indicated the resulting flow distribution would be within a few percent of that achieved under hot fire conditions.

The collector head used for the liquid side testing consisted of 784 tubes arranged in a 28 x 28 square matrix approximately 3.6 in. on a side. The injector was placed so that the orifice outlets were over the collector head and 1/2 in. above it. Water was flowed through the injector at a flow rate of 1.8 lbm/sec for a period of approximately 55 sec and collected by the AID facility. The resulting distribution, in terms of (lbm water collected per tube) $\times 100.0$, is shown in Figure 63 which also shows the radial distribution required to obtain a uniform mixture ratio distribution assuming that the fuel circuit flows at its design distribution. The measured oxidizer distribution was highly nonuniform, varying from a factor of 2 greater to a factor of 4 less than the desired flow.

Since each vane was individually water flowed and its distribution verified within $\pm 8\%$ of the desired condition prior to the injector assembly, the maldistribution shown in Figure 63 was attributed to (1) a difference between the individual vane flow characteristics and the assembly flow characteristics, (2) interaction between the vanes, and (3) inability of the rectangular grid of the flow test apparatus to match the radial pattern of the injector.

A difference between the individual vane and assembly flow characteristics was confirmed by visual observation of the orifice flow characteristics during the water flow and by measurement of an increased ΔP . Differences between the individual vane and assembled injector ΔP suggested that

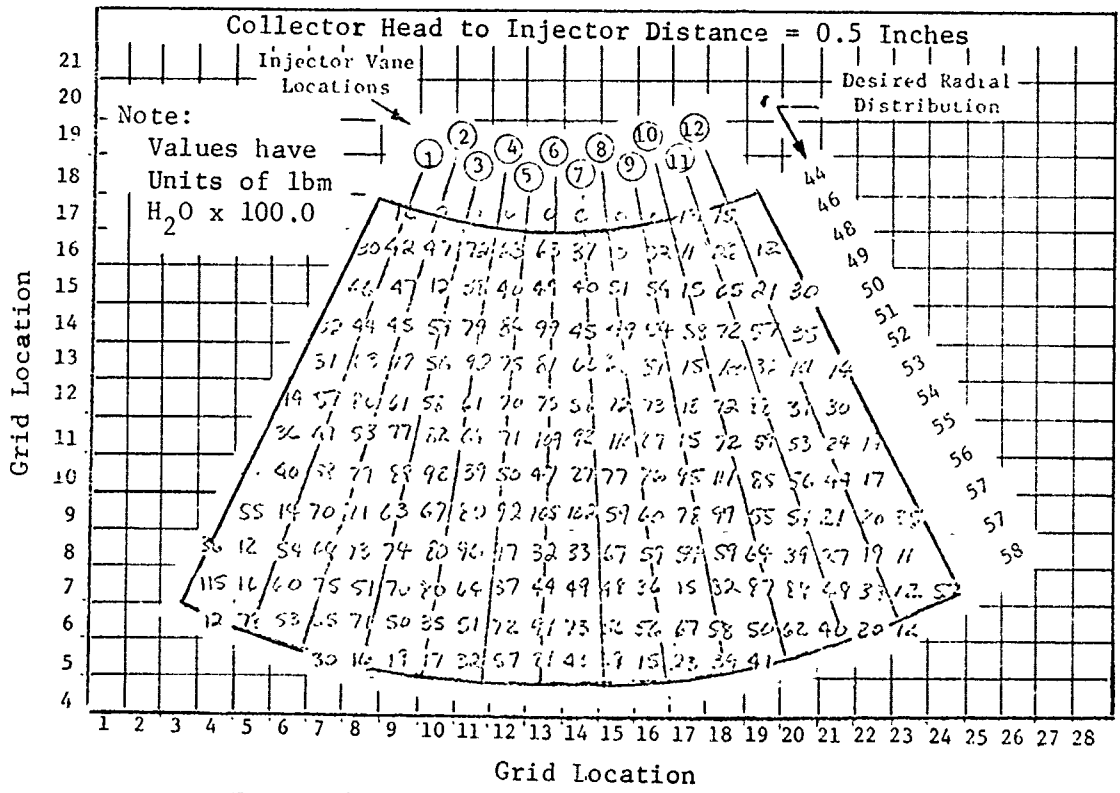
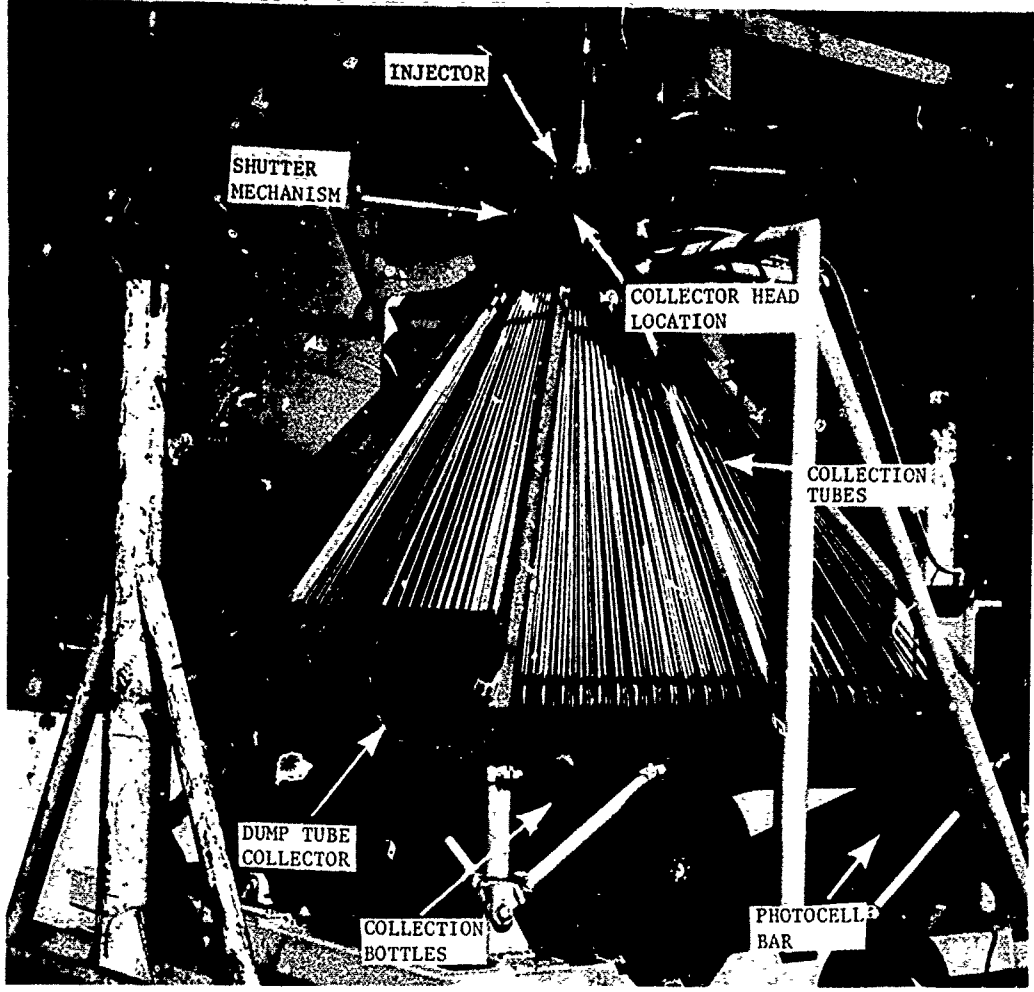


Figure 63. Oxidizer Circuit Mass Distribution

III, B, Fabrication (cont.)

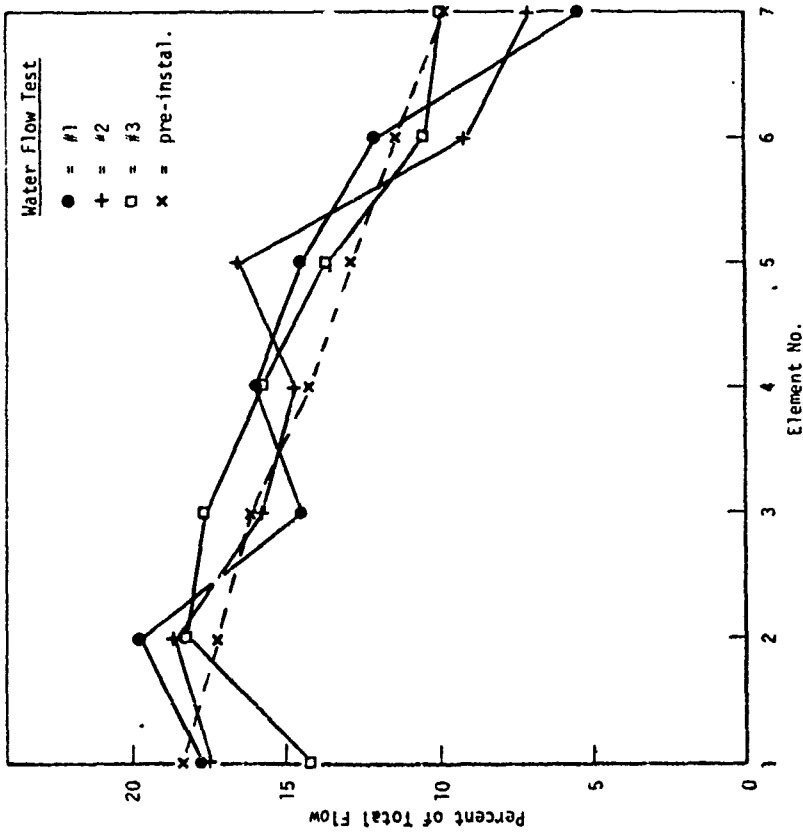
approximately 22% of the total flow passage area was blocked. The oxidizer inlet manifold may also have had an effect on the vane distribution since it could not be simulated for the individual vane flow testing. The manifold should have a secondary effect on the flow distribution because of the relatively large vane resistance.

The possibility of vane flow characteristic changes resulting from the injector assembly braze process was investigated by flowing the two outermost vanes, SN 18-1 and SN 10-2, using the same flow apparatus which had been used for the individual vane flow tests. The vanes toward the center of the sector could not be reflowed because of the physical inability to isolate individual vanes. Comparison of the individual vane flow data and the new data is presented in Figure 64. Although difficulty was encountered in aligning the collector over the two vanes as indicated by the spread of the data for repeat tests, the shape of the data matches the pre-installation flow measurements, indicating that for these two vanes the flow distribution over the length of the vane was unaffected. The two vanes tested showed no evidence of plugging and therefore did not necessarily resemble inboard vanes. Braze alloy placement and control of the braze flow was least difficult with the edge vanes. The flow distribution of the inboard vanes can only be inferred from the data shown in Figure 63. Since the apparent flow area decrease cannot be accounted for by the number of plugged orifices, it is concluded that some of the flow passages were partially obstructed by braze alloy, either at the entrance to the vane or within the metering passages.

(3) Cold Flow Data Analysis

A performance and compatibility analysis of the sector injector was conducted using the data gathered from the gas and liquid cold flow testing. The gas distribution and the liquid distribution, as determined from cold flow test results, were input into a computer program which overlaid these

Vane 18-1



Vane 10-2

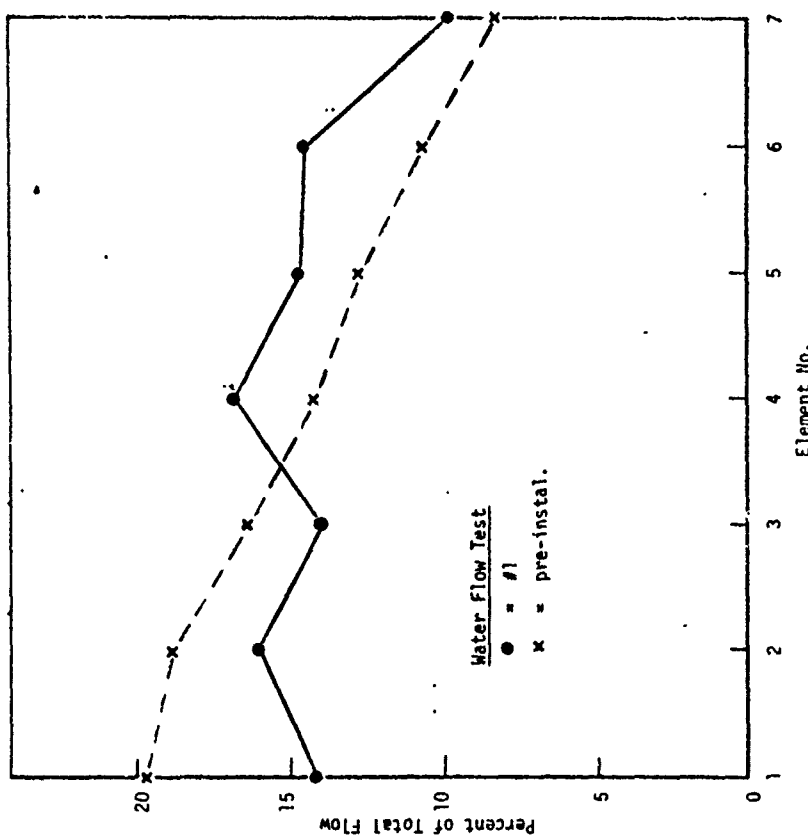


Figure 64. Vane Flow Distribution Measured Prior to and Following Installation

III, B, Fabrication (cont.)

distributions to determine a resulting mass, mixture ratio, and combustion temperature distribution. The combustion temperature distribution assuming 100% energy release is shown in Figure 65.

The performance analysis was based on the mass and mixture ratio distribution data assuming simple mass-weighted stream tube flow characteristics. The analysis was made for maximum thrust conditions* ($P_c = 1500$ psia) at an overall mixture ratio of 6.0 and an expansion area ratio of 2.7. Predicted performance parameters based on one-dimensional equilibrium flow conditions are as follows:

Characteristic velocity c^*	=	7130 ft/sec
c^* efficiency	=	94%
Specific impulse vacuum	=	340 lbf-sec/lbm
I_{sp} efficiency	=	93.6%

The performance estimates were considered minimum values for two reasons: first, the stream tube assumption used for the performance calculations implicitly assumes that no mixing occurs within the combustion chamber from the point where cold flow measurements were made to the nozzle throat. Additional mixing within the combustion chamber would significantly improve the performance in this case. Second, the hydrogen gas at full thrust conditions should have a more uniform distribution than that measured for the nitrogen simulant because boundary layer buildup will be smaller.

*A performance analysis at the 5:1 throttle point ($P_c = 300$ psia) was made during the analysis of the sector injector hot fire test results (see Section III,C,3).

NOTE: Assumes 100% Energy Release Efficiency

Combustion Chamber Cross-Section as Viewed from the Injector to the Nozzle Throat

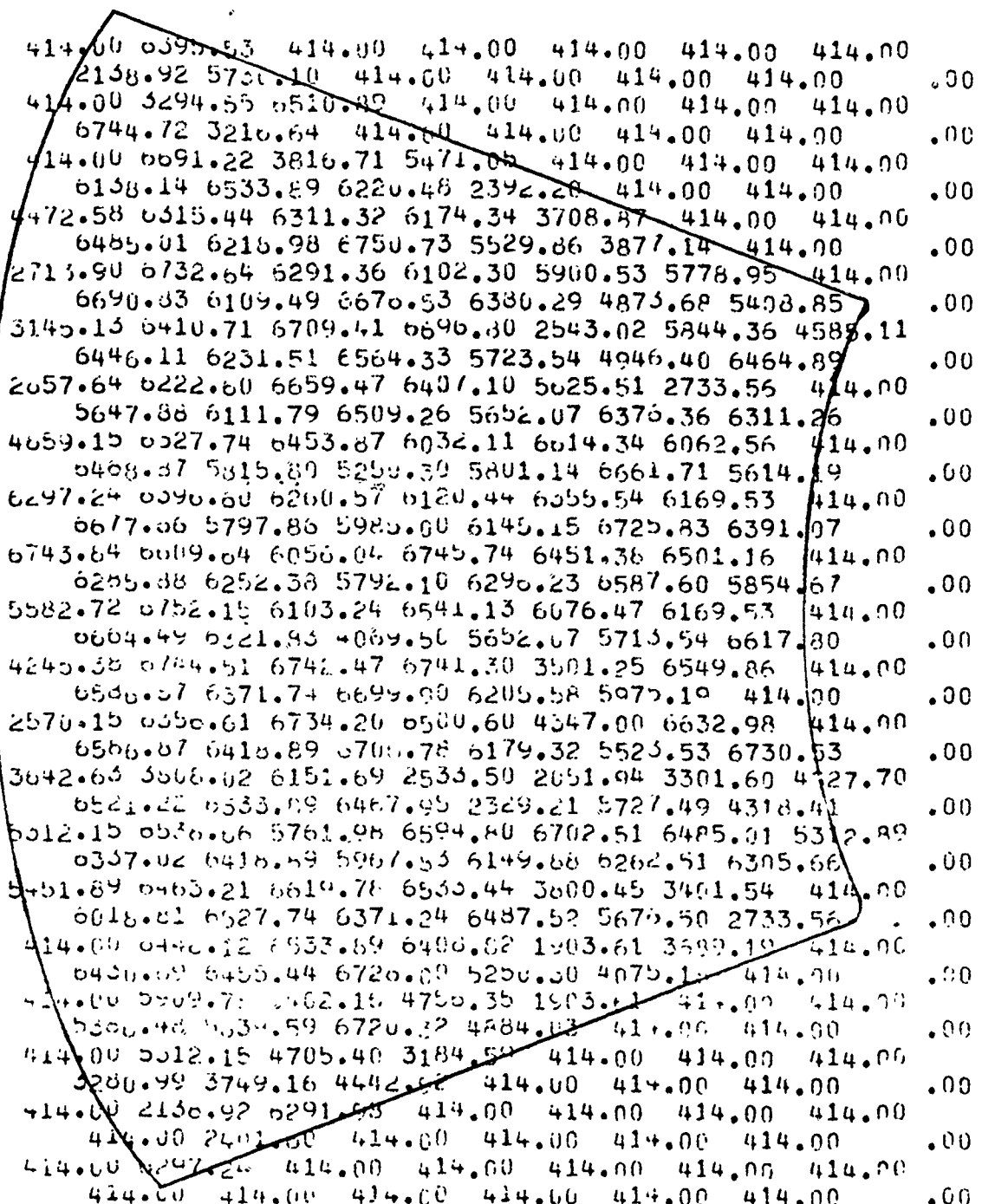


Figure 65. Injector Combustion Temperature Distribution

III, B, Fabrication (cont.)

e. Conclusions Regarding Injector Fabrication

(1) Brazing of bimetallic vanes is feasible. Vanes fabricated on the program were proof tested to 2500 psia without failure.

(2) A three-step injector fabrication process consisting of the following would allow higher temperature braze alloys (such as Nicoro 80) to be used at the vane-to-body joint:

- (a) Bond copper and center stainless steel platelets using electroless nickel at 1850°F.
- (b) Braze insulator platelets and end plates to above assembly using 0.0005-in.-thick Nicoro at 1825°F.
- (c) Braze vane assemblies to stainless steel body using Nicoro 80 at 1730°F.

(3) Since the Palcusil 5 and 10 braze alloys exhibit much greater flow and diffusion properties than the gold-based braze alloys, their use in the area of Nicoro and electroless nickel bonds is not recommended.

(4) Fuel and oxidizer circuit flow testing is necessary to the identification of fabrication-induced anomalies as well as the prediction of performance.

2. Water-Cooled Axial Throat Thrust Chamber Sector

a. Component Fabrication

The water-cooled sector thrust chamber (ref Section III,A) fabrication process was examined during its design to determine (1) if the gas-side wall should be made to final size or with a heavy wall which would be machined to size following brazing and (2) if the ribs of the nontubular coolant passages should be integral with the gas-side or the backside member.

III, B, Fabrication (cont.)

It was determined that, by using the components as electrodes for a final EDM match machining operation, gas-side and backside members would be matched sufficiently well that a good braze joint could be achieved with heavy walled parts which would be subsequently finish machined. The ribs of the coolant passages were made integral with the gas-side wall so that the brazed interface would be located in a cooler zone.

The water-cooled sector thrust chamber consisted of one-seventh of the full size annular thrust chamber but incorporated an axial throat of this unit which allowed direct measurement of thrust. Figures 19 and 20 allow comparison of the geometry of an axial throat sector thrust chamber and a similar sector with an E-D nozzle contour. Figure 66 shows the axial throat sector which was built from four individual copper brazements which were then joined to construct the final unit. These parts were:

Left and Right Side Plates - These were flat and uncontoured.

Internal Member - This part was one-seventh of the body of revolution which would constitute the central plug of an annular thrust chamber. It was a compound curved part with its outside diameter forming the gas-side of the combustion zone. Figure 67 shows the gas-side and backside parts of the internal member prior to brazing.

External Member - This part was one-seventh of the body of revolution which would constitute the shroud or outer member of an annular thrust chamber. It also was compound curved but the gas-side was on its inside diameter (ref Figure 68).

The fabrication of the water-cooled axial throat sector thrust chamber proceeded without incident through the contour and coolant channel machining of each pair of components for the four "sides" of the thrust chamber.

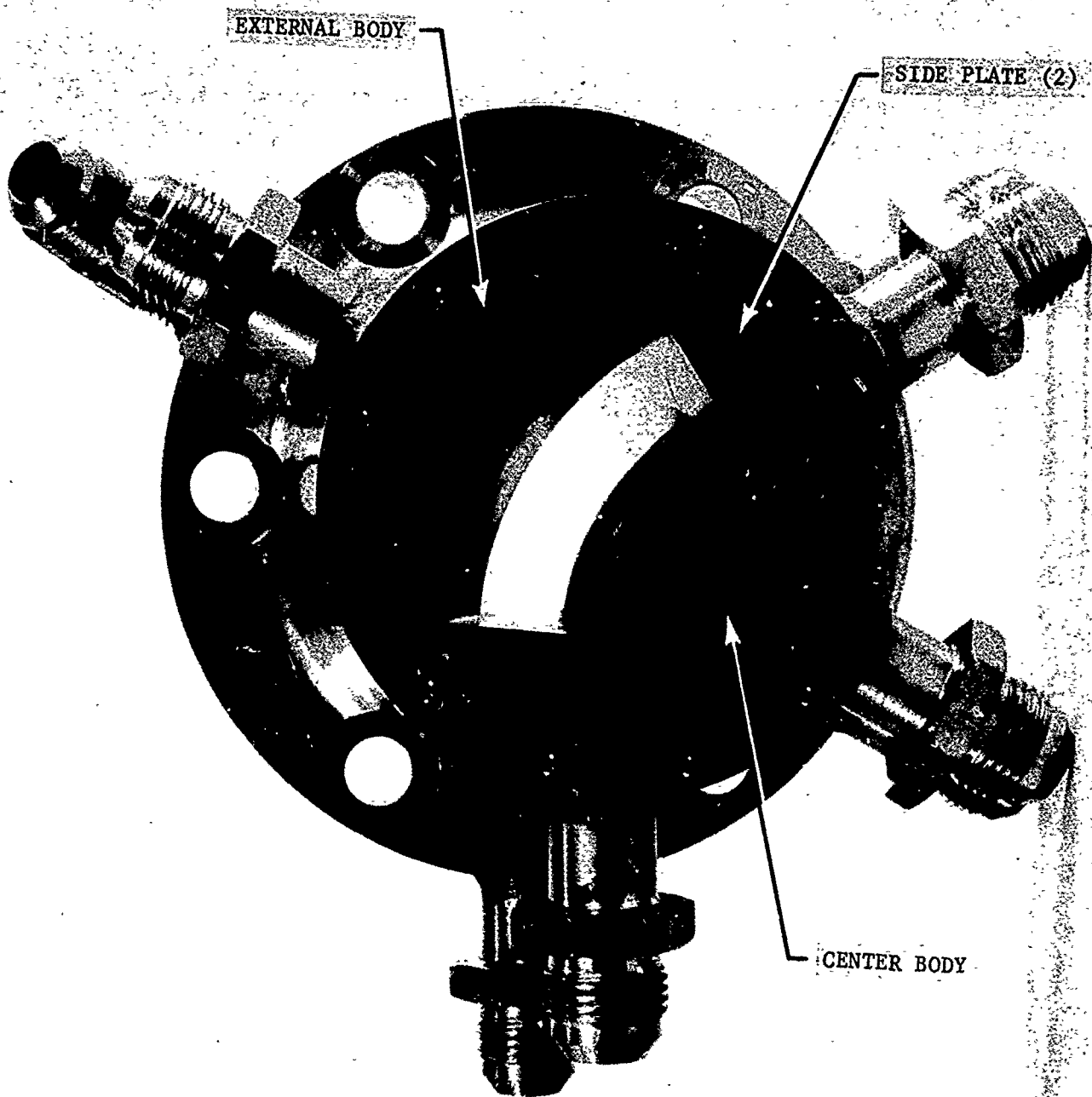


Figure 66. Axial Throat Sector (End View)

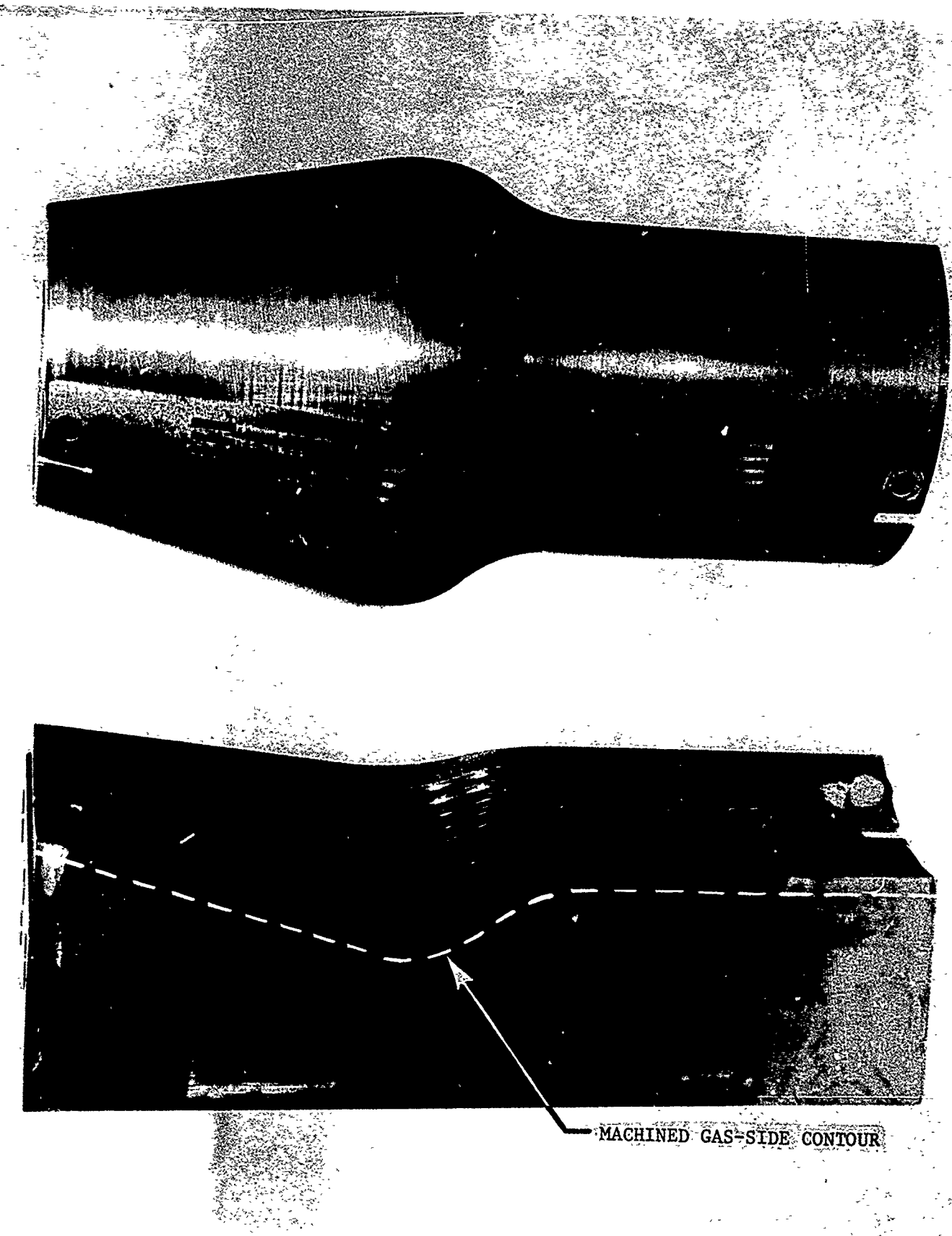


Figure 67. Chamber Centerbody Side Components

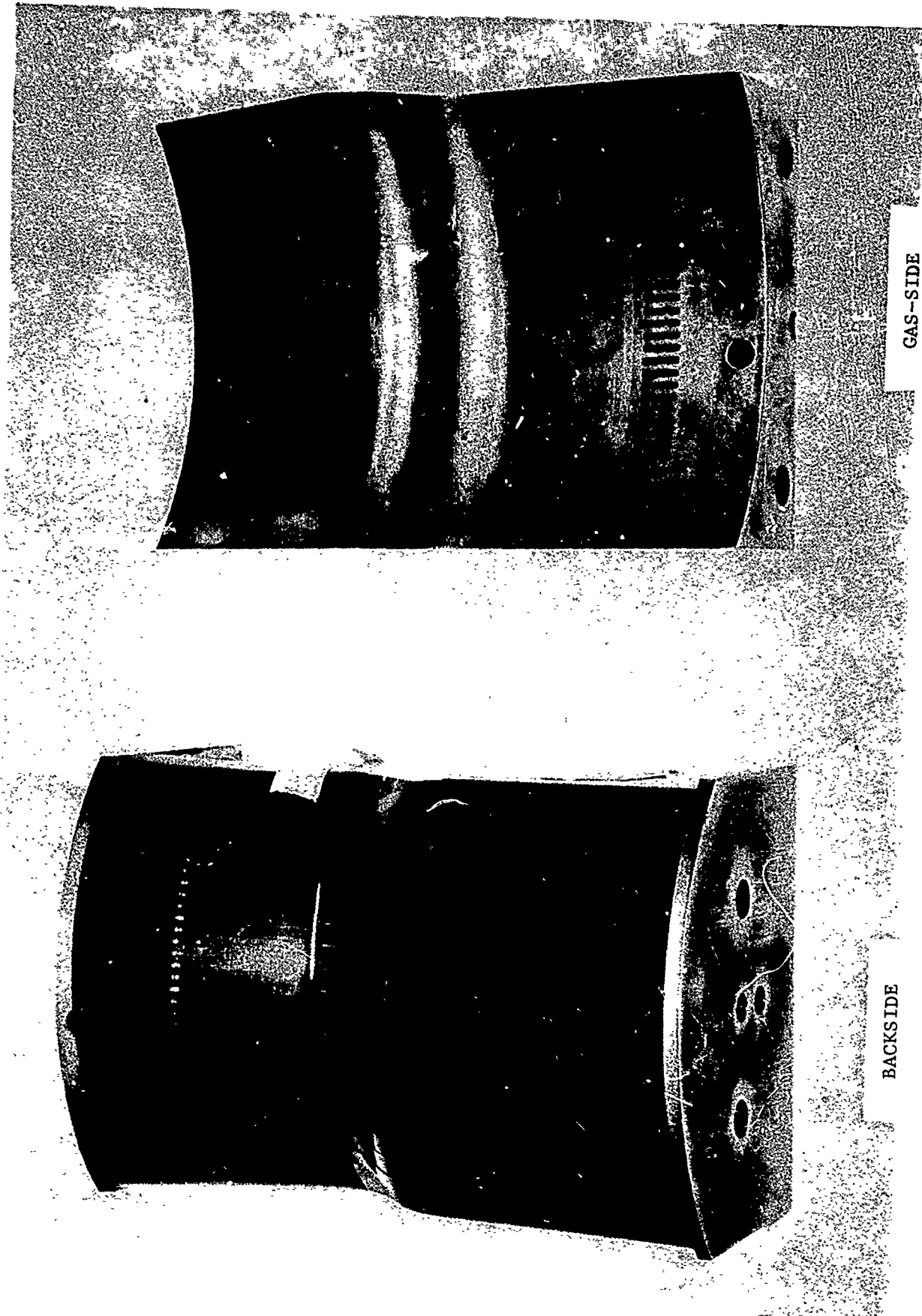


Figure 68. Chamber Outboard Side Components with Braze Foil Pattern
Installed

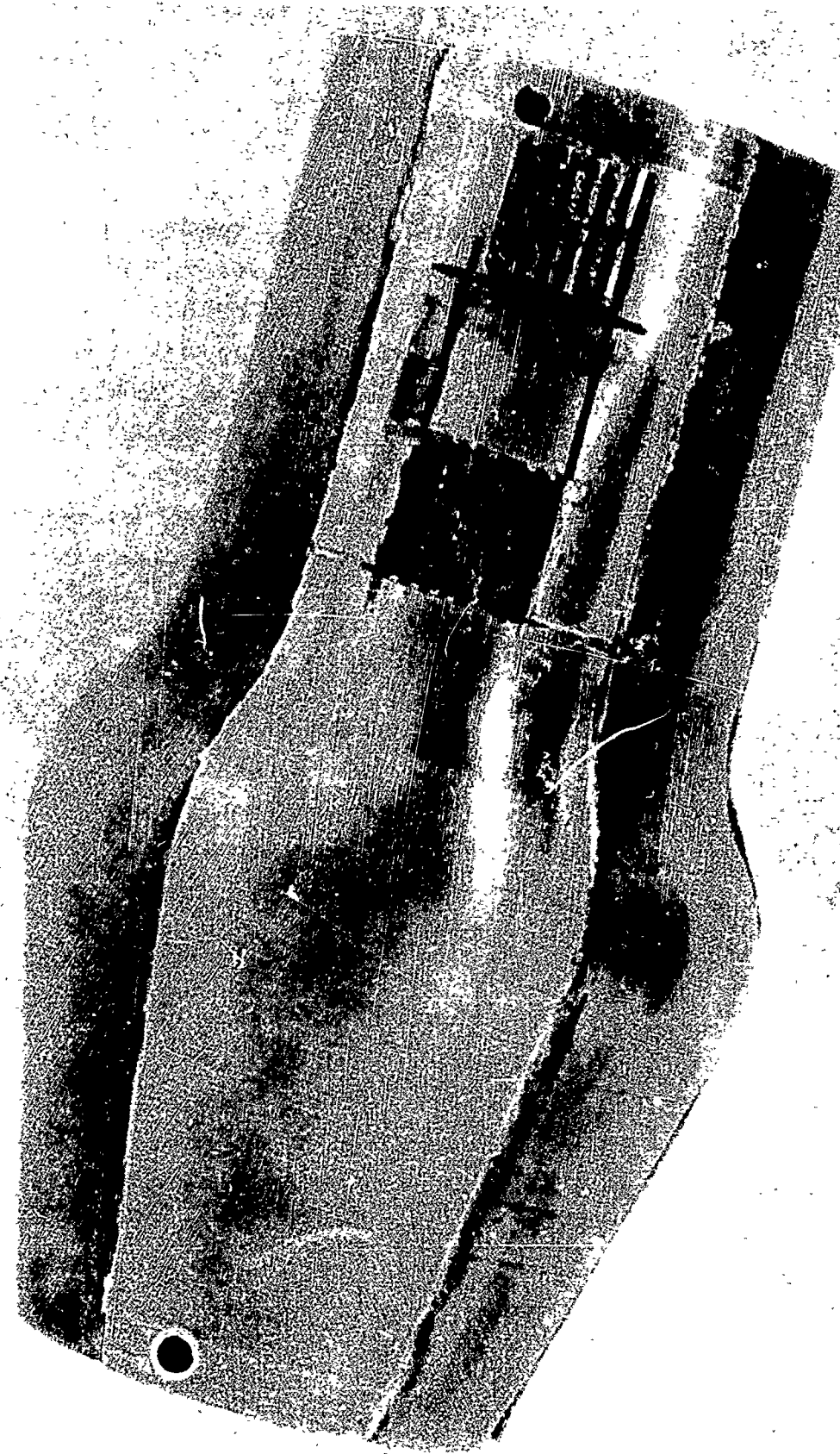
III, B, Fabrication (cont.)

The manifold section feed slots, which conveyed water to and from outboard manifolds to the coolant channels, were also machined. The first brazement was of the member (PN 1161393) which formed the surface of the internal plug. This part was brazed using 0.001-in.-thick Nioro (82% Au, 18% Ni) foil applied over the lands of the slotted part. The foil was held in place with acryloid cement. Following brazing, the gas-side contour was finish machined. Proof test of this part resulted in a separation at the coolant channel land-to-cover brazed interface. This occurred as the channel pressure was raised from 500 to 725 psi. An acceptable part was intended to safely meet 2500 psia. The delamination occurred over the convergent nozzle to a region approximately one inch aft of the throat station.

A portion of the gas-side surface was removed following the failure to allow examination of the brazed interface. This revealed the local braze alloy thicknesses to be from 0.003 to 0.005 in. which was in excess of the anticipated 0.0015 in. fitup gap. There also was evidence of braze alloy starvation (some areas were not covered) and contamination at the braze interface. Figure 69 shows the delaminated part and the removed slotted gas-side wall.

Following review of the part configuration and the braze processes used, it was concluded that the fitup at the braze interface was faulty due possibly to a failure to stress relieve the parts following machining or inadequate load during braze. It was found that the use of feeler gages for a quantitative fit check of the entire interface prior to brazing was inadequate. There also was concern that the acryloid cement which held the braze foil in place could have caused contamination due to inadequate venting of the coolant passages during the braze process.

Figure 69. Centerbody Which Ruptured During Proof Test



III, B, Fabrication (cont.)

These reviews resulted in the decision to rework the damaged part to a point at which it would be ready for braze. The required rework consisted of machining the gas-side (slotted) member off, resurfacing the mating part, and making and fitting a new slotted cover to form the gas side. An EDM "kiss-off" machining operation in which the slotted member was used as the anode was used to achieve the final fitup. Previously, this was done prior to cutting the slots. Concurrently, braze procedures were experimentally evaluated prior to proceeding with the thrust chamber brazement. The braze process evaluation program was directed toward solution of the following problems:

- (1) Identification of the quantity of the alloy necessary to provide adequate wetting and still preclude plugging of the channels due to the presence of excess alloy.
- (2) Definition of the surface preparation necessary to ensure part fitup and adequate alloy wetting and venting procedures to allow boiloff of unwanted hydrocarbons.

The evaluation program which is described below resulted in the confirmation of fitup, inspection, and braze procedures which were successfully used in the fabrication of the water-cooled sector thrust chamber components which are shown in Figures 70 and 71.

b. Braze Evaluation Program

(1) Specimen Configuration

The selected specimen design duplicated the cylindrical portion of the internal member of the sector thrust chamber but eliminated the convergent-divergent section which incorporates the compound curvature. The sector thrust chamber's dimensions, with regard to lands, grooves and radius of

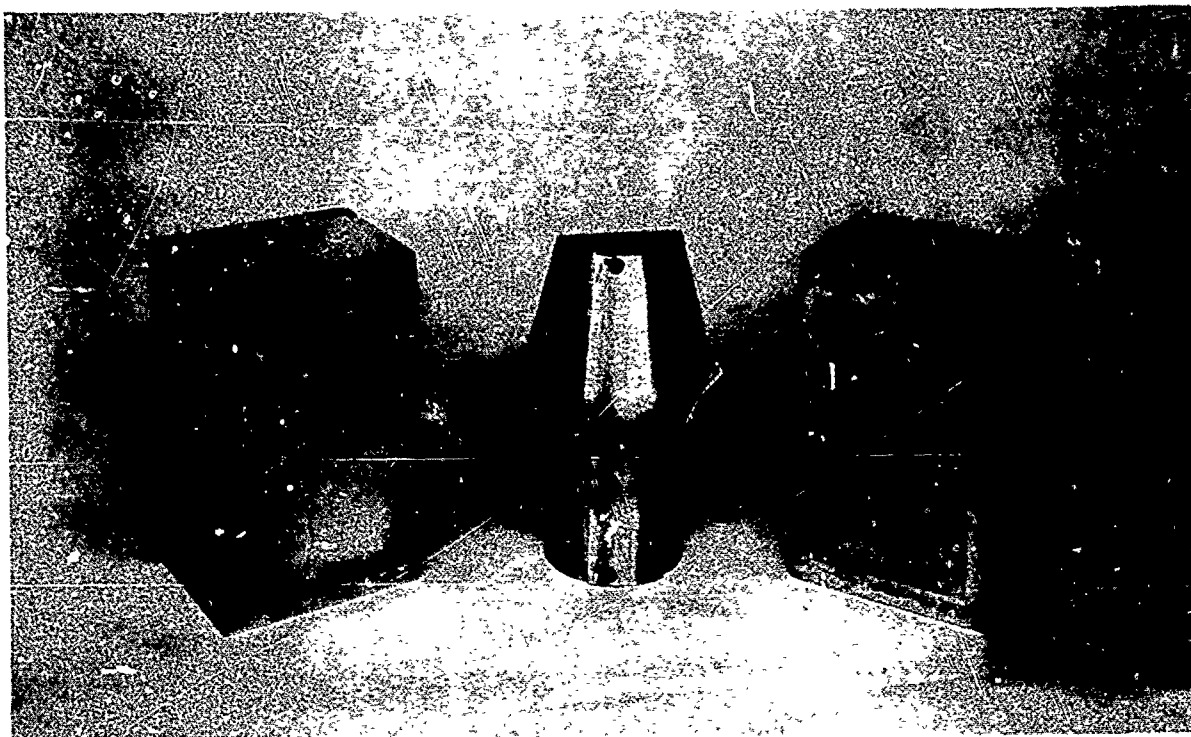


Figure 70. Chamber Centerbody and Side Panel Components After Proof Test

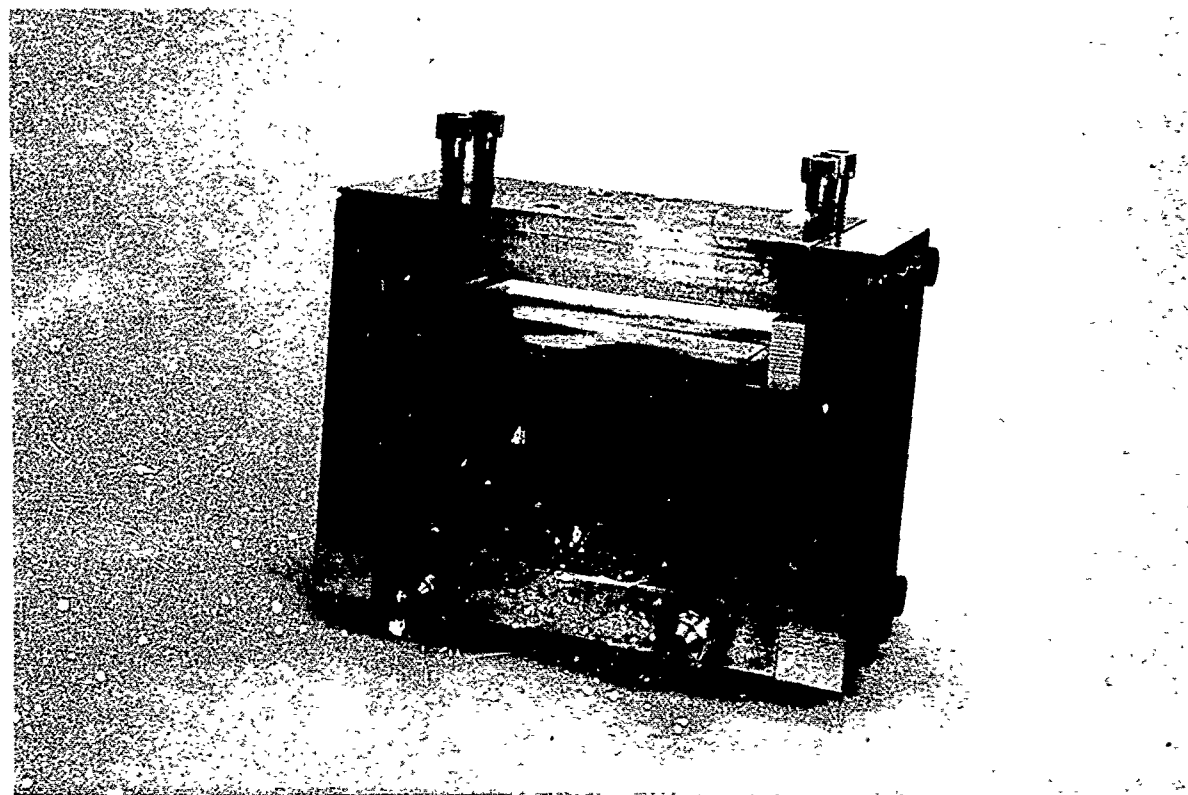


Figure 71. Chamber Side Panel Installed in Proof Test Fixture

III, B, Fabrication (cont.)

curvature, were incorporated into the test specimen. One specimen was brazed at an angle to simulate the effect of compound curvature. Figure 72 shows a typical specimen.

(2) Fitup

All specimens were made from OFHC copper and were annealed after final machining. They were then placed in an EDM machine and, by using one part as an anode and the other part as the cathode, intimate contact was assured at the interface. Following removal from the EDM machine, they were solvent cleaned and fitup checked using Dykem Blue which was applied to a thickness of 0.002 in. on one of the two mating parts. This check was performed by bringing the surfaces into contact under a minimal load, using pins for alignment and prevention of part movement. Contact was evaluated by examination of the amount of Dykem dye transferred from the male portion to the female portion. Acceptable parts had to exhibit 100% transfer.

(3) Brazing

All brazing parameters were in accordance with the following tabulation using Nioro (82% Au, 18% Ni) braze alloy:

<u>Specimen Number</u>	<u>Foil Thickness, in.</u>	<u>Furnace Parameters</u>	<u>Load, lb</u>	<u>Remarks</u>
1	0.001	Cycle No. 1	20	
2	0.001	Cycle No. 2	45	
3	0.002	Cycle No. 2	45	
4	0.002	Cycle No. 2	45	Brazed on inclined plane to check for channel blockage.
5	0.002	Cycle No. 2	45	See comments relating to Specimen No. 5 (Section III,B,2,b,(4)).

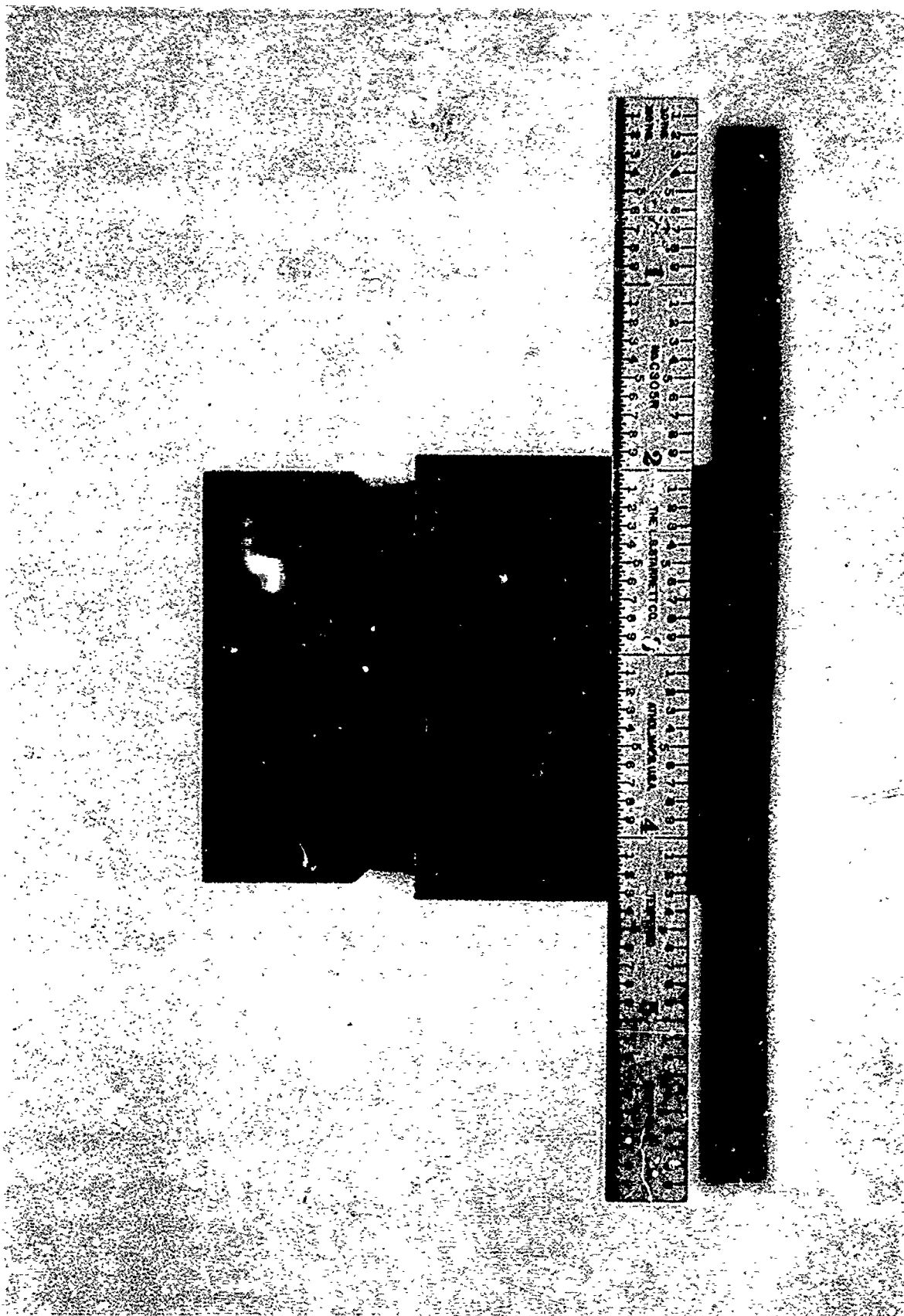


Figure 72. Sectioned Braze Specimen

III, B, Fabrication (cont.)

Furnace Parameters:

Cycle No. 1: Heat to 1700°F and stabilize at temperature for 10 min. Thermal stability was indicated when the two thermo-couples located at either end of the part were within 15°F of each other.

Raise temperature to 1820°F and hold for 10 min. Reduce temperature 30°F per hour to 1700°F and furnace cool to room temperature.

Cycle No. 2: Same as Cycle No. 1, except cool to room temperature from 1820°F to minimize time above the solidus of the brazing alloy.

{ Test Specimen

Specimen No. 1: This was drilled and reamed for 1/4-in.-dia pins at both ends of the part. Fitup was checked with Dykem Blue on the matching surfaces. The bluing transfer indicated high spots at the interface of the dowel pin holes and the ends of the parts which were removed by hand filing. The fitup rechecked with bluing. This process was repeated until the surfaces indicated a good contact. The parts were identified as Serial No. 1 (see Figure 73). Both parts were then thoroughly cleaned with acetone and a 1-mil sheet of Nioro foil was spot welded into place (see Figure 74). The dowel pins used for alignment during the EDM machining were replaced and the two parts assembled. The assembly was then placed into the Brew vacuum furnace with the channels in the up position as shown in Figure 75. The entire assembly was subjected to the following braze cycle No. 1 described above.

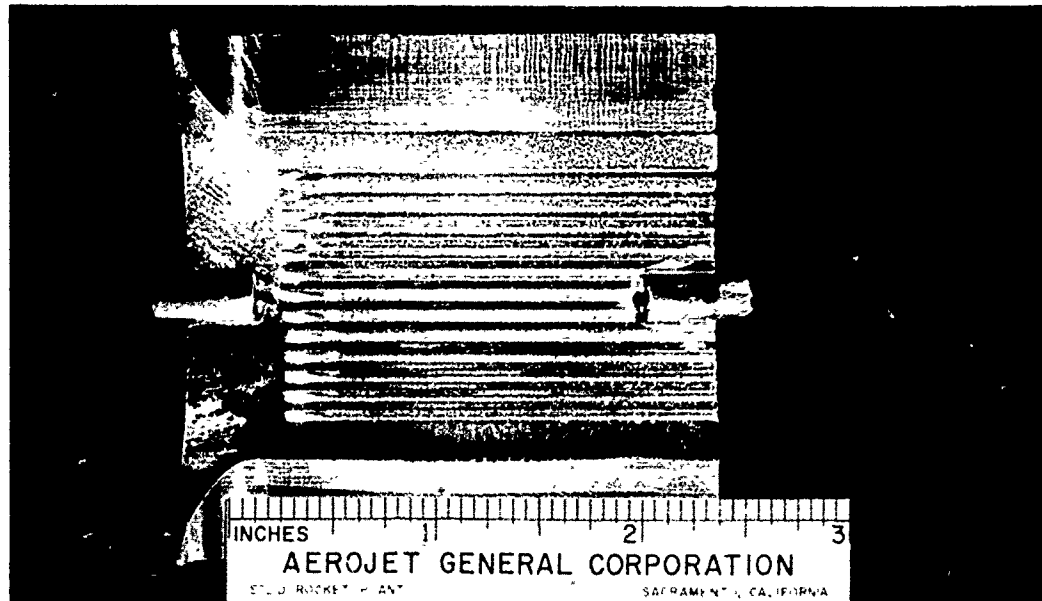


Figure 73. Specimen No. 1 After Fitup Check. Note areas in which Dykem Blue has not transferred, indicating marginal contact.

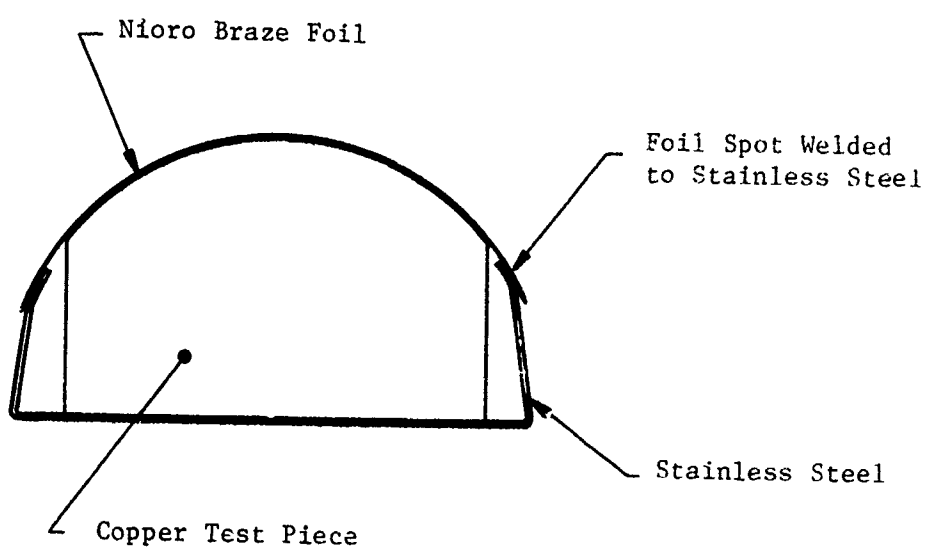


Figure 74. Method of Applying Braze Foil
to Curved Specimen Body

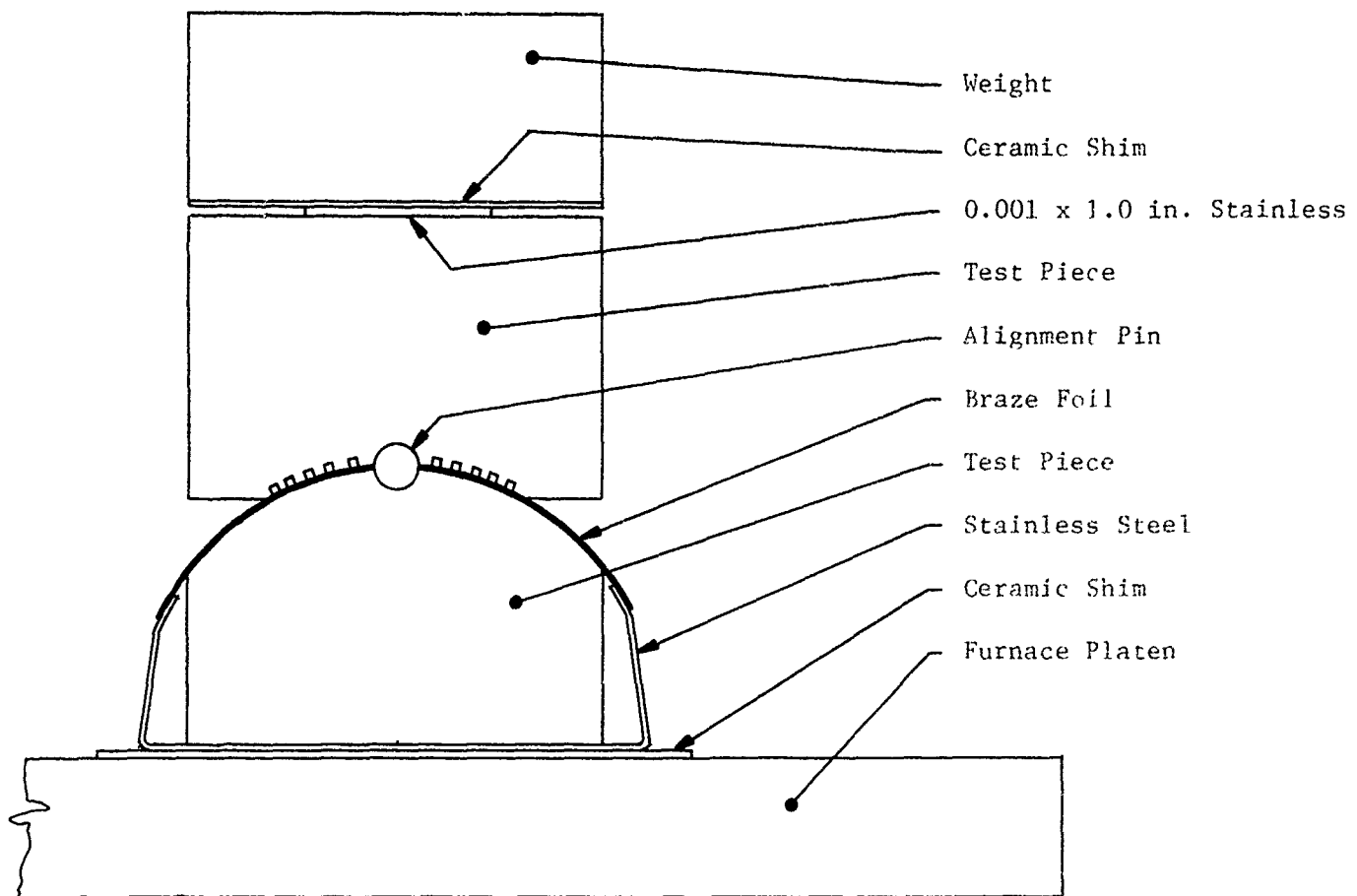


Figure 75. Method of Brazing Specimen Assembly

III, B, Fabrication (cont.)

The specimen was then cut into three equal lengths for evaluation by the cognizant engineering personnel. The results are presented in Section III,B,2,b,(2).

Specimen No. 2: The specimen was drilled and reamed to receive 1/4-in.-dia pins at both ends of the parts and then EDM machined to remove the burrs created by this operation. The parts were cleaned in solvent and given a clean-up and stress relieving cycle in hydrogen at 1800°F for 20 minutes. The matching contours were then checked with Dykem Blue and the results photographed and shown as SN 2 in Figure 76.

The parts were subjected to a chemical cleaning procedure using dilute hydrochloric acid. Braze layup was done using 1-mil Nioro braze foil and the same technique as utilized on Specimen No. 1. The parts were placed in a vacuum furnace and brazed with Cycle No. 2.

Specimen No. 3: This specimen was prepared employing the same procedures used for SN 2. The contours, as checked using Dykem Blue, are shown in Figure 77. The parts were chemically cleaned in dilute hydrochloric acid. The specimen differed from SN 2 in that two thicknesses of 0.001-in. braze foil were used instead of a single thickness of 0.001-in. braze foil. The brazing cycle and load were the same as those used for Specimen No. 2.

Specimen No. 4: This specimen was prepared using the same procedures in effect for Specimen No. 3 (see Figure 78 for results of fitup check). The specimen was brazed on an inclined platen to simulate the compound curvature of the actual part and to determine if the braze alloy would run down-hill, resulting in channel blockage. The setup used to fix the braze angle is shown in Figure 79.

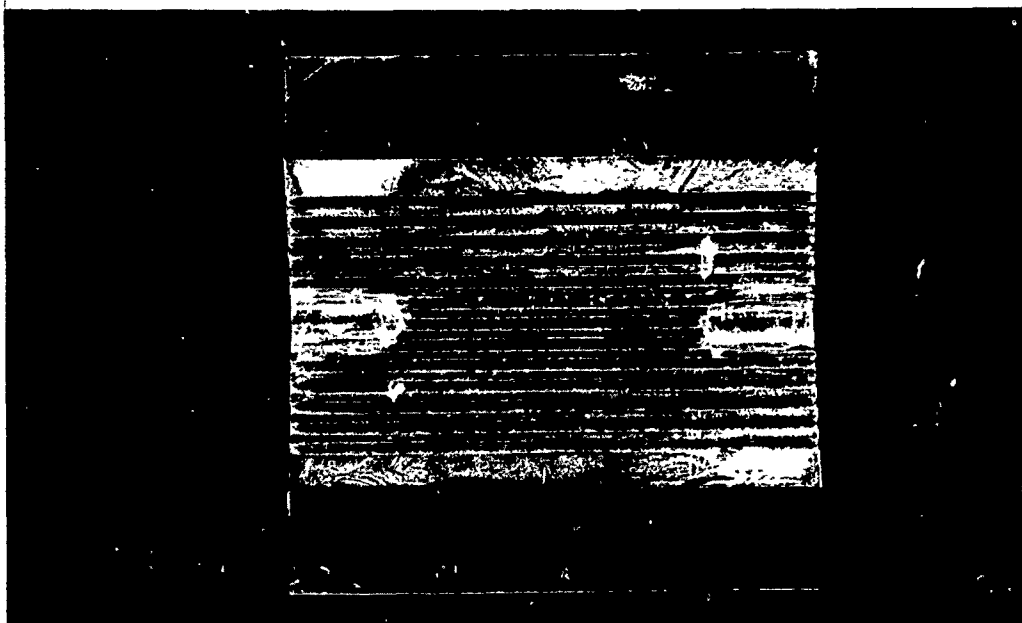


Figure 76. Specimen No. 2 After Fitup Check. Dye transfer is generally acceptable. Suspect areas exist in upper left and lower right.

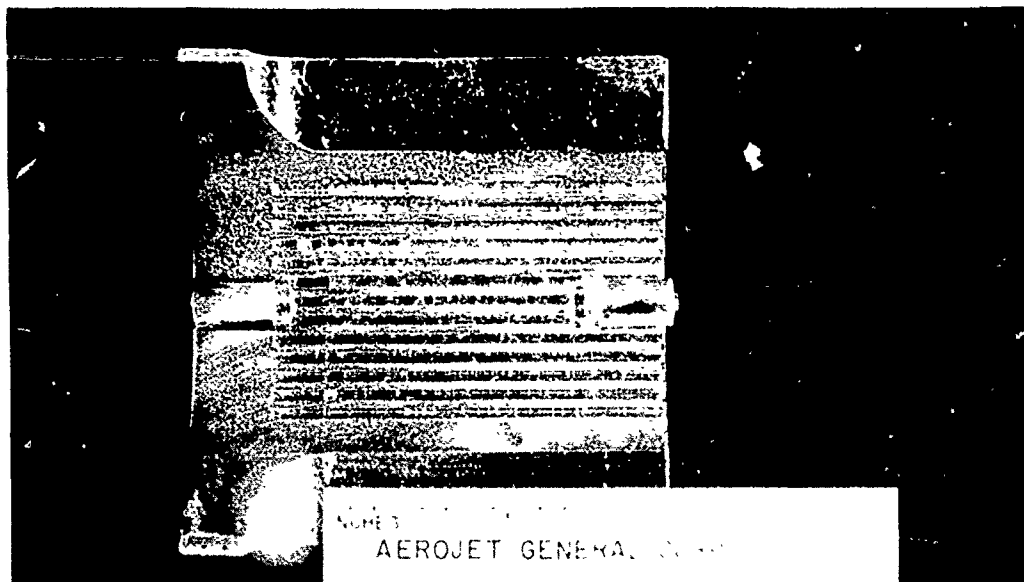


Figure 77. Specimen No. 3 After Fitup Check. Note that indications of transferred dye exist in all braze areas. Pull test results for this specimen showed the highest strength of all samples tested.



Figure 78. Specimen No. 4 After Fitup Check. Based on the amount of dye transferred, fitup appears to be equivalent to that observed for Specimen No. 3.

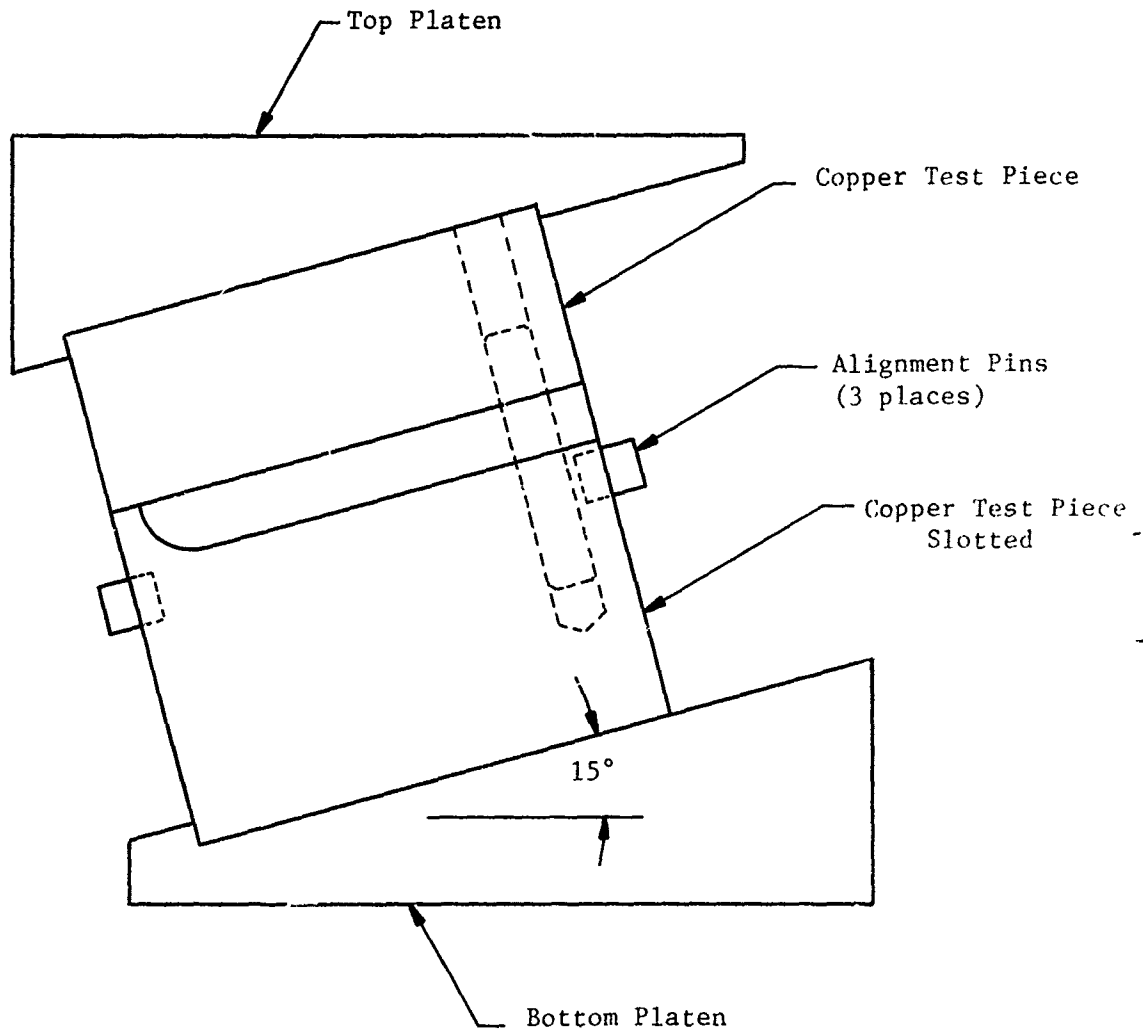


Figure 79. Braze Setup to Evaluate Effect of Angle

III, B, Fabrication (cont.)

Specimen No. 5: This specimen was prepared using the same procedures in effect for Specimen No. 3 (see Figure 80 for results of fitup check). This specimen simulated the positioning of the braze foil on a convergent-divergent surface whose compound contour makes it difficult to apply the braze foil without overlapping or wrinkling. A template was made which translated the compound curvature to a flat surface. A sketch of the template is shown in Figure 81. Braze foil was cut and applied as shown in Figure 82. Sheet No. 1 was cut on the dotted line, sheet No. 2 on the solid line. The widths of the cuts were 0.005 to 0.10 in. wide and the sheets were positioned so that the cuts were staggered as shown. Sheet No. 3 was uncut and its end was butted against the ends of sheets 1 and 2 at the centerline of the part. Sheet No. 4 was then laid on top of No. 3 and overlapping sheets 1 and 2 by 0.030 in. The part was positioned flat in the furnace with the channels in the up position. Braze cycle and load were the same as that employed for Specimen No. 3. Following the braze run, the part was sectioned 0.030 in. from the centerline for examination of the effect of overlapping the braze alloy.

(5) Specimen Evaluation

A primary objective of this braze evaluation which is summarized in Table VIII was to demonstrate a braze joint quality which would deform the copper slots prior to rupture of the braze. This was demonstrated by cutting full cross sections through each of the braze specimens, calculating the area, and determining the load in pounds per square inch at failure. A 19,800 psi stress at failure was recorded for Specimen No. 3 (see Figure 83). Based on these results, the selected parameters for use in brazing component parts of the 1/7 cooled sector body were in accordance with the brazing parameters used for Specimen No. 3.

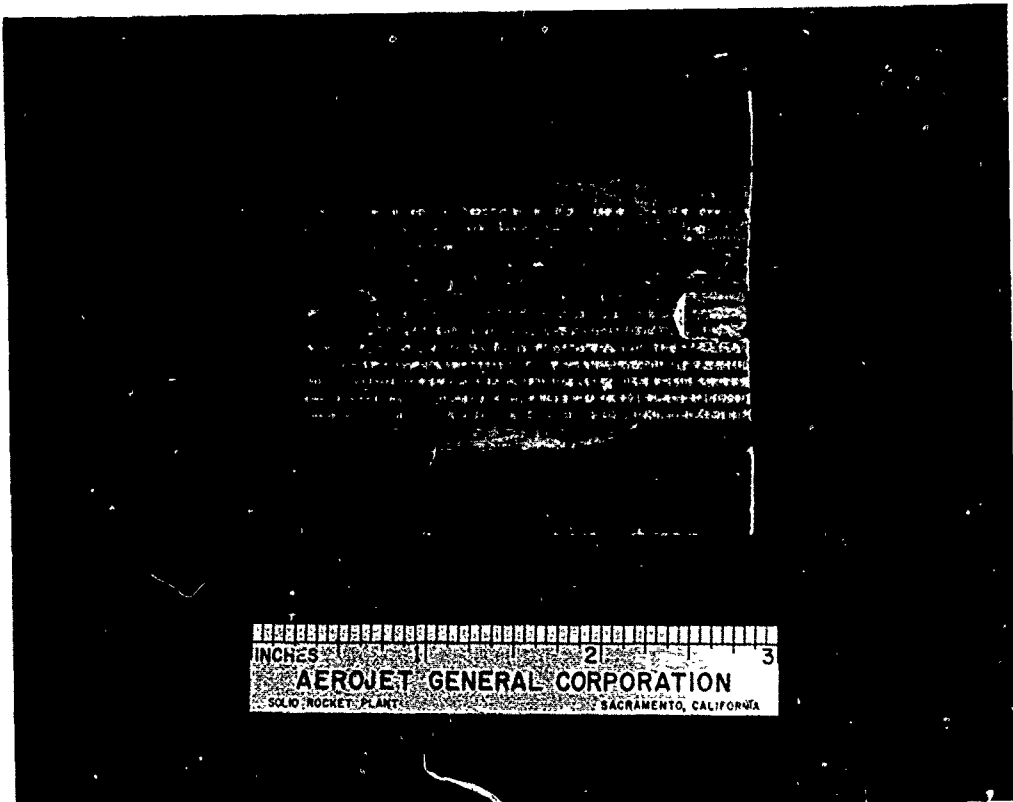


Figure 80. Specimen No. 5 After Fitup Check. Results indicate satisfactory fit over all lands but marginal contact on wide land in upper right and lower left. Post-brazing examination results show that the marginal contact has reduced the stress to failure over the optimum results reported for Specimen No. 3.

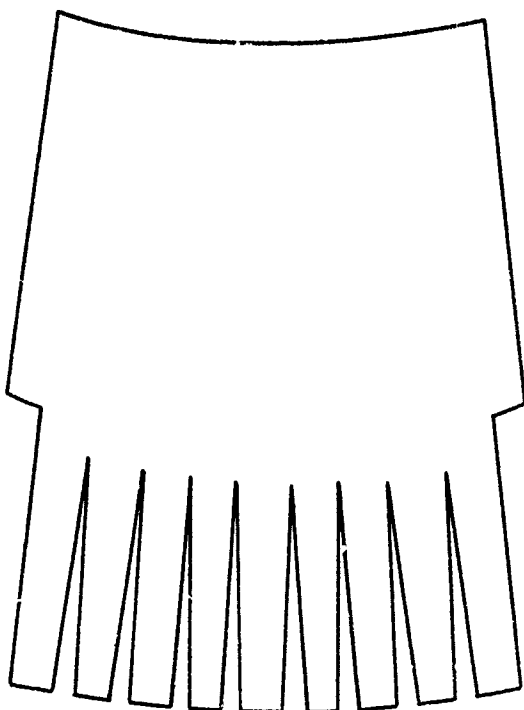


Figure 81. Template Used to Layout Braze Alloy
Prior to Placement on the Curved
Sector Body

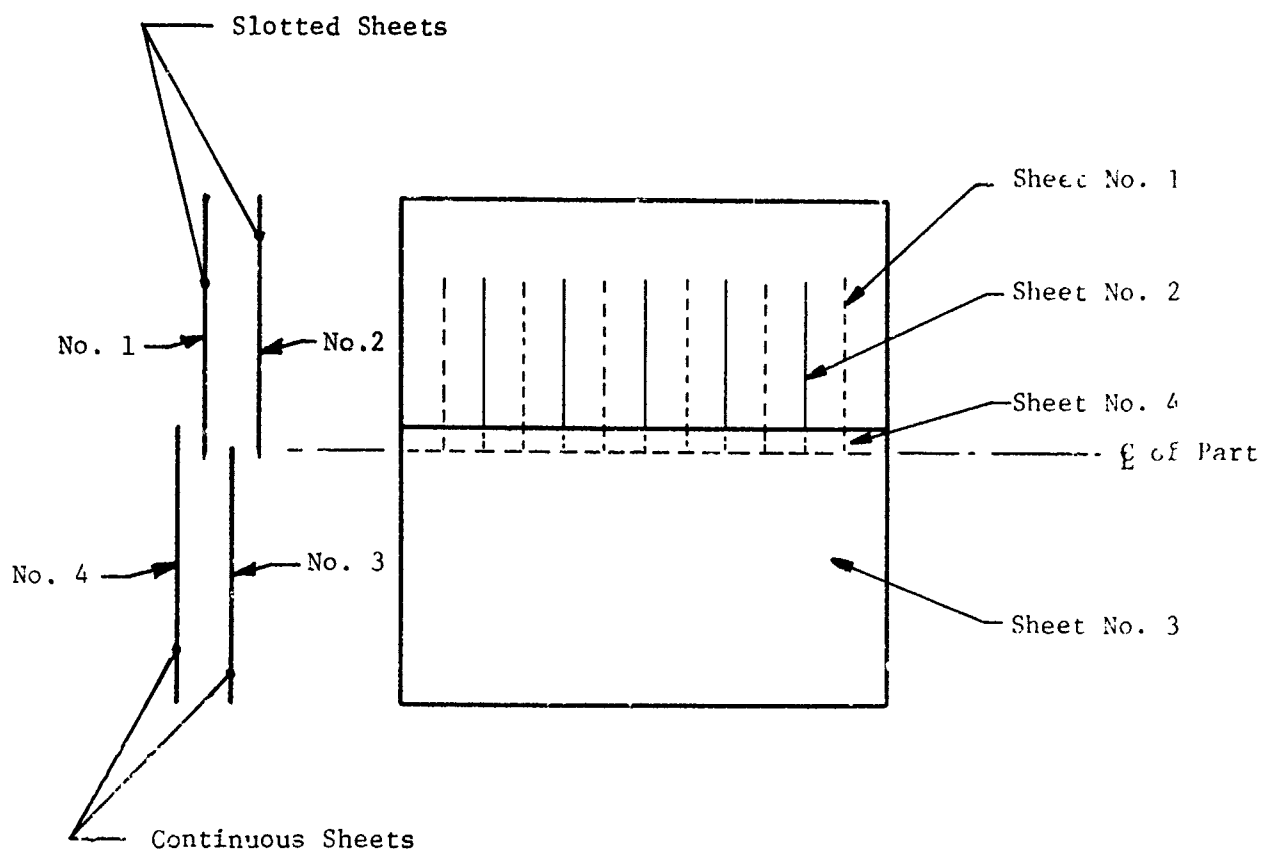
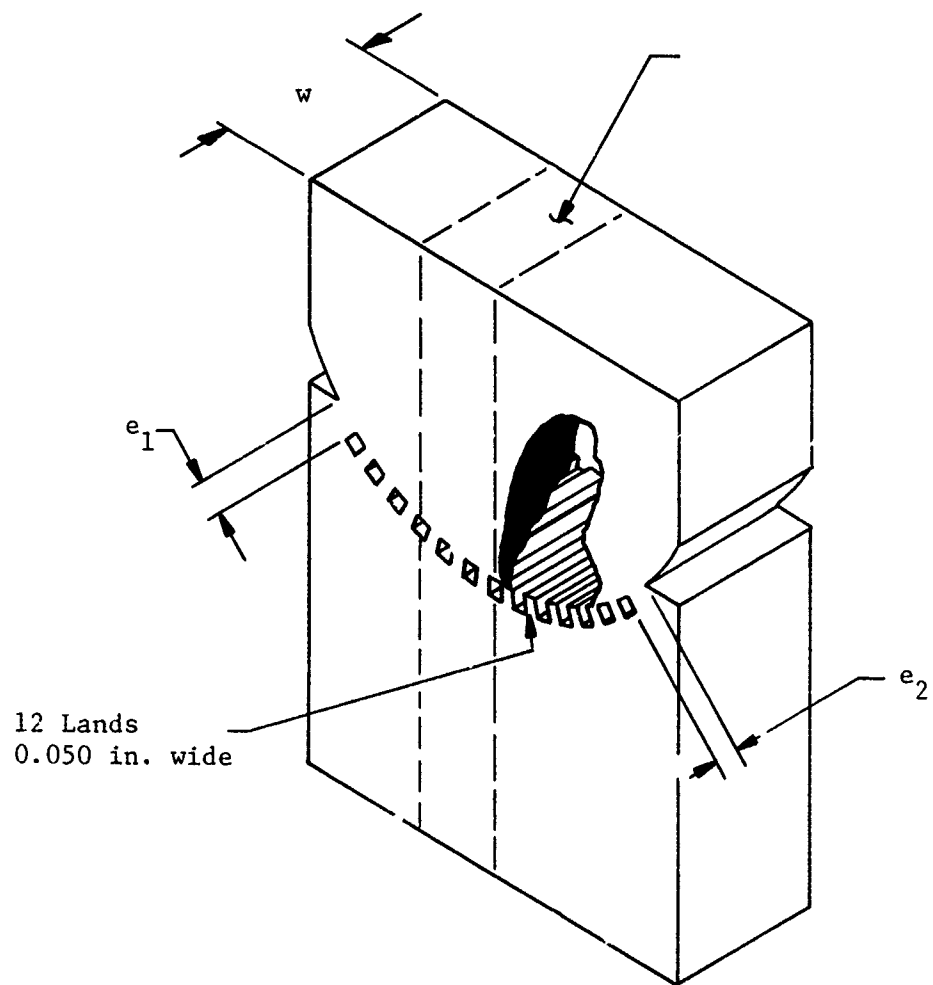


Figure 82. Method of Cutting and Applying Braze Foil to the Curved Sector Body

TABLE J111
CHAMBER BRAZE EXPERIMENTS

Component	Evaluation Objectives	Fitup	Stress Relief	Cleanout	Braze Alloy	Loading During Braze (Contact Pressure)	Braze Cycle	Results
Initial Chamber Segment	--	EDM prior to slotting	After rough machining	Hydrogen bright anneal after EDM. Acetone at assembly.	Noro 1 mil thick on contacting interfaces. Hold by acrylic cement.	4 psi	Heated to 1700°F and stabilized in hydrogen furnace. Increased w/ 1820°F and held for 30 min. Reduced to 1600°F. Furnace cooled.	Delaminated during pressure test. Evidence of contamination, poor fit and lack of braze alloy.
Specimen 1	Evaluate fit check technique, effect of additional alloy, increased loadings, reduced cooling rates and revised sequence.	EDM after slotting. Fit check to verify prior to final cleaning and assembly.	After slotting and EDM fitup.	Stress relief in hydrogen. Acetone clean after fit check.	Noro 1 mil thick over entire surface (foil spans channel grooves). Retained mechanically.	8 psi concentrated over channeled area	Heated to 1700°F and stabilized. Increased w/ 1820°F and held for 10 min. Cooled at 30°F per hour to 1600°F. Remove power and furnace cool.	Slow cooling resulted in extended time above the liquidus temperatures. Braze alloy diffused into the copper parts, resulting in a diffusion bonded interface. One end of the specimen did not braze. Some evidence of incomplete cleaning was noted and the contact during fit check was not as complete as the other specimen areas.
Specimen 2	Revised cleaning procedure with a return to the original part cooling schedule.			Stress relief in hydrogen. Acetone clean after fit check. Chemical clean as part of the final assembly operation.	Noro 2 mils thick over entire surface.		Heated to 1700°F and stabilized. Increased w/ 1800°F and held for 10 min. Remove power and furnace cool.	Specimen well brazed. Some indication that more alloy was needed by lack of fillets at braze interfaces.
Specimen 3	Determine effect of increased alloy quantity.							Same appearance as Specimen 3.
Specimen 4	Effect of gravity on alloy flow tendencies.							Good braze fillets at braze interfaces. No evidence of excess braze alloy in channels.
Specimen 5	Effect of improved alloy placement technique							Same appearance as Specimen 3.



<u>Specimen No.</u>	<u>w, in.</u>	<u>e₁, in.</u>	<u>e₂, in.</u>	<u>Area, in.²</u>	<u>Load, lb</u>	<u>Stress, lb/in.²</u>
1B	0.82	0.187	0.187	0.798	4620	5800
2B	0.72	0.187	0.187	0.701	8580	12,230
3B	0.70	0.219	0.219	0.725	14,350	19,800
4B	0.781	0.234	0.203	0.809	10,350	12,800

Figure 83. Braze Sample Pull Test Results

III, B, Fabrication (cont.)

In general, the information gained from the visual examination of each of the specimens used in this evaluation correlated well with the results of the mechanical pull tests. Post-braze examination of Specimen No. 1 substantiated the fact that quality of the braze joint was directly related to fitup. Areas of Specimen No. 1 which showed marginal contact (see Figure 85) exhibited poor wetting and braze adherence. Increasing the load during brazing as was done on Specimen No. 2 improved the fit and increased the load necessary to fail the part. However, reference to Figures 84a and 84b which show the polished cross sections of Specimen No. 2 after brazing, indicated marginal fillet formation, thus pointing up the need for additional braze alloy. Figures 85 and 86, which show the braze interface after samples from Specimen No. 1 and 2 had been pulled to failure, confirm the fact that marginal braze material was present on both of these specimens. Increasing the thickness of the braze foil on Specimen No. 3 while using the higher load of Specimen No. 2 markedly improved the quality of the braze joint. Reference to Figure 87, which represents the braze interface after a sample from Specimen No. 3 had been pulled to failure, shows the plastic deformation which occurred in the parent metal prior to failure of the joint. Figures 88a and 88b, which represent polished cross sections of Specimen No. 3 after brazing, do show fillet formation; however, fillet formation is not considered optimum for the class of alloy used. Based on the results of the 19,800 psi load at failure, the parent metal deformation noted at failure, and the fact that some fillet formation was noted and taking cognizance of the fact that any reduction in channel volume was undesirable, the decision was made not to increase the foil thickness beyond 2 mils and the brazing conditions used for Specimen No. 3 were adopted for use on the actual detail part components.

Specimen No. 4 was brazed on an inclined plane to simulate the flow characteristics of 2-mil brazing alloy when used on a convergent-divergent section. (See Figure 89 for view of surface after pull test.) Examination of this specimen subsequent to brazing was done by sectioning the brazed part

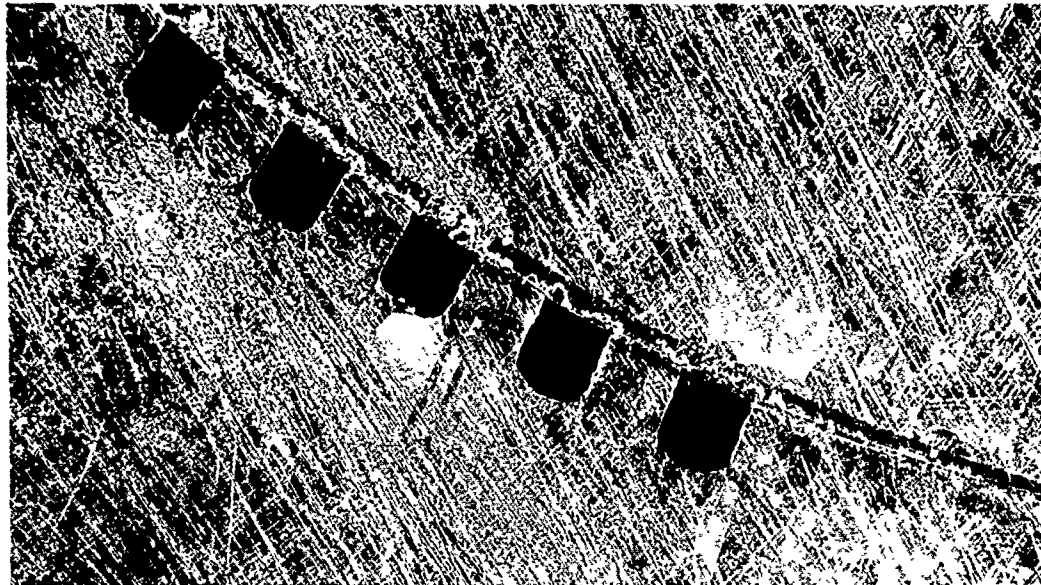


Figure 84a. Specimen No. 2 After Brazing. Note the excellent contact at the land areas which indicates satisfactory fitup. Also note the complete absence of fillet formation which indicates alloy starvation for this application.

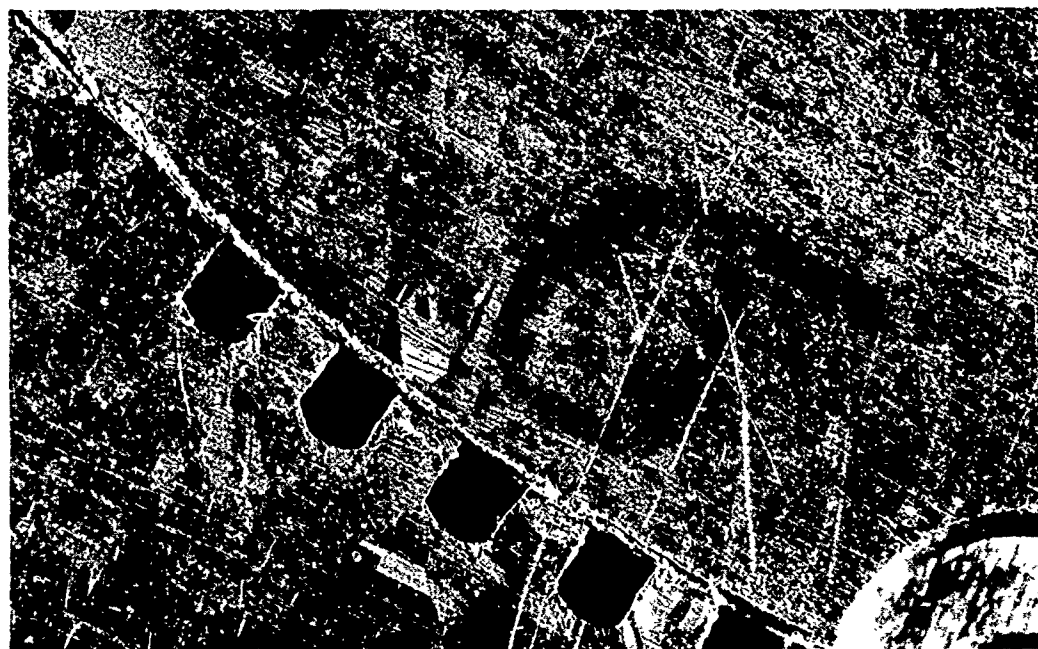


Figure 84b. Specimen No. 2 After Brazing

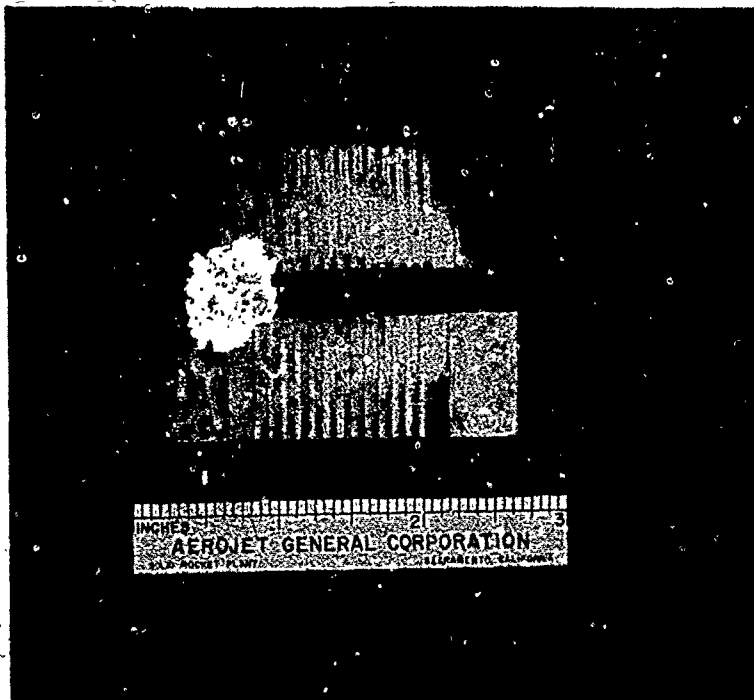


Figure 85. Specimen No. 1 After Pull Test

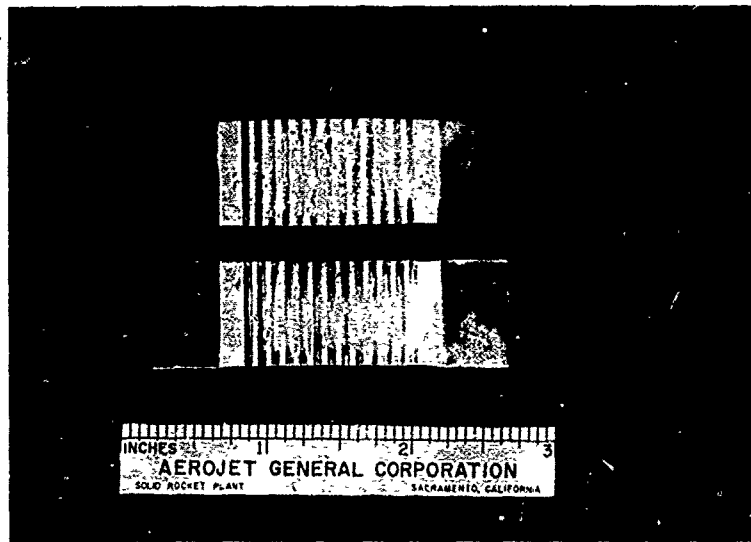


Figure 86. Specimen No. 2 After Pull Test. The results indicate significant improvement in fitup but the amount of alloy still appears to be marginal.

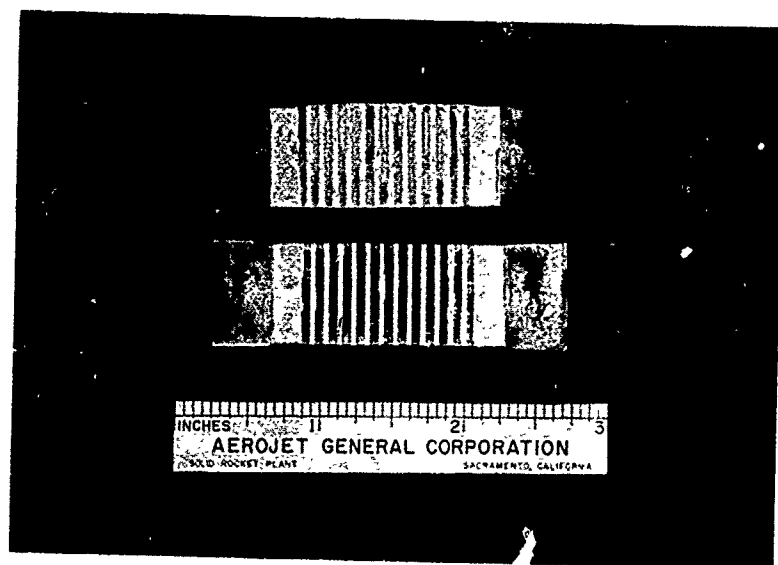


Figure 87. Specimen No 3 After Pull Test. Note that considerable plastic deformation occurred prior to failure.

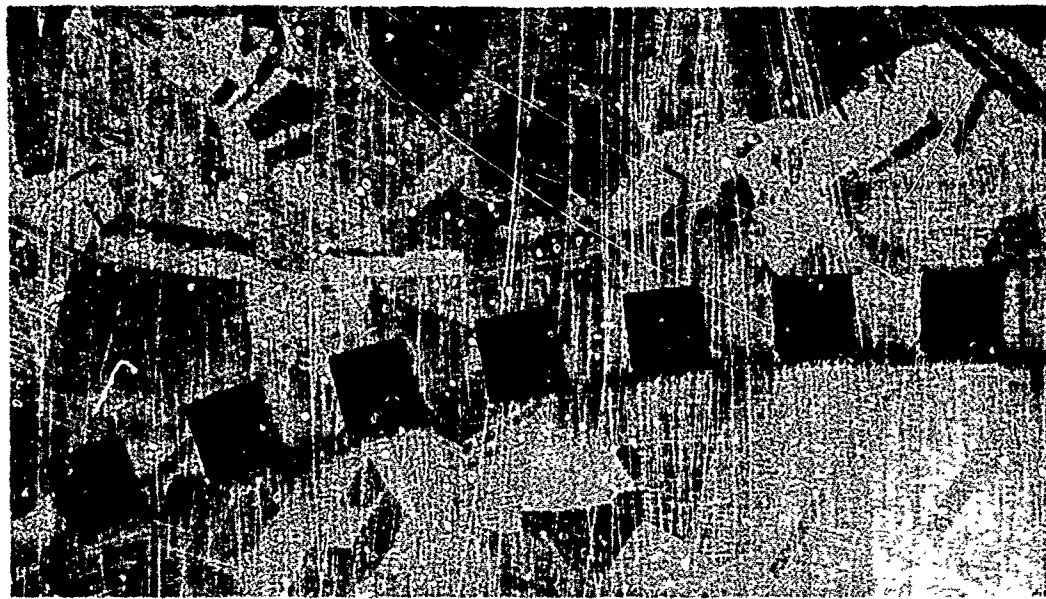


Figure 88a. Specimen No. 3 After Braze. The quality of the braze joint appears to be good. Note the minimal fillet formation which indicates that the 2-mil thickness foil is still marginal for this application.

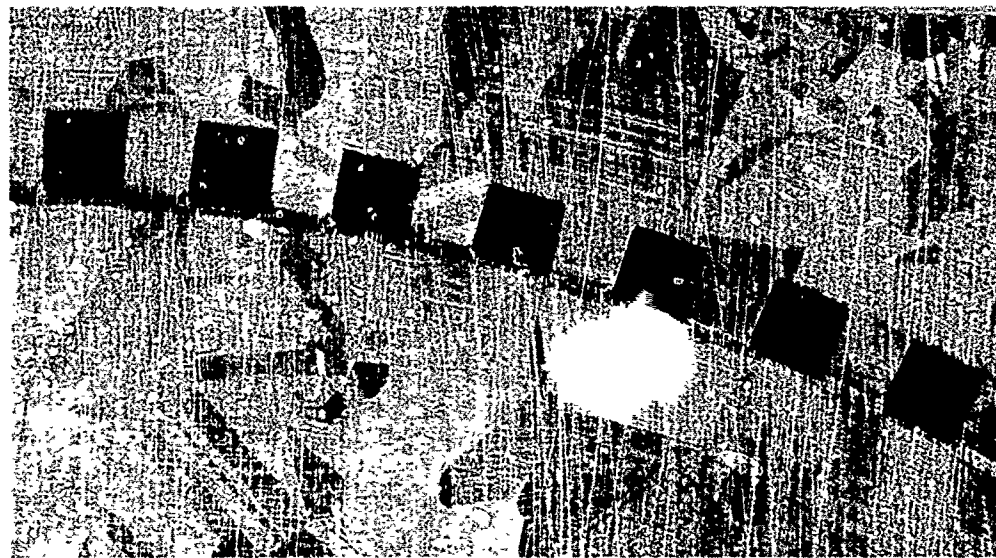


Figure 88b. Specimen No. 3 After Braze

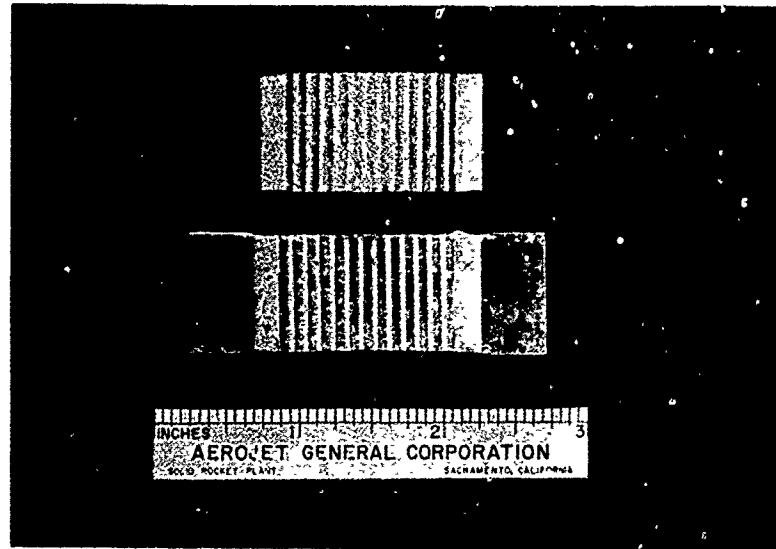


Figure 89. Specimen No. 4 After Pull Test. Principal failure is in the parent metal and all mating surfaces show good fitup and an adequate amount of alloy.

III, B, Fabrication (cont.)

as shown in Figure 72. Results of the visual observation of the cross section revealed no channel blockage due to flow and buildup of braze material along the inclined plane. The final specimen in this group (No. 5) evaluated the overlapped braze foil (ref Figure 82) to be used in the thrust chamber convergent-divergent area. A post-braze examination of this specimen showed no blockage.

c. Thrust Chamber Assembly

The thrust chamber components (left and right side, internal and external members) were brazed using the procedure proven on specimen numbers 3, 4, and 5. They were then finish machined, proof tested to 2500 psia, and prepared for final assembly.

The initial part brazed (a side plate) was discovered to have a poor braze (leakage was evident). This was due to a lower than planned braze temperature caused by thermal conduction to the water-cooled rams of the braze furnace. Improved insulation and added thermocouples were used on the subsequent parts. The defective part was repaired by the replacement of the milled gas-side member.

Ultrasonic inspection processes were used to inspect side plate and internal member braze joints. The C-scan traces obtained with the side plates whose gas-side surfaces were machined to size prior to braze were readable and showed good bonds which were confirmed by the 2500 psia proof tests. On these tests, the crystal was located on the thick-walled side of the assembly. Readings taken from the thin wall (gas wall side) were not usable due to the fact that the wall is too thin to obtain good resolution.

The internal and external members were also ultrasonic inspected prior to finish machining. The C-scan traces were not decipherable due to the curvature of the brazed interface. At the time of the ultrasonic inspection process, the exterior surfaces of the assembly are flat. Ultrasonic inspection of the finish machined part, whose gas-side wall is essentially parallel to the braze interface, was not successful due to the wall being too thin.

III, B, Fabrication (cont.)

It was concluded that the only adequate method for inspection of the braze interface was the proof test operation. Ultrasonic inspection of the braze bond would have required an intermediate machining operation to provide a thick gas-side wall which was "parallel" to the braze interface.

The final assembly procedure required machining the sides of each of the four components so that they could be joined by brazing. The braze ment was then machined round and installed and brazed into a cylindrical housing which contained the inlet and out-water manifold fittings. The braze procedures were as follows:

<u>Component</u>	<u>Alloy</u>	<u>Braze Temperature</u>
Left and right sides	Nioro	1825°F
Internal member	Nioro	1825°F
External member	Nioro	1825°F
Four sides to each other	Nicoro 80	1750°F
Four-sided subassembly-to-circular housing	Palcusil 10 (Ag 58%, Cu 32%, Pd 10%)	1625°F

Figure 90 shows the finished assembly.

Delays anticipated in the fabrication of the water-cooled sector thrust chamber resulted in the fabrication of an identical unit of a heat sink configuration. This part was all copper and the four sides interfaced in the same manner as on the water-cooled unit. It was assembled using Nicoro 80 alloy to join the four sides which were then machined round and installed in a steel cylinder using Palcusil 10 (Ag 58%, Cu 32%, Pd 10%) alloy. This assembly was then final machined. The finished chamber assembly is shown in Figures 91 and 92.

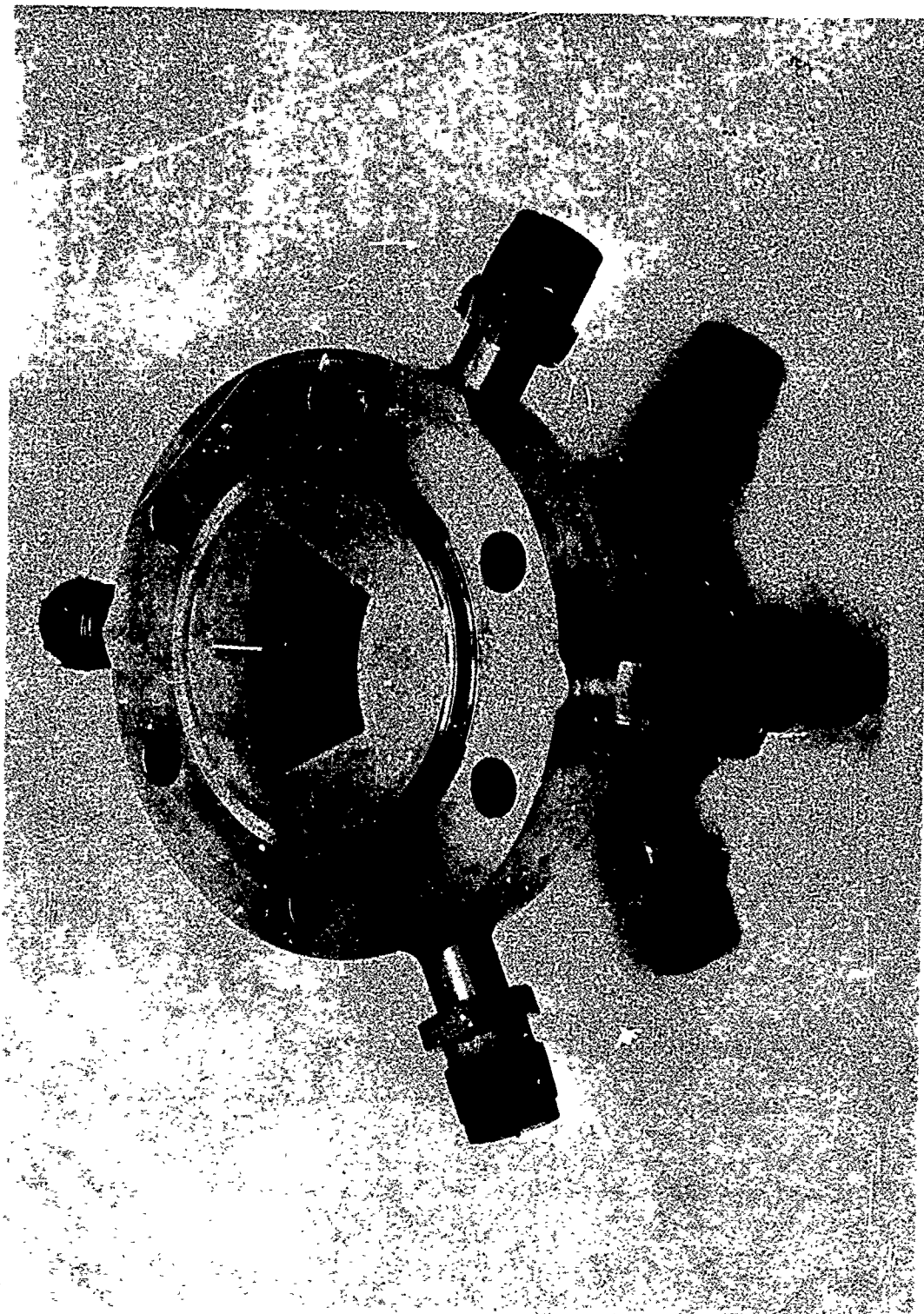


Figure 90. Water-Cooled Axial Throat Chamber (Forward End)

Figure 91. Copper Axial Throat Sector Chamber

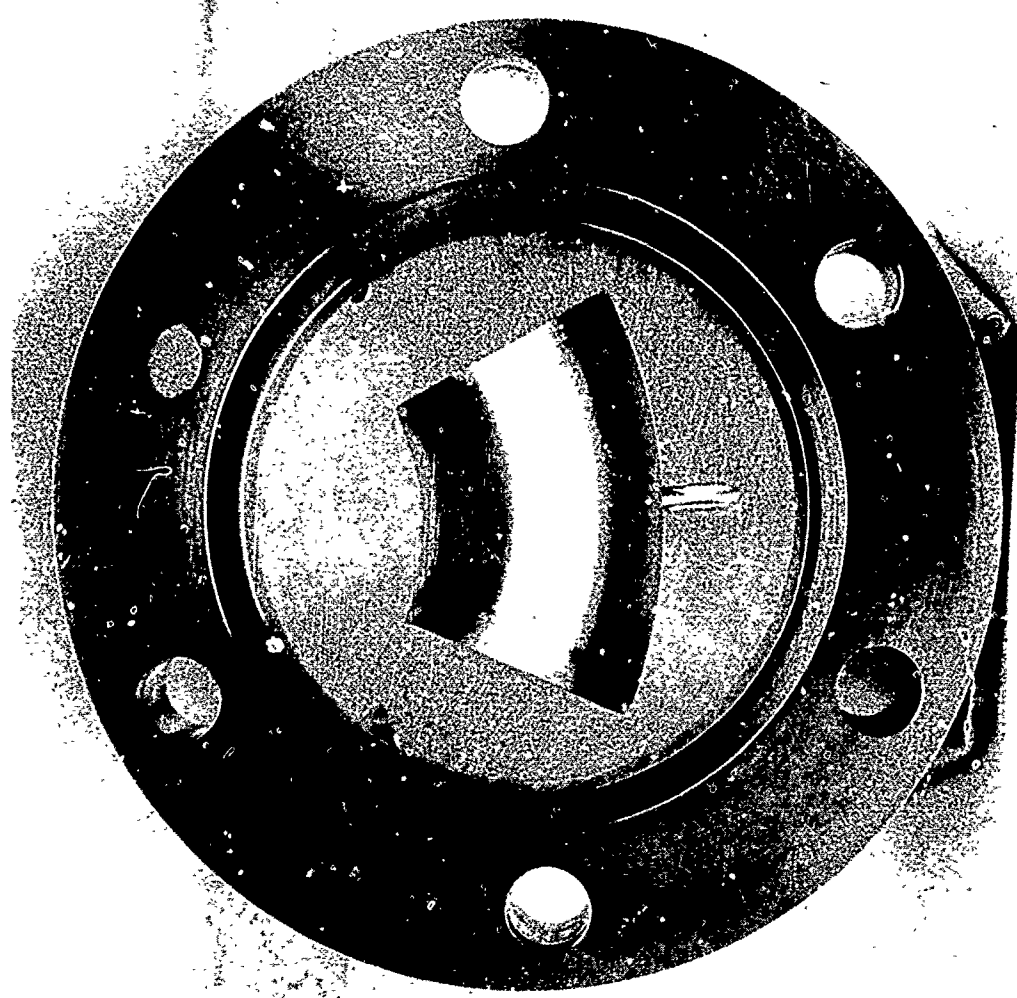




Figure 92. Copper Axial Throat Chamber (Aft End)

III, B, Fabrication (cont.)

d. Conclusions Regarding Chamber Fabrication

(1) Heavy-walled parts of compound curvature can be brazed successfully. Success is dependent on achieving precise component fitup, means of braze alloy placement, and proper fixturing of the braze assembly. The following methods are used to attain this:

- (a) Post-machining fitup by using an ELOX technique to "burn" the components together at the braze interface removes burrs and assures proper fit.
- (b) Application of 0.002-in.-thick Dykem Blue to one of the pair of mating parts. Dye transfer to the other denotes fitup within 0.002 in.
- (c) Heavy-wall parts with flat surfaces which match braze furnace platens eliminate the need for elaborate tooling. Alignment pins used must be oriented to preclude binding and distortion.
- (d) 0.002-in.-thick braze foil applied over the entire surface ensures adequate wetting and good fillets with an absence of braze buildup or plugging.

(2) Ultrasonic inspection of brazed interfaces is not adequate to confirm bond quality. Results were usually conservative.

(3) Use of heavy walls (gas side) which are later machined to the required thickness is a viable technique for nontubular thrust chamber fabrication. This process avoids the need for extensive tooling, i.e., expandable bladders to contain thin-wall gas-side members. Nominal wall thicknesses of 0.040 in. were maintained. This was verified on the destructive inspection of the failed centerbody (Figure 69).

III, B, Fabrication (cont.)

(4) Slot milling using conventional cutters is adequate to form coolant passages, provided a post-machining ELOX operation is used to remove burrs and provide proper fitup.

(5) The heavy-walled brazement concept can be applied to cylindrical parts as evidenced by copper body to steel manifold brazement.

III, Discussion (cont.)

C. TESTING

Testing on the program was accomplished in two areas, namely, igniter verification tests and sector thrust chamber assembly (TCA) testing. The program plan called for an existing ignition system to be used on the test program. Since the existing unit had not been previously operated at the required test conditions, an analytical study was conducted to verify the applicability of the system and a short hot-fire test series was accomplished to verify its operation.

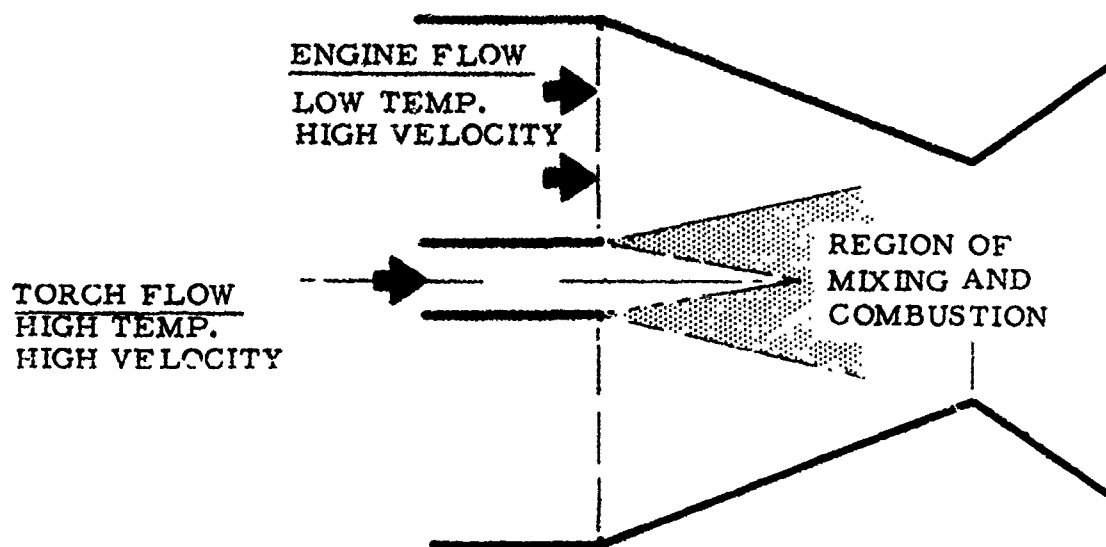
The sector TCA was subjected to a series of six tests at nominal chamber pressures of 300 psia and 700 psia using heat sink and water-cooled axial throat chambers. The sixth test resulted in a failure of the water-cooled chamber and termination of TCA testing.

The following sections describe (1) the ignition analysis and igniter verification testing, (2) the TCA testing, and (3) the results of the sector TCA tests.

1. Ignition Analysis and Testing

This analysis examined the applicability of an existing igniter to the E-D nozzle program. The igniter flow rates and mixture ratio were selected and a start sequence identified.

The problem of igniting an oxygen/hydrogen mixture with a jet of high velocity, hot combustion gases is illustrated in Figure 93. The hot jet exchanges energy with the cold gas mixture through turbulent mixing. Ignition occurs when the gas mixture temperature is raised above its autoignition temperature for a period of time exceeding the ignition delay time. The criterion for ignition is that the residence time of the gas mixture in the jet exceeds the ignition delay time.



IGNITION CONTROLLED BY:

- MIXING
 - RELATIVE VELOCITIES
 - IGNITER SIZE AND GEOMETRY
- COMBUSTION
 - REACTION KINETICS
 - TEMPERATURE
 - MIXTURE RATIO
 - GAS VELOCITIES

Figure 93. O_2/H_2 Torch Ignition Mechanism

III, C, Testing (cont.)

The ignition delay time depends upon the temperature, mixture ratio, and pressure. An ignition delay equation, presented in Reference 18, was used to describe the relationship between these variables. The mixing characteristics between the hot jet and the cold gas mixture are described by the semi-empirical coaxial jet equations presented in Reference 19. These equations were programmed on the UNIVAC 1108 computer to calculate the igniter jet velocity, temperature, mixture ratio, jet residence time, and ignition delay time as a function of both the radial and axial position in the jet. Ignition is indicated at any point in the jet where the residence time exceeds the ignition delay time. It was found that ignition is generally first indicated along the jet centerline since this is the region of highest temperature.

The factors which influence ignition are the igniter jet temperature, which is determined by the igniter MR, and the igniter jet size, which is determined by the igniter flow rate (i.e., P_c and throat size). The influence of each of these factors was determined for the E-D nozzle igniter system shown in Figure 94. The calculations were made assuming the igniter jet to be injected axially with a stream of cold (300°R) gaseous oxygen. The jet centerline ignition delays and gas residence times are plotted in Figures 95, 96 and 97. Figure 95 shows the effect of igniter MR on ignition on the 0.085 in.-dia igniter tube. It is apparent that a minimum igniter MR of 2.0 is required to ensure ignition.

The effect of increasing the igniter flow rate by raising the igniter chamber pressure is illustrated in Figure 96. To produce ignition at an MR of 1.5, it would be necessary to run the igniter pressure up to 1000 psia. A similar effect can be obtained by increasing the igniter throat diameter to 0.250 in. as indicated in Figure 97.

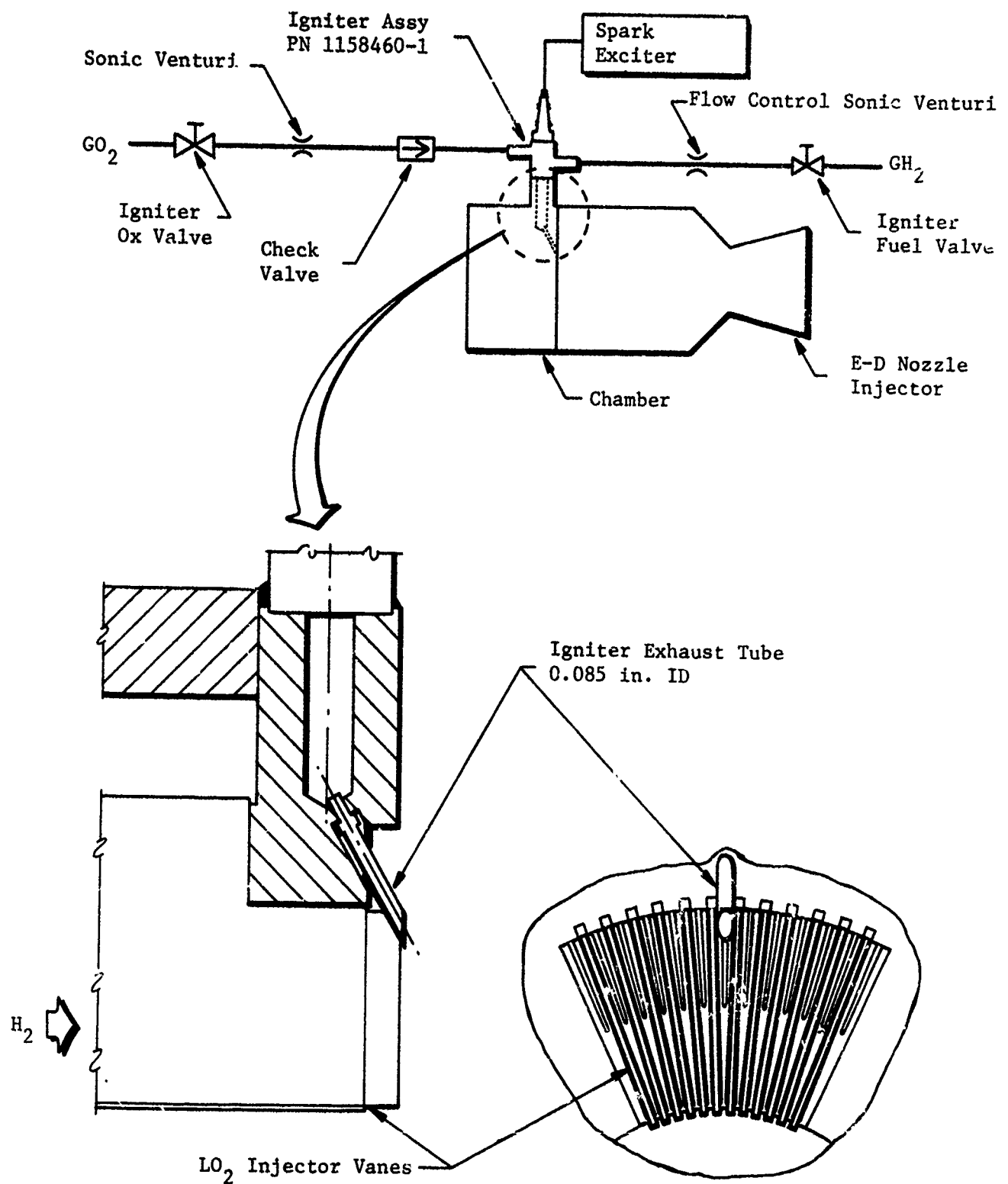


Figure 94. E-D TCA Igniter System

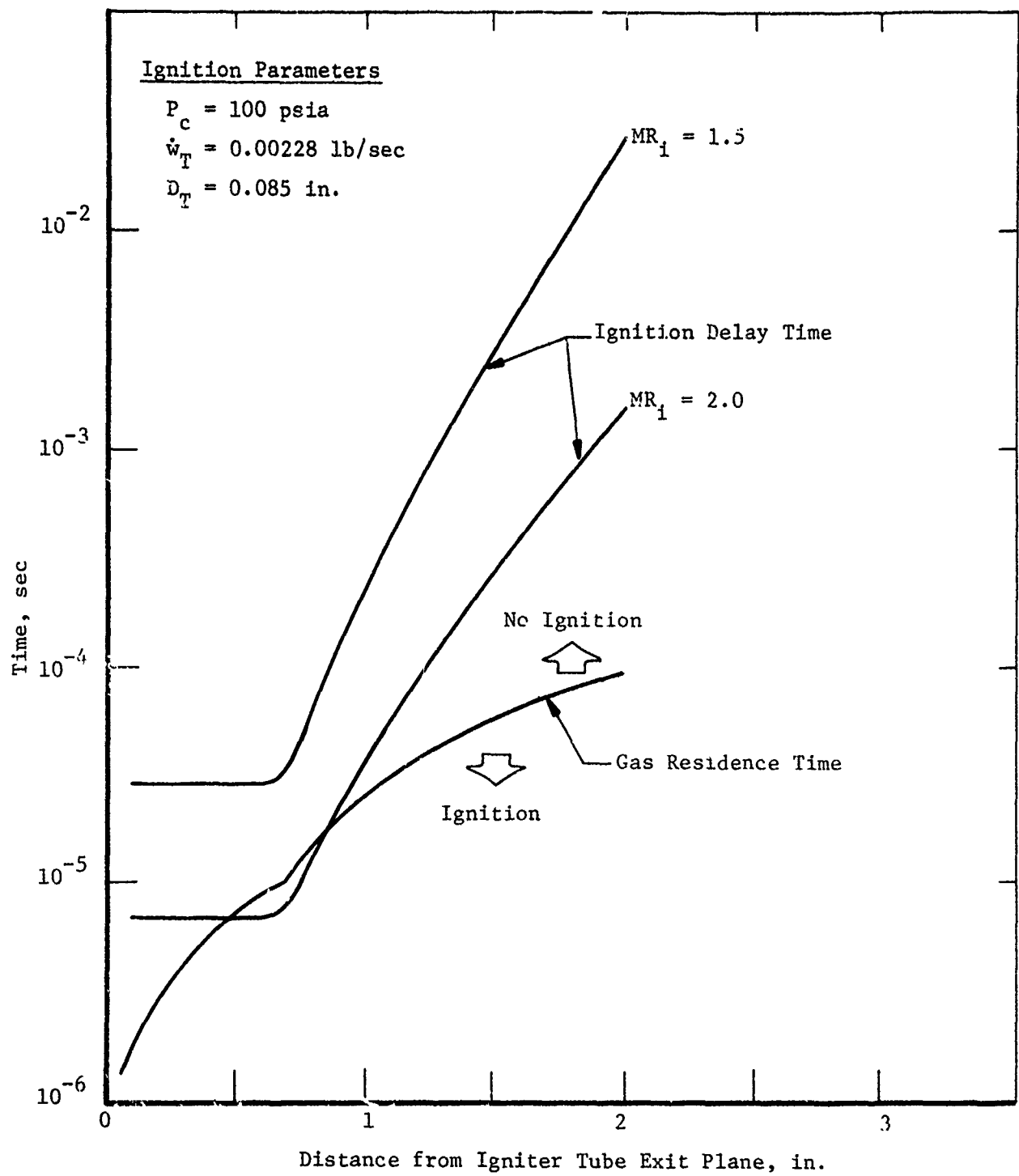


Figure 95. Effect of Igniter MR on Ignition

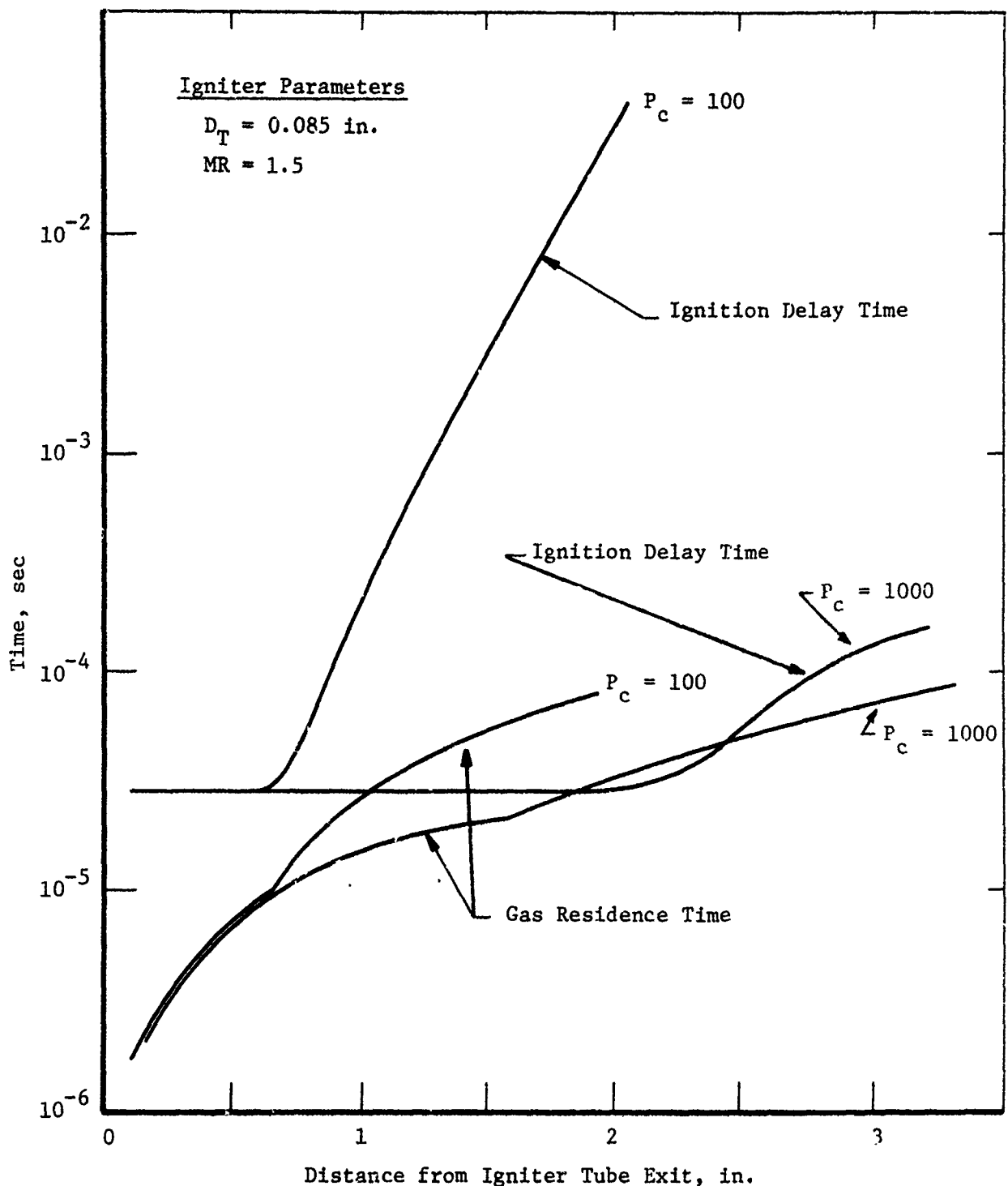


Figure 96. Effect of Igniter P_c on Ignition

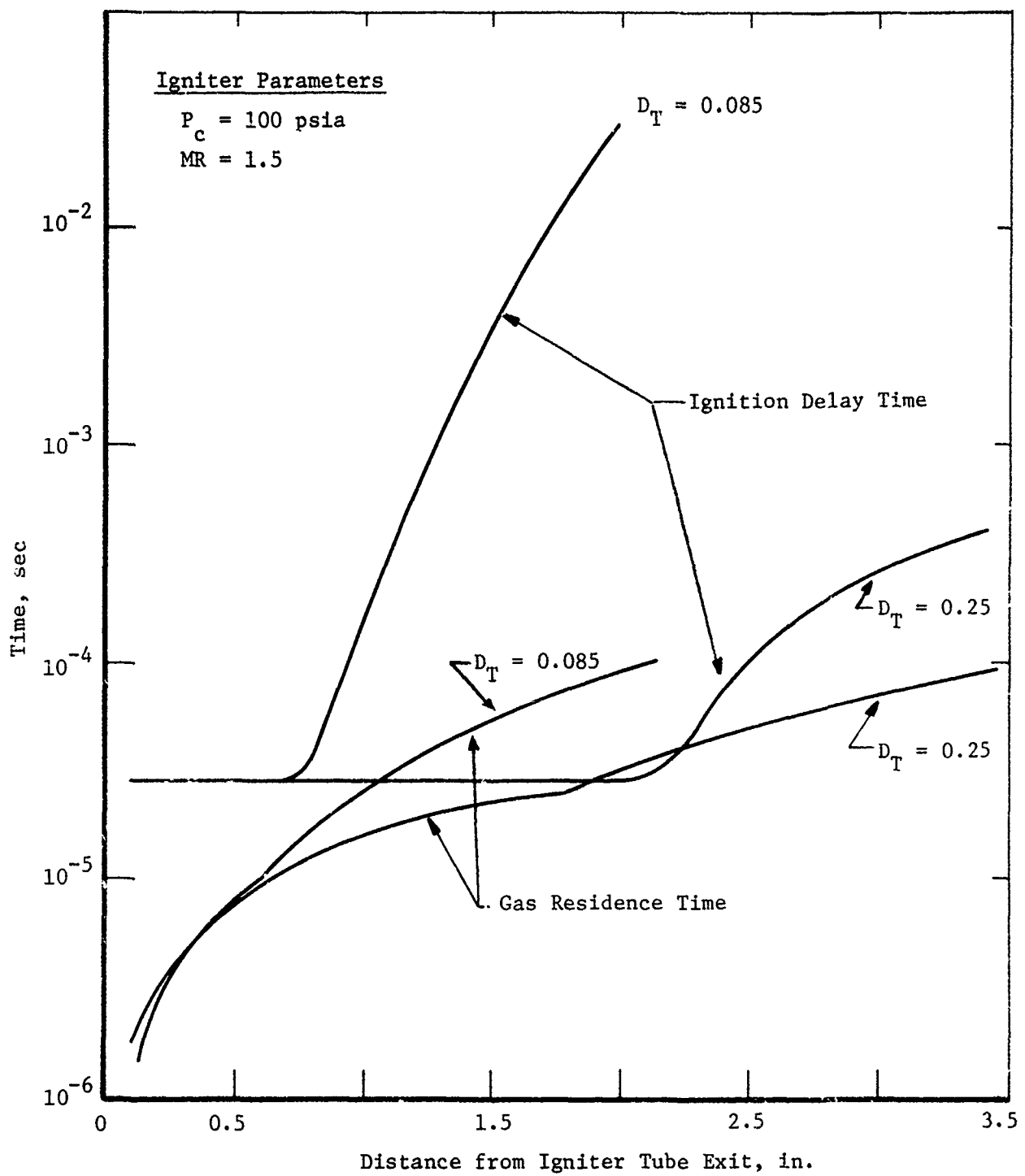


Figure 97. Effect of Igniter Throat Size on Ignition

III, C, Testing (cont.)

Although it was possible to produce ignition by either increasing the chamber pressure to 1000 psia or increasing the igniter throat diameter to 0.250 in., neither technique was practical within the existing constraints. Operation at 1000 psia would cause overheating of the uncooled igniter hardware, resulting in hardware damage, and the igniter tube could not be made larger in diameter due to the restriction of the injector vane spacing. Use of an elongated igniter tube was considered; it was rejected due to compatibility problems which could be caused by blockage of the injector hydrogen flow. The selected igniter operating conditions are listed below:

$$\begin{aligned}P_c &= 100 \text{ psia} \\MR &= 2.0 \\\dot{w}_T &= 0.00228 \text{ lb/sec} \\D_T &= 0.085 \text{ in.}\end{aligned}$$

The selected E-D nozzle injector start sequence, based on the above studies, is shown in Figure 98. The igniter valves are sequenced so that the spark begins about 100 ms ahead of the igniter flow. Igniter fuel and oxidizer are started simultaneously. The oxidizer valve is sequenced such that the oxidizer manifold pressure begins to rise 100 to 150 ms after igniter ignition. The fuel valve is sequenced so that the fuel manifold pressure begins to rise 20 to 30 ms after the start of oxidizer flow. The slight oxidizer lead is required to permit ignition between the igniter exhaust and the injector oxidizer prior to the introduction of the cold hydrogen. Hydrogen leads are to be avoided since there is a danger of quenching the igniter exhaust.

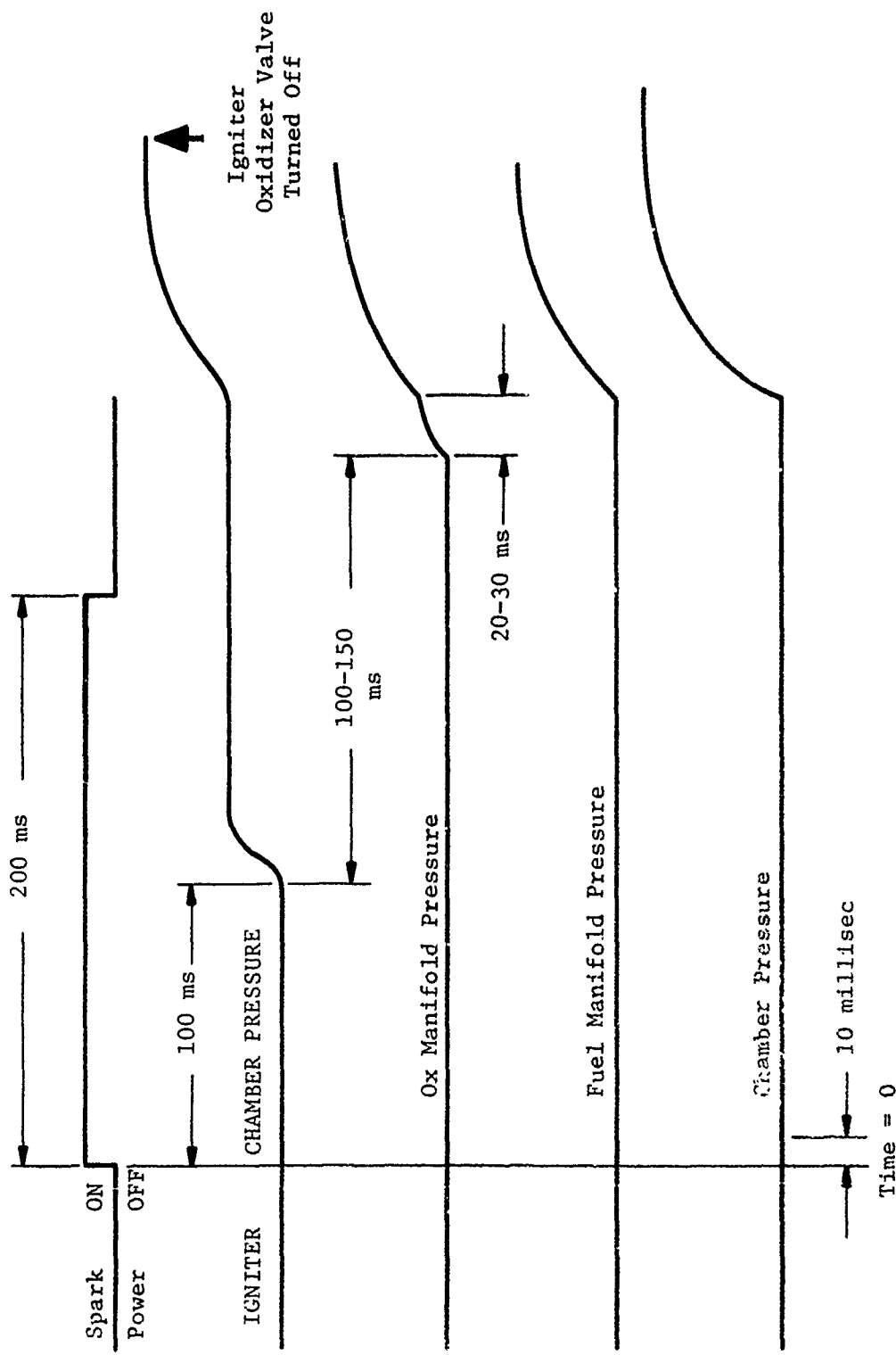


Figure 98. Injector Start Sequence

III, C, Testing (cont.)

An injector-to-igniter assembly, which simulated the injector installation, was fabricated and tested to verify hardware durability and to provide igniter response information for subsequent use in defining the start sequence. Figure 99 shows the hardware after testing. The test results are shown in Figure 100.

The igniter performed well on all tests with no observed ignition delay. The unit was then held for the sector thrust chamber hot fire testing later in the program.

2. Sector TCA Testing

a. Facility Buildup and Preparation

All fire testing was accomplished in Test Area A (Research Physics Laboratory). Preparation included thrust mount fabrication and flow system modification. The completed facility is capable of handling TCA's using LO₂/GH₂ propellants with thrust levels of up to 25K. Figure 101 and Table IX show the system schematic and attendant nomenclature; a photograph of the facility is shown in Figure 102.

b. Testing

The sector TCA was subjected to a total of six tests which are summarized in Table X. These tests were preceded by a series of igniter checkout tests which confirmed excellent igniter operation with no measurable ignition delay. During the test series, the propellant feed system performed excellently. Smooth engine ignition was accomplished on all tests using approximately a 30-ms oxidizer lead to the injector. A typical engine test is shown in Figure 103; note chamber pressure was extremely smooth. The appropriate nomenclature is shown in Table IX. The high frequency transducer located in the fuel manifold showed no indication of high frequency instability.

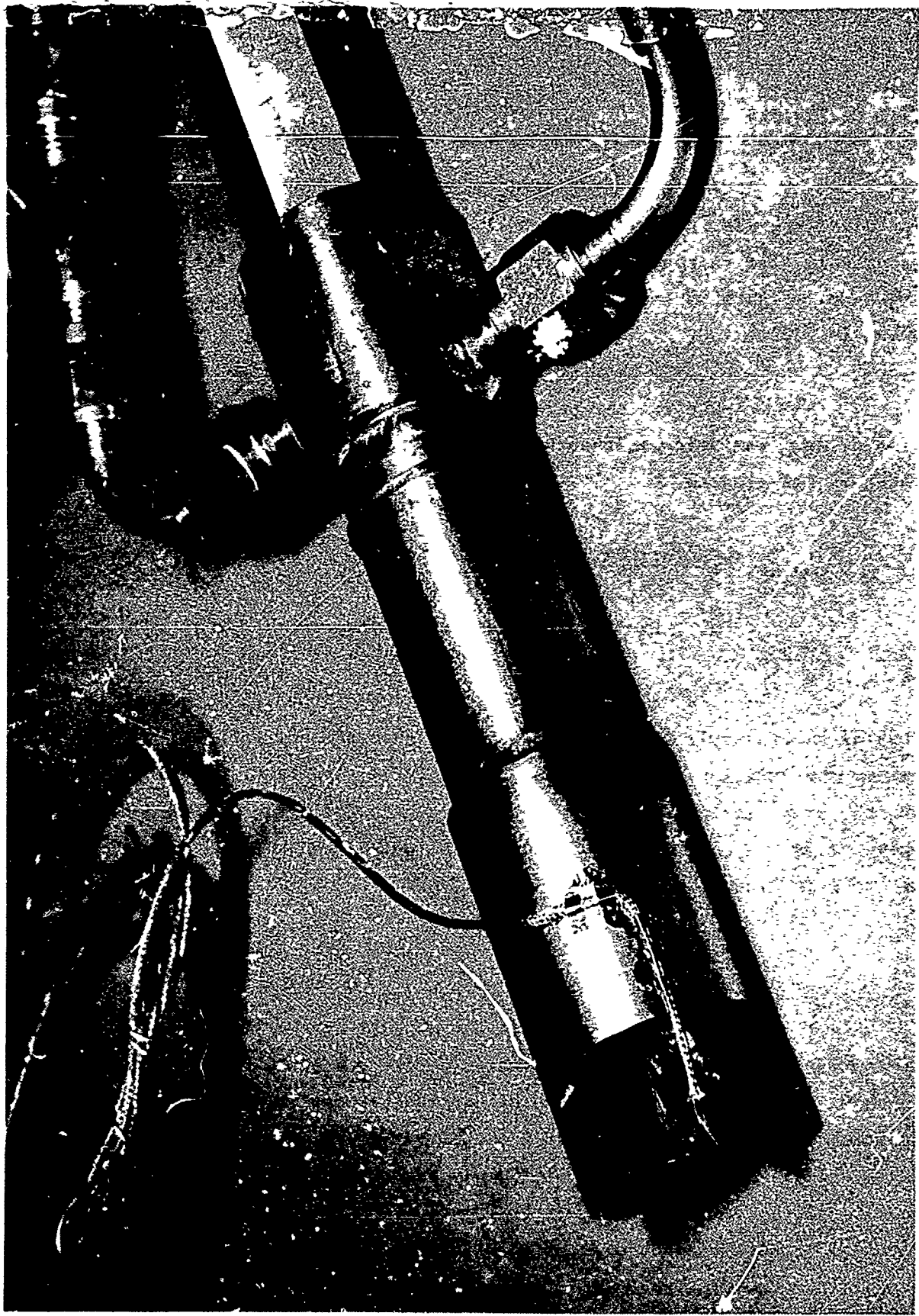
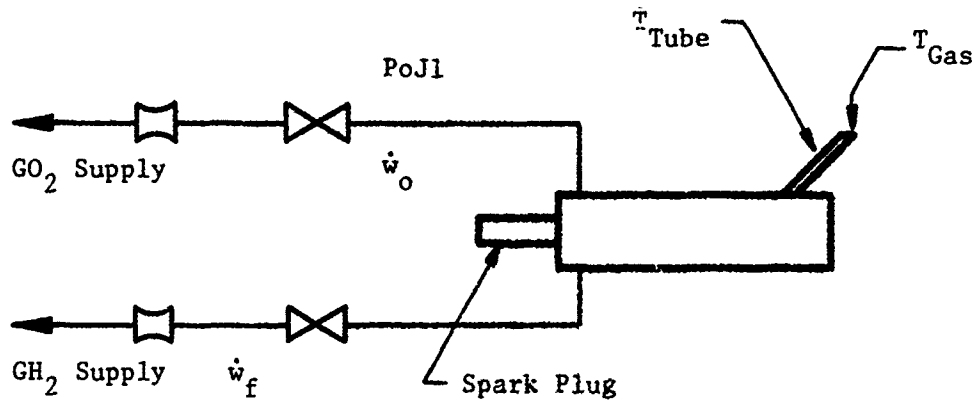
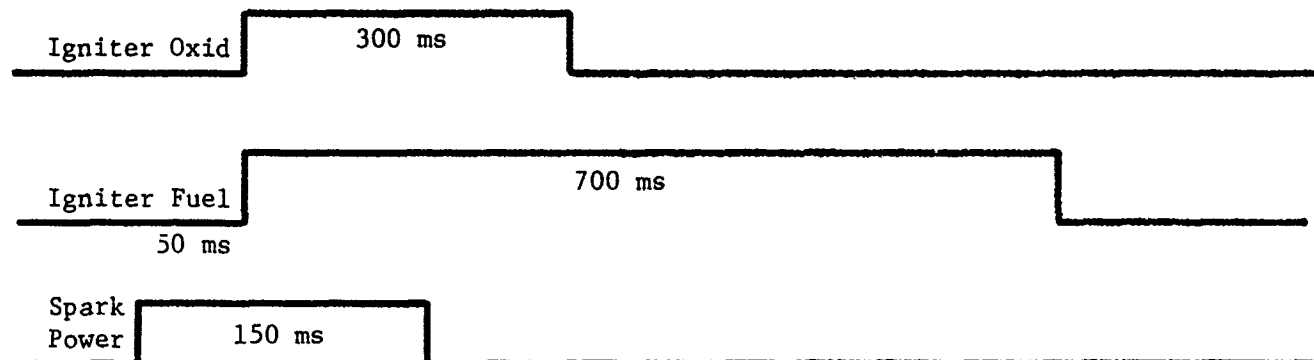


Figure 99. Ignition Test Apparatus



START SEQUENCE



Test No.	\dot{w}_o , lb/sec	\dot{w}_f , lb/sec	Igniter Ox Manifold Pressure, psia	Igniter Mixture Ratio (MR)	Igniter Tube Temp, °F	Gas Temp, °F	Firing Duration, sec
1	0.00173	0.00173	141	1.0	610	1300	0.3
2	0.00232	0.00173	161	1.34	880	1740	0.3
3	0.00232	0.00145	158	1.6	985	2010	0.3
4	0.00232	0.00116	141	2.0	1140	*	0.3

*Thermocouple inoperative.

Figure 100. Ignition Test Results

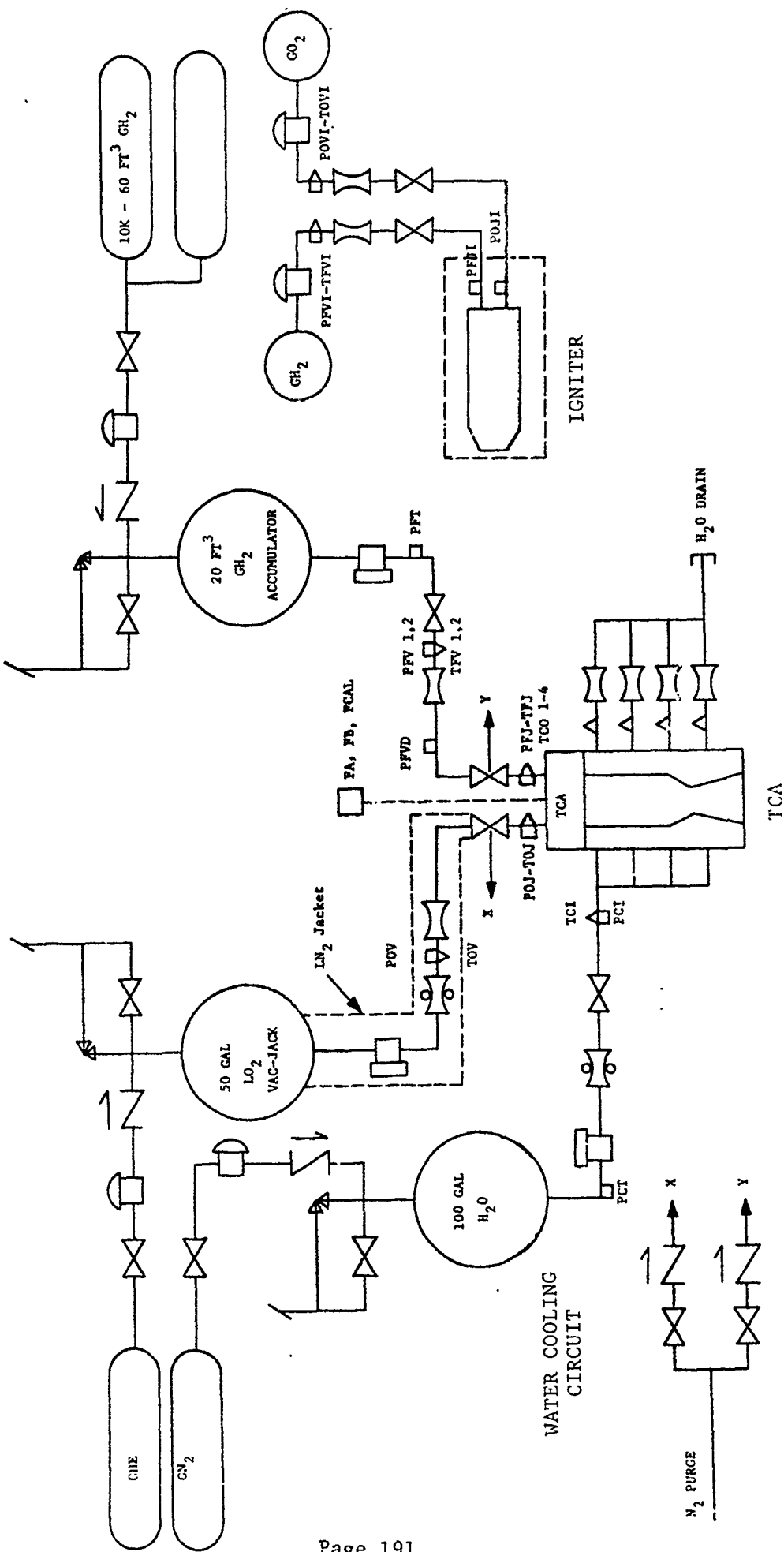


Figure 101. Test Schematic for Water-Cooled Chamber/Sector Injector

TABLE IX
TCA TESTING NOMENCLATURE

PCT	- Pressure, water coolant tank
TC1	- Temperature, coolant inlet
PC1	- Pressure, coolant inlet
POV	- Pressure, oxidizer venturi
TOV	- Temperature, oxidizer venturi
POJ	- Pressure, oxidizer injector inlet
TOJ	- Temperature, oxidizer injector inlet
FA	- Thrust channel A
FB	- Thrust channel B
FCAL	- Thrust calibration
PFT	- Pressure, fuel tank
PFV1,2	- Pressure, fuel venturi inlet (2)
TFV1,2	- Temperature, fuel venturi inlet (2)
PFVD	- Pressure, fuel venturi outlet
PFJ	- Pressure, fuel injector inlet
TFJ	- Temperature, fuel injector inlet
TCO	- Temperature, coolant outlet
PFVI	- Pressure, igniter fuel venturi inlet
TFVI	- Temperature, igniter fuel venturi inlet
POVI	- Pressure, igniter oxidizer venturi inlet
TOVI	- Temperature, igniter oxidizer venturi inlet
PFJI	- Pressure, igniter fuel inlet
POJI	- Pressure, igniter oxidizer inlet
LOTCV	- Oxidizer thrust chamber valve trace
LFTCV	- Fuel thrust chamber valve trace
FTCV	- Signal to fuel thrust chamber valve
OTCV	- Signal to oxidizer thrust chamber valve
IOTCV	- Signal to igniter oxidizer valve
IFTCV	- Signal to igniter fuel valve
SPK	- Signal to spark power supply

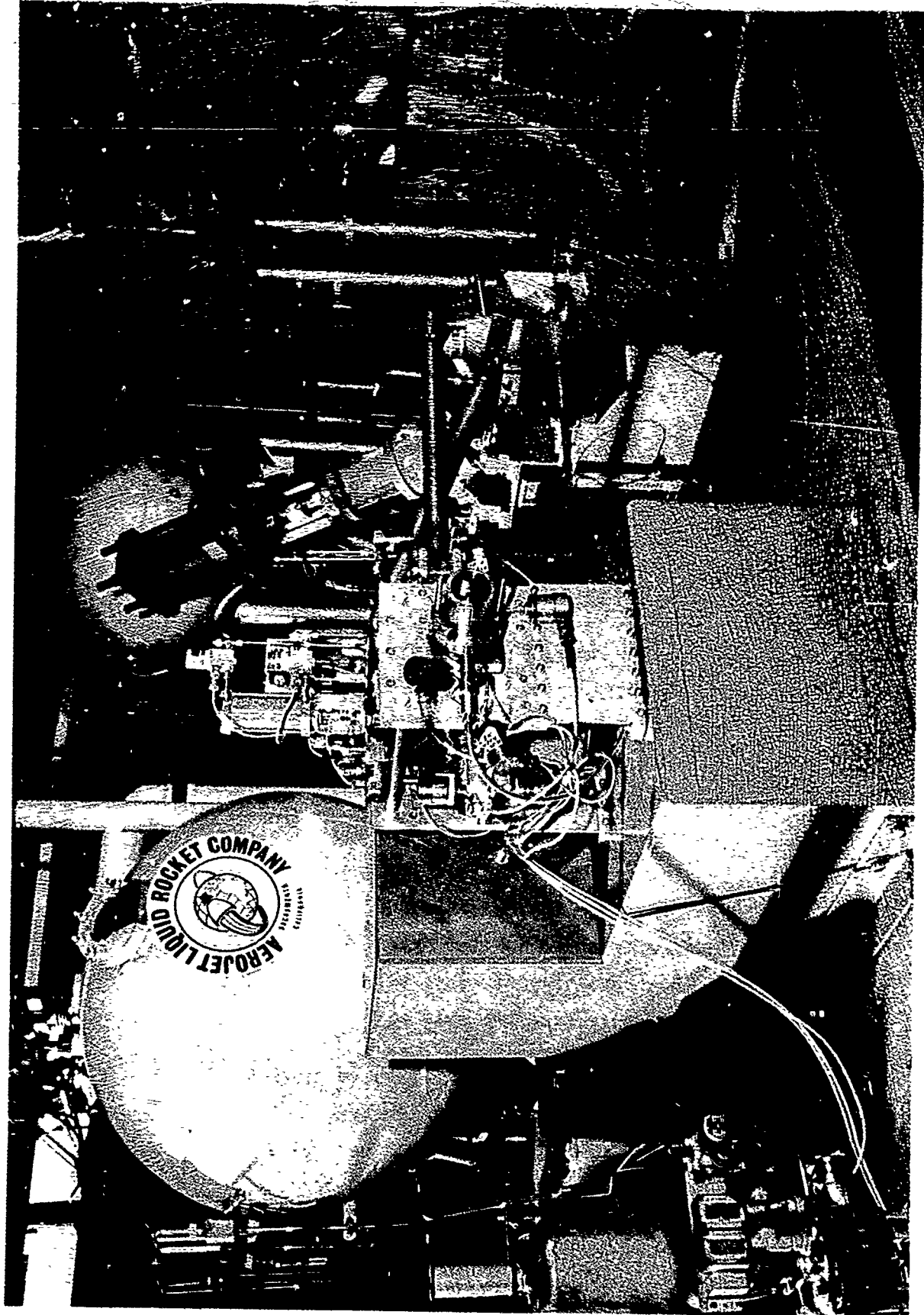


Figure 102. Mounted Thrust Chamber and Injector

SECTOR THRUST CHAMBER TEST DATA PERFORMANCE SUMMARY

Test No.	103	103	104	104	105	105	106
Data Period	1.08-1.26	1.74-1.92	1.10-1.28	1.72-1.90	0.98-1.16	1.62-1.80	4.92-5.06
P_c (meas), psia	326	323	320	319	330	327	747
P_{oj} , psia	406	400	406	400	440	426	1200
P_{fj} , psia	363	362	353	350	357	352	825
\dot{w}_{LO_2} , lb/sec	1.41	1.41	1.47	1.48	1.61	1.63	3.22
\dot{w}_{H_2} , lb/sec	0.280	0.271	0.250	0.244	0.230	0.223	0.585
\dot{w}_T , lb/sec	1.69	1.69	1.72	1.73	1.85	1.85	3.81
MR_{TCA}	5.036	5.203	5.880	6.066	7.000	7.309	5.504
$\bar{F}_{S.L.}$, lb	512	500	505	492	519	504	1220
$I_{sp}(S.L.)$, sec	303.0	296.0	293.6	284.4	282.1	272.4	320.2
$I_{sp}(\text{vac})$, sec	329.3	323.0	318.9	311.5	306.4	296.5	332.2
c^* , ft/sec	7714	7639	7440	7357	7173	7057	7517
A_t , in. ²	1.243	1.243	1.243	1.243	1.243	1.243	1.19
A_e , in. ²	3.092	3.092	3.092	3.092	3.092	3.092	3.081
A_e/A_t	2.488	2.488	2.488	2.488	2.488	2.488	2.488
T_{oj} , °R	198	190	190	186	198	186	180
T_{fj} , °R	493	499	493	499	492	496	500
$I_{sp}(\text{ODE})$, vac, sec	370.8	368.9	361.0	356.0	346.9	342.4	368.0
$c^*(\text{ODE})$, ft/sec	7865	7820	7630	7580	7320	7230	7730
% $I_{sp}(\text{vac})$	88.8	87.6	88.4	87.5	87.9	86.6	90.3
% c^*	98.1	97.7	97.5	97.1	98.0	97.6	97.2

Nomenclature:

- P_c - Chamber pressure (measured at the injector face)
- P_{oj} - Injector oxidizer manifold pressure
- P_{fj} - Injector fuel manifold pressure
- F - Thrust
- A_t - Throat area
- A_e - Exit area
- T_{oj} - Injector oxidizer manifold temperature
- T_{fj} - Injector fuel manifold temperature

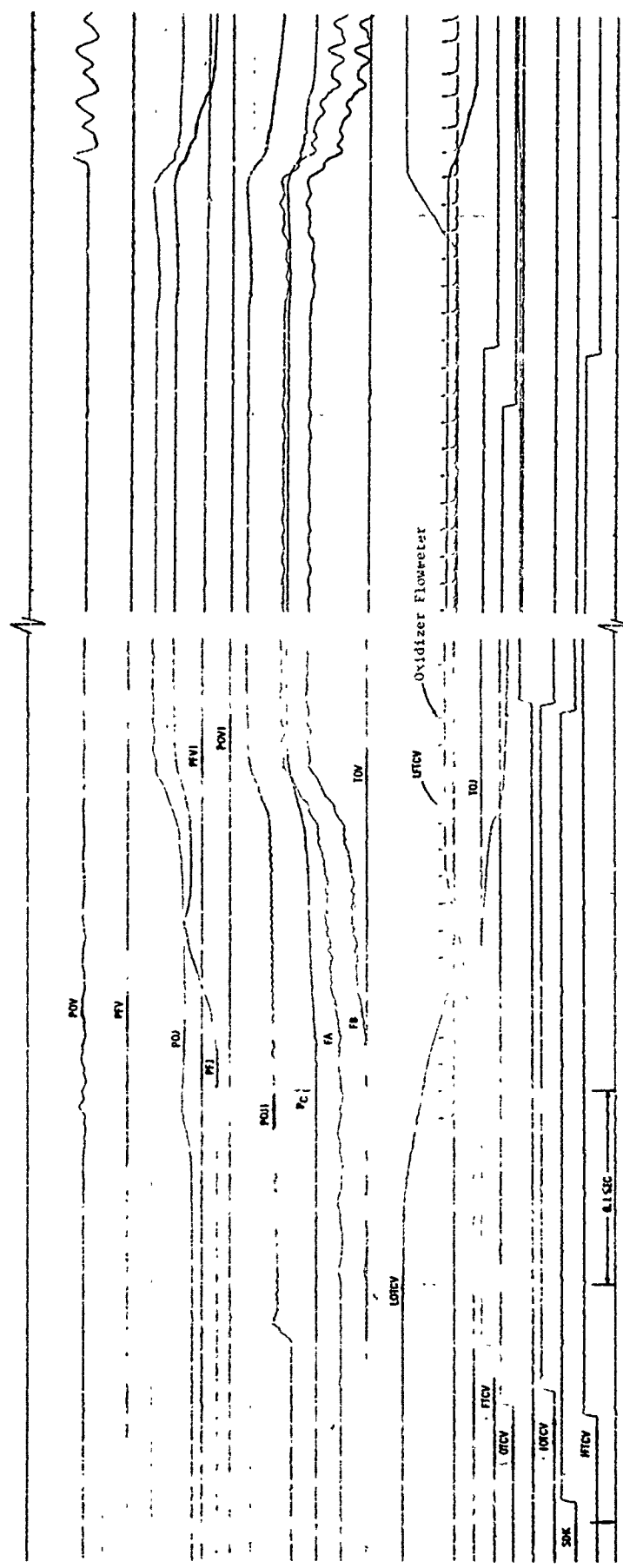


Figure 103. Test 3K-6-104 oscilloscope trace

III, C, Testing (cont.)

Tests -101 through -105 were all run at a nominal chamber pressure of 300 psia using the uncooled axial throat chamber.

The first two of the tests shown above were to checkout the system and verify engine start sequence. Tests -103 through -105 were a mixture ratio survey to determine injector performance. The water-cooled chamber was installed for Test -106, which was to be run at a nominal chamber pressure of 700 psia. Test data indicate that the chamber failed approximately 250 ms into the run and that the failure was due to a reduction in coolant water flow attributed to the formation of ice in the coolant passages during pretest oxidizer cold flows and injector prechill. Posttest examination of the injector revealed no damage; two of the thrust chamber's four sides were burned out. The procedures used prior to and during the test are described below.

A summary of the test data taken at two time periods for each test is shown in Table X.

The failure of the water-cooled chamber resulted in termination of the sector TCA test program and is discussed in the following paragraphs.

(1) Pretest Procedures

Several water cold flow tests were conducted on the water-cooled chamber prior to engine testing. These tests were conducted both prior to installation of the thrust chamber on the test stand and with the fully assembled unit on the stand using the coolant feed system. These tests are summarized below:

Pre-Installation Flow Tests - The four chamber cooling circuits were flowed individually at 1400 psia inlet pressure to obtain Kw values; the reduced pressures were used to ensure the safety of the individuals conducting

III, C, Testing (cont.)

the test. The results were compared to data obtained on the individual panels (corrected for predicted manifold ΔP) prior to their final brazing, then corrected to the 1400 psig inlet test pressure.

Chamber Section	Location	Water Flow Rates, lb/sec		
		(1) Pred. @ 1400 psi	(2) Meas. @ 1400 psi	Pred. 2000 psi Based on (2)
23 chan.	Outer body	5.33	4.45	5.31
13 chan.	Inner body	3.03	2.58	3.08
15 chan.	Side plate	3.56	3.55	4.24
15 chan.	Side plate	4.02	3.55	4.24
	Total	15.94	14.13	16.87

The difference in predicted side plate flows (1) is due to measured flow differences prior to assembly of the four side members into the thrust chamber. Measurements (2) at 1400 psia indicated the two side plates flowed identically on the assembled chamber.

These data indicated an increase in pressure drop of 16% which was attributed to errors in predicting manifold pressure drop. As a result, it was decided to run all tests at the maximum design inlet pressure of 2000 psi in order to (1) achieve the desired flow rate, (2) achieve highest possible cooling margin at the lower chamber pressures, and (3) to avoid resetting coolant pressures between tests.

Installed Flow Tests - Approximately ten water flow tests were conducted with the chamber ready for firing using the water feed system shown in Figure 101. These tests are summarized below:

III, C, Testing (cont.)

(a) Test No. 1 - This test was conducted at reduced pressure and resulted in 40% overshoot in water manifold pressure (at 500 psia). This was using GN_2 for actuation of the water valve.

(b) Test No. 2 - The second flow test followed a change in the actuation fluid to a mixture of water and glycol. This resulted in elimination of the pressure spike.

(c) Tests No. 3 through 9 - Water tank set pressures, system ΔP , and flow rates were then established over the range of 500 to 2000 psi. These data resulted in the decision to run the system at a constant inlet pressure of 2000 psi for the 700 and 1100 psia chamber pressure test series; this gave a water flow rate of 17.7 lb/sec which was calculated to be thermally adequate. The measured flow of 17.7 lb/sec was only 6% higher than the predicted value of 16.9 lb/sec based on the individual circuit flow tests at reduced pressure.

(d) Tests No. 10 and 11 - The final cold flow tests were in recognition that freezing in the coolant passages was a potential problem. The following fire simulation test was accomplished to ensure that the engine start sequence would not result in freezing of the coolant. An oxidizer cold flow was run for \approx 3.0 sec to obtain set pressures and flow rates. A following 10-sec delay simulated the time required to initiate a fire test, followed by a water flow test. The water circuit responded as it had during item (c) with full flow confirmed by the water flow meter. This test was considered to show that plugging due to freezing was not a problem under normal conditions.

(2) System Safety Device

Two parameters were used either to halt or prevent a test:

(a) To ensure proper coolant inlet pressure/water flow rate, the chamber water inlet pressure sampling was initiated prior to engine valve sequence; a minimum value of 1500 psi was established.

III, C, Testing (cont.)

(b) Beginning 100 ms after igniter shutdown, a chamber pressure less than 500 psi (for a 700 psi nominal P_c) would terminate the test.

(3) Test 3K-6-106

Nominal test conditions were to be as follows:

MR = 6.0
 P_c = 700 psia
Duration = 10 sec

During the oxidizer cold flow (III,C,2,b,(1),(d)), it was noted that the LO_2 flow rate was approximately 20% low using predicted set pressures. Subsequently, two more cold flow tests were conducted to establish proper flow rates. These resulted in the actual test sequence being unlike that simulated in the flow testing (item III,C,2,b,(1),(d) above).

Test fire sequencing successfully established on the prior 300 psi tests was followed; namely (1) a 3-sec oxidizer flow to chill the oxidizer circuit and ensure liquid at the OTCV, (2) fuel and oxidizer purge, and (3) automatic sequence to fire which included a 30-ms oxidizer lead. This sequence was considered to ensure the most safe start since the liquid flow through the vanes prevents fuel from entering the vanes during the start transient.

Posttest examination of the records revealed that the water valve opened normally (some 4 sec prior to engine valves). Water flow meter data show the line and manifold fill. This was followed by extremely low flow which increased to about 30 to 40% of nominal at initiation of chamber pressure; inlet pressure was constant at 2000 psi. Engine chamber pressure held constant for approximately 250 ms, then started to decay, indicating throat erosion. The 500 psi shutdown terminated the test after 1.7 sec.

III, C, Testing (cont.)

(4) Conclusions

(a) The data discussed above indicate that there was substantially reduced coolant water flow. This was due to ice which formed in the coolant passages subsequent to oxidizer cold flow tests used for final tank pressure settings.

(b) Actual pretest oxidizer cold flows imposed on the chamber exceeded the conditions simulated during the flow test described in Section III,C,2,b,(1),(d) above.

(c) The shutdown parameters used were not adequate to prevent failure due to low coolant flow. Future tests should use the flow meter output as a kill parameter in conjunction with inlet pressure.

c. Sector Injector Test Data - Performance Analysis

Test data and corresponding calculated thrust chamber performance from four sector tests are shown in Table X. The first three tests included in Table X (Nos. -103, -104 and -105) were conducted at a nominal chamber pressure of 300 psia using an uncooled copper heat sink combustion chamber. The last test (No. -106) was conducted at a nominal chamber pressure of 700 psia using the water-cooled thrust chamber. The combustion chamber failed during the latter test at approximately 250 msec and thus only very short duration data are available.

The performance results from the first three (uncooled) sector tests are shown as a function of mixture ratio in Figure 104. Also included in the figure for comparison are the various theoretical specific impulse

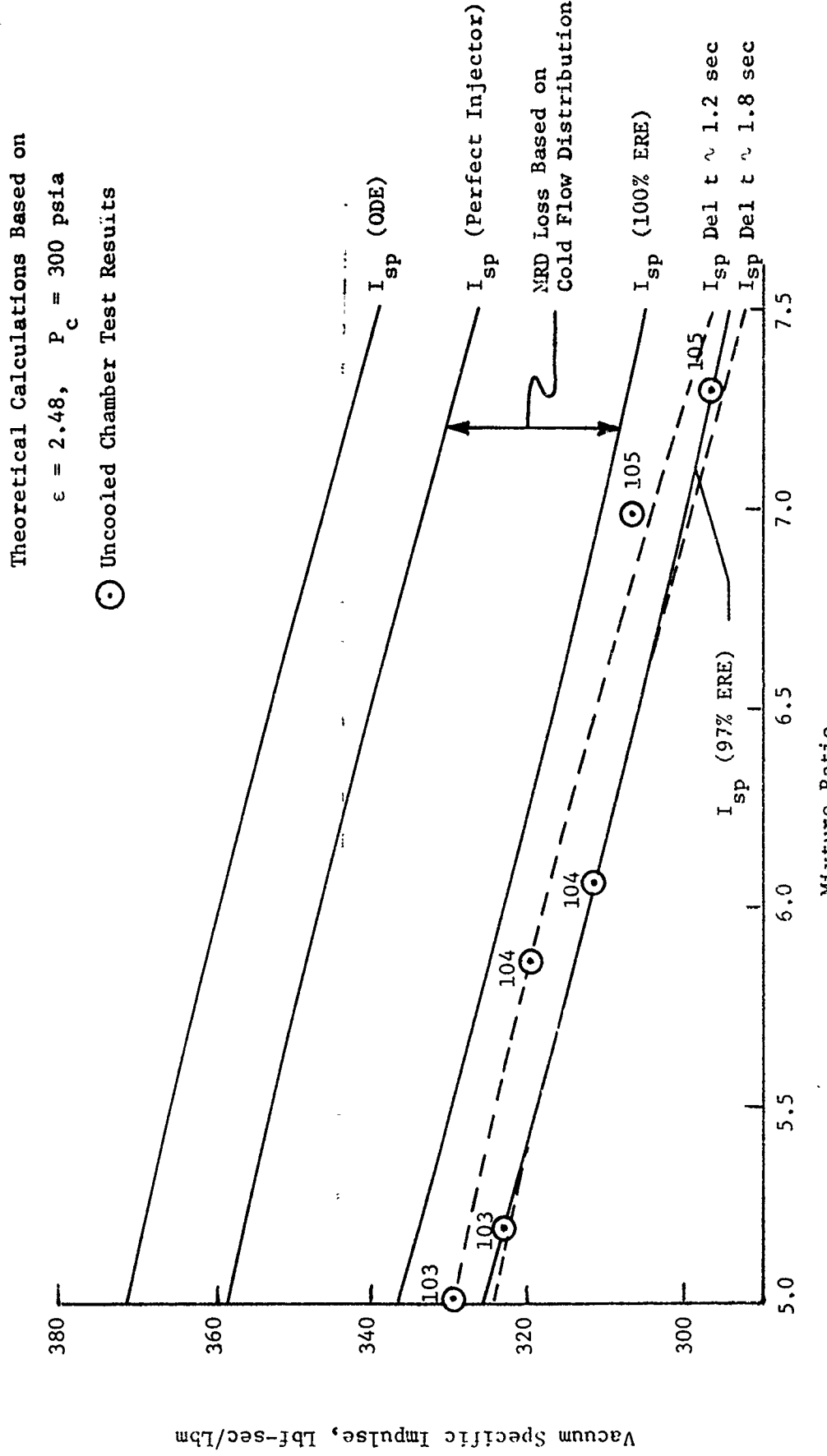


Figure 104. E-D Sector Thrust Chamber Test Performance

III, C, Testing (cont.)

calculations* based on (1) One-Dimensional Equilibrium (ODE); (2) perfect injector ($I_{sp}(ODE)$ = KL-BLL-DL); (3) $I_{sp}(100\% ERE)$ ($I_{sp}(\text{perfect injector})$ = MRDL); and (4) $I_{sp}(97\% ERE)$ ($I_{sp}(100\% ERE)$ = $0.03 I_{sp}(ODE)$). The measured performance efficiencies ($I_{sp \text{ test}}/I_{sp(ODE)}$) varied from approximately 90.3% to 86.6% and were primarily influenced by the test data period indicating that steady-state conditions may not have been reached.

The mixture ratio distribution performance loss shown in Figure 103 was determined from a stream tube analysis based on the mixture ratio distribution established from cold flow testing (see Section III,C,2,b,(1)). The mixture ratio distribution performance loss calculated on this basis varied from 5.7% at a mixture ratio of 5.0 to 6.3% at mixture ratios of 6.0 and 7.0.

The kinetic loss (KL \sim 1.0 lbf-sec/lbm) was calculated using the JANNAF One-Dimensional Kinetic (ODK) computer program. The boundary layer loss (BLL \sim 8 lbf-sec/lbm) was calculated using the boundary layer chart procedure described in Appendix B of CPIA No. 178. The divergence loss (DL \sim 4 lbf-sec/lbm) was calculated using a method-of-characteristics annular nozzle computer program (FD0027).

Comparison of the experimental performance data and the theoretical specific impulse calculations based on the measured cold flow distribution indicate that a 97% energy release efficiency was achieved at the 300 psia operating level near the end of the test duration (see Figure 103). The injector efficiency ($1.0 - [I_{sp}(\text{perfect injector}) - I_{sp(\text{test})}] / I_{sp(ODE)}$), which includes the combined effects of mixture ratio maldistribution and incomplete energy release, is approximately 0.90 over the range of mixture ratio investigated.

*Theoretical specific impulse calculations were made using the procedures recommended by the JANNAF Liquid Rocket Performance Subcommittee (CPIA No. 178). Nomenclature is as follows: KL = kinetic loss, BLL = boundary layer loss, DL = divergence loss, MRDL = mixture ratio distribution loss, ERL = energy release loss, and ERE = energy release efficiency.

III, C, Testing (cont.)

An assessment of performance using c^* data showed the characteristic velocity efficiency, based on the chamber pressure measured at the head end of the combustion chamber, to be approximately 0.97 to 0.98 over the range of test conditions. The chamber pressure port was located in the injector body with its inlet between the oxidizer vanes just upstream of the vane's trailing edge and, thus, the measured c^* values shown in Table IX must be corrected for stagnation pressure loss because of combustion at finite Mach number as well as total pressure loss across the vanes.

The magnitude of the stagnation pressure correction is approximately 4% which results in corrected c^* efficiencies between 93.2 and 94.4%. The nozzle and kinetic losses account for a total of 3.5% as identified above. This, combined with the calculated MRD loss, results in injector c^* efficiencies approaching 100% which indicate a somewhat higher ERE than the 0.97 value calculated based on thrust measurements. A pressure loss of 2% across the vanes must be added to obtain agreement between c^* and thrust-based performance. This value is considered in general agreement with calculated and flow test derived fuel pressure drop, recognizing that there are uncertainties regarding the effect of combustion at the vane's trailing edge. It is concluded that the I_{sp} -based 0.97 ERE is confirmed by the c^* data and that this value is an accurate assessment of the performance of the tested vaned injector.

Although the program goal of 99.5% ERE was not demonstrated, the data obtained from the combination of analysis, cold flow testing, and hot firing identifies the principal areas for improvement. The largest loss by far is due to nonuniform propellant distribution. The cold flow measurements clearly indicate this problem and loss calculations show the magnitude of the performance decrement. However, the actual distribution during hot fire cannot be determined and, in all likelihood, was different than that inferred from the cold flow. It

III, C, Testing (cont.)

is concluded that modifications to either the basic injector design or combustion chamber length should be avoided. Any future activity should be directed to the avoidance of the orifice plugging which was experienced. Cold flow and hot fire testing of an unplugged unit would allow a more accurate assessment of the element performance. A second consideration is the fact that the vaporization efficiency of the injector is predicted to increase with increasing chamber pressure. Although the vaporization analysis predicts complete vaporization at the 300 psia level, it is conceivable that there is some inaccuracy in this calculation. Testing at higher chamber pressures for reasonable durations would verify the analysis.

d. Sector Injector Test Data - Vane Data

The injector vane thermocouples responded well on all tests, reaching steady state in approximately 0.5 sec. The steady-state temperature data from the four thermocouples obtained on Tests -103 through -106 are shown below; the test chamber pressure, mixture ratio, and oxidizer circuit Kw values are also noted.

Test	Temperature, °F				Oxidizer Circuit Kw	MR	P_c , psia
	Vane No. 1		Vane No. 2				
	Inner	Outer	Inner	Outer			
-103	13	-91	-22	-129	0.156	5.2	323
-104	4	-104	-33	-147	0.156	6.02	320
-105	-13	-126	-55	-163	0.157	7.3	330
-106	-67	-99	-107	-139	0.150	5.5	747

Conclusions to be drawn from the above temperature data are: temperature gradients from inboard to outboard locations on the vanes are on the order of 30 to 116°F and vane temperatures decrease with increasing mixture ratio and chamber pressure. Visual inspection of the vanes revealed no evidence of discoloration or heat marks that would be indicative of local vane overheating.

III, C, Testing (cont.)

The experimental values of oxidizer circuit Kw are based on liquid oxygen density at measured inlet values of temperature and pressure (Toj and Poj). These values, compared to the value of 0.144 obtained during water flow, indicate that the oxygen remained in the liquid state at the 300 psia chamber pressure level. If a significant amount of gaseous oxygen was produced, the test Kw values would be less than the water flow Kw. Further, in going from the 300 to 700 psi level, the test Kw's would have increased as the amount of gaseous oxygen decreased. The pressure drop data, combined with the above temperatures, indicate that the oxidizer remained liquid even at the minimum chamber pressure. This conclusion substantiates the design of the insulation platelets. The measured temperature gradient of 32°F (-106) compares favorably with the predicted gradient of 35°F obtained from Figure 43.

REFERENCES

1. Rao, G.V.R., "Exhaust Nozzle Contour for Optimum Thrust," Jet Propulsion, 28, June 1958, pp 377-383.
2. Rao, G.V.R., "Analysis of a New Concept Rocket Nozzle," Liquid Rockets and Propellants Progress in Astronautics and Rocketry, Vol 2, M. Summerfield (ed.), Academia Press, New York, 1960.
3. Rao, G.V.R., et al., Investigations of Gas Dynamic Problems in AGC Integrated Engine Components Feasibility Program, Final Report, AGC P.O. No. A29567, National Engineering Science Co., January 1963.
4. Priem, R. J., and Heidmann, M. F., Propellant Vaporization as a Design Criterion for Rocket-Engine Combustion Chambers, NASA TR R-67, 1960.
5. JANNAF Interim Performance Calculation Methodology for Use in the SSME Proposal Response, Addendum No. 1 to the CPIA Publication No. 178, December 1970.
6. Pieper, J. L., ICRPG Liquid Propellant Thrust Chamber Performance Evaluation Manual, Report 178, Chemical Propulsion Information Agency, September 1968.
7. McBride, B., and Gordon, S., ICRPG One-Dimensional Equilibrium Reference Program, NASA SP-273, 1971
8. One - Dimensional Kinetic Nozzle Analysis Computer Program, ICRPG Performance Standardization Working Group, 30 July 1968 (available through CPIA), AD 841201.
9. Two - Dimensional Kinetic Nozzle Analysis Computer Program, ICRPG Performance Standardization Working Group, 30 July 1968 (available through CPIA), AD 841200.
10. JANNAF Interim Performance Calculation Methodology for Use in the SSME Proposal Response, adopted by the Performance Standardization Working Group, 14 December 1970.
11. Turbulent Boundary Layer Nozzle Analysis Program, ICRPG Performance Standardization Working Group (available through CPIA), AD 841202.
12. Mueller, T. J., "Determination of the Turbulent Base Pressure in Supersonic Axisymmetric Flow," Journal of Spacecrafts and Rockets, Vol 5, No. 1, January 1968.

REFERENCES (cont.)

13. Ito, J., "Friction Factors in Turbulent Flow in Curved Pipes," Trans-ASME. D, 81, 1959, pp 123-134.
14. Hess, H. L., and Kunz, H. R., "A Study of Forced Convection Heat Transfer to Supercritical Hydrogen," ASME Paper No. 63-WA-205, 1963.
15. Heat Transfer to Cryogenic Hydrogen Flowing Turbulently in Straight and Curved Tubes at High Heat Fluxes, NASA CR 678, 1967.
16. Taylor, M. F., "Applications of Variable Property Heat Transfer and Friction Equations to Rocket Nozzle Coolant Passages and Comparison with Nuclear Rocket Test Results," AIAA Paper No. 70-661, 1970.
17. Louison, R., and Pieper, J. L., Hydraulic Analysis of the Titan III Second Stage Injector, ALRC TCER 9642:0107, 25 September 1969.
18. Brokaw, R. S., Tenth Symposium on Combustion, The Combustion Institute, Pittsburgh, Pa., 1965, p 269.
19. Forstall, Jr., W., and Shapiro, A. H., Momentum and Mass Transfer in Coaxial Gas Jets, Meteor Report No. 39, Dept of Mech Engr, MIT, July 1969.
20. Hines, W. S., Development of Injector/Chamber Compatibility Analyses, Final Report AFRPL-TR-70-12, March 1970.
21. Ingebo, Robert D., Penetration of Drops into High-Velocity Airstreams, NASA TM X-1363, April 1967.